SPIN-POLARIZED ELECTRON TRANSPORT THROUGH ORGANIC MAGNETIC MOLECULES

ASHIMA

A thesis submitted for partial fulfilment of

the degree of Doctor of Philosophy

Institute of Nano Science and Technology, Mohali,
Knowledge city, Sector-81, SAS Nagar, Manauli PO, Mohali 140306, Punjab, India.
Indian Institute of Science Education and Research Mohali,
Knowledge city, Sector-81, SAS Nagar, Manauli PO, Mohali 140306, Punjab, India.

August 2022

Dedicated to my Parents

Declaration

The work presented in this thesis has been carried out by me under the guidance of Prof. Md. Ehesan Ali at the Institute of Nano Science and Technology, Mohali. This work has not been submitted in part or in full for a degree, a diploma, or a fellowship to any other university or institute. Whenever contributions of others are involved, every effort is made to indicate this clearly, with due acknowledgement of collaborative research and discussions. This thesis is a bona fide record of original work done by me and all sources listed within have been detailed in the bibliography.

Ashima

In my capacity as the supervisor of the candidate's thesis work, I certify that the above statements by the candidate are true to the best of my knowledge.

Prof. Md. Ehesan Ali

Acknowledgment

You can do right things and you can even do it for the right reasons
But if you don't have a right guidance, you can never bit a right target.

The process of earning a doctorate is long and is certainly not done singlehandedly. With a great sense of gratitude, here, I would like to take an opportunity to acknowledge the people who stood beside me in this journey.

First and foremost, I would like to express my sincere gratitude to my supervisor **Prof. Md. Ehesan Ali** for introducing me to world of scientific research. His constant vigilance, great enthusiasm, positive outlook, valuable suggestions, and worthy criticism helped me to carry on with my projects. He gave me enough freedom in thinking and choosing my own problems. *Hard skills can be learned, soft skills make the difference*. I owe him my sincere thanks starting from teaching me the art of writing a manuscript to polishing my communication skills, instigating self-confidence and widening up my critical thinking approach. I must confess that I couldn't expect for a better outcome.

Besides my supervisor, I would like to extend my gratitude to my Ph.D. committee: **Dr. Suvankar Chakraverty** and **Dr. Chandan Bera** for their feedback and encouragement in the annual evaluation meetings. Their critical comments has always stimulated me to widen my research from various perspectives. I am extremely grateful to my experimental collaborators **Dr. Jayamurugan Govindasamy** and **Prof. Prakash P. Neelakandan** for giving me an opportunity to work with them and expanding my knowledge base.

I extend my deep appreciation to all the TSCM lab members. The kind help and support of TSCM group members have made my study and life at INST Mohali a cherished time. I am indebted to my seniors **Dr. Prabhleen Kaur** and **Dr. Aashish Bhatt** for their invaluable advises and teaching me the computational techniques. I am especially grateful to have **Rishu Khurana** as my companion who was my roomate, labmate as well as a co-author in a couple of projects. Her strenuous support and co-operation made my Ph.D. journey much smoother. I am thankful to **Aritra Mukhopadhyaya** who always went out of his way to solve our HPC and computer problems. Discussions on different scientific problems with **Shahjad Ali** deserve a special mention. A big thank also goes to **Shikha Sharma, Sakshi Nain** and **Manish**

Kumar for their constant help and encouragement. I would also like to thank them all for helping me proofread this thesis.

I would like to offer my thanks to **Dr. Munish Sharma** for his invaluable guidance and my co-authors **Dr. Marco Berritta** and **Aakanksha Sud**. I had the great fortune to nurture long-term friendship with **Kalyani Chordiya** and **Sameer Gupta** who always motivated me to set the bars high. A special thanks goes to **Dr. Rameshwar Lal Kumawat** who was always available to answer my questions about SIESTA. I am also glad to meet **Ambuj, Aseesh** and **Prateek** as Intern students.

Life is always been a tough task without good friends. I owe a big thank to my school friend **Ishu Aman Garg** who instigated me to join the Ph.D. programme and has always been there for me. **Chirag Miglani** was a constant throughout who always stood beside me through thick and thin of this journey. The support from **Vibhuti Mahajan** and **Priya Sachdeva** has been treasured. I feel pleasured to thank **Dr. Ramesh Reddy** from NITK Surathkal and **Deepak Garg** from BARC Mumbai, to whom I met at IISc Bangalore conference, for the constructive conversations and best wishes.

The funding agencies made it all possible. I would like to thank the Department of Science and Technology (DST) and the Institute of Nano Science and Technology (INST) Mohali, India, for providing me with Ph.D. fellowship and the infrastructural support. The financial support provided by INST Mohali for attending conferences is gratefully acknowledged.

I could have hardly completed my Ph.D. without the unconditional love and support from my family. I can't thank enough my father, who defined the ideology for my family, the man behind it all. My mother's blessings to complete my Ph.D. programme. Much appreciation and love goes to my brother, **Kanav Bajaj** and my sister, **Anam Mudit Mehta** who has been a constant source of energy and delight during this period of struggle. The tremendous support from the entire family and friends gave me enough strength to add a feather of a Ph.D. in the cap of ***Bajaj Family***.

Last, the Almighty for giving me strength to pursue this path.

Ashima

Abstract

The generation of spin polarized current and its transportation through molecular-species is a pre-requisite for spintronic devices delivering metallic features for one spin channel while insulating for the other. The primary aim of the thesis is to uncover the potential of Organic Magnetic Molecules (OMMs) for spintronic applications. The first principle description of spin polarization across metal-molecule-metal junction in general is not trivial and there are many open questions regarding the effect of presence of localized spin centers on electron transport through a molecular junction. In this thesis, we focus on the fundamental understanding of spin-polarized quantum transport phenomena mediated by organic radicals and proposal of novel strategies to incite sustainable spin polarization in molecular devices. The rational design and synthesis of thermally stable OMMs exhibiting strong magnetic exchange interactions ($2J$) has always remained a challenge due to transient nature of radical species. At first, we have investigated the electronic and magnetic properties of one of the recently emerged and thermally stable 1,2,4-benzotriazinyl (Blatter's) radical with the simultaneous modelling of several Blatter's based diradicals exhibiting strong ferromagnetic exchange interactions. Using a genre of DFT and wavefunction based CASSCF/NEVPT2 methods, we have introduced X-annulation as a novel strategy to reach even higher values of $2J$ with the simultaneous rigidification of molecular structure.

In the view of device applications, much cultivated stable organic radicals are then incorporated in a single molecule junction setup between two gold electrodes. Employing non-equilibrium Green's function (NEGF-DFT), we investigated the effect of localized spin centers on electron transport through molecular junctions. Quantum Interference (QI) effects play a crucial role in controlling the molecular conductance by allowing or prohibiting the electron to propagate across junction via constructive and destructive QI effects. We demonstrated that incorporating a radical center manipulates the QI features in such a way that meta coupled radicals yield high conductance as compared to para ones. This scenario is in complete contrast to non-magnetic molecules where para coupled molecules are predicted to be better conductors. Apart from the anomalous QI features, the spin filtering efficiency of several radicals attached to the framework of pentacene is investigated. We show that presence of unpaired electron is not a sole requirement to incite spin polarization in junctions. Several factors inherited from the electronic structure of radical moiety plays a decisive role in inducing spin filtering effects.

In another approach to achieve ultrafast control over spin polarization, we have pro-

posed a stimuli-based spin filter by utilizing a photo-responsive endoperoxide (EPO) based single molecule device. The photo-irradiation of EPO triggers the homolytic cleavage of the peroxide O–O bond generating a diradical intermediate centred on two O-atoms which facilitates high spin filtering efficiency when placed between gold electrodes. The broken conjugated scenario due to the peroxide bridge of EPO hinders the propagation of de Broglie waves across the molecular skeleton. On the other hand, the diradical intermediate of EPO yields high conductance for one of the spin configurations. The key role played by quantum interference (QI) effects in the dramatic modulation of conductance arising due to different degrees of conjugation along the photochemical reaction pathway of EPO is demonstrated.

Finally, with an objective to induce spin polarization for long range electron transport, we employed higher order polyacenes and cumulenes with intrinsic open shell ground state. Apart from the spin filtering effects, we investigated the length dependence of the conductance for aforementioned molecules with pronounced diradical character. The recent accomplishments in the design of molecular nanowires characterized by an increasing conductance with length, in violation to classical Ohm's law, has embarked the origin of "anti-ohmic" wires. This highly desirable behaviour for long-charge transport is investigated within unrestricted DFT formalism with spin and spatial symmetry breaking. The contrasting features of transmission spectra in closed shell (CSS) and open shell (OSS) state eventually evolves in the form of inverted attenuation factors in CSS and OSS ground state. An increase in conductance is observed in CSS state, while the onset of OSS ground state with the increasing molecular length enforces the regular decay of conductance. We postulate the preferential existence of molecule in CSS ground state as a guiding rule to observe the desired anti-ohmic behaviour.

Keywords: Molecular Spintronics, Single molecule junctions, Organic radicals, Blatter's radical, Magnetic exchange interactions, Spin filters, NEGF-DFT, Quantum interference, Endoperoxides, Anti-Ohmic.

Contents

List of Abbreviations

GMR	Giant Magnetoresistance
MCBJ	Mechanically Controllable Break Junction
STM	Scanning Tunneling Microscope
SFE	Spin Filtering Efficiency
SMMs	Single Molecule Magnets
CISS	Chiral Induced Spin Selectivity
HOMO	Highest Occupied Molecular Orbital
SOMO	Singly Occupied Molecular Orbital
LUMO	Lowest Unoccupied Molecular Orbital
PTM	Polychlorinated Triphenyl-Methyl
TEMPO	Tetramethylpiperidin-N-oxyl
NN	Nitronyl Nitroxide
OVER	Oxo-Verdazyl
NO	Nitroxy
PO	Phenoxy
TMM	Trimethylenemethane
PAHs	Polycyclic Aromatic Hydrocarbons
OSS	Open-shell Singlet
CSS	Closed-shell Singlet
NOON	Natural Orbital Occupation Number
CI	Configuration Interaction
ESR	Electron Spin Resonance
SQUID	Superconducting Quantum Interference Device
QI	Quantum Interference
EM	Extended Molecule
NEGF	Non-equilibrium Green's function

DFT	Density Functional Theory
BOA	Born-Oppenheimer Approximation
HF	Hartree-Fock
SCF	Self-Consistent Field
KS	Kohn-Sham
SIC	Self-Interaction Correction
LDA	Local Density Approximation
GGA	Generalised Gradient Approximation
WBL	Wide Band Limit
BS-DFT	Broken Symmetry DFT
CBS-DFT	Constrained Broken Symmetry DFT
CASSCF	Complete Active Space Self-Consistent Field
NEVPT2	n-Electron Valence State Perturbation Theory
UNO	Unrestricted Natural Orbitals
SIE	Self-Interaction Errors
MCSCF	Multi-configurational self-consistent field
MRPT	Multi-reference perturbation theory
OMMs	Organic Magnetic Materials
WFT	Wave Function Theory
FM	Ferromagnetic
AFM	Anti-ferromagnetic
MO	Molecular Orbital
DQI	Destructive Quantum Interference
CQI	Constructive Quantum Interference
CG	Conjugate Gradient
MPSH	Molecular Projected Self-consistent Hamiltonian
EC	Eigenchannels
DOS	Density of States
EPO	Endoperoxide

List of Figures

List of Tables

CHAPTER 1

Introduction

1.1 Molecular Spintronics

During the last decades, the rapid development in electronics has continued to follow Moore's law[1]. The realization of devices exhibiting an increasing number of transistors per computer chip has revolutionised the field of electronics by increasing the speed of data processing with reduced power consumption. In the pursuit of ongoing ultimate miniaturization of electronic devices, a new branch of molecular electronics has emerged with an idea of constructing the integrated circuits at an atomic or molecular level. The description of such nanoscale conductors where a functional molecule is interfaced with external electrodes requires a complete quantum-mechanical treatment of electrons.[2] The first concrete idea of using single molecules as electronic components was the molecular rectifier, suggested by Aviram and Ratner in 1974.[3] Tremendous applications of molecular electronics for next generation nanoelectronics has been realized experimentally including molecular rectifiers[4,5], switches[6,7], transistors[8] and interconnects.[9,10]

In the mainstream charge based electronics, only the charge of electron is manipulated to transport, read or write information. However, to meet the ever increasing demands of data storage and processing efficiency, the field of spintronics emerged out

as a promising alternative to charge-only based electronics. Spintronics exploits the intrinsic spin of electron and its associated magnetic moment as a carrier of information, in addition to the fundamental electronic charge. The spin based technology has become popular in a short span of time and is widely used to achieve improved functionalities for data storage and processing. The origin of spintronics can be traced back to discovery of giant magnetoresistance (GMR) effect in 1988. One of the scientific discovery that has moved from academic laboratory to industrial mass production of every read-head of high-density hard drives resulting in the award of 2007 Nobel Prize in physics to Albert Fert and Peter Grunberg.[11,12] The GMR effect was observed in magnetic multilayers which effectively demonstrated a significant change in resistance upon changing the relative magnetization of adjacent ferromagnetic layers. At present, spintronics encompasses a diverse range of phenomena addressing the problem of injecting, manipulating and detecting the electrons spins in solid state systems. The great potential of spintronic devices has been demonstrated in the production of Magnetoresistive Random Access Memories (MRAM), spintronic logic devices, magnetic field sensors, magnetic biosensing etc.[13,14]

Since 1999, another pillar of spintronics emerged out as an art of driving the spin through molecules, i.e. Molecular Spintronics. The blossoming field of molecular spintronics, at the crossroads between molecular electronics and spintronics, aimed at exploring how the unique properties offered by the molecules can marry the requirement of spin-based devices.[15] Molecular materials, in particular organic semiconductors, offer additional functionalities to device due to their long spin relaxation time, which permit them to retain the spin information over relatively long times.[16] Other advantages of the molecular materials includes their low density, flexibility, transparency and chemical versatility. Apart from these, the spin states of molecular magnets can be controlled with different stimuli (e.g. switchability with light, electric field, mechanical force, etc.).[17,18] The key ingredient for realizing a molecular spintronic device is the generation of spin polarization i.e., creating a non-equilibrium spin population. Conventionally, this can be achieved in two principal ways, first is by placing a non-magnetic molecular bridge between two ferromagnetic electrodes, while the other approach includes coupling of a magnetic molecule between two non-magnetic electrodes. Using the two aforementioned approaches, various possible spintronic devices are constructed which mainly falls into the following two categories:

(a) Molecular Spin Valves: Molecular spin valve is one of the basic spintronic device that consists of a non-magnetic molecule sandwiched between two ferromagnetic (FM) electrodes. Spin polarized charge carriers are first injected from the first FM electrode, transport or tunnel through the non-magnetic molecule and are detected after reaching the second FM electrode. When the relative magnetization direction of the two FM electrodes are parallel, the spin-polarized charge carriers experience less spin dependent scattering on the drain electrode and lead to a low resistance state, while the antiparallel configuration yields high-resistance state. The relative magnetization direction of two FM electrodes is changed by applying an external magnetic field, thus adjusting the resistance of the device which is referred to as the spin valve effect. The relative change of the resistance value is defined as magnetoresistance (MR) ratio (MR $(\%) = (R_H - R_L)/R_L \times 100\%$), where R_H and R_L refer to average high resistance and average low resistance, respectively. As mentioned earlier, this GMR effect or spin valve effect was initially demonstrated for bulk magnetic/semiconductor heterostructures.[19] In 2002 Emberly et al. first predicted spin valve effect in molecular junction composed of a benzenedithiolate molecule between two Nickel electrodes using a tight-binding model.[20]

(b) Molecular Spin Transistors: The single molecule transistor represents a three-terminal device with a single magnetic molecule embedded between non-magnetic source and drain electrodes. The current passes through a magnetic molecule and gate electrode is used to tune the electron transport properties.[21] The most challenging part is to create nanometer spaced electrodes, with a separation width of only one molecule. Such nanogaps are most commonly created by the mechanically controllable break junction (MCBJ) technique, where the conducting wire is broken by mechanical strain.[22] Other possibility is to use scanning tunneling microscope (STM) tip as one electrode and the conducting substrate as the second one.[23] The spin of the central magnetic molecule interacts differently with the spin-up and spin-down electrons moving from source electrode to drain electrode which results in different transmission probability of spin-up and spin-down electrons and is called spin filtering effect. An ideal spin filter delivers metallic features for one spin channel and insulating for the other. An important evaluation criterion for the performance of spin-filter devices is the spin filtering efficiency (SFE), defined as $SFE = |T\uparrow - T\downarrow|/|T\uparrow + T\downarrow|$, where $T\uparrow$

and $T\downarrow$ represent the transmission coefficients for the spin-up and spin-down electrons, respectively.

To date, much of the spin-based devices have used magnetic spin valves, where large external magnetic field is required to reverse the direction of magnetization of one of the magnetic layer in device structure. To achieve an efficient control of the magnetic properties on the molecular scale, molecular species with intrinsic magnetic moment have attracted considerable attention. Molecules featuring unpaired spins, such as present in many transition metal complexes and in organic radicals, display rich behavior, in particular, kondo signatures[24] and shot noise resulting from the spin-correlations[25] have been studied. In experiments, the presence of an unpaired electron can be detected through the measurement of the Kondo resonance, originating from the interaction between the unpaired spin localized on the molecule and the conduction electrons.[26,27] A large variety of organometallic molecules exists with one or more transition metal or rare earth metal ions as inner magnetic core surrounded by organic ligands.[28] These single molecule magnets (SMMs) have been exploited successfully to produce strongly spin polarized current.[29] Organic radicals are other potential candidates for such spin-filtering components due to the weak spin-orbit coupling, hyperfine interactions and expected long spin relaxation time. The main issue of using radicals for laboratory studies is that the number of known air-stable radicals are very limited. Most of the radical species have very short lifetime and are highly reactive towards oxidation. The transient nature of radical is even more problematic when it is interfaced with conducting electrodes and metallic substrates. In most of the cases, the radical gets oxidized spontaneously due to the charge transfer at metal-molecule interface. Thus, readily losing its open-shell character when bound in a junction. However, the recent advancements in the experimental techniques have made possible the synthesis of room-temperate stable organic radicals that can be imaged by STM. Intense research efforts are going to integrate such stable radicals in molecular junctions.[30,31] Besides this, the molecules without any intrinsic magnetic moment but with a helical molecular structure, such as DNA and peptides, have also been described to display chiral induced spin selectivity effect (CISS) in a variety of device configurations.[32,33] To gain the fundamental understanding of spin selective quantum transport, in this thesis work, we have mainly used organic radicals as discussed below in details.

1.2 Organic Radicals

Organic radicals are open shell species composed of light elements, mostly, H, C, N, O and S. The presence of unpaired electron in highest occupied molecular orbital (HOMO) makes the radical highly reactive towards dimer/polymerization, hydrogen abstraction, etc, leading to the loss of open shell character. Nevertheless, many persistent and stable radicals have been isolated at ambient conditions and have been around for many decades.[34] Two major strategies are commonly used to improve the stability of organic radicals. The first is the topological protection of the spin bearing atom with the bulky substituents, and the other one is increasing the delocalization of unpaired electrons over a large part of the atomic skeleton.[35] The first persistent radical triphenylmethyl was reported by Gomberg in 1900 by sterically protecting the central sp^2 hybridized carbon atom with three phenyl rings to eliminate contact with external active species.[36] Total or partial chlorination on three phenyl rings provides polychlorinated triphenylmethyl radicals (PTM), with enhanced thermal and chemical stability stemming from the bulky chlorine atoms. Another example is the prototypical 2,2,6,6,-tetramethylpiperidin-N-oxyl (TEMPO) radical, synthesized a half-century ago, stable enough to handle in air due to the steric protection provided by four methyl groups. Employing the second strategy of enhanced π-delocalization, several stable nitroxides and α-nitronyl nitroxide (NN) derivatives have been synthesized with the unpaired electrons delocalized between the nitrogen and the oxygen atoms.[37,38] Verdazyl radicals forms another family of stable radicals where the unpaired electrons are delocalized onto the heterocycle containing the nitrogen atoms.[39] Other stable radical candidates includes but not limited to dithiadiazolyl, phenoxy, phenalenyl, aminyl and hydrazyl radicals (shown in Fig. 1.1).[35,40] Recently, 1,2,4-benzotriazinyl (Blatter) radical has emerged out as an another promising candidate possessing remarkable thermal stability.[41] Such stable radicals have significantly contributed in the development of the molecule-based magnetism.

Molecular species containing two unpaired electrons are called diradicals, in which two spin sources (mono-radicals) are bridged by a non-magnetic spacer. The two unpaired electrons residing in singly occupied molecular orbitals (SOMO) can potentially exist either in a spin paired singlet state leading to antiferromagnetic interactions or a spin parallel triplet state with ferromagnetic coupling.[42] The magnetic properties of

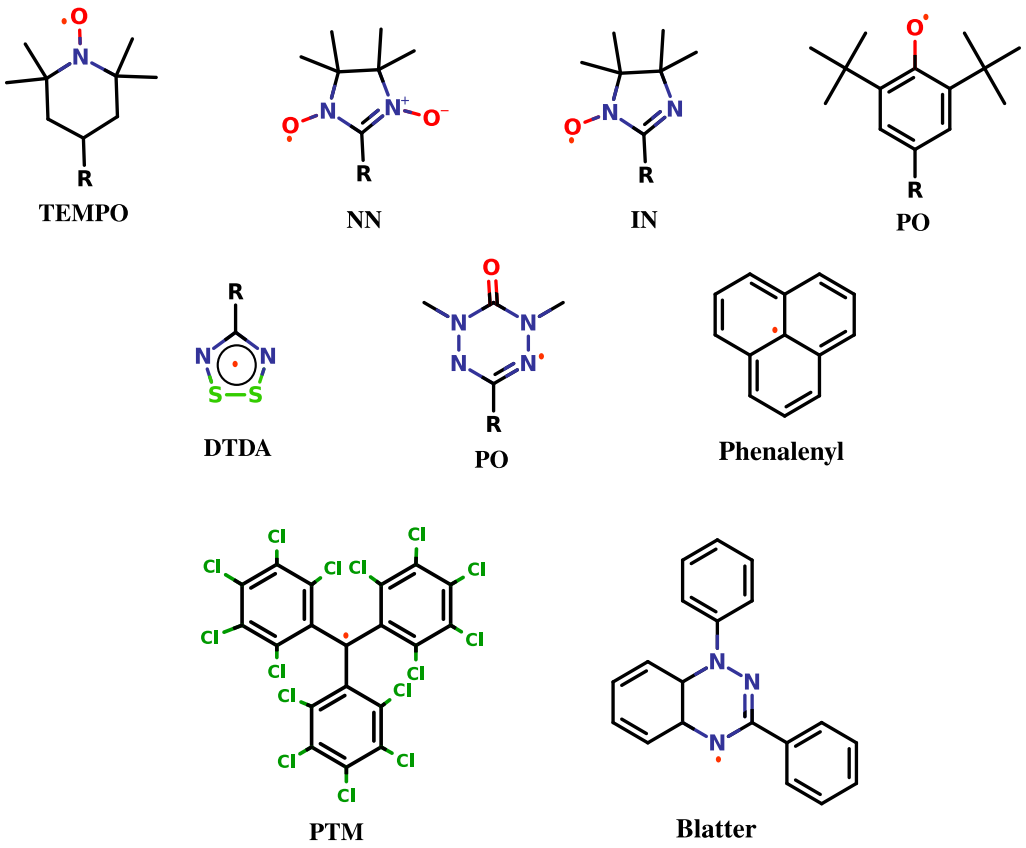

Figure 1.1: Molecular structures of a few of the stable organic radicals.

diradicals are characterised by magnetic exchange coupling constant ($2J$) values. The sign of $2J$ indicates the nature of the exchange interactions between the two spin centers, with a positive sign indicating ferromagnetic coupling, whereas an antiferromagnetic interaction is indicated by negative $2J$ value. The structural and electronic properties of coupler bridging the radicals play a crucial role in controlling the intramolecular magnetic exchange interactions. A number of NN based diradical molecules were comprehensively studied in DFT framework to understand the influence of length and aromaticity of coupler by Ali and Datta.[43,44] Numerous reports have demonstrated that the shorter coupler lengths favor stronger magnetic interactions, while the dihedral angle between radical and coupler planes must be as low as possible for effective spin propagation.[45–47] It has also been found that torsional effects can cause spin-crossover to occur from ferromagnetic ground state to antiferromagnetic state and vice-versa.[48] Apart from the coupler, various other approaches based on the structural modifications

have also been used to tune the magnetic properties. Latif et al. studied the effect of introducing various substituents in the coupling pathway of Schlenk diradicals and observed an increase in the $2J$ values with electron withdrawing substituent groups.[49] The significant role played by lowest unoccupied molecular orbital (LUMO) in controlling the extent and mechanism of exchange interactions was highlighted by Shil et al. by demonstrating that the diradicals with linear couplers yields stronger exchange coupling constants as compared to those with angular couplers.[50] In a recent study, Burnea et al. explored the non-covalent interactions, specifically hydrogen bonding, as a strategy to enhance the magnetic coupling in a diradical.[51]

Advancing a step closer towards the spintronic applications of organic radicals, recent progress has been devoted to fabrication of these magnetic molecules on surface and single molecule junction environment. In this context, Torrent et al. functionalised different surfaces with PTM radicals subjected to different interactions including Van der Waals, electrostatic, coordination and covalent bond, and found that magnetic character of molecule is preserved on the surface in all the cases.[52] Poggini et al. described a strategy to assemble a monolayer of NN radicals on surface keeping the paramagnetic character preserved.[53] Preserving the open shell character of radicals when interfaced with metallic electrodes is another big challenge. Till date, only a few of the persistent radicals have seen the light of the day with the preserved open shell character in junction. PTM radical has been proved to be stable in junctions showing kondo features and enhanced conductance[54,55] while TEMPO radical based junctions has demonstrated positive magnetoresistance.[30] When radicals are incorporated into metal-molecule-metal junctions, the presence of SOMO results in sharp resonances in the transmission function $T(E)$ near the Fermi level of electrode. These resonances near the Fermi energy are highly sought after features in molecular electronics, resulting in high charge transport efficiency. Recent STM measurements has revealed iminonitroxide substituted wires has 3.2 times higher conductance than the methyl substituted reference.[56] Similar enhancement in conductance has been observed for phenothiazine based radical cation[57] and oxoverdazyl based radical molecular junctions.[58] Although the redox properties of organic radicals have been successfully employed to enhance charge transport in molecular junctions, however the coupling of radicals with the spin dependent transport phenomena is far from being trivial. In a theoretical study, Herrmann and coworkers first reported in 2010 that organic radicals could be used as a

component of spin filters.[59,60] The presence of unpaired spin lift the spin orbital degeneracies and brings the MO level of one spin orientation closer to the Fermi level of the electrodes. This opens up new spin-dependent conduction channel and results in higher conductance of one spin type over the other. Followed by this, Smeu et al. investigated the spin filtering efficiency of various σ and π-type radical systems.[61,62] Shil et al. came up with the use of a high spin organic diradical as a component of the spin filter.[63] Noteworthy, most studies have been theoretical and the spin-selective transport through organic radicals remain still to be proved experimentally.

1.3 Diradicaloids

Delocalized diradicals can be further divided into Kekulé and non-Kekulé molecules. Non-Kekulé molecules (as discussed above) contain unpaired electrons due to the topology of the π electron arrangement such as trimethylenemethane (TMM) and m-quinodimethane (m-QDM) type diradicals. On the other hand, in Kekulé structures, the unpaired electrons are π-bonded.[64] In Kekulé molecules, termed as diradicaloids, both the closed-shell and open-shell resonance forms coexist and contribute to the overall nature and properties of the ground state.[65] Considering Clar's aromatic π-sextet rule,[66] which states that the resonance forms with the largest number of disjoint aromatic π-sextets (benzenoid forms) contribute more to the ground state electronic structures, several polycyclic aromatic hydrocarbons (PAHs) with open shell singlet (OSS) have been developed in the last decade. For example, a few of the longer (PAHs) with smaller HOMO-LUMO gaps are predicted to exist in OSS ground state, followed by a triplet state a few kcal/mol higher in energy. The list of diradicaloids (shown in Fig. 1.2) includes but not limited to zethrenes starting with heptazethrene,[67] anthenes,[68] *n*-acenes longer than hexacene,[69,70] extended quinodimethanes,[71] indofluorenes,[72] and related diindenoacenes.[73]

The theoretical understanding of these diradicaloids began with the introduction of the concept of "diradical character".[65] In simple words, diradical character expresses how diradical a compound is. A variety of indices have been proposed to estimate the extent of diradical character, which includes the natural orbital occupation number (NOON) analysis of the lowest unoccupied natural orbital,[74] Head-Gordon Indices,[75] Configuration Interaction (CI) coefficient's[76] and spin contamination.[77] The indicator

1.3 Diradicaloids

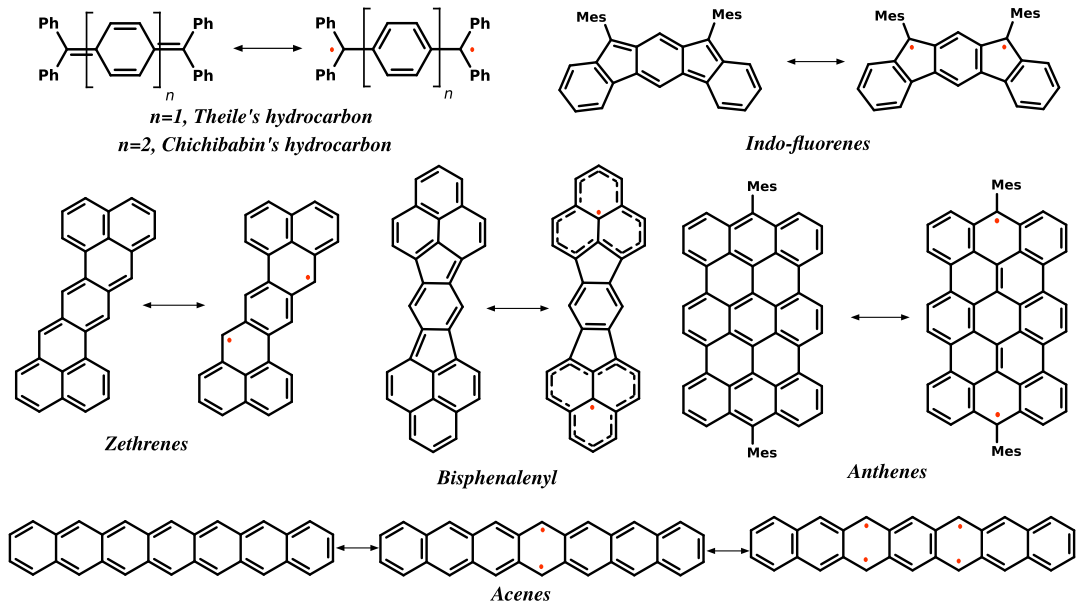

Figure 1.2: A few of the representative open-shell singlet diradicaloids.

y has become the traditional label for diradical character, which can range in value between 0 and 1, where a value of *y*=1 is a purely open-shell/diradical compound and a value of *y*=0 corresponds to completely closed shell molecule. Most of the reported diradicals have a *y* value between 0.5 and 0.99, and molecules that have *y* indices below 0.4 often display any properties associated with diradicals. The value of *y* can vary greatly for a given diradicaloid depending upon the basis set and the level of theory used to perform the calculations.

The unique electronic, optical, and magnetic properties of diradicaloids arising from the coexistence of electron-deficient closed-shell (quinoidal) and relatively electron-rich aromatic open-shell (diradical canonical) structures include narrow HOMO-LUMO energy gaps,[78], electron spin resonance (ESR) signals, a magnetic response in a superconducting quantum interference device (SQUID) magnometer[79] and convertible spin states.[80] These properties make diradicaloids the potential candidates for molecular electronics and spintronics. In this context, Yang et al. reported two highly stable and electrically conducting organic diradicaloids based on fused quinoidal oligothiophene derivative.[81] The diradical characters of diradicaloids strongly rely on the conjugation length, and only large-size PAHs are predicted to exhibit a pronounced diradical character in their ground state. This novel feature of diradicaloids could be exploited to facil-

itate long-range charge and spin transport. Only a few of the recent studies have shown the effect of diradical character on the molecular conductance and spin filtering. In a theoretical report, Stuyver et al. has established a positive correlation between diradical character and molecular conductance for the systematic design of wires exhibiting an increasing conductance with an increase in molecular length referred to as anti-ohmic wires.[82] Pilevarshahri et al. demonstrated that higher acenes can act as efficient spin filters when incorporated between gold electrodes via thiol linkers in an asymmetric way.[83] In a recent report, Kim et al. experimentally demonstrated that a closed shell quinoid structure is suitable for facilitating electrical charge transport in OFET devices while an open-shell structure could induce stable and enhanced spin characteristics.[84] Albeit, the role of intrinsic open shell character of diradicaloids in tuning the overall conductance and spin filtering efficiency with the increasing molecular length still remain to be understood.

1.4 Perspective of the Thesis

A key step towards the development of molecular spintronic devices is to design high-performance spin filters with large spin polarization as well as high conductance. Stable organic radicals are highly sought after candidates for efficient spin filters. Strong intramolecular spin–spin interactions between unpaired electrons in organic radicals are of utmost importance from the viewpoint of molecular magnetism. The full rationalization of the properties of these magnetic molecular materials for spintronic applications requires a complete theoretical understanding of the spin-selective quantum transport phenomena at nanoscale. Moreover, there are many open questions regarding the effect of localized spin centers on the overall transport of electrons and spin polarization across the junction. The rich variety of available stable radicals further offers various magneto-structural correlations of magnetic molecules to explore for the efficient charge transport.

The main objective of the thesis revolves around the fundamental understanding of spin-dependent transport properties mediated by single radical molecular junctions and to propose new concepts to incite sustainable spin polarization in molecular devices. It begins with the modeling of stable Blatter's based organic diradicals with strong intramolecular ferromagnetic exchange interactions *(Chapter 3)*. The integration of stable

radicals in the molecular junctions is described in *Chapter 4*, wherein the dependence of molecular conductance on the topological structure of radicals is investigated. Aspects of quantum interference (QI) are highlighted in the presence of unpaired spins localized on the molecule bridging the electrodes. In *Chapter 5*, transient spin polarization effects are realized by using a photo-responsive endoperoxide (EPO) based single molecule device. *Chapter 6* revolves around the plausible use of diradicaloids with intrinsic open shell character for efficient long-range charge transport. The desired anti-ohmic behavior is investigated for molecular wires bearing pronounced diradical character in their ground state.

CHAPTER 2

Computational Methodology

In this chapter, a brief overview of the theoretical foundations of the computational methods used in this thesis is presented. It begins with a glimpse of the theoretical background of density functional theory (DFT) which has been employed for the electronic structure and transport calculations in the thesis. In the second part, various DFT and wavefunction based methods to compute the magnetic exchange interactions are discussed. Finally, the quantum transport theory is discussed within Landauer Formalism, followed by the implementation of NEGF-DFT method.

2.1 The Many Body Problem: Solutions and Methods

2.1.1 The Many-Body Problem

The description of electronic structure of molecules and solids entail the correct understanding of how a large number of particles, i.e., electrons and nucleons interact with each other. This can be obtained by solving a many body equation for the energy E as

$$\hat{H}\Psi(r_1, r_2, ..., R_1, R_2, ...) = E\Psi(r_1, r_2, ..., R_1, R_2, ...) \tag{2.1}$$

where $\Psi(r_1, r_2, ..., R_1, R_2, ...)$ is the wavefunction, r_i corresponds to the position of

electrons and R_i is the analogous position for the ith nuclei. $\hat{H}$ represents the quantum mechanical Hamiltonian, which can be explicated as:

$$\hat{H} = -\sum_{i}^{N_e} \frac{\hbar^2}{2m_e}\nabla_i^2 + \sum_{i}^{N_N} \frac{\hbar^2}{2M_I}\nabla_I^2 + \frac{1}{2}\sum_{I\neq J}^{N_N} \frac{e^2 Z_I Z_J}{4\pi\varepsilon_\circ R_{IJ}} - \frac{1}{2}\sum_{i,I}^{N_e,N_N} \frac{e^2 Z_I}{4\pi\varepsilon_\circ R_{iI}} + \frac{1}{2}\sum_{i\neq j}^{N_e} \frac{e^2}{4\pi\varepsilon_\circ r_{ij}} \quad (2.2)$$

Here, the first two terms in the eq. 2.2 are the kinetic energy of electron and nuclei with mass m_e and M_I respectively. Later three terms describe the potential energy from Coulomb interaction between different nuclei, electrostatic attraction between nuclei-electrons and finally the last term arises from electron-electron interactions. The exact numerical solution to above mentioned equation for many electrons is unsolvable analytically and computationally feasible for a few electrons only. Thus, one must rely on approximations that allows us to reduce the number of variables involved. The first assumption comes from the fact that large mass of the nuclei as compared to electron makes the nuclei static relative to the motion of electrons. This is the basis of Born-Oppenheimer Approximation (BOA) which assumes that dynamics of nuclei could be neglected by considering them frozen as compared to electrons. In that case, we can assume that the Hamiltonian is separable and one can separate the electronic wavefunction from that of nuclei

$$\Psi = \Psi_e(r_1, r_2, ...)\Psi_N(R_1, R_2, ...) \quad (2.3)$$

Within BOA, the last term of Eq. 2.3 can be treated as a constant and one only need to solve the electronic part of the wavefunction. Therefore, the many-body problem reduces to

$$\hat{H}_e\Psi_e = E\Psi_e \quad (2.4)$$

with many-body Hamiltonian written as

$$\hat{H}_e = -\sum_{i}^{N_e} \frac{\hbar^2}{2m_e}\nabla_i^2 + \frac{1}{2}\sum_{i\neq j}^{N_e} \frac{e^2}{4\pi\varepsilon_\circ r_{ij}} - \frac{1}{2}\sum_{i,I}^{N_e,N_N} \frac{e^2 Z_I}{4\pi\varepsilon_\circ R_{iI}} \quad (2.5)$$

Although the use of BOA simplifies the initial many-body problem involving nuclei and electrons to many-body problem involving electrons only, however the solution of electronic Hamiltonian (Eq. 2.5) is still far from being easy. Thus, one must look for

other ways to solve the many-body Hamiltonian by reducing the number of degrees of freedom.

2.1.2 The Hartree-Fock method

One possibility of solving this problem comes from the approximation which assumes that the total N-body wavefunction of the system can be approximated by a product of single-electron wavefunctions. However, the electron-electron repulsion term (second term in Eq. 2.5) makes it impossible to separate the coordinates for each electron and to treat them separately. One possibility of solving this problem comes from the Hartree-Fock method. Hartree approximated the electron-electron repulsion term in an average way. Instead of calculating the repulsion term between all the electron pairs, he assumed that we can calculate the effective repulsion experienced by an electron due to average field of all the electrons. In this way, we can separate the electron-electron repulsion term into one-electron terms and write the Hamiltonian as a sum of one-electron operators:

$$\hat{H}_e = \sum_{i=1}^{N_e} f(x_i)\ ,\ f(x_i) = -\frac{\hbar^2}{2m_e}\nabla_i^2 - \frac{1}{2}\sum_{I}^{N_N}\frac{e^2 Z_I}{4\pi\varepsilon_\circ R_{iI}} + V^{HF}(r_i) \tag{2.6}$$

where V^{HF} is the average electrostatic potential experienced by ith electron due to all the other electrons. $f(x)$ is the one-electron operator, called the fock operator. Although using the fock operator, one can break down the multi-electron Schrodinger equation into a set of one-electron equations, the Hartree-Fock potential (V^{HF}) depends on the total wavefunction. Thus, making the problem nonlinear which is solved iteratively using self-consistent field (SCF) procedure. Further, according to Pauli exclusion principle, the total electronic wavefunction must be anti-symmetric. Therefore, we can write total wavefunction as a anti-symmetric product of single particle wavefunctions in the form of N×N determinant called the Slater determinant as:

$$\Psi^e_{HF}(x_1, x_2, ...x_N) = \frac{1}{\sqrt{N!}}\begin{vmatrix} \chi_1(x_1) & \chi_2(x_1) & \cdots & \chi_N(x_1) \\ \chi_1(x_2) & \chi_2(x_2) & \cdots & \chi_N(x_2) \\ \vdots & \vdots & & \vdots \\ \chi_1(x_N) & \chi_2(x_N) & \cdots & \chi_N(x_N) \end{vmatrix} \tag{2.7}$$

Here, $\chi_i(x)$ is an one-electron wave functions, where each of them is a function of three spatial coordinates and one spin coordinate written as $\chi_i(x) = \psi_j(r)\varsigma(s)$. The anti-symmetric nature introduces some degree of correlation between electrons of same spin, which is called exchange-correlation. However, it does not account for correlation between electrons with opposite spins. An extension to Hartree Fock method is Configuration Interaction (CI), which utilises the linear combination of all the possible Slater determinants to describe electronic systems. However, in large scale electronic structure calculations, wavefunction-based methods such as these are prohibitively expensive in computational terms. Thus, an approach is required which significantly reduces the number of variables and enables to calculate electronic properties for larger multi-electron systems with high degree of accuracy.

2.1.3 Density Functional Theory

A possible way to reduce the number of degrees of freedom is offered by Density Functional Theory (DFT). Unlike the Hartree-Fock theory which deals with many-electron wavefunction, the electron density is used as a fundamental property in DFT. Whereas the N-electronic wavefunction is a function of $3N$ space coordinates and N spin coordinates, the electron density is only a function of three variables. As a matter of the fact, irrespective of the size of system, electron density keeps up the same number of variables, thus making the DFT based treatments easy to use in respect of their time consumption and flexibility as compared to *ab initio* methodology. In 1964, Hohenberg and Kohn showed that ground state energy of E of a N-electron system is a unique functional of the ground state electron density (ρ)[85], which can be expressed as

$$E_\circ = E[\rho(r)] = \hat{T}[\rho(r)] + \hat{V}_{Ne}[\rho(r)] + \hat{V}_{ee}[\rho(r)] \tag{2.8}$$

The three terms on the right-hand side of Eq. 2.8 makes up the kinetic energy $\hat{T}$, the electron-nucleus $\hat{V}_{Ne}$ and electron-electron interaction $\hat{V}_{ee}$. The potential energy of interaction between electron and nuclei can be written as

$$\hat{V}_{Ne} = \int v(r)\rho(r)dr = \int v_{ext}(r)\rho(r)dr \tag{2.9}$$

In DFT, $v(r_i)$ is called the external potential (v_{ext}) acting on electron i, since it is produced by the charges external to the system of electrons. Thus, $\hat{V}_{Ne}[\rho(r)]$ is known, but the functionals $\hat{T}[\rho(r)]$ and $\hat{V}_{ee}[\rho(r)]$ are unknown. Thus, we have

$$E_\circ = E[\rho(r)] = \int v_{ext}(r)\rho(r)dr + \hat{T}[\rho(r)] + \hat{V}_{ee}[\rho(r)] = \int v_{ext}(r)\rho(r)dr + F[\rho(r)] \quad (2.10)$$

where the functional $F[\rho(r)] = \hat{T}[\rho(r)] + \hat{V}_{ee}[\rho(r)]$, is independent of the external potential. The difficulty in the DFT formalism is that the nature of functional $F[\rho(r)]$ is unknown.

The Hohenborg and Kohn theorem does not tell us how to calculate $E_\circ$ from $\rho_\circ$, since the functional F is unknown, nor it tells how to find $\rho_\circ$ without first finding the wavefunction. A key step was taken in 1965 when Kohn and Sham devised a practical method for finding $\rho_\circ$ and for finding $E_\circ$ from $\rho_\circ$.[86] The essence of Kohn-Sham (KS) approach is that they split the unknown functional in to two parts. The first part considered that electrons are non-interacting particles for which $\hat{T}[\rho]$ and $\hat{V}_{ee}[\rho]$ are calculated exactly from ρ and that include the main contributions to the ground state energy. In the other part, the electron-electron interactions are considered by the introduction of small correction term. According to KS formalism, the ground state electronic energy of n-electron system can be written as

$$\begin{aligned} E[\rho] = -\frac{1}{2}\sum_{i=1}^{n}\int \psi_i^*(r_1)\nabla_i^2\psi_i(r_1)dr_1 - \sum_{\chi=1}^{N}\int \frac{Z_\chi}{r_{\chi i}}\rho(r_1)dr_1 \\ +\frac{1}{2}\int\int \frac{\rho(r_1)\rho(r_2)}{r_{12}}dr_1dr_2 + E^{XC}[\rho] \end{aligned} \quad (2.11)$$

where ψ_i's are called Kohn-Sham (KS) orbitals for the non-interacting electrons. The first and second term accounts for the kinetic energy and nuclear-electronic repulsion of non-interacting electrons, whereas the last two terms represents the electron-electron interactions in form of Coulombic repulsion between electrons and exchange correlation term respectively.

Within the KS formulation, the ground state electron density $\rho(r)$ at a point r is written in terms of KS orbitals as

$$\rho(r) = \sum_{i=1}^{n} |\psi_i(r)|^2 \quad (2.12)$$

From Eq. 2.11 and Eq. 2.12, we can therefore find $E_\circ$ from ρ, if we can find the KS orbitals and the functional E_{xc} is known.
The KS orbitals are found by solving the KS equation using variational theorem.

$$\hat{h}_i\psi_i(r_i) = \mathcal{E}_i\psi_i(r_i) \tag{2.13}$$

where $\hat{h}_i$ represents the KS Hamiltonian operator which can be expressed as

$$\hat{h}_i = -\frac{1}{2}\nabla_i^2 - \sum_{\chi=1}^{N}\int\frac{Z_\chi}{r_{\chi i}} + \int\frac{\rho(r_2)}{r_{12}}dr_2 + V^{XC}[r_1] \tag{2.14}$$

The exchange-correlation potential V^{XC} is found as functional derivative of exchange-correlation energy as

$$V^{XC}[r] = \frac{\delta E^{XC}[\rho(r)]}{\delta\rho(r)} \tag{2.15}$$

Hence, the term V^{XC} can be readily obtained from E^{XC}. However, the problem with DFT is that no one knows what the correct functional $E^{XC}[\rho]$ is. Therefore, various approximate DFT functionals are used to estimate E^{XC} and V^{XC}. How does one do a DFT calculation with an approximated functional E^{XC}? One starts with an initial guess for ρ, which is usually found by superposing the calculated electron densities of individual atoms at the chosen molecular geometry. From the initial guess of $\rho(r)$, an initial estimate of V^{XC} is found using Eq. 2.15. The initial V^{XC} is used to solve the KS Eq. 2.13 and Eq. 2.14 for the initial estimate of KS orbitals. The initially found ψ_i's are used to get an improved electron density using Eq. 2.12. The improved ρ is then used to calculate improved V^{XC}, which is then used to find improved ψ_i's and so on. The iterations continue until there is no further change in density and KS orbitals. KS-DFT calculation is thus a kind of SCF calculation involving iterations until self-consistency between exchange correlation potential V^{XC} and KS orbitals is reached.

The exchange correlation energy in eq. 2.11 contains the following components: the kinetic correlation energy, exchange energy (arising from the antisymmetry requirement), Coulombic correlation energy (associated with inter-electronic repulsions) and a self-interaction correction (SIC). Conventionally, the functional E^{XC} is written as the

sum of exchange energy functional E^X and correlation energy functional E^C as

$$E^{XC}[\rho] = E^X[\rho] + E^C[\rho] \tag{2.16}$$

The two types of approximations which are generally used to approximate E^{XC} are the local density approximation (LDA)[87] and the generalised gradient approximation (GGA)[88,89]. In the first case, one considers that ρ varies extremely slowly with the position as that of homogeneous electron gas with electron density ρ. Then $E^{XC}[\rho]$ is given by

$$E_{xc}^{LDA}[\rho] = \int \rho(r)\epsilon_{xc}(\rho)dr \tag{2.17}$$

where ϵ_{xc} is the exchange plus correlation energy per electron in a homogeneous electron gas with electron density ρ. LDA can also be applied to spin-polarized system and is often referred to as the local-spin-density approximation (LSDA). Whereas in the LDA, electrons with opposite spins pair with each other in the same spatial KS orbitals, the LSDA allows electron with opposite spins to have different spatial KS orbitals $\psi_{i\alpha}^{KS}$ and $\psi_{i\beta}^{KS}$. The generalization of DFT that allows different orbitals for electrons with different spins is called **spin-DFT**. In spin-DFT, one deals with separate electron density $\rho^\alpha(r)$ and $\rho^\beta(r)$ due to spin α and β electrons. E_{xc} becomes the functional of two quantities: $E_{xc} = E_{xc}[\rho^\alpha, \rho^\beta]$. Separate KS eigen-value equations are solved for spin α and β orbitals. For LSDA, Eq. 2.17 takes the form:

$$E_{xc}^{LSDA}[\rho^\alpha, \rho^\beta] = \int \rho(r)\epsilon_{xc}(\rho^\alpha, \rho^\beta)dr \tag{2.18}$$

The second case, i.e., generalised gradient approximation (GGA) is an extension of the former case and introduce terms depending on the gradient of the charge density. A common way to do this is by including the gradients of ρ^α and ρ^β in the integrand. Thus,

$$E_{xc}^{GGA}[\rho^\alpha, \rho^\beta] = \int f(\rho^\alpha(r), \rho^\beta(r), \nabla\rho^\alpha(r), \nabla\rho^\beta(r))dr \tag{2.19}$$

where f is some function of the spin densities and their gradients.

Although the accuracy of LDA and GGA is acceptable as long as the structural properties are concerned, it dramatically fails in predicting the electronic properties of certain class of semiconductors that possess strong correlations between electrons. The ap-

proximated xc functionals tends to over-delocalize the valence electrons and induces the so called "bandgap problem". This in turn imposes difficulties in utilizing LDA/GGA to predict accurate intramolecular magnetic exchange interactions, formation energies, and transition states, etc. One of the corrective approaches employed to relieve the DFT electronic bandgap problem is the DFT+U correction method which can be added to the local and semilocal density functionals offering LDA+U and GGA+U methods.[90] The basic role of the U correction is to treat the strongly correlated electronic states (d and f orbitals) with an additional Hubbard-like term, while treating the rest of the valence electrons by the normal DFT approximations.[91] However, a disadvantage of the DFT+U method is that there is no unique way to parameterize the U. As another alternative, hybrid functionals are formulated, as discussed below.

2.1.3.1 Hybrid functionals

In hybrid functionals, a linear combination of the Hartree–Fock (HF) exact exchange energy and a given semilocal exchange and correlation functional is used.[92]

$$E_{XC}^{hybrid} = aE_X^{HF} + (1-a)E_X^{DFT} + E_C^{DFT} \tag{2.20}$$

where a is the fitting parameter that determines the amount of non-local exchange in the hybrid approximation. E_X^{HF} is the exact HF exchange energy, E_X^{DFT} approximate exchange energy in DFT and E_C^{DFT} is DFT correlation energy. . The well known hybrid functionals that have been used in this thesis includes the B3LYP and PBE0 functional. The B3LYP functional mixes in 20% HF exchange, while PBE0 mixes in 25% exact exchange. As will be demonstrated later in the Appendix1 (Section A.6), the inclusion of exact exchange has a profound effect on the magnetic exchange interactions.

2.2 Computation of Magnetic Exchange Interactions

2.2.1 The Spin Hamiltonian

The physical description of magnetic coupling in a broad class of systems including organic diradicals, inorganic complexes as well as ionic solids is based on the use of well-known Heisenberg Hamiltonian. Accordingly, the magnetic exchange interactions between two spin sites, say A and B, can be best described by the Heisenberg-Dirac-van Vleck (HDvV) spin exchange Hamiltonian as

$$\hat{H}_{HDvV} = -2J\hat{S}_A\hat{S}_B \tag{2.21}$$

where $2J$ is the exchange coupling parameter and $\hat{S}_A$ and $\hat{S}_B$ are the local spin operators acting on the interacting sites A and B, respectively. The eigenfunctions of the Heisenberg Hamiltonian are simply spin eigenfunctions, and $2J$ is directly related to the energy difference corresponding to these eigenstates. The *HDvV* Hamiltonian produces a spin-ladder of states with total spins ranging from $S_{max} = S_A + S_B$ and $S_{min} = S_A - S_B$. For a diradical system containing two unpaired electrons, the effect of exchange coupling between two unpaired spins ($S_A = S_B = ½$) affords two possible spin states with $S_{max} = 1$ corresponds to the triplet state with parallel orientation of the electronic spins resulting in ferromagnetic interaction. While, $S_{min} = 0$ represents singlet state with anti-parallel spins resulting in an antiferromagnetic interaction between them. The $2J$ value is then expressed as energy difference between singlet and triplet states as:

$$2J = E_S - E_T \tag{2.22}$$

A positive sign of $2J$ indicates ferromagnetic (FM) coupling with triplet ground state and negative $2J$ reflects antiferromagnetic (AFM) coupling with singlet ground state. Further, the different configurations arising from the distribution of two unpaired electrons in two magnetic orbitals consists of one triplet and three singlets, viz, $T = |\phi_1(\alpha)\phi_2(\alpha)|$; $S_1 = |\phi_1(\alpha)\phi_2(\beta)|$; $S_2 = |\phi_2(\alpha)\phi_2(\beta)|$ and $S_3 = \frac{1}{\sqrt{2}}|\phi_1(\alpha)\phi_2(\beta) - \phi_2(\alpha)\phi_1(\beta)|$, where $\phi_{1/2}$ denotes magnetic orbitals and α/β are spin up/down electrons. Due to multi-determinant nature of singlet state, $E_{S=0}$ gives poor approximation to singlet state. The theoretical calculation of the magnetic exchange interactions requires accurate deter-

mination of singlet and triplet energies from a multi-configurational approach. The wave-function based correlation treatment such as CASSCF method, offers a reasonable choice taking care of static correlation, however it becomes computationally extremely demanding or even impossible to handle for large molecules. Broken Symmetry DFT (BS-DFT) bypass the need for a multideterminant approach by using a single determinant broken symmetry solution as discussed below in details.

2.2.2 Broken-Symmetry DFT

A more widespread, reliable and computationally less expensive approach to the problem of calculating $2J$ value is the broken symmetry (BS) method developed by Noodleman and co-workers.[93,94] According to Noodleman, when the magnetic orbitals (SOMOs) are allowed to interact by overlapping in SCF procedure, a state of mixed spin symmetry and lowered space symmetry is obtained, which is referred as mixed spin or broken symmetry (BS) state.[93] The energy of the BS state is the weighted average of the energies of the pure spin multiplets. The $2J$ value can then be determined from the energies of the BS state and the highest spin multiplet.

In broken-symmetry approach, one starts with spin-unrestricted formalism, in which there are different orbitals for different spins, to obtain the solutions for the determinants of high spin (HS) and broken spin symmetry. It is further worthy to mention that in spin-unrestricted formalism, none of the HS and BS determinants are the eigenfunctions of $\hat{S}^2$. Following the description of the BS state given by Ruiz et al.[95], for a system with two unpaired electrons in two nonorthogonal orbitals a and b localized on two different atoms, the M_s=1 component of high-spin triplet is written as

$$\phi(S = 1, M_s = 1) = \frac{|ab|}{(2 - 2 < a|b >^2)^{1/2}} \tag{2.23}$$

The lowest singlet state is described by using BS wave functions. Two different BS solutions are possible namely

$$\sigma^1_{BS} = \frac{|a\bar{b}|}{\sqrt{2}} \tag{2.24}$$

$$\sigma^2_{BS} = \frac{|\bar{a}b|}{\sqrt{2}} \tag{2.25}$$

where the bar over an orbital indicates occupation with a spin-down electron. An adequate singlet function can be obtained as a linear combination of the two BS determinants as

$$\phi(S = 0) = \frac{\sigma^1_{BS} - \sigma^2_{BS}}{\sqrt{2 - 2 < \sigma^1_{BS} | \sigma^2_{BS} >}} \tag{2.26}$$

The M_s=0 component of the triplet state can also be constructed from the two BS solutions as

$$\phi(S = 1, M_s = 0) = \frac{\sigma^1_{BS} + \sigma^2_{BS}}{\sqrt{2 + 2 < \sigma^1_{BS} | \sigma^2_{BS} >}} \tag{2.27}$$

where $< \sigma^1_{BS} | \sigma^2_{BS} >$ represents overlap integral between two BS solutions. Calculating the energy expectation value for the wavefunction in Eq.2.26 and subtracting from the energy of triplet state yields the expression for singlet-triplet gap as

$$2J = \frac{2(E_{BS} - E_T)}{1 - < \sigma^1_{BS} | \sigma^2_{BS} >} \tag{2.28}$$

Assuming that the spin polarization of the inner closed shells can be neglected, the overlap integral $< \sigma^1_{BS} | \sigma^2_{BS} >$ can be approximately calculated from the overlap integral between two SOMOs a and b, i.e., $S^2_{ab} =< a|b >^2$. As proposed by Caballol et al.[96] Eq. 2.28 can then be written as

$$2J = \frac{2(E_{BS} - E_T)}{1 - S^2_{ab}} \tag{2.29}$$

Afterwards, diverse spin-projected methods depending on the degree of overlap between the magnetic orbitals were proposed. As proposed by Noodleman et al.,[94] for a sufficiently small overlap, Eq. 2.29 reduces to

$$2J = \frac{2(E_{BS} - E_T)}{S^2_{max}} \tag{2.30}$$

Ruiz et al.[95] proposed an expression for evaluation of $2J$ which was further modified by Illas et al. (Eq. 2.31) for the systems with sufficiently large overlap integral, that

generally happens for binuclear transition metal complexes.[97]

$$2J = \frac{2(E_{BS} - E_T)}{S_{max}(S_{max} + 1)} \tag{2.31}$$

The modified version of Eq.2.30 was then proposed by Yamaguchi and co-workers,[98] which estimate the value of $2J$ through the following expression:

$$2J = \frac{2(E_{BS} - E_{HS})}{\hat{S}^2_{HS} - \hat{S}^2_{BS}} \tag{2.32}$$

Eq. 2.32 retains its validity over the whole range of coupling strengths and reduces to the Noodleman equation in the weak coupling limit.

2.2.3 Constrained DFT

In the light of superior balance of accuracy and low computational cost, BS-DFT has proven to be a valuable tool in the electronic structure toolbox. However, traditional DFT functionals tends to suffer from self-interaction errors (SIE) which results in spurious delocalization of the density. This shortcoming of the DFT functionals naturally plague BS-DFT as well for the computations of exchange coupling and is largely responsible for grossly overestimated $2J$ values. To mitigate this shortcoming, constrained DFT (CDFT) offers a partial workaround that overcome the effects of SIE to some extent by constraining the charge and spin on the specified molecular fragments.[99] As first presented by Dederichs et al.[100], one can accomplish the ground state energy $E(N)$, of the system with the constraint that the volume Ω contains exactly N electrons, by supplementing the traditional DFT energy functional $E[\rho(r)]$ with a Lagrange parameter V that takes into account the constraint as

$$E(N) = \min_{\rho} \left[E[\rho(r)] - V\left(\int_{\Omega} \rho(r) d^3r - N \right) \right] \tag{2.33}$$

To compute the exchange couplings within the spin-constraint density functional theory, two sub-regions A and B localized at two spin centers are selected.[101] The spin-constraints are defined as

$$\int_A \rho^{\alpha\beta}(r)dr = N_A \quad , \quad \int_B \rho^{\alpha\beta}(r)dr = N_B \tag{2.34}$$

where N_A and N_B are the specified constraint values of the total number of unpaired electrons and $\rho^{\alpha\beta}(r)$ is the spin density

$$\rho^{\alpha\beta}(r) = \rho^{\alpha}(r) - \rho^{\beta}(r) \tag{2.35}$$

For performing CDFT calculations within the BS scheme (CBS-DFT), one needs to apply the spin density constraints independently to both BS and HS determinants.[102] To do so, one introduces two Lagrange multipliers γ_A and γ_B and optimizes a new functional of electron density (ρ)

$$W[\rho^{\alpha}, \rho^{\beta}, \gamma_A, \gamma_B] = E^{KS}[\rho^{\alpha}, \rho^{\beta}] + \gamma_A \left(\int_A \rho^{\alpha\beta}(r) dr - N_A \right) + \gamma_B \left(\int_B \rho^{\alpha\beta}(r) dr - N_B \right) \tag{2.36}$$

The imposed spin density constraints act independently to BS and HS states to obtain the energies of HS and BS states. Finally, Eq. 2.29 is then used to compute the $2J$ values. For the work performed in this thesis, we have used Löwdin population to identify the subregions, called as zones, and constrained spin moments. The detailed zone selection criteria for the work performed is described in Appendix 1, Section. A.1.

2.2.4 Multi-configurational methods (MCSCF)

For the molecular systems with strongly correlated electrons, such as radicals, transition metal complexes, etc., the description of the electronic structure with the single-configuration wavefunction becomes insufficient. The near-degeneracy of the occupied and virtual orbitals lead to wavefunctions in which several determinants contribute considerably, rather than just one configuration. The presence of low-lying excited states impose another challenge for electronic structure theory to treat both the ground state and low-lying excited states in a balanced way. The theoretical treatment of such strongly correlated systems require multi-reference (MC-SCF) methods. However, DFT in its present form is restricted to single-reference systems. In the MC-SCF method, the wavefunction is obtained from a linear combination of determinants representing configurations or configuration state functions (CSFs).[103]

The most popular and simplest MCSCF method is complete active space self-consistent field (CASSCF) method developed by Roos and co-workers.[104] CASSCF limits the full CI calculations by dividing the orbital space in to three subspaces, i.e. in-

active, active and virtual orbitals. The orbitals are placed in their respective subspaces by the user based on chemical intuition. The CASSCF wavefunction is generated by assigning a fixed number of active electrons N in the number of active orbitals n, denoted as CAS(N,n). The inactive doubly occupied orbitals are kept frozen as core orbitals, while virtual orbitals remains unoccupied. The active orbitals undergo full CI, i.e., all possible configurations obtained by distributing N active electrons among the n active orbitals consistent with the given user-defined spin and spatial symmetry constraints are considered. Since multiple configurations contribute to the active space the active orbitals can have non-integer occupancies. For a given CASSCF active state, the wavefunction can be written as

$$|\Psi^0\rangle = \sum_i C_i \, |\phi_i^0\rangle \tag{2.37}$$

where C and $|\phi^0\rangle$ are the configuration expansion coefficient and Slater determinants (or CSFs) respectively. The energy of the CASSCF wavefunction is written as

$$E = \frac{\langle\Psi^0| \, \hat{H} \, |\Psi^0\rangle}{\langle\Psi^0|\Psi^0\rangle} \tag{2.38}$$

The success of CASSCF calculation depends on the choice of active space and the set of actual starting orbitals. A CASSCF calculation can be made more accurate by making the active space larger, but the calculation becomes rapidly too expensive due to steep increase in the number of CSFs. While the CASSCF wavefunction captures strong correlation within the active space, it neglects weak or dynamic correlation. To get further accuracy, CASSCF is often used as a reference wavefunction for multi-reference perturbation theory (MRPT) approach, by which dynamical correlation can be included. Examples of the later includes complete active space perturbation theory (CASPT2)[105] or N-electron valence state perturbation theory (NEVPT2).[106]

In this thesis, the CASSCF method has been applied to compute magnetic exchange interactions. To run CASSCF, firstly a DFT calculation is performed to generate a set of starting orbitals. The unrestricted natural orbitals (UNOs) are used for defining the active space and providing starting orbitals for CASSCF.[107] Starting from a minimal active space CAS(2,2), containing two unpaired electrons in two SOMOs, a common recipe is followed for the systematic expansion of active space up to CAS(10,10).[108] The corresponding CASSCF wave function is then used as a reference unperturbed

wave function for subsequent NEVPT2 calculations for the treatment of dynamical correlation. Finally, the computed energies in singlet and triplet state have been used in Eq. 2.22 to quantify the $2J$ values. The detailed selection criteria of the active space and calculated $2J$ values with extended CAS spaces for the work performed is presented in Appendix 1, Section. A.2.

2.3 Quantum transport theory

2.3.1 Setting up the transport Problem

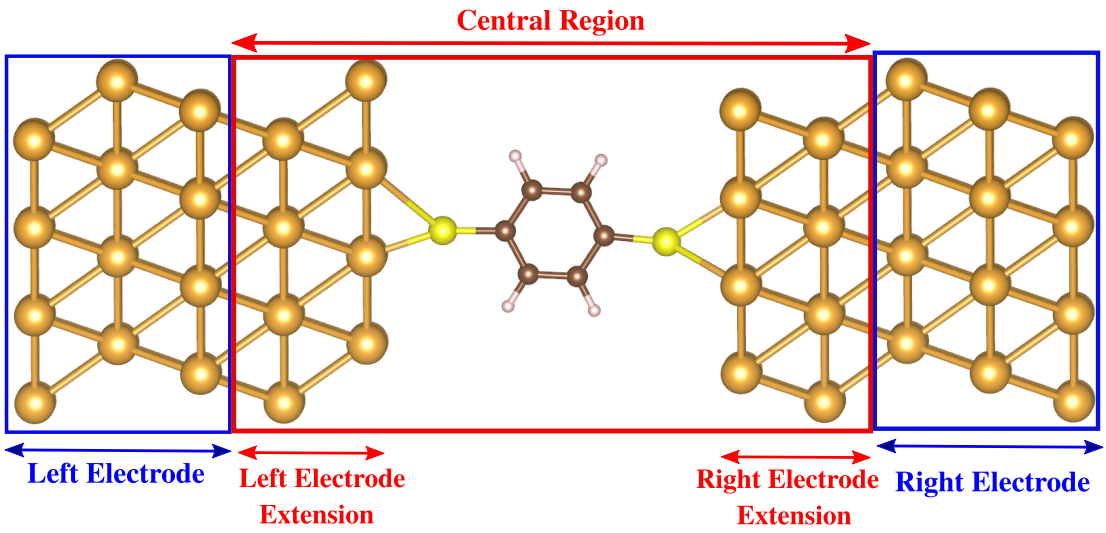

Figure 2.1: Representation of the device setup for the transport calculations showing a benzene molecule sandwiched between two gold electrodes using thiol linker atoms. The red enclosure represents the central/extended molecule, while blue enclosures corresponds to left and right electrodes.

For modelling atomic scale circuits, a complete quantum mechanical description of electron transport introduces a treatment in terms of wavefunctions and transmission probabilities. The typical system used to study quantum transport problem is a two-probe device comprising of two charge reservoirs bridged by a molecular species.[109] As shown in Fig. 2.1, the device setup consists of two bulk (left and right) electrodes and central scattering region. The latter consists of central molecule and few layers

of electrode and is thus called as "extended molecule". The left lead (L) couples to extended molecule (EM), which in turn is coupled to right lead (R).

Now, in order to find electron's wavefunction, one needs to diagonalise the Hamiltonian (H) matrix. Due to the presence of bulk electrodes, H in this case is infinite, which can be treated using Bloch's theorem. But, on the other hand, the interaction between bulk electrodes and extended molecule breaks the translation symmetry and system is not translationally invariant. Hence, Bloch's theorem can not be directly applied for the entire system. A possible solution to this problem is to consider the states inside the electrode as Bloch states associated to the semi-infinite electrodes. These states are then scattered by potential created by the EM. One can then use Green's function[110] or a wavefunction approach[111,112] to calculate the ground state electronic properties of EM. Thus, the total wavefunction can be considered as a combination of Bloch states for electrodes and localised atomic-like states for EM.

Moving on to the electrostatics of the problem, the main consideration here is that the electrodes have a tendency to preserve local charge neutrality. Due to which an arbitrary potential develop over the extended molecule. This potential needs to be calculated self-consistently under the boundary conditions that it must match to electrodes at boundaries of EM. Otherwise, a discontinuity in potential profile leads to spurious scattering. Thus, in order to achieve a good match of the potential at boundaries, few layers of electrode are usually included in EM. Moreover, the assumption that semi-infinite electrodes are defect-free and have regular periodic structure is no longer valid near extended molecule. When bonded to molecules, an electrode might undergo geometrical reconstructions. Thus, it is advisable to treat few layers of electrode self-consistently in EM.

2.3.2 The Landauer formalism: A scattering problem

The Landauer formalism describes the problem of tunnel junction as a scattering problem where the incoming waves of electron are scattered by an arbitrary potential developed across the molecule and expresses the electrical conductance in terms of quantum mechanical transmission probability of the one electron wavefunction.[113] The problem can be formulated in terms of one-dimensional scattering problem (shown in Fig. 2.2).

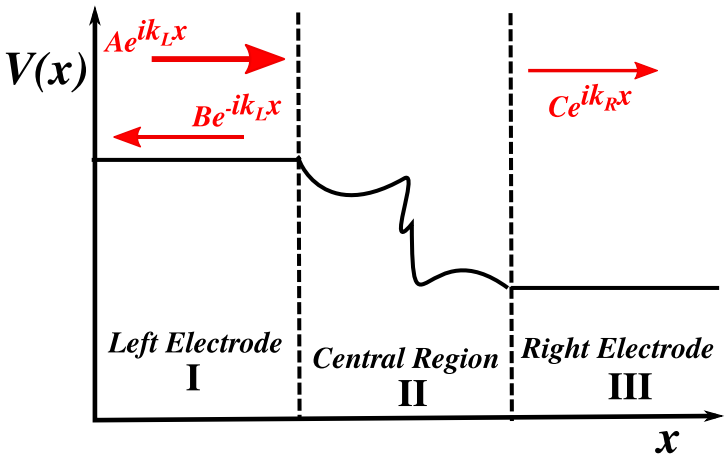

Figure 2.2: Schematic of one-dimensional scattering problem. The potential is assumed to be constant in left and right electrodes, viz, V_L and V_R. In the middle region, the potential is arbitrary, say $V(x)$. Left electrode consists of incoming wave $A\exp(iK_Lx)$ and reflected wave $B\exp(-iK_Lx)$, while right electrode consists of transmitted wave $C\exp(iK_Rx)$.

We assume that potential is constant in left region $V(x) = V_L$ and right region $V(x) = V_R$. The potential can have any arbitrary form $V(x)$ in middle region. Consider free electrons with energy E are injected from left and are scattered by potential $V(x)$ in middle region. The time-independent Schrödinger equation for L and R region can be written as

For Region L:

$$\frac{-\hbar^2}{2m}\frac{\partial^2\Psi_L}{\partial x^2} + V\Psi_L = E\Psi_L \Rightarrow \frac{\partial^2\Psi_L}{\partial x^2} + \frac{2m}{\hbar^2}(E - V_L)\Psi_L = 0 \Rightarrow \frac{\partial^2\Psi_L}{\partial x^2} + K_L^2\Psi_L = 0 \quad (2.39)$$

Similarly for Region R:

$$\frac{\partial^2 \Psi_R}{\partial x^2} + \frac{2m}{\hbar^2}(E - V_R)\Psi_R = 0 \Rightarrow \frac{\partial^2 \Psi_R}{\partial x^2} + K_R^2 \Psi_R = 0 \tag{2.40}$$

where

$$K_L^2 = \frac{2m(E - V_L)}{\hbar^2} \ , \ K_R^2 = \frac{2m(E - V_R)}{\hbar^2} \tag{2.41}$$

The general solutions to Eq. 2.39 and Eq. 2.40 can be written as

$$\Psi_L = A\exp(iK_L x) + B\exp(-iK_L x) \ , \ \Psi_R = C\exp(iK_R x) + D\exp(-iK_R x) \tag{2.42}$$

The terms $A\exp(iK_L x)$ and $C\exp(iK_R x)$ represent waves moving in the positive x-direction, while $B\exp(-iK_L x)$ and $D\exp(-iK_R x)$ correspond to waves moving in the negative x-direction. Since, no wave is reflected from the right electrode to the left, the coefficient D must vanish. Thus, Eq. 2.42 can be re-written as

$$\Psi_L = A\exp(iK_L x) + B\exp(-iK_L x) \ , \ \Psi_R = C\exp(iK_R x) \tag{2.43}$$

where $A\exp(iK_L x)$, $B\exp(-iK_L x)$ and $C\exp(iK_R x)$ represent the incident, reflected and transmitted waves respectively.

The reflection and transmission coefficients, R and T, are then defined as ratio of reflected to the incident beams and transmitted to the incident beams respectively, as

$$R = \frac{reflected\ current\ density}{incident\ current\ density} = \frac{J_R}{J_{in}} \tag{2.44}$$

$$T = \frac{transmitted\ current\ density}{incident\ current\ density} = \frac{J_T}{J_{in}} \tag{2.45}$$

Since, the incident wave is $\Psi_i = A\exp(iK_L x)$, the incident current density is given by

$$J_{in} = \frac{i\hbar}{2m}\left(\Psi_i(x)\frac{\partial \Psi_i^*}{\partial x} - \Psi_i^*(x)\frac{\partial \Psi_i}{\partial x}\right) = \frac{\hbar K_L}{m}|A|^2 \tag{2.46}$$

Similarly, the reflected and transmitted current density can be written as

$$J_R = -\frac{\hbar K_L}{m}|B|^2 \ = \ J_T = \frac{\hbar K_R}{m}|C|^2 \tag{2.47}$$

Combining Eq. 2.46 and Eq. 2.47, yields reflection and transmission coefficient as

$$R = \frac{|B|^2}{|A|^2} \ , \ T = \frac{K_R}{K_L}\frac{|C|^2}{|A|^2} \tag{2.48}$$

The coefficients A, B and C can be determined by imposing the continuity of total wavefunction and its derivative at boundaries of scattering potential.

We will now present a derivation of the Landauer formula that is by no means rigorous, but nonetheless it shows what are the major assumptions in this approach. The basic assumptions considered in the derivation of Landauer formula is that the transport is assumed to be coherent, i.e. inelastic scattering mechanisms are considered to be absent.

Consider a single transverse mode, moving from the left to right electrode in the reciprocal space. The moving electron scatters elastically in the scattering region. For simplicity, we assume a uniform electron gas with charged density n per unit length. The current moving from left to right electrode can be written as

$$I^{L\to R} = \frac{e}{L}\sum v f_L(E) = \frac{e}{L}\sum \frac{1}{\hbar}\frac{\partial E}{\partial K} f_L(E) \tag{2.49}$$

where v is the velocity of electron with energy E and $f_L(E)$ is the Fermi-Dirac distribution function of the left electrode. The summation in Eq. 2.49 can be transformed into integral, mathematically, as

$$\sum_k \to \sigma \times \frac{L}{2\pi}\int dk \tag{2.50}$$

where σ= 2, corresponds to two spin orientations. Eq. 2.49 can then be written as

$$I^{L\to R} = \frac{2e}{h}\int f_L(E)\, dE \tag{2.51}$$

If T is the transmission probability of electron through the scattering region, then the reflection probability is defined as $1 - T$. Accordingly, the current moving to left electrode can be written as

$$I^{R\to L} = \frac{2e}{h}\int [f_L(E)\,(1-T) \ + \ f_R(E)\,T]dE \tag{2.52}$$

where the first term in integral represent back scattered electrons and second term cor-

responds to the transmitted electrons. The total current is then given by

$$I^{total} = I^{L\to R} + I^{R\to L} = \frac{2e}{h}\int [f_L(E) - f_R(E)]T\,dE \tag{2.53}$$

Within the linear response regime, $f_{L/R}(E) \approx \mu_{L/R}$. This implies that total current can be rewritten as

$$I^{total} = \frac{2e}{h}\,T\,[\mu_L - \mu_R]\,dE \tag{2.54}$$

Putting $\mu_L - \mu_R = eV$, where V corresponds to applied bias voltage, Eq. 2.54 becomes

$$I^{total} = \frac{2e^2}{h}\,TV \tag{2.55}$$

The conductance of the system is given as

$$\mathcal{G} = \frac{I}{V} = \frac{2e^2}{h}\,T \tag{2.56}$$

For a multi-channel system, Eq. 2.56 can be generalized to be

$$\mathcal{G} = \frac{2e^2}{h}\sum_i T_i \tag{2.57}$$

where $\sum_i$ indicates the sum is performed over all the channels. Eq. 2.57 is called the Landauer Formula. Since T is a dimensionless number ranging from 0 to 1, $2e^2/h$ has the dimensions of conductance and is called as quantum of conductance, $\mathcal{G}_\circ = 2e^2/h = 7.75 \times 10^{-5}\ \Omega^{-1}$. Eq. 2.57 is valid for one-dimensional and spin-degenerate systems at low voltage. Generalizing it to higher dimensions, $T(E)$ can be calculated as a scattering matrix problem, which relates the incoming and outgoing wavefunctions with respect to the scattering potential as

$$|\Psi\rangle_{in} = S\,|\Psi\rangle_{out} \tag{2.58}$$

The elements of scattering matrix, S, connects to incoming/outgoing states. The absolute square of each component of matrix yields the probability of transmission from an incoming state to corresponding outgoing state. If arranged in the blocks signifying

transmission (t) and reflection (r), S can be written as

$$S = \begin{pmatrix} r & t' \\ t & r' \end{pmatrix} \tag{2.59}$$

The total conductance for the non-degenerate spin channels can then be written as

$$\mathcal{G} = \frac{e^2}{h}\Sigma_\sigma \Sigma'_{ij} T^\sigma_{ij} = \frac{e^2}{h}\Sigma_\sigma Tr[t_\sigma t^\dagger_\sigma] = \frac{G_\circ}{2}\Sigma_\sigma Tr[t_\sigma t^\dagger_\sigma] \tag{2.60}$$

where Σ'_{ij} indicates that sum is performed over all the channels near the Fermi energy and σ indicates spin index ($\sigma = \uparrow, \downarrow$).

2.3.3 Non-equilibrium Green's function

As already mentioned, we are dealing with an infinite dimensional non-periodic problem. The problem can be written down in terms of retarded Green's function G by solving the Green's function equation

$$(ES - H)G = I \tag{2.61}$$

where I stands for identity matrix and S is the overlap matrix. The Hamiltonian of the transport setup divided into three parts: central region (C), semi-infinite left (L) and right (R) leads is determined as

$$H = \begin{pmatrix} H_L & \tau_L & 0 \\ \tau_L^\dagger & H_C & \tau_R^\dagger \\ 0 & \tau_R & H_R \end{pmatrix} \tag{2.62}$$

In the above equation, H_L, H_C and H_R denote the Hamiltonian matrices of left, center and right components. $\tau_{L/R}$ stands for the interaction between the left/right electrode and central region. Interaction between left and right electrode is assumed to be zero, means there is no direct tunneling between the leads. Similarly, using the block-diagonal structure, Green's function (G) can be described as

$$G = \begin{pmatrix} G_L & G_{LC} & G_{LR} \\ G_{CL} & G_C & G_{CR} \\ G_{RL} & G_{RC} & G_R \end{pmatrix} \tag{2.63}$$

Substituting H and G to Eq. 2.61, we get

$$\begin{pmatrix} ES - H_L & -\tau_L & 0 \\ -\tau_L^\dagger & ES - H_C & -\tau_R^\dagger \\ 0 & -\tau_R & ES - H_R \end{pmatrix} \begin{pmatrix} G_L & G_{LC} & G_{LR} \\ G_{CL} & G_C & G_{CR} \\ G_{RL} & G_{RC} & G_R \end{pmatrix} = I \tag{2.64}$$

Upon solving the Eq. 2.64, the Green's function described in Eq. 2.63 becomes

$$G = \begin{pmatrix} g_L(1 + \tau_L G_{CL}) & g_L \tau_L G_C & g_L \tau_L G_{CR} \\ G_{CL} & G_C & G_{CR} \\ g_R \tau_R G_{CL} & g_R \tau_R G_C & g_R(1 + \tau_R G_{RC}) \end{pmatrix} \tag{2.65}$$

where $g_{L/R} = (ES - H_{L/R})^{-1}$ is the surface Green's function of the L/R electrode uncoupled to the central region. The final expression for retarded Green's function of central region G_C can be obtained from Eq. 2.65 and considering the products involving the second column of Green's function matrix in Eq. 2.64

$$-\tau_L^\dagger g_L \tau_L G_C + (ES - H_C) G_C + -\tau_R^\dagger g_R \tau_R G_C = 1 \tag{2.66}$$

G_C can be then be written as

$$G_C = (ES - H_C - \Sigma_L(E) - \Sigma_R(E))^{-1} \tag{2.67}$$

where $\Sigma_L(E) = \tau_L^\dagger g_L \tau_L$ and $\Sigma_R(E)(\mathrm{E}) = \tau_R^\dagger g_R \tau_R$ are the self-energies of semi-infinite left and right electrodes. The self-energy is associated to the energy level shift and energy level broadening of discrete molecular levels in the presence of electrodes and can be defined from the real and imaginary part of self-energies as

$$\Delta_{L/R}(E) = Re[\Sigma_{L/R}(E)] \tag{2.68}$$

$$\Gamma_{L/R}(E) = i[\Sigma_{L/R}(E) - \Sigma_{L/R}^\dagger(E)] = -2Im[\Sigma_{L/R}(E)] \tag{2.69}$$

The broadening of molecular energy level is associated with the lifetime of the electronic state on the molecule. Stronger the coupling of molecule with electrode, more will be the broadening of energy levels and quicker the electrons can flow from electrode to molecule or vice-versa. Thus, lifetime ($\mathcal{J}$) is inversely proportional to the broadening of states such that $\mathcal{J}\Gamma = \hbar$. The final expression for Green's function of central region (Eq. 2.67) contains all the information about the electronic structure of the central scattering region attached to electrodes. Thus the infinite dimensional problem is reduced to the dimension of central region. The self-energies includes all the information of the semi-infinite electrodes. Thus, we can focus only on G-matrix of the central scattering region and effective Hamiltonian can be written as

$$H_{eff} = H_C + \Sigma_L(E) + \Sigma_R(E) \tag{2.70}$$

2.3.4 NEGF combined with DFT

In the above sections, two seemingly dissimilar theoretical frameworks are presented. In the first section DFT formalism is presented which is used to calculate the electronic structure of periodic systems and finite molecules. On the other hand, the second section deals with the electron transport problem for an open system using NEGF. However, DFT cannot handle alone the systems with no translational invariance and the effect of external electrical field. Thus, it is natural to interface the two aforementioned tools into a single formalism. NEGF-DFT method allows quantum chemical modelling of molecules under non-equilibrium conditions wherein DFT is first used to calculate a single-particle Hamiltonian, which is followed by NEGF formalism wherein non-equilibrium density matrix is calculated self-consistently by including the effects of semi-infinite leads and the external bias. Below we discuss two different DFT approaches employed in this thesis to study coherent spin-polarized electron transport through a single molecule junction.

1. Self-consistent NEGF with periodic models: The starting point of this method is the SIESTA[114] electronic structure DFT approach which produces a single particle Kohn-Sham Hamiltonian and is capable of treating large scale systems. In this method, the effect of core electrons is described by norm-conserving pseudopotentials[115] and valence electrons are expanded in a basis set of numerical atomic orbitals with finite range.

This is followed by calculation of non-equilibrium charge density of an open system via Green's function using TranSIESTA [116] that has been interfaced with SIESTA electronic structure package.

As discussed in first section, the region of interest is separated into three parts, left (L), central (C) and right (R). The atoms in L(R) are assumed to be the parts of the left(right) semi-infinite bulk electrodes, thus allowing periodic description of electrodes. The Hamiltonian and density matrix is assumed to be converged to the bulk values in the region L and R. Thus, the Hamiltonian, overlap and density matrices differ from the bulk values only in C, C-L and C-R parts. Thus, in order to obtain transport properties we only need to describe the finite L-C-R part of the infinite system which can be represented as

$$\begin{pmatrix} H_L + \Sigma_L & \tau_L & 0 \\ \tau_L^\dagger & H_C & \tau_R \\ 0 & \tau_R^\dagger & H_R + \Sigma_R \end{pmatrix} \tag{2.71}$$

Within the periodic approach, the upper and lower part of Hamiltonian $H_{L(R)} + \Sigma_{L(R)}$ are determined from the two separate bulk calculations for the left and right electrodes. The electrodes have periodic boundary conditions in the z-directions and are solved using Bloch's theorem. The Hamiltonian of central region is calculated self-consistently in a localized basis set. The TranSIESTA then calculates the non-equilibrium density matrix employing NEGF technique. [117]

Within the periodic approach, the normally available functionals include only LDA and GGA, which underestimate the energy gap between empty and occupied orbitals due to self-interaction error. This results in overestimated conductance values. This limitation can be improved to some extent by using second approach discussed below using more sophisticated hybrid functionals.

2. Non-self-consistent NEGF with cluster models: The second approach describes the electrodes as a small finite cluster of metal atoms without imposing any periodic boundary condition. This allows to perform a common quantum chemical molecular calculation on electrode-molecule-electrode setup. The green's function of the electrodes are calculated in the wide-band-limit (WBL) approximation [118] assuming a constant density of states as

$$(g_X)_{ij} = -i \cdot \pi \cdot DOS^{\,constant} \cdot \delta_{ij} \tag{2.72}$$

In this approach, electronic structure calculations are first performed using any of quantum mechanical code (Gaussian, ORCA, Q-Chem or Turbomole) to extract the required Hamiltonian and overlap matrices. The transport module is then implemented as a post-processing tool (*Artaios*)[119] which is usually restricted to zero bias. Thus hyrbid or long-range corrected exchange-correlation functionals can be employed to achieve better orbital energies and consequently transport properties.

CHAPTER 3

Design of Blatter's Diradicals with Ferromagnetic Exchange Interactions

3.1 Introduction

Organic magnetic materials (OMMs) are of current interest because of their potential applications in several disciplines that exploits their magnetic [120,121], spintronic [20,122] and superconducting behavior. [123] Easy and precise control over the structural and electronic properties of the organic molecules allows their precise fabrication into devices with extensive applications in high density spin-based memory storage devices and processing units. [15,124] One of the persisting issues with OMMs is to obtain room temperature stable organic radicals with the desired electronic and magnetic properties. The development of such novel organic ferromagnetic materials exhibiting thermal stability as well as strong magnetic exchange interactions would play the central role in molecular spintronic applications and magnetic logic devices. [20,125] In organic diradicals two unpaired spins reside in the two singly occupied molecular orbitals (SOMOs) that are localized in the two spatially separated molecular regions. The parallel and antiparallel alignment of two unpaired spins in a diradical give rise to atleast two states, i.e., a high spin (triplet) and low spin (singlet) respectively. [42,77]

In search of stable organic diradicals, a number of stable organic diradicals have been reported over the last few decades e.g. nitronyl nitroxide (NN), oxoverdazyl (OVER), dithiadiazolyl (DTDA), nitroxide (NO), phenoxyl (PO) and imino nitroxide (IN).[43,126–128] Recently, Rajca and his co-workers succeeded in synthesizing couple of stable organic diradicals based on 1,2,4-Benzotriazinyl radical.[129,130] The later was first reported by Blatter and co-workers in 1968 and popularly known as Blatter's radical in the literature[131]. Here onwards it will be referred as Blatter's radical or **Bl** (see Fig. 3.1a). Owing to the thermal stability of the radical with melting point 111-112 °C and decomposition onset at 269 °C, the radical was found to be super stable radical[132]. Despite the exceptional thermal and moisture stability, the radical remains relatively less explored for a long time due to its insufficient accessibility because of its difficulty in synthesis. Kountentis et al. over the last few years have established easy synthetic procedures for such super stable Blatter's radicals that opens up novel possibilities and regenerated interest for such radicals.[132–134] Fig. 3.1a and 3.1b shows the basic structure and spin density distribution of Blatter's radical. Apart from the spin bearing triazinyl ring (marked as A) containing 3 N-atoms, the radical possess three functional aromatic rings (marked as B, C and D in Fig. 3.1a). Ring D exhibits negligible spin density and is thus, spin isolated. Ring C possesses small delocalization tails of the unpaired electron essentially localized on the triazinyl ring (ring A) whereas ring B contains the major proportion of the unpaired electron. This extensive unpaired spin delocalization over the molecular frame makes the radical super-stable in nature and increases the possibility of tuning the magnetic coupling through numerous pathways mediated via ring B and ring C.

In the present work we have computationally investigated the electronic structure and magnetic peroperties of the Blatter's radical. The first-principle based computation of the magnetic exchange interaction is indeed a challenging task and a trustable black-box method is yet to be developed.[135,136] In the current work, apart from the traditional DFT based broken-symmetry methods, we have adopted spin-constraint DFT (CBS-DFT) to compute the exchange couplings. Further, a mandatory course to multireference methods is performed using symmetry adopted methods such as CASSCF and CASSCF-NEVPT2 to achieve an appropriate quantitative description of the exchange couplings. Upon validation of the adopted computational methods and techniques to compute $2J$ values, we envision a tantalizing prospect to reach even higher values of $2J$

with simultaneous rigidification of molecular structure by employing planarized analogue of prototypical Blatter's radical shown in Fig. 3.1c. The planar counterparts are attained by peri-annulation accomplished with the connection of C8 and C10 positions with a chalcogen (X= O, S and Se) called here as X-annulation. The modulation of exchange coupling upon planarization of Blatter's radical has been explored using both ring B (called here as Class B diradicals) and ring C (called here as Class C diradicals) as a coupler which mediates the exchange interactions between spin centers.

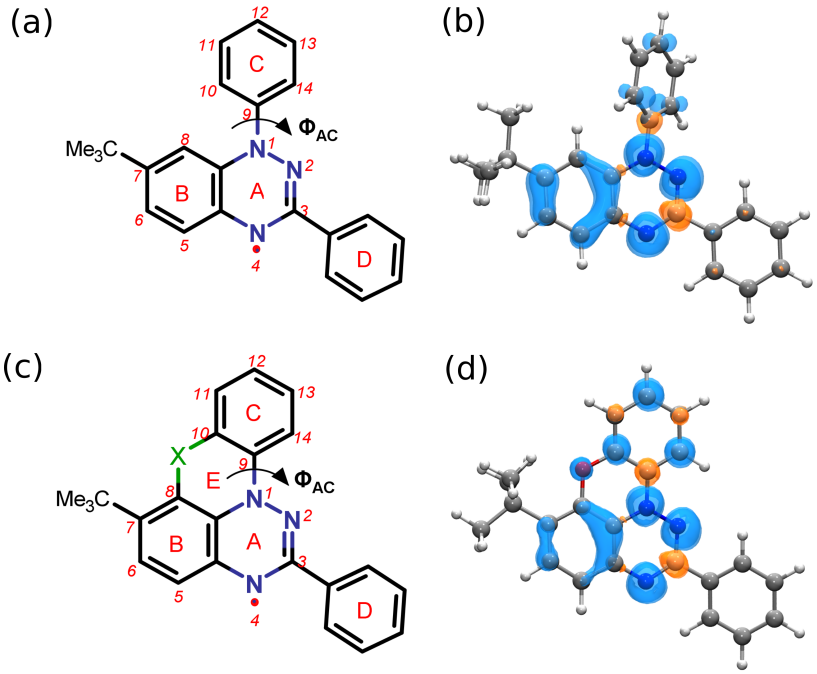

Figure 3.1: (a) 1,2,4-benzotriazinyl (Blatter's) radical with triazinyl ring containing three N-atoms (marked as A) and three aromatic rings marked as B, C and D, ϕ_{AC} is the dihedral angle between ring A and ring C. (b) Spin density distribution where blue and orange color represents α and β spin with an isovalue of 0.002 $\mu_B/Å^3$. (c) Planar analogue of Blatter's radical obtained by annulation at C8 and C10 position with **X** (X = O, S and Se). (d) Spin density distribution for X = O case.

3.2 Computational Methodology

The molecular geometries of all the radical species are optimized applying the B3LYP[137] hybrid functional and def2-TZVP basis set[138]. The open-shell molecular

species are treated using the spin-unrestricted Kohn-Sham (UKS) method within the DFT framework. Resolution of the Identity (RI) approximation along with the auxiliary basis set def2/J has been used[139]. Chain of spheres (COSX) numerical integration are used for the Hartree-Fock exchange to speed up the calculations without losing its accuracy. Tight convergence limits and increased integration grids (grid5) are used throughout.

To compute the magnetic exchange interactions, two different density based approaches namely broken-symmetry DFT (BS-DFT) and spin-constraint broken-symmetry DFT (CBS-DFT) are adopted. The varying degrees of self-interaction errors associated with the traditional DFT functionals results in the spurious delocalization of the magnetic orbitals and hence over predicted $2J$ values.[140,141] To mitigate these prevailing shortcomings, spin-constraint DFT (CBS-DFT) appears as a promising approach in which molecule is subjected to spin density constraints within the specified spatial zones.[99,101] The detailed criteria employed for zone selection in CBS-DFT calculations is discussed in Section A.1 of Appendix-1. The magnetic exchange interactions ($2J$) are computed in BS-DFT approach using the B3LYP/def2-TZVP method in *ORCA*[142] quantum chemical code. While for CBS-DFT the adopted methodology is B3LYP/6-31G(d) in the *NWChem*[143] quantum chemical code. The magnetic coupling constants are extracted for the density based approaches using Eq. 3.1 from the respective energy differences between the triplet and broken-symmetry state.

$$2J = 2\frac{(E_{BS} - E_T)}{S^2_{max}} \tag{3.1}$$

To obtain the $2J$ values in the symmetry-adopted multi-configurational methods, the complete active space self-consistent field (CASSCF) calculations are performed[136]. Starting from the minimal active space that contains the two unpaired electrons in two magnetic orbitals i.e. CAS(2,2), the active spaces were extended upto CAS(10,10) to indentify its role on the computed exchange interactions. The energy gaps between LS and HS states for the designed diradicals are calculated using CASSCF/def2-TZVP methodology on the optimized geometries. CASSCF calculation accounts the large extent of the static electronic correlation. The dynamical correlation is further included in a perturbative treatment with n-electron valence state perturbation theory (NEVPT2) method[144]. The unrestricted natural orbitals (UNO)[145] are chosen as the initial orbitals

for CASSCF and for CASSCF-NEVPT2, the CASSCF optimized orbitals are considered. The value of $2J$ is calculated using Eq. 3.2. The detailed criteria followed for selection of active space and character of selected active orbitals is shown in Section A.2 of Appendix-1.

$$E_S - E_T = 2J \tag{3.2}$$

3.3 Results and Discussions

The unique spin distribution of the Blatter's mono-radical among the three nitrogen atoms within the triazinyl ring makes the radical super stable in nature. In the following subsection we will discuss the role of X-annulation in Blatter's mono-radical. Followed by a comprehensive discussion, the complete method standardization for determining the strength of exchange coupling constant ($2J$) is provided. Upon validation of the adopted computational methods to compute $2J$ values, the role played by X-annulation in controlling the exchange interactions is discussed for Blatter's diradicals.

3.3.1 X-annulation in Blatter's monoradical

As a general feature of parent Blatter's radical (shown in Fig. 3.1a), the steric interactions between C8-H and C10-H result in a large dihedral angle between ring A and ring C with ϕ_{AC}= 54.02° (tabulated in Table 3.1). This high torsional angle between the π rings inhibits the delocalization of spin density from the spin bearing triazinyl ring to the aromatic ring C (spin density plot shown in Fig. 3.1b). One of the possible remedy to this inhibition could be a coplanar π substituent at N1 which can promote maximum spin delocalization at ring C and thus can significantly affect the magnetic properties. In this light, Kaszynski et al. demonstrated the concept of planar Blatter's radical with the synthesis of planar Blatter's radical by connecting C8 and C10 positions with oxygen and sulphur annulation.[146,147] As tabulated in last column of Table 3.1, O-annulation results in a much smaller dihedral angle of ϕ_{AC}= 3.04°, thus approaching the completely planar geometry. However, owing to the bulkiness, X=S and Se results in moderate dihedral angles of 20.54° and 29.96° respectively. The DFT based Löwdin spin populations computed at B3LYP/def2-TZVP level and summed up over the indi-

vidual aromatic rings of the Blatter's radical listed in Table 3.1 unambiguously confirms the modification in the spin density distribution brought about by X-annulation. The decrease in spin density on ring A and ring B for X-Bl as compared to parent Blatter (Bl) reveals that upon X-annulation, the spin density is drained from ring A and B towards ring C in such a way that it results in a transfer of total 10.5% of spin density from benzotriazinyl core (ring A + ring B) to ring C upon O-annulation. Similarly for S-Bl and Se-Bl, ring annulation results in a net transfer of 8.6% and 6.6% respectively from benzotriazinyl core to ring C. This consequently leads to an increase in the spin density on the ring C from 0.058 in Bl to 0.132 (plus ρ_O = 0.029) in O-Bl. Followed by this, S-Bl and Se-Bl also yields enhanced spin delocalization over ring C with a spin density of 0.111 (plus ρ_S = 0.030) and 0.100 (plus ρ_{Se} = 0.021) respectively. The enhanced spin delocalization over ring C in X-Bl as compared to parent Bl can also be evidently observed from the spin density plot of Bl and O-Bl shown in Fig. 3.1c and Fig. 3.1d respectively.

Table 3.1: Löwdin spin-density on the individual aromatic rings (A, B, C and D) and dihedral angle between ring A and ring C (ϕ_{AC}) of Blatter's radical and X-annulated counterparts with X= O, S and Se using B3LYP/def2-TZVP method.

Radical	$\sum\mu$(Ring)				ϕ_{AC}
	Ring A	Ring B	Ring C	Ring D	
Bl	0.791	0.250	0.058	-0.015	54.02
O-Bl	0.750	0.203	0.132	-0.010	3.04
S-Bl	0.752	0.214	0.111	-0.012	20.54
Se-Bl	0.758	0.223	0.100	-0.014	29.96

3.3.2 Method validation to compute 2*J* values

In 2016, Rajca et al. synthesized two stable diradicals by coupling Blatter's radical with nitronyl nitroxide (NN) and imino nitroxide (IN) using ring C as a coupler between two radical moieties. An exchange interactions of 174.80 cm^{-1} was observed by them for Bl-NN(C) (shown in Fig. 3.2a).[129] Later in 2019, Rajca et al. reported another Bl-NN derivative by utilizing the coplanar ring B as a coupler between the triazinyl ring and the NN radical (called here as Bl-NN(B)) (shown in Fig. 3.2b), with significantly strong

exchange coupling of 608.50 cm^{-1}.[130]

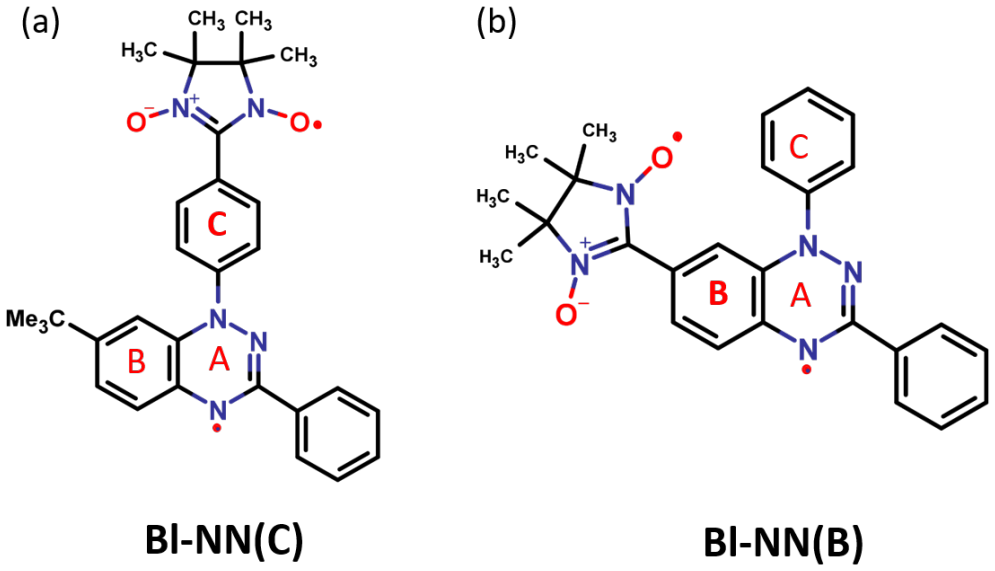

Figure 3.2: Blatter's radical coupled with nitronyl-nitroxide (NN) (a) Ring C is used as a coupler between Blatter and NN radicals, **Bl-NN(C)**, (b) Ring B is used as a coupler between two radical moieties, **Bl-NN(B)**.

The computed exchange interactions for Bl-NN(C) using various density and wave-function based methods are tabulated in Table 3.2 and illustrated in Fig. 3.3a. Within the traditional broken-symmetry approach, the hybrid B3LYP functional provides an overestimated exchange coupling of 397.80 cm^{-1}. Generally DFT functionals tends to strongly delocalize the magnetic orbitals especially for highly conjugated molecules. Such spurious delocalization of the magnetic orbitals often leads to the overprediction of the $2J$ values[148,149]. One of the remedy to these shortcomings is spin-constraint density functional theory (CDFT) in which the spin-density could be localized in the specified spatial regions.[150]. Adopting the recipe of the constrained broken-symmetry DFT calculations (CBS-DFT), the computed exchange interactions for **Bl-NN(C)** are found to be 219.40 cm^{-1}. Thus, CBS-DFT remarkably improves the exchange interactions as compared to the standard broken-symmetry approaches.

Furthermore, to obtain an intriguing understanding of the computed exchange interactions, the symmetry adopted wave function theory (WFT) based multi-configurational methods are also adopted. The choice of the active space [i.e. n active electrons in m

Table 3.2: Computed magnetic coupling constants ($2J$) and spin-states energies for **Bl-NN(C)** using different density functional theory and wave-function based methods.

Method	Energy(Eh)		$2J(cm^{-1})$
	HS	LS	
BS-DFT	-1586.74819	-1586.74728[a]	397.80
CBS-DFT	-1587.13946	-1587.13896[a]	219.47
CASSCF(2,2)	-1577.56828	-1577.56784	96.56
CASSCF(4,4)	-1577.58252	-1577.58213	85.59
CASSCF(6,6)	-1577.62865	-1577.62784	177.77
CASSCF(8,8)	-1577.65545	-1577.65479	144.85
CASSCF(10,10)	-1577.66511	-1577.66451	131.68
CASSCF(2,2)-NEVPT2	-1584.48586	-1584.48505	177.77
CASSCF(4,4)-NEVPT2	-1584.46724	-1584.46641	182.16
CASSCF(6,6)-NEVPT2	-1584.47128	-1584.47036	201.91
CASSCF(8,8)-NEVPT2	-1584.47373	-1584.47285	193.13
CASSCF(10,10)-NEVPT2	-1584.47081	-1584.46939	311.65
exp. (Rajca et al.)	-	-	174.80

[a] Instead of LS state energy the total energy of the broken-symmetry (BS) state is provided.

active orbitals CAS(n,m)] requires rigorous observations of the MOs and strong chemical intuitions.[151] In this work, the active spaces are selected based on the unrestricted natural orbitals (UNO)[145] that was obtained from the UKS optimized orbitals. Various active spaces i.e. from the minimal active space CAS(2,2) to CAS(10,10) are examined. In case of minimal active space i.e. CAS(2,2) the two magnetic orbitals, which contain the unpaired electrons in the radical centers are chosen. Incidentally these orbitals are basically the singly occupied natural orbitals SONOs (SOMOs). The computed exchange interactions using CASSCF(2,2) is 96.56 cm^{-1}, but it remarkably improves to 177.77 cm^{-1} with the inclusion of the dynamical electronic correlations in CASSCF(2,2)-NEVPT2 calculation. The magnetic orbitals involved are mainly localized both on the Bl as well as on NN. However one of the SOMOs is indeed delocalized over the central phenyl ring connecting both the radical centers. Thus, quite promising results with minimal CAS can be attributed to the SOMOs that has taken into account the radical centers as well as the coupler. To incorporate the correlation effects of the π-orbitals stemming from the conjugated spacer the CAS(4,4), CAS(6,6), CAS (8,8) and CAS(10,10) active spaces are incorporated in the MCSCF calculations. In CASSCF

calculations, the 2J values indeed depend on the CAS space, however the dependency is not linear with the size of the active space (see Fig. 3.3a), though the total energy decreases with the increase of electronic degrees of freedom. The computed exchange interactions for Bl-NN(C) in the minimal active space is 96.56 cm^{-1}, while maximum value 177.77 cm^{-1} is obtained for CASSCF(6,6). The lowest energy solutions i.e. highest active space i.e. CAS(10,10) provides a value of 131.36 cm^{-1}. The inclusion of dynamical correlations through NEVPT2[144] on the respective CASSCF optimized orbitals reveals a quite consistent 2J values for all the active orbitals considered except CAS(10,10) (See Table 3.2 and Fig. 3.3a). The largest (10,10) active space strongly overestimate the exchange interactions. This is due to the overestimation of the electron correlations of larger number of unoccupied orbitals. Considering a good match between the theory and experimental exchange interactions and role of dynamical and non-dynamical contributions to exchange interactions, the CASSCF(2,2)-NEVPT2 calculations are found to be quite promising.

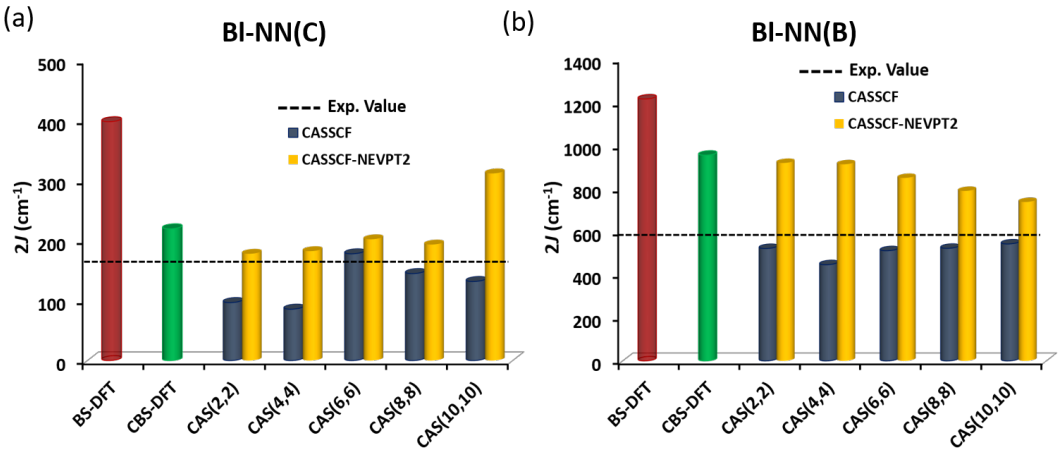

Figure 3.3: Computed magnetic exchange coupling constants (2J) for (a) **Bl-NN(C)**, (b) **Bl-NN(B)** with different DFT and wave-function based methods. The black dotted line represents the experimental exchange coupling by Rajca et al.

The computed exchange couplings and spin-state energies for Bl-NN(B) are tabulated in Table 3.3 and shown in Fig. 3.3b. Similar to Bl-NN(C), BS-DFT provides an overestimated 2J value of 1216.78 cm^{-1}, while CBS-DFT provides a better estimation with 2J value of 644.45 cm^{-1} for Bl-NN(B) as well. Surprisingly, for Bl-NN(B), along with BS-DFT, the more reliable CASSCF(2,2)-NEVPT2 also results in slightly

Table 3.3: Computed magnetic coupling constants ($2J$) and spin-states energies for **Bl-NN(B)** using different density functional theory and wave-function based methods.

Method	Energy(Eh)		$2J(cm^{-1})$
	HS	LS	
BS-DFT	-1429.557139	-1429.554367	1216.78
CBS-DFT	-1429.886794	-1429.885326	644.45
CASSCF(2,2)	-1421.384120	-1421.381742	521.97
CASSCF(4,4)	-1421.429316	-1421.427281	446.68
CASSCF(6,6)	-1421.444003	-1421.441672	511.65
CASSCF(8,8)	-1421.463400	-1421.461018	522.84
CASSCF(10,10)	-1421.482759	-1421.480284	543.17
CASSCF(12,12)	-1421.500785	-1421.497894	634.57
CASSCF(2,2)-NEVPT2	-1427.545405	-1427.541216	919.48
CASSCF(4,4)-NEVPT2	-1427.529706	-1427.525545	913.34
CASSCF(6,6)-NEVPT2	-1427.514054	-1427.510182	849.90
CASSCF(8,8)-NEVPT2	-1427.511512	-1427.507915	789.54
CASSCF(10,10)-NEVPT2	-1427.510599	-1427.507236	738.17
CASSCF(12,12)-NEVPT2	-1427.502981	-1427.499362	794.37
exp. (Rajca et al.)	-	-	608.50

[a] Instead of LS state energy the total energy of the broken-symmetry (BS) state is provided.

overestimated exchange coupling by producing the $2J$ value of 919.48 cm^{-1} as compared to the experimentally reported value of 608.50 cm^{-1}.[130] However, the source of this ambiguity was predicted as mainly due to different dihedral angle ϕ_{AC} obtained from the crystal geometry, which is known to have a non-negligible effect on the exchange coupling.[152] The crystal structure yields smaller ϕ_{AC}= 39.07°as compared to B3LYP/def2-TZVP geometry exhibiting ϕ_{AC}= 51.40°. The CASSCF(2,2)+NEVPT2 calculations on the crystal geometry yields a better $2J$ value of 784.05 cm^{-1} (see Section A.5 of Appendix-1). Apart from the geometrical difference, extended CAS calculations on both the crystal (see Table A.3 in Appendix-1) and optimized geometry (Table 3.3 and Fig. 3.3b) reveals further sequential improvement in dynamical correlation with increasing CAS space. The closest agreement with the reference value of 608.50 cm^{-1} is obtained with NEVPT2 based on extended CAS(10,10) producing $2J$ value of 738.17 cm^{-1} at B3LYP/def2-TZVP optimized geometry and 659.81 cm^{-1} at crystal geometry. The apparent low performance of CAS(2,2) space to deal with Bl-

NN(B) is attributed to the SOMOs (shown in Fig. A.6 of Appendix-1) having node on the bridging C (sp^2) atom of O-N-C-N-O fragment of NN moiety and thus, does not taking into account the spin polarization effects on the bridging atoms which are more prominent in Class B due to more spin dense connecting site C7 in Class B as compared to C12 in Class C diradicals. The role of bridging C-atom of O-N-C-N-O fragment of NN radical in the reference CAS space was also demonstrated in an early report by Calzado et al.[136]

3.3.3 Magnetic exchange interactions in X-annulated Blatter's diradicals

After gaining insights into the redistribution of spin density within Blatter's radical upon X-annulation, an intriguing quest arises for how the X-annulation can affect the existing ferromagnetic interactions in Blatter's based diradicals. The model X-annulated systems are thus conceptualized based on Bl-NN diradicals discussed in the previous section. Further, depending upon the coupler ring, diradicals in this work have been divided into two distinct classes, the one in which ring C of Blatter's radical is used as a coupler to connect NN (shown in Fig. 3.4a) are described as "Class C" with the corresponding spin density distribution for Bl-NN (C) and O-Bl-NN (C) shown in Fig. 3.4b,c respectively. The other coupled via ring B (shown in Fig. 3.4d) is described as "Class B" with the spin density distribution for Bl-NN (B) and O-Bl-NN (B) shown in Fig. 3.4e,f respectively.

Following the same recipe to compute $2J$ values for X-annulated diradicals, we observed that X-annulation significantly affects the degree of exchange coupling (Table 3.4 and Fig. 3.5). Interestingly, for Class C diradicals, X-annulation resulted in remarkably strong ferromagnetic exchange coupling with an appreciable increase in $2J$ values by a factor of 2 to 3 as compared to Bl-NN(C) (listed in top panel of Table 3.4). Among the three chalcogens, O-congener produced the strongest exchange coupling for which the $2J$ value increases upon O-annulation by a factor of 2.85 with BS-DFT and the most promising CASSCF(2,2)-NEVPT2 also reveals a significant enhancement in $2J$ value from 177.77 cm^{-1} for Bl-NN(C) to 595.32 cm^{-1} for O-Bl-NN(C). An analogous increase is also observed for S and Se analogs in the series.

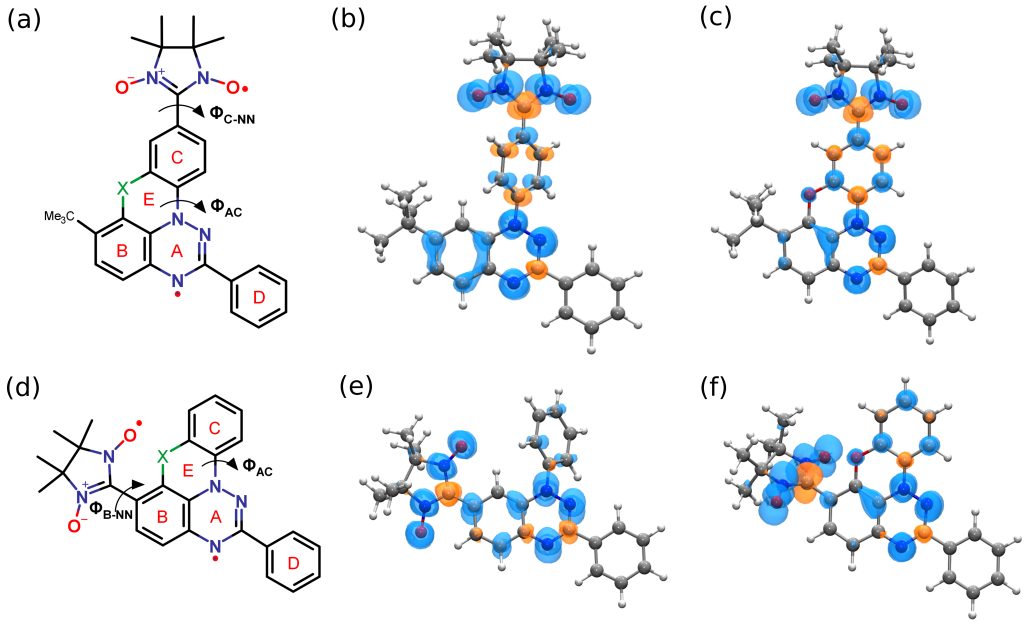

Figure 3.4: X-annulated Blatter's radical coupled to nitronyl nitroxide (NN) (a) Class C coupled via ring C, **X-Bl-NN(C)**. (b-c) Spin density distribution for **Bl-NN(C)** and **O-Bl-NN(C)** where blue and orange color represents α and β spin respectively with an isovalue of 0.003 $\mu_B/Å^3$. (d) Class B, **X-Bl-NN(B)** coupled via ring B. (e-f) Spin density distribution for **Bl-NN(B)** and **O-Bl-NN(B)**.

While in complete contrast to Class C, Class B diradicals (listed in bottom panel of Table 3.4) displays a drastic decrease in $2J$ values upon X-annulation, with the least $2J$ value being observed for X=O. For O-Bl-NN(B), both BS-DFT as well as CASSCF(2,2)-NEVPT2 results in a drop of $2J$ value by a factor of ~ 4 from 919.48 cm^{-1} for Bl-NN(B) to 217.30 cm^{-1} for O-Bl-NN(B). The similar decrease in $2J$ values also manifests in S-Bl-NN(B) and Se-Bl-NN(B), but with slightly larger exchange couplings as compared to O-Bl-NN(B). The substantial variation in $2J$ values brought upon X-annulation is also shown in Fig. 3.5 for both Class B and Class C.

As already discussed for monoradicals, the salient electronic feature of X-annulated counterparts is the nearly planar geometry and enhanced spin delocalization over the ring C. Gratifyingly, this characteristic feature promotes the spin spin interactions for Class C and vice-versa the case for Class B which is reflected in the form of enhanced exchange couplings for Class C and reduced ones for Class B. The spin density distribution for Class C and Class B Bl-NN diradicals and O-annulated counterparts shown

Table 3.4: Calculated magnetic exchange coupling constants for Class B and Class C Bl-NN diradicals with X-annulation using BS-DFT, CBS-DFT, CASSCF(2,2) and CASSCF(2,2)-NEVPT2.

Diradicals	$2J(cm^{-1})$				
	BS-DFT	CBS-DFT	CASSCF(2,2)	CASSCF(2,2)+ NEVPT2	Exp. Rajca et al.
Bl-NN(C)	397.80	219.47	96.56	177.77	174.80
O-Bl-NN(C)	1132.54	631.18	324.50	595.32	-
S-Bl-NN(C)	893.98	489.92	241.11	454.52	-
Se-Bl-NN(C)	824.76	453.85	217.35	416.02	-
Bl-NN(B)[a]	1216.78	644.45	521.97	919.48	608.50
O-Bl-NN(B)	280.60	151.89	152.55	217.30	-
S-Bl-NN(B)	632.88	350.32	327.05	528.55	-
Se-Bl-NN(B)	716.54	393.56	351.85	617.67	-

[a] Calculations on crystal geometry (Rajca et al.) yields $2J$ value of 1072.26, 566.74, 458.53 and 784.05 cm^{-1} using BS-DFT, CBS-DFT, CASSCF(2,2) and CASSCF(2,2)-NEVPT2 respectively.

in Fig. 3.4 and tabulated in Table 3.5 reveals the anticipated modification in the spin distribution upon X-annulation. For Class C diradicals, X-annulation results in the reduction of spin density on the benzo-triazinyl core wherein for ring A, it decreases from 0.765 for Bl-NN(C) to 0.709, 0.720 and 0.726 and ring B yields a decrease from 0.245 to 0.192, 0.202 and 0.212 for X=O, S and Se respectively. This overall displacement of the spin density from the benzo-triazinyl core to the ring C accumulates an additional spin density of 0.06, 0.04 and 0.03 over the ring C for X=O, S and Se respectively as compared to 0.008 in case of Bl-NN(C). The enhanced spin delocalization over ring C promotes the unidirectional magnetic coupling between spin centers via ring C which is reflected in the form of increased $2J$ values. Apart from the modification in spin density, an increased $2J$ value is also associated with the reduced dihedral angle between the coupler C and spin carriers, i.e., ϕ_{AC} and ϕ_{C-NN}. For O-Bl-NN(C), ϕ_{AC} reduces to nearly zero (4.17°) from a twisted angle of 52.88° in Bl-NN(C). This coplanar coupler-radical center plane further promotes effective spin propagation and vividly support strong exchange interactions.

Similarly, for Class B diradicals, X-annulation promote the spin delocalization to the ring C from 0.062 for Bl-NN(B) to 0.132 for O-Bl-NN(B) but with a simultane-

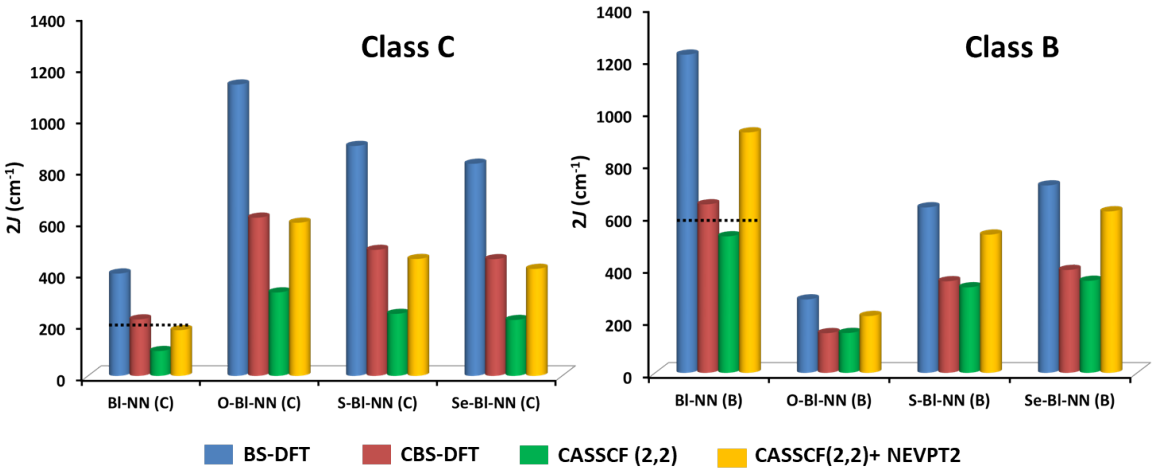

Figure 3.5: Variation in magnetic exchange coupling ($2J$) for X-annulated Class C (left) and Class B (right) Bl-NN diradicals. Blue, red, green and yellow bars indicate the calculated exchange coupling constants using BS-DFT, CBS-DFT, CASSCF(2,2) and CASSCF(2,2)-NEVPT2 respectively. The black dotted line over Bl-NN(C) and Bl-NN(B) represents the experimental $2J$ value. For Class C, $2J$ values increases upon X-annulation and vice-versa for Class B.

ous decrease in spin density on ring B which acts as a spin coupling unit for Class B diradicals from 0.188 to 0.162 for Bl-NN(B) and O-Bl-NN(B) respectively. Further, the dihedrals ϕ_{AC} and ϕ_{B-NN} that describes the extent of planarity and the conjugation between coupler units and two radical centers also reveals an anomalous trend. Similar to Class C, X-annulation results in reduced dihedral angle ϕ_{AC}, from 51.41° for Bl-NN(B) to 0.30° for O-Bl-NN(B), thus approaching the planar geometry. However, this is also accompanied by an increase in dihedral angle ϕ_{B-NN} from 20.40° for Bl-NN(B) to 51.41° for O-Bl-NN(B) due to repulsive interactions between NN spin center and X-atom attached at the consecutive C7 and C8 positions respectively. Thus, the decreased spin delocalizaion over the coupler B and the increased molecular twist ϕ_{B-NN} inhibits the spin-spin interactions and results in decreased $2J$ values for Class B diradicals.

Table 3.5: Löwdin spin-density computed at B3LYP/def2-TZVP level on the individual aromatic rings of Blatter's and NN radical, dihedral angles for both Class C and Class B Bl-NN diradicals and the X-annulated counterparts.

Diradicals	$\sum\mu$					Dihedral Angles[a]	
	Ring A	Ring B	Ring C	Ring D	NN	ϕ_{AC}	ϕ_{C-NN}/ϕ_{B-NN}
Bl-NN(C)	0.765	0.245	0.008	-0.015	1.05	52.88	22.38
O-Bl-NN(C)	0.709	0.192	0.068	-0.011	1.08	4.17	16.30
S-Bl-NN(C)	0.720	0.202	0.049	-0.012	1.075	20.99	20.25
Se-Bl-NN(C)	0.726	0.212	0.030	-0.013	1.074	28.71	16.45
Bl-NN(B)	0.709	0.188	0.062	-0.012	1.091	51.41	20.40
O-Bl-NN(B)	0.725	0.162	0.132	-0.009	1.032	0.30	51.14
S-Bl-NN(B)	0.703	0.167	0.110	-0.012	1.059	19.75	42.27
Se-Bl-NN(B)	0.706	0.170	0.102	-0.012	1.06	25.86	42.87

[a] The dihedrals ϕ_{AC}, ϕ_{C-NN} and ϕ_{B-NN} are shown in Fig. 3.4.

3.4 Conclusions

Adopting the density functional theory as well as wavefunction based multi-configurational methods we have investigated the magnetic exchange interactions for recently synthesized Blatter's based diradicals i.e. Bl-NN(C) and Bl-NN(B). The standard broken-symmetry (BS-DFT) calculations strongly overestimate the exchange interactions. However, the constrained spin-density based broken-symmetry approach (CBS-DFT) is found to be highly promising method for computations of the exchange interactions. Theoretically pronounced multi-configurational techniques such as CASSCF and CASSCF-NEVPT2 methods are also adopted to compute the magnetic exchange interactions. The later method includes both the static as well as dynamical electron correlation effects into the exchange interactions and remarkably produces the $2J$ value of 177.7 cm^{-1}, for which Rajca et al. observed 172.50 cm^{-1} for Bl-NN(C). It has been realized that the minimal active spaces i.e. 2 unpaired electrons in the 2 magnetic orbitals, CAS(2,2), are quite reasonable choice here for the Blatter'coupled diradicals in computing the exchange interactions.

Upon validation of the applied computational methods, the foregoing results demonstrate the influential role played by X-annulation in controlling the magnetic exchange interactions in Blatter's based diradicals. Two distinct classes of Bl-NN diradical, i.e. Class C and Class B reveals paradoxical scenario of exchange couplings upon

X-annulation. Class C diradicals result in an appreciable increase in $2J$ values, while a drastic decrease is observed for Class B diradicals. This remarkable variation in $2J$ values is rationalised in terms of variation of spin density distribution and molecular torsional angles. We propose that the systematic modification of spin density via X-annulation will facilitate the thermally robust and easily synthesizable diradicals with remarkable strong ferromagnetic exchange interactions.

CHAPTER 4

Effect of Quantum Interference in Organic Spin Filters

4.1 Introduction

With the ongoing downscaling of electronic devices, molecular spintronics has attracted intense research interest for various technological applications including high density memory storage, magnetic logic devices, magnetic sensors and so on.[153,154] The major challenge is to incite the spin polarized electron transport through a single magnetic molecule connected to source and drain so that wealth of interesting phenomena such as spin-valve, spin-crossover, spin filtering, Kondo effect, etc could be observed.[24,155] Among them, spin filters are the devices that preferentially favours the transport of an electron of one spin orientation over the other. Organic magnetic molecules are potential candidates for spin filtering effects owing to the weak spin-orbit and hyperfine interactions. The use of organic radicals as components of spin filters was first reported by Herrmann and coworkers.[59,60] The degeneracy splitting of spin-up and spin-down orbitals in organic radicals bring the MO level of one spin orientation closer to the the Fermi level of electrodes, thus resulting in higher conductance of one spin type over the other.[156]

The capability to tailor the electron spin with an enhanced control over electron transport in organic molecular materials has become the biggest challenge for molecular spintronics.[157] Of the various quantum effects that can be exploited in phase coherent regime, Quantum Interference (QI) plays a fundamental role in controlling the current through single molecule devices.[158] QI effects are associated with coherent superposition of de Broglie waves traversing along multiple paths[159]. The most striking feature of QI is the appearance of sharp dips in transmission close to the Fermi energy which appear when the phases of the electron traversing along different pathways of the molecule exactly cancel each other, thus leading to destructive quantum interference (DQI) and an obvious decrease in conductance. On the other hand, interference manifests itself in a constructive (CQI) way when the electron waves traversing along different pathways are in-phase with each other. A single benzene molecule where the electrodes are attached meta with respect to each other is expected to exhibit low conductance due to destructive quantum interference, while para-coupled analogue is predicted to be a better conductor.[160] This switching from CQI to DQI on changing the connectivity has been established starting from a single benzene molecule to various polycyclic hydrocarbons.[161,162] But only few reports have described QI effects in systems exhibiting spin polarization.[25,163–165]

In this study we probed the spin polarized transport using organic radicals as spin selective transmission source. Our aim is to investigate the dependence of conductance on the topological structure of the radicals, i.e., how combinations of para and meta couplings affect the spin polarized transport through the organic spin filters. Molecular bridges based on pentacene as central bridging unit are considered. We examined how the transition from CQI to DQI observed in parent pentacene on moving from para to meta connection is affected by attaching a radical across the pentacene core. Organic radicals including Nitroxy (NO$^{\bullet}$), Phenoxy (PO$^{\bullet}$) and Methyl ($CH_2^{\bullet}$) are attached to central benzene ring of pentacene core, which is coupled to gold electrodes via thiol linkers as shown in Fig. 4.1. The electron transport in molecular junctions has been explored using a fully self-consistent non-equilibrium Green's function (NEGF) approach with the complete periodic description of electrodes.[110]

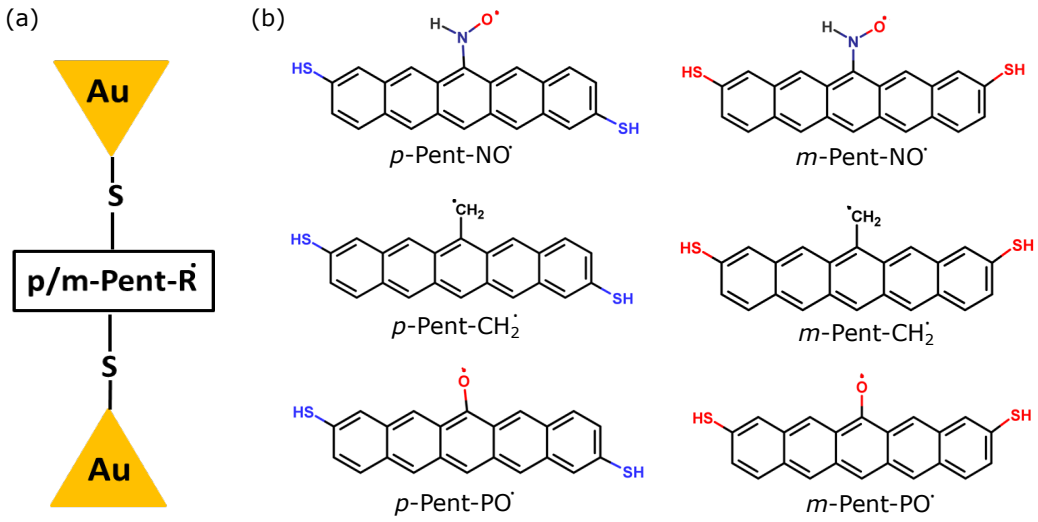

Figure 4.1: **(a)** Pentacene based radicals with para (*p*) and meta (*m*) coupling of terminal benzene rings of pentacene to gold electrodes via thiol (S) anchoring group. **(b)** Molecular structures of investigated pentacene based radicals where Nitroxy (NO˙), Methyl (CH_2˙) and Phenoxy (PO˙) radicals are attached to central benzene ring of pentacene core.

4.2 Computational Details

The spin dependent charge transport characteristics of all the molecules are investigated using NEGF-DFT technique as implemented in *SIESTA* package.[114] The system studied consists of pentacene based radicals presented in Fig. 4.1b bridged between two gold electrodes in a two probe transport structure, consisting of three parts: left electrode, central scattering region and right electrode, as shown in Fig. 4.2. In the first step, isolated molecules (shown in Fig. 4.1b) are optimized including the two S-H bonds at both the ends using B3LYP/def2-TZVP method in *ORCA*.[142] The optimized pentacene-radical systems are then placed between two gold electrodes by removing the terminal H-atoms and forming S-Au bonds.

The Au electrodes are modeled as Au(111) 5×5 surface with 3 layers in transport direction. The scattering region is composed of molecule connected to the conical gold junction containing four Au atoms on both sides and an additional 5×5 layer to replicate the bulk electrode. Geometry optimization is then performed for Au-Pentacene-Au junction with DFT as implemented in *SIESTA* code, with PBE exchange correlation

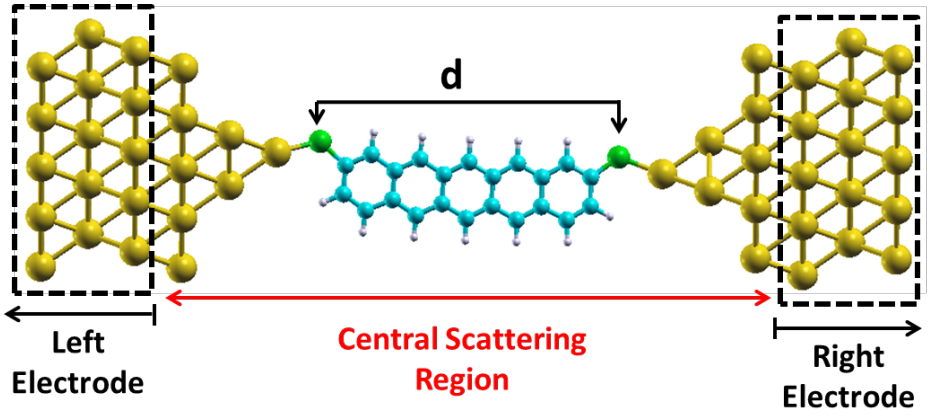

Figure 4.2: Device setup of Au-Molecule-Au junction with pentacene bridge coupled to Au(111) electrodes via sulphur atoms. The central scattering region consists of conical gold junction with an additional 5×5 layer of Au and central molecule. Semi-infinite left and right electrodes extend up to z=$\pm\infty$.

functional.[114] During the optimization, all the gold atoms were fixed in their bulk lattice positions and only molecule is allowed to relax within the junction. In the relaxed junction, Au-S distance is found to vary from 2.35 to 2.40 Å. The electronic charge transport properties are obtained using *TranSIESTA* code, which allows a periodic description of electrodes.[116] Norm-conserving pseudopotentials are used to describe the core electrons, double-ζ polarized (DZP) basis set is used to describe the valence electrons of molecular atoms and gold atoms.[115] The generalized gradient approximation (GGA) is used for exchange correlation function. A mesh cutoff of 300 Ry is used with Brillouin zone sampling using $3\times3\times10$ k-points. All the calculations are converged by using the conjugate gradient (CG) algorithm. The convergence tolerance in the density matrix is set to 10^{-4} eV, whereas the residual forces on all the atoms are lesser than 0.02 eV/Å.

The implementation of NEGF formalism in combination with DFT (NEGF-DFT) has been thoroughly described in Chapter-2. The quantity of interest here is electron transmission function , $T_\sigma(E)$, which represents the probability with which an electron of spin σ (up/down) and energy E can transmit from the left electrode to right electrode, through central scattering region. The transmission function is calculated as the trace of the product of coupling matrices $\Gamma_{L/R}$ and the Green's function of the central scattering

region as

$$T_{\sigma}(E) = Tr(\Gamma_R G \Gamma_L G^{\dagger})_{\sigma} \tag{4.1}$$

The zero bias conductance is then obtained as

$$G = G_{\circ} T(E_F) \tag{4.2}$$

where $G_{\circ} = 2e^2/\mathrm{h}$ is the quantum of conductance.

The spin filtering efficiency (SFE)[166] at the Fermi level is then given by

$$SFE = \frac{|T_{up}(E_F) - T_{down}(E_F)|}{T_{up}(E_F) + T_{down}(E_F)} \tag{4.3}$$

The transmission spectra is interpreted in terms of Transmission Eigenchannels (EC) and Molecular Projected Self-consistent Hamiltonian (MPSH states) which is obtained by projecting the Hamiltonian on the molecular orbitals of the central molecule. The wave functions of EC and MPSH states are obtained by using *Inelastica* package.[167]

4.3 Results and Discussions

4.3.1 QI in Pentacene based radicals

The spin resolved transmission spectra for parent pentacene and pentacene based radical systems under study is shown in Fig. 4.3. For parent pentacene, the dip residing between HOMO and LUMO resonances near the Fermi energy drops to $\sim 10^{-5}$ in *m*-Pent, while owing to constructive interference, *p*-Pent yields a dip of the order of 10^{-3}. Further, being a closed shell molecule bearing no magnetic center, parent pentacene exhibits no spin polarization. However, for radical systems, the spin-up and spin-down transmission spectra differs significantly due to splitting of the degeneracy caused by an unpaired electron.

The transmission spectra of all the radical species under study (shown in Fig. 4.3) reveals that for all the meta connected radicals, the maximum achieved value of transmission peaks is about 0.95 for both the spin orientations. However, when the lead positions change from meta to para, the amplitude of transmission peaks decreases to

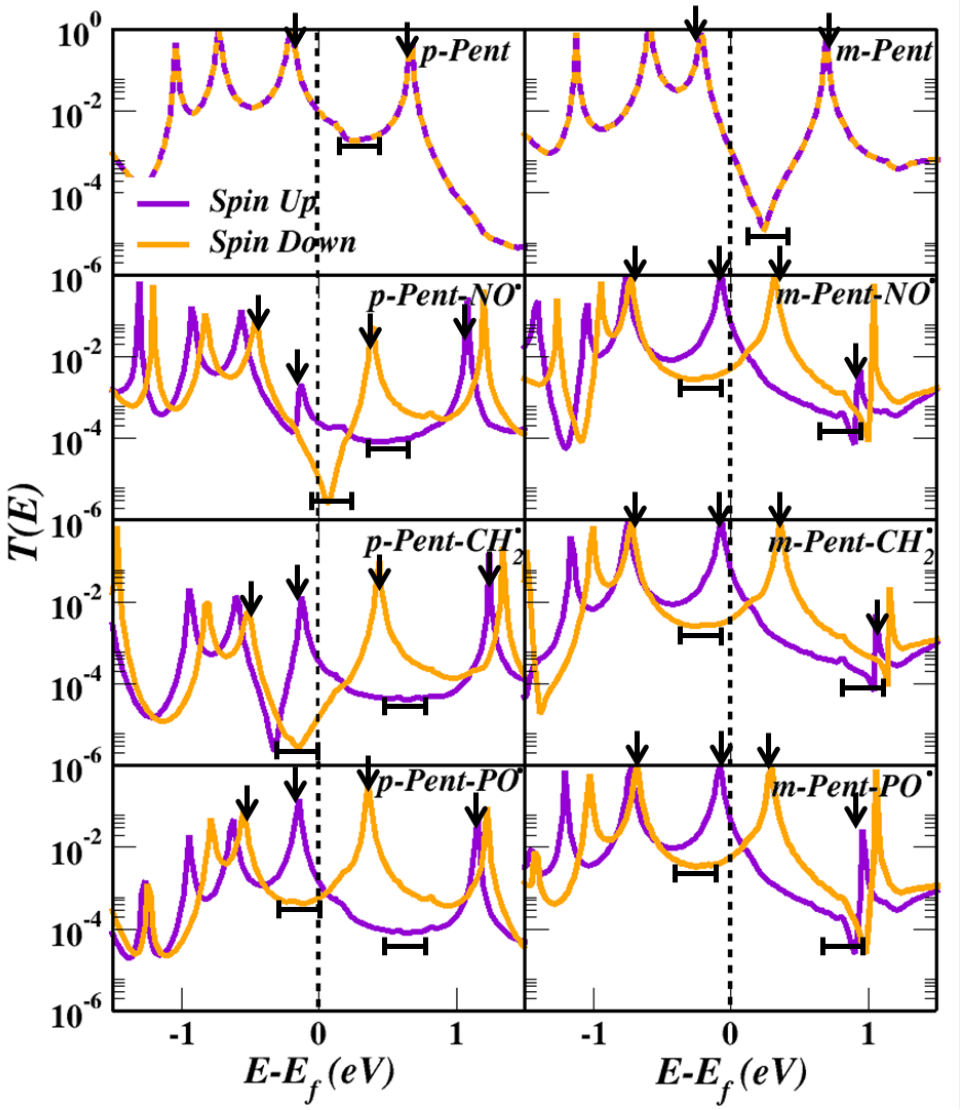

Figure 4.3: Spin resolved transmission spectra for para and meta connected pentacene (top panel) and pentacene based radicals (NO$^{\bullet}$, $CH_2^{\bullet}$, PO$^{\bullet}$) where spin-up and spin-down transmission is denoted by purple and orange respectively. The vertical dotted lines denote the position of the Fermi level. The arrows marked over the peaks below and above the Fermi level denote HOMO and LUMO resonance respectively wherein the arrows pointing towards purple peaks denote spin-up resonance and those towards orange peaks are for spin-down resonance. The dips residing between HOMO and LUMO resonances are also marked for both the spin channels.

around 0.10 for both spin orientations. For spin-up orientation, the sharp dip ascribed to DQI in *m*-Pent is shifted to higher energy of about 0.80 eV in meta connected radicals. As a result, the suppression effect imposed by DQI dip is much weaker yielding higher conductance of the order of 10^{-2} near the Fermi energy. In contrast, for para-connected radicals, a significant decrease in the transmission amplitude of HOMO and LUMO resonance peaks results in an inefficient transmission and decreased conductance of the order of 10^{-4}. This reversal of para-meta conductance upon attachment of radical is found to be even more prominent for spin-down orientation. For para connected radicals, DQI features with sharp dips of the order of 10^{-6} are evidently observed near the Fermi energy except *p*-Pent-PO$^{\cdot}$. This clearly indicates the modulation from CQI to DQI in para connection upon attachment of localized radical center. On contrary, for meta connected radicals, the minima of the dip residing between spin-down HOMO and LUMO resonances at ∼-0.20 eV is observed to be the order of 10^{-3}, with no absolute DQI features as observed in parent *m*-Pent. This again points towards the crossover from DQI to CQI in meta connection by attaching a localized radical center. In nutshell, one of the spin orientation yields same QI pattern as of non-magnetic pentacene but accompanied by the change in order of para-meta conductance, while the other spin orientation results in complete reversal of QI effects as observed in parent pentacene.

Table 4.1: Calculated conductance for spin-up ($\mathcal{G}_{\text{up}}$) and spin-down ($\mathcal{G}_{\text{down}}$) channels, total conductance ($\mathcal{G}_{\text{total}}$) in units of $\mathcal{G}_0$ and spin filtering efficiency (SFE) for para and meta connected pentacene based radicals.

Molecule	Anchor	$\mathcal{G}(\mathcal{G}_\circ)$			SFE(%)	para/meta
		$\mathcal{G}_{\text{up}}$	$\mathcal{G}_{\text{down}}$	$\mathcal{G}_{\text{total}}$		
Pent	para	9.65×10^{-3}	9.66×10^{-3}	1.93×10^{-2}	0.0	8.53×10^{0}
	meta	1.13×10^{-3}	1.13×10^{-3}	2.26×10^{-3}	0.0	
Pent-NO$^{\cdot}$	para	2.39×10^{-4}	1.10×10^{-5}	2.50×10^{-4}	91.2	3.37×10^{-3}
	meta	7.01×10^{-2}	4.82×10^{-3}	7.49×10^{-2}	87.0	
Pent-$CH_2^{\cdot}$	para	3.54×10^{-4}	1.48×10^{-5}	3.68×10^{-4}	92.1	5.13×10^{-3}
	meta	6.80×10^{-2}	3.70×10^{-3}	7.17×10^{-2}	82.6	
Pent-PO$^{\cdot}$	para	1.42×10^{-3}	5.54×10^{-4}	1.97×10^{-3}	43.8	3.68×10^{-2}
	meta	4.80×10^{-2}	5.48×10^{-3}	5.34×10^{-2}	79.5	

The zero bias conductance illustrated in Table 4.1 also reveals that switching from para to meta connectivity causes the total conductance ($\mathcal{G}_{\text{total}}$) to drop by an order of magnitude in parent pentacene core. In contrast, for the pentacene based radicals, the same operation causes the conductance of both spin channels as well as total conductance to increase by two orders of magnitude for NO˙ and CH_2˙ and one order of magnitude for PO˙. Thus, indicating the strong reversal of QI effects observed in non-magnetic pentacene by attached radical moieties, thereby making meta connected radicals more conductive than para ones. The reversal of para/meta order of conductance can also be seen clearly from sharp decrease in para/meta conductance ratio, which is of the order of 10^0 for parent pentacene, but has decreased to 10^{-3} for NO˙ and CH_2˙ radicals and 10^{-2} for PO˙ radical. Herrmann et al. also anticipated the change in para/meta conductance ratio on introducing a radical group or any closed shell substituent that participates in π electron system, however, no clear correlation was made based on QI effects.[60]

Apart from the observed anomaly in QI effects in the radical molecular junctions, all the radical systems results in significant spin polarization for both para and meta connections. As illustrated by transmission spectra, shown in Fig. 4.3, a conduction peak is observed just below the Fermi energy for spin-up orientation (marked by arrow over purple peak below the Fermi energy). This peak pinned to the Fermi energy for all the radical cases, corresponds to the non-bonding character of singly occupied molecular orbital (SOMO) of the radical species. While for spin-down orientation no such pinning is observed wherein HOMO and LUMO resonance peaks are positioned symmetrically below and above the Fermi energy respectively. Further, the spin filtering efficiency (SFE) calculated using Eq. 4.3 is tabulated in Table 4.1. A perfect spin filtering of more than 75% is achieved for all para and meta connected radicals while for *p*-Pent-PO˙ a moderate SFE of 43.8% is obtained. The spin density plots (Fig. B.4 in Appendix-2) reveals that for all the radical systems under study, the spin density is not only localized on the radical centers, but is completely delocalized on entire pentacene backbone.

Further, the anomaly observed in QI effects by the radical centers is strongly supported by calculated zero-bias conductance of the hydroxy or methyl derivatives of the radical systems shown in Fig. 4.1b, deliberately making them non-radical species. The obtained zero bias conductance of para and meta connected non-radical counterparts tabulated in Table 4.2 is found to be concordant with pentacene i.e., para is more conductive than meta. Thus, supporting our observation that radical unpaired electron is

playing an anomalous role in tuning the conductance of molecular junction with localized spin centers.

Table 4.2: Calculated conductance for spin-up ($\mathcal{G}_{up}$) and spin-down ($\mathcal{G}_{down}$) channels, total conductance ($\mathcal{G}_{total}$) in units of $\mathcal{G}_\circ$ for para and meta connected pentacene based non-radicals.

Molecule	Anchor	$\mathcal{G}(\mathcal{G}_\circ)$			para/meta
		$\mathcal{G}_{up}$	$\mathcal{G}_{down}$	$\mathcal{G}_{total}$	
Pent	para	9.65×10^{-3}	9.66×10^{-3}	1.93×10^{-2}	8.53×10^{0}
	meta	1.13×10^{-3}	1.13×10^{-3}	2.26×10^{-3}	
Pent-NOH	para	8.54×10^{-3}	8.55×10^{-3}	1.70×10^{-2}	11.2×10^{0}
	meta	7.32×10^{-4}	7.79×10^{-4}	1.51×10^{-3}	
Pent-CH_3	para	9.53×10^{-3}	9.54×10^{-3}	1.90×10^{-2}	7.66×10^{0}
	meta	1.20×10^{-3}	1.28×10^{-3}	2.48×10^{-3}	
Pent-POH	para	1.18×10^{-2}	1.18×10^{-2}	2.36×10^{-2}	3.02×10^{0}
	meta	3.81×10^{-3}	4.00×10^{-3}	7.80×10^{-3}	

Finally yet importantly, the above discussed transport calculations are performed within GGA approximation. The unavoidable self-interaction errors (SIEs) associated with exchange-correlation functionals of DFT results in underestimated energy gaps between empty and occupied orbitals which may cause large currents and overestimated conductance as compared to experimental values.[168,169] Thus, to go beyond GGA approximation, we also performed non-periodic calculations using hybrid density functional, following an alternative cluster approach. In this approach, the transmission functions are obtained using a NEGF based post processing tool *ARTAIOS*.[119,170] The optimized pentacene-radical systems are first placed between two Au_9 clusters, approximating the electrode surface, fixing Au-S distance to 2.40 Å. In the next step, single point calculations are carried out for cluster-molecule-cluster system at B3LYP/LANL2DZ level to extract the hamiltonian and overlap matrices needed for transport calculations. A rather simpler wide-band limit approximation is employed for electrode, which assumes that density of states (DOS) of electrode is independent of the energy. The inversion of para/meta conductance relation on attaching a radical is also evident from the transmission spectra obtained from cluster approach employing

hybrid B3LYP functional (shown in Fig. B.5 in Appendix-2). Within this approach, much better electronic structures of the scattering regions are produced. Owing to the higher HOMO-LUMO gap provided by the use of B3LYP as compared to the PBE functional, broader dips are observed near the Fermi energy. Thus, clearly revealing higher conductance of meta connected radicals as compared to the para ones.

4.3.2 Molecular orbitals perspectives in electron transport

Since QI effects are purely quantum mechanical effects and are associated to the molecular properties in junction such as its structure and symmetry. Thus, to elucidate the origin of the significant difference in para/meta conductance ratio in radical molecular junctions, we investigated the electronic properties of the molecule in junction. Since the coupling between the electrode and molecule will also modify the molecular orbitals (MOs) through rehybridization. Thus, the modified MOs are visualized by molecule projected self-consistent Hamiltonian (MPSH) eigenstates.[171,172] The transmission characteristics are further investigated in terms of the transmission eigenchannels, as discussed in the subsequent subsections.

4.3.2.1 Frontier MPSH Orbitals

MPSH orbitals represent the modified molecular orbitals (MOs) and their energy levels in the presence of surrounding electrodes.[172] According to the orbital symmetry rules derived by Yoshizawa and co-workers,[173,174] at an energy E around the Fermi level the contribution from the frontier HOMO and LUMO orbitals is mainly responsible for Green's function, which is written as

$$G_{lr}^{mol}(E) = \frac{C_{l,HOMO}C^{\star}_{r,HOMO}}{E - \varepsilon_{HOMO}} + \frac{C_{l,LUMO}C^{\star}_{r,LUMO}}{E - \varepsilon_{LUMO}} \tag{4.4}$$

where $C_{l/r,HOMO}$ and $C_{l/r,LUMO}$ are the MO coefficients of the HOMO and LUMO at the connecting sites l and r and $\varepsilon_{HOMO/LUMO}$ are the HOMO/LUMO orbital energies. Since the signs of denominators are opposite in Eq. 4.4 for the energy E located between the HOMO and LUMO. Hence, QI is determined by the signs of the numerators of the two terms. When the numerators have same sign, the contribution from HOMO and LUMO will cancel each other and results in DQI. On contrary, if numerators have

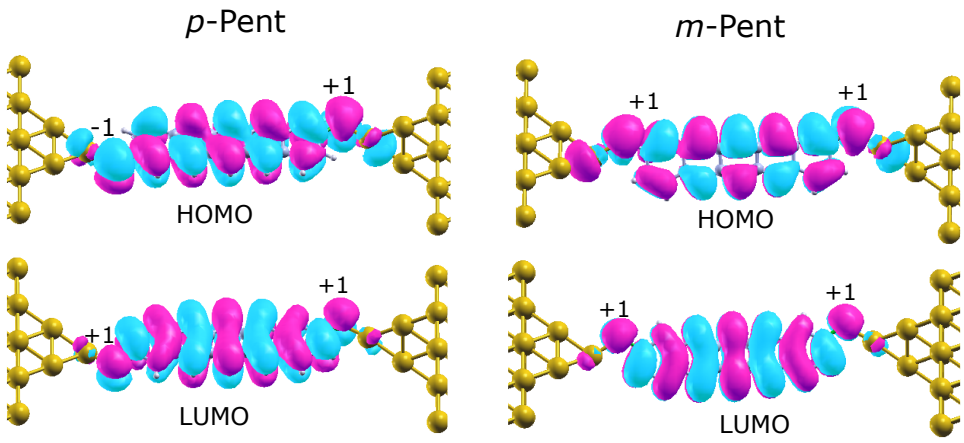

Figure 4.4: Spatial distribution of MPSH frontier orbitals for *p*-Pent and *m*-Pent in molecular junctions. Pink and cyan colors denote the positive and negative parity of the molecular orbitals with isovalue 0.02 a.u. and is represented by +1 and -1 marked over the anchoring S atoms.

opposite signs, CQI is predicted. However, if all four involved amplitudes $C_{l,HOMO}$, $C^{\star}_{r,HOMO}$, $C_{l,LUMO}$, $C^{\star}_{r,LUMO}$ do not have significant magnitude, then it results in an inefficient transmission, but not necessarily the typical DQI.

The spatial distribution of the frontier MPSH orbitals for *p*-Pent and *m*-Pent are shown in Fig. 4.4. The pink and cyan colors represent the positive and negative parity of the MOs and is denoted by +1 and -1 on sulphur atoms respectively. For *p*-Pent, the signs of the coefficients at two sulphur atoms are opposite for HOMO but are same for LUMO. Thus, according to Eq. 4.4, the HOMO coefficients product is negative and LUMO coefficients product is positive, this results in opposite signs of two numerators and hence CQI for *p*-Pent. However, for *m*-Pent, the signs of the coefficients at two sulphur atoms are same for both HOMO and LUMO, thus the contributions from HOMO and LUMO will cancel each other and result in DQI for *m*-Pent.

For radical molecular junctions, due to the presence of non-bonding MO near the Fermi energy, the orbitals of one of the spin orientation do not approximate the exact orbital symmetry. As a result, the orbital symmetry rules might not be fully applicable for both the spin orientations. Here, this also calls for the rules that can reliably capture CQI and DQI in spin polarized molecular junctions with localized radical centers. Nevertheless, when the orbital coefficients of HOMO and LUMO have same sign at the contact positions, a cancellation will always occur somewhere in the window of interest, despite

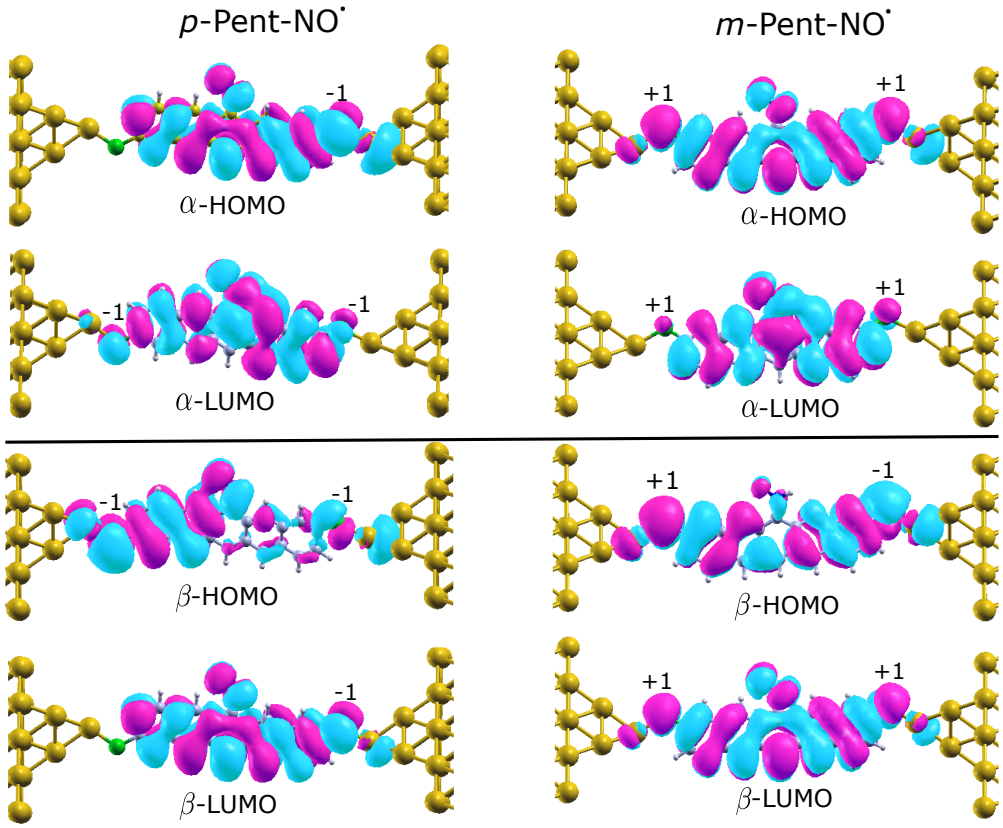

Figure 4.5: Spatial distribution of spin-up (top panel) and spin-down (bottom panel) MPSH frontier orbitals for *p*-Pent-NO˙ and *m*-Pent-NO˙ in molecular junctions. Pink and cyan colors denote the positive and negative parity of the molecular orbitals with isovalue 0.02 a.u. and is represented by +1 and -1 marked over the anchoring S atoms. Low orbital density on terminal S-atoms of *p*-Pent-NO˙ reveals inefficient transmission. For *m*-Pent-NO˙, DQI and CQI is predicted for spin-up and spin-down electrons respectively.

of the asymmetrical orbital distribution. Fig. 4.5 illustrates the spin-up and spin-down frontier MPSH MOs of *p*-Pent-NO˙ and *m*-Pent-NO˙ in junction. For *p*-Pent-NO˙, both α-HOMO and β-LUMO exhibits negligible orbital density at the left terminal S-atom indicating weak coupling to left electrode and hence inefficient transmission. While for *m*-Pent-NO˙, although the orbital density on left S-atom of α-LUMO is small, however, the signs of the coefficients at two sulphur atoms are positive for both α-HOMO and α-LUMO. This clearly indicates the partial cancellation of the two terms in Eq. 4.4 and hence signatures of DQI in spin-up orientation of *m*-Pent-NO˙. For spin-down electrons, all the terminal S-atoms bear significant amplitude with the product of the coefficients being negative for HOMO and positive for LUMO giving clear prediction of CQI in spin-down orientation of *m*-Pent-NO˙.

4.3.2.2 Transmission Eigenchannels

Transmission Eigenchannels (EC) provide an intuitive picture of the electron transport by breaking the transmission into non-mixing channels where each EC has a well defined transmission probability.

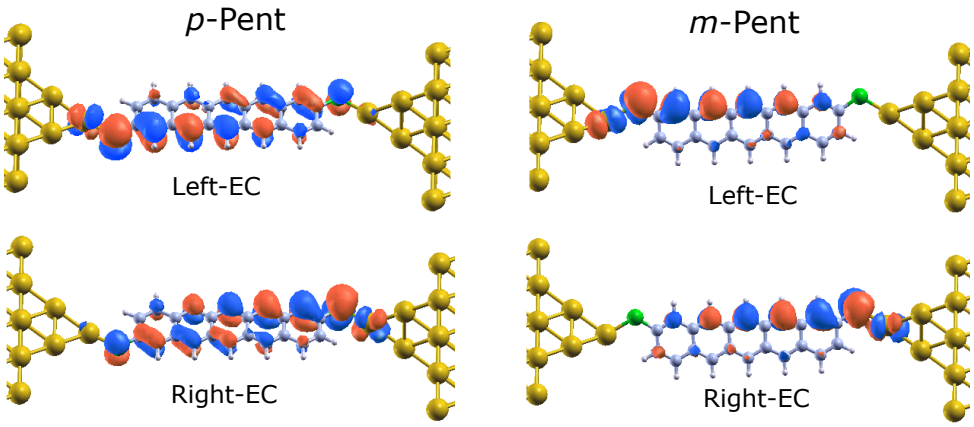

Figure 4.6: Transmission Eigenchannels (EC) of *p*-Pent and *m*-Pent. Terminal coupling is weak for *m*-Pent than *p*-Pent.

Fig. 4.6 illustrates the ECs for *p*-Pent and *m*-Pent. For *p*-Pent, both the pathways connecting left and right electrode are equally conductive with strong terminal coupling at both the ends for both Left-EC and Right-EC. However, for *m*-Pent, only shorter pathway connecting left and right electrode is conductive with relatively weaker coupling

at one of the terminating end. Thus, both the Eigenchannels of *m*-Pent are only partially open for conduction, in contrast to fully conductive channels of *p*-Pent, which strongly supports the lower conductance of *m*-Pent as compared to *p*-Pent attributed to QI effects.

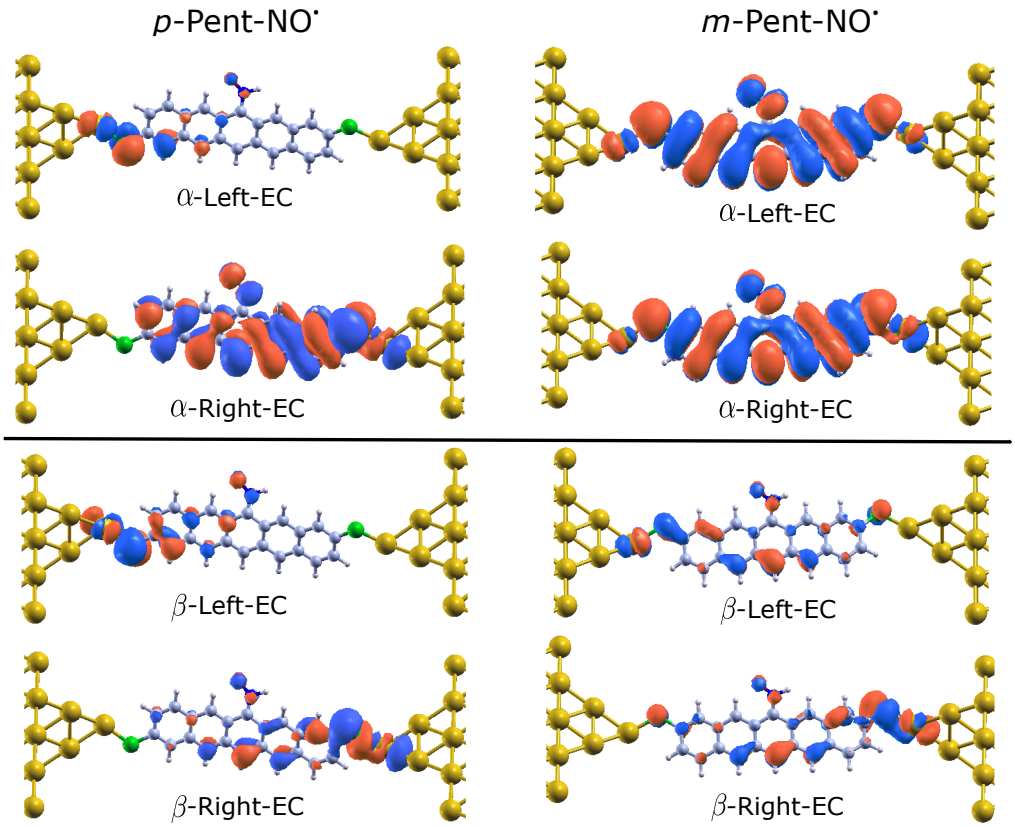

Figure 4.7: Transmission Eigenchannels (EC) for spin-up (top panel) and spin-down (bottom panel) channels of *p*-Pent-NO· and *m*-Pent-NO·. ECs of *p*-Pent-NO· are either blocked by radical center or by terminal thiol group.

For *p*-Pent-NO· and *m*-Pent-NO·, both the spin ECs are illustrated in Fig. 4.7. In case of *p*-Pent-NO· the EC is either blocked by radical center or is partially conductive due to weak terminal coupling. In contrast, *m*-Pent-NO· exhibits fully conductive channels with strong terminal coupling for both the spin channels. Thus clearly indicating higher conductance of *m*-Pent-NO· than *p*-Pent-NO·. Apart from this, spin-up ECs are more conductive than spin-down channels for both *p*-Pent-NO· and *m*-Pent-NO· except α-Left-EC of *p*-Pent-NO·. The higher conductance of spin-up electrons as compared to

the spin-down electrons is also revealed from transmission spectra (in Fig. 4.3) with α-HOMO lying near the Fermi energy than β-HOMO, thus indicating perfect spin filtering in radical molecular junctions.

4.3.3 Spin filtering in NN and OVER radicals

Apart from the aforementioned radicals, we investigated the spin polarized transport across two other stable organic radicals i.e. nitronyl nitroxide (NN) and oxo-verdazyl (OVER), shown in Fig. 4.8. Owing to the stability, both the radicals are expected to give spin polarized transmission curves with high SFE. However, the spin-resolved transmission spectra shown in Fig. 4.9a reveals an unusual resemblence of α and β transmission curves for the two radicals under study. It indicates that although the two radicals are stable enough, they cannot act as good spin filters.

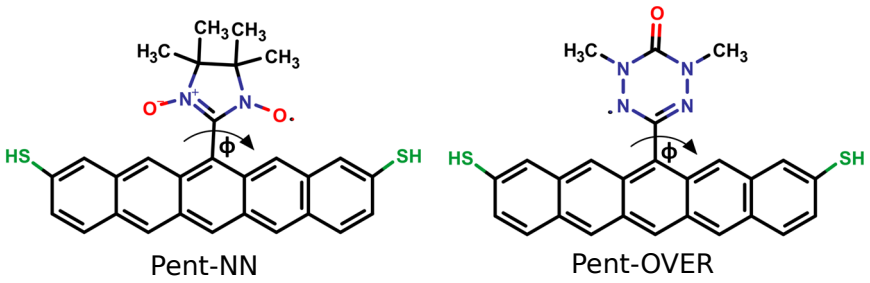

Figure 4.8: Pentacene connected to stable organic radicals nitronyl nitoxide **(Pent-NN)** and oxo-verdazyl **(Pent-OVER)**. Thiol groups at both the ends serve as linkers to gold electrodes. ϕ is the dihedral angle between radical moiety and pentacene core.

The detailed analysis of optimized geometry reveals a non-planar arrangement of pentacene-radical system, where the radical centre is oriented perpendicular to the plane of the pentacene core due to steric hindrance. **Pent-NN** was found to exhibit a dihedral angle of $\phi = 64.2^{\circ}$ between NN and pentacence core in gas-phase (B3LYP/def2-TZVP optimized structure), which changes to 55° when inserted in junction. **Pent-OVER** is even more twisted with a dihedral angle of $\phi = 84.8^{\circ}$ in gas phase which further increases to 97.2° in junction. This orthogonal arrangement of radical moiety w.r.t to pentacene bridging molecule forbids the participation of π-orbitals of radical bearing unpaired electron in spin transport. The spin density plots for molecules in junction,

shown in Fig. 4.9b, also illustrates the localization of spin density only on radical centre due to non-planar arrangement and hence not participating in transmission.

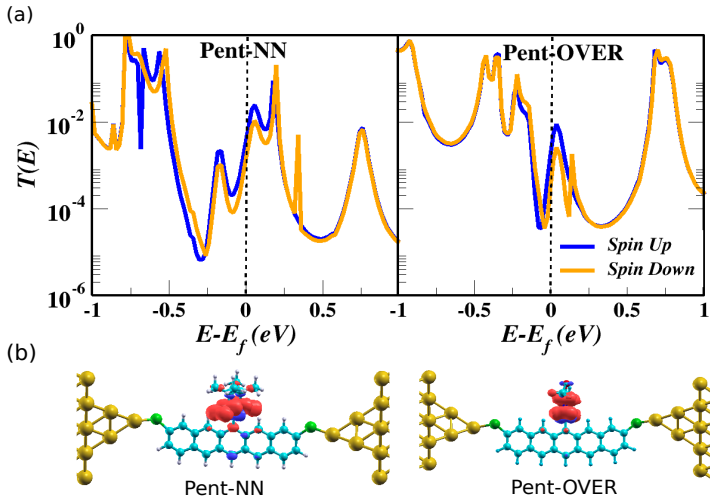

Figure 4.9: (a) Spin-resolved transmission spectra for **Pent-NN** and **Pent-OVER**. (b) Spin density plots for junctions containing Pent-NN and Pent-OVER.

One of the strategy to utilize such stable radicals for spin-filtering is to have a conjugated, planar arrangement of the radical centre to the pentacene instead of the perpendicular orientation where the radical is decoupled to the pentacene core. To do so, we connected NN and OVER to pentacene via Ethynyl spacer, as shown in Fig. 4.10a, denoted as Pent-Ethynyl-NN and Pent-Ethynyl-OVER. On inserting the ethynyl spacer, two contrasting factors influencing the spin transport will come into picture. One is the increase in overall distance of the radical from pentacene framework on incorporating the ethynyl spacer, which will decrease the participation of radical in transport. Other is the molecular geometry, i.e., the planar arrangement of the radical to the pentacene will enhance the participation of the radical.

The transmission spectra shown in Fig. 4.10b, indicates significant spin-polarization for Pent-Ethynyl-NN and Pent-Ethynyl-OVER. The extensive delocalization of spin density shown in Fig. 4.10b on the bridging molecule due to planar configuration also facilitates the spin-dependent electron transport in this case. Thus, the relative orientation of the radical w.r.t to bridging molecule plays a decisive role in tuning the spin polarization.

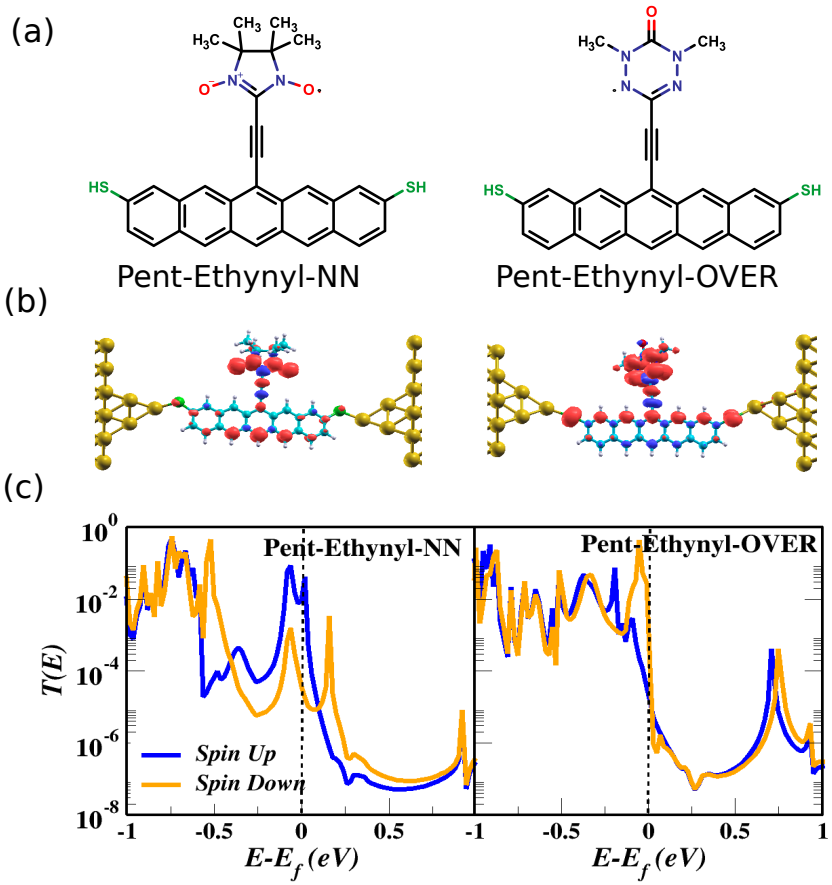

Figure 4.10: (a) NN and OVER connected to pentacene via ethynyl spacer, Pent-Ethynyl-NN and Pent-Ethynyl-OVER, (b) Spin-density plots for junctions containing Pent-Ethynyl-NN and Pent-Ethynyl-OVER, (c) Spin-resolved transmission spectra for Pent-Ethynyl-NN and Pent-Ethynyl-OVER.

4.4 Conclusion

We theoretically investigated the QI effects in spin polarized junctions and realized the anomalous behavior of QI stemming from localized radical spins in molecular junctions. The exchange splittings split the energy levels in the radical junctions and invoke the anomaly in QI patterns in such a way that for meta connected radicals, DQI dip observed in parent *m*-Pent is shifted to higher energy for one of the spin orientation, thereby increasing the conductance at the Fermi level, while it completely transforms to a CQI feature for other spin orientation. For para connected radicals, one of the

spin orientation yield usual CQI feature as of parent *p*-Pent but accompanied with decreased conductance at the Fermi level, however, other spin orientation results in complete crossover to DQI feature. In conclusion, meta connected radicals yields higher conductance than para ones for both spin orientations, which is in complete contrast to non-magnetic pentacene as well as non-radical analogues of all the radicals under study.

We further demonstrate that for the non-magnetic pentacene, the absence of magnetic centers results in spin-independent transport in acene based junctions. High spin filtering efficiency is observed for the radical systems with substantial delocalization of spin density on the entire pentacene backbone. The spin-polarized transport across the most stable organic radicals NN and OVER reveals that although both the radicals exhibits localized magnetic centres, but both of them acts as inefficient spin filters. This clearly indicates that the presence of unpaired electron is not a sole requirement for inciting spin polarization. The molecular geometry of the radical plays a significant role in controlling the spin filtering. An appropriate control over the geometry can yeild significant spin polarization in such stable radical systems. Thus, we believe that our findings provide a potential approach to facilitate future design attempts of single localized spin molecular junctions.

CHAPTER 5

Spin Filtering Effects in Photo-Responsive Single Molecule Junctions

5.1 Introduction

The use of persistent organic radicals for inciting the spin polarized current through a single molecule connected to source and drain electrodes is well understood from previous chapter. However, instead of the use of permanent magnetic subunits, the more practical route is the development of stimuli-responsive systems that can switch between two distinct spin states once triggered with external stimuli such as light, mechanical force, electric field, magnetic field and chemical stimuli.[175] Light has been widely used as the most promising external control stimuli for designing single molecule electrical switches whose conductance can be reversibly turned on and off.[176] In this context, many photochromic molecules including azobenzene, diarylethene, stilbene, spiropyran have been utilized as single molecule electrical switches since they can be reversibly switched between two stable structures upon light irradiation.[177,178] However, for molecular spintronics, a long standing quest is the evolution of the light-responsive molecular spin system in which intramolecular spin alignment can be controlled by the

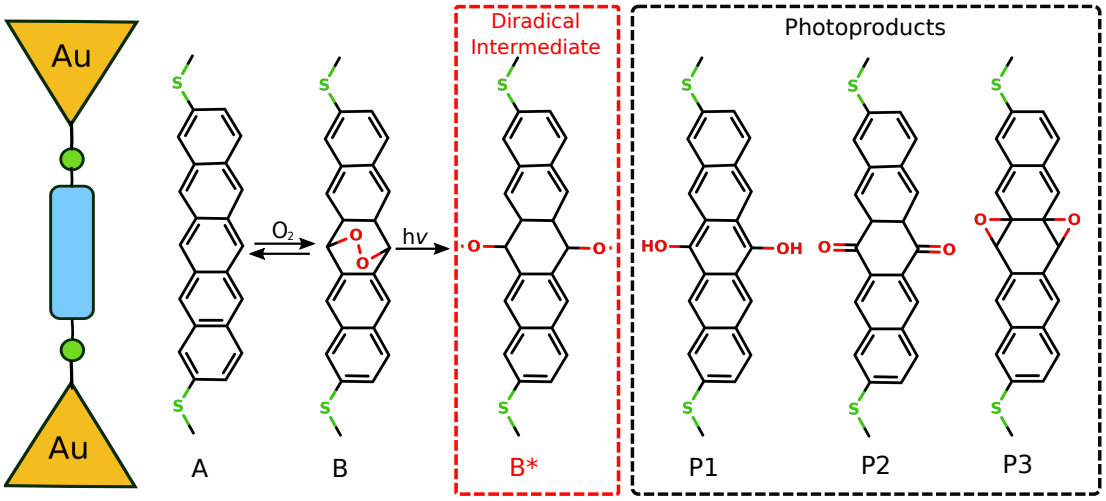

Figure 5.1: Junction schematic and molecular structures of the intermediates involved in the photochemical reaction of endoperoxide (EPO). The parent pentacene (A) in the presence of molecular oxygen yields pent-EPO (B). The photoexcited diradical intermediate state (B*) shown in red enclosure decomposes into various possible photoproducts including dihydroxypentacene (P1), pentaquinone (P2) and diepoxypentacene (P3) rearrangement products shown in black enclosure.

action of light.[179] The integration of such photoactive units in solid state devices could potentially yield efficient ultrafast manipulation of a spintronic device. However, owing to the highly reactive nature of the radical species, the realization of such photomagnetic switches in device applications with the persistent spin sources is a challenging task and has not been accomplished yet. On the other hand, transient spin carriers could be of utmost importance here to achieve ultrafast control of molecular spintronic properties.

In this work, we propose an optically driven spin filter employing endoperoxide (EPOs) based molecular junctions where the molecule is coupled to gold electrodes. As illustrated in Fig. 5.1, when exposed to air and light, acenes undergo a reaction with aerated oxygen to give EPOs with O-O single bond as a peroxidic bridge in the central ring. Upon further photoexcitation, the homolytic cleavage of the peroxide O-O bond takes place producing diradical intermediate along the reaction pathway.[180] The generated diradical intermediate eventually decomposes into quinones, hyrdoxyquinones or diepoxides as rearranged photoproducts.[181] The likely existence of a diradical intermediate reachable by the photoactivation of EPO ground state is unambiguously reported and has been exploited for numerous photobiological processes.[182–184] Despite their ob-

vious appeal as spin polarized candidates, EPOs have seldom been used in molecular spintronics. Here, we undertake a theoretical study, demonstrating that the spin selective transmission mediated by the diradical intermediate of EPO can be successfully employed to induce transient spin polarization. We analyze how the structural reorganization and the changes in molecular electron density distribution by optical excitation affects the transport properties in junctions with a primary focus on the involved diradical intermediate. Furthermore, the results demonstrate the key role played by quantum interference (QI) effects in controlling the conductance throughout the entire photochemical reaction pathway.

5.2 Computational Details

Firstly, the geometries of isolated molecules involved in the photochemical reaction pathway, that is, A, B, B*, P1, P2 and P3 (shown in Fig. 5.1) are optimized including the two S-H bonds at both the ends using B3LYP/def2-TZVP method in *ORCA*.[142] As depicted in Fig. 5.2, the optimized molecules are then sandwiched between two gold Au(111) electrodes after the dissociation of terminal hydrogen atoms from the thiol anchoring groups to form single molecule junctions. As described in previous chapter, the same device model is used to perform the spin dependent electron transport calculations using *TranSIESTA* code,[116] adopting NEGF-DFT method.[110,185]

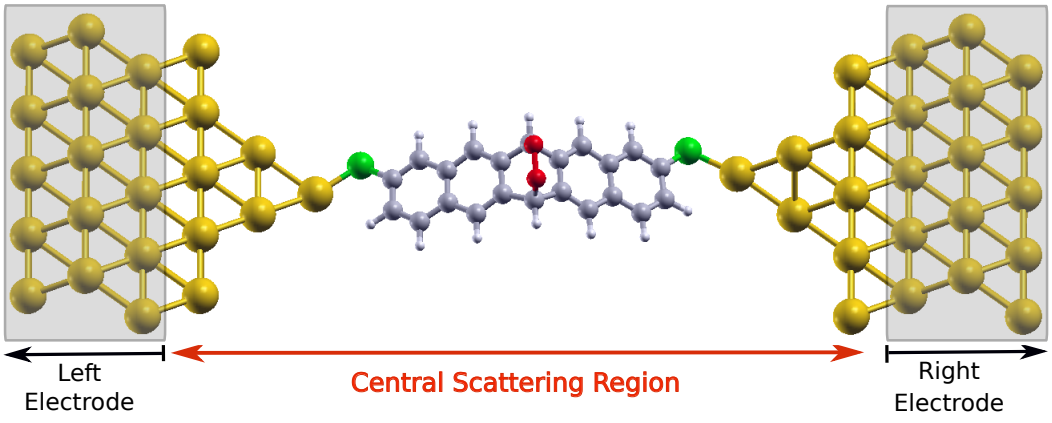

Figure 5.2: Device set up of Au-Molecule-Au junction used in electron transport calculations illustrating pent-EPO molecule placed between two Au(111) electrodes via sulphur anchoring atoms. Central scattering region consists of central molecule and 4-atom conical gold junction with an additional 5×5 layer of Au atoms.

Norm-conserving pseudopotentials are used to describe the core electrons.[115] DZP basis set is used for molecular atoms while SZP basis set is used for Au-atoms. A mesh cutoff of 300 Ry is used with Brillouin zone sampling using $3 \times 3 \times 10$ k-points in x, y and z directions. The electron transport is along z-direction. The transmission function is computed in the spirit of Landauer-Büttiker[186] formalism using Eq. 4.1 to Eq. 4.3 presented in Chapter-4.

5.3 Results and Discussion

The gas phase geometries of the isolated molecules involved in the photochemical pathway of EPOs (shown in Fig. 5.1) are optimized at B3LYP/def2-TZVP level. The geometric comparison reveals that for B and B*, besides the O-O cleavage ($d_{\text{o-o}}$), butterfly bending of pentacene moiety defined as the angle (ϕ) between the two flaps bisected by mirror plane containing the O-O bridge (shown in Fig. 5.3a) serve as another degree of freedom characterizing O-O homolysis products. In equilibrium geometry, pent-EPO (B) is characterized by a distance $d_{\text{o-o}}$= 1.47 Å and angle ϕ = 126.49°.

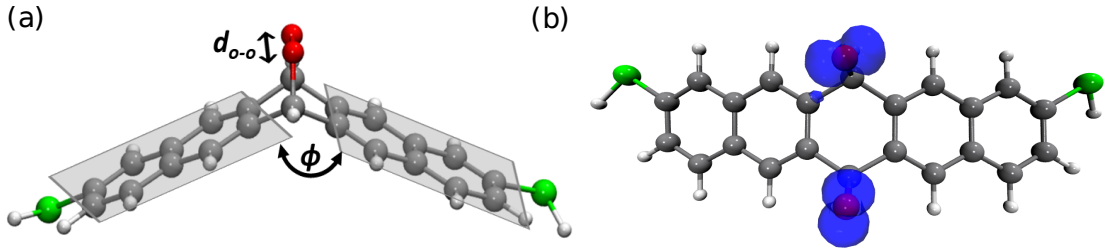

Figure 5.3: (a) Molecular geometry of pent-EPO (B) optimized at B3LYP/def2-TZVP level where $d_{\text{o-o}}$ is the distance between two O-atoms and ϕ is the angle between two planes bisected by the mirror plane containing O-O peroxide bridge. (b) Spin density plot of diradical intermediate (B*) obtained using B3LYP/def2-TZVP method illustrating spin density localized on two O-atoms.

For EPOs, it has already been demonstrated that upon irradiation, an electron is excited from $\pi^{\star}_{\text{oo}}$ to antibonding $\sigma^{\star}_{\text{oo}}$ which corresponds to the homolytic cleavage of O-O bond leading to first excited state.[187–189] Using MS-CASPT2/CASSCF methods, Mollenhauer et al. computed the photochemical pathway leading to O-O bond dissociation showing that the photo-dissociation process is governed by the degeneracy of four

singlet plus four triplet states and predicted the diradical intermediate geometry corresponding to 8-fold degeneracy.[190] Since the determination of electronically excited states of EPO is not the prime focus of this work, we obtained the ground state structure of diradical species (B*) that can function as the electronically excited diradical intermediate of pent-EPO (B) by the homolytic scission of peroxide O-O bond and found it to be adiabatically located at 0.92 eV from pent-EPO (B) ground state. The structure corresponding to diradical intermediate (B*) shows a larger distance of $d_{\text{o-o}}$ = 3.54 Å and more planar pentacene moiety as compared to pent-EPO (B) with ϕ = 156.39°. This is in fair agreement to the excited state geometry predicted by Mollenhauer et al. using SA-CASSCF methods for anthracene-EPO.[190] Apart from this, broken symmetry calculations on B* state at B3LYP/def2-TZVP level reveals singlet triplet energy gap of 73.05 cm^{-1} with a ferromagnetic ground state and $< S^2 >_{BS}$ value of 1.00 indicating ideal diradical configuration of B* in low spin state. The spin density plot of B* shown in Fig. 5.3b also illustrates that homolytic O-O scission in EPO breaks the spin symmetry and yields ferromagnetic ordering with the spin density localized on the two O-atoms. The intermediate diradical centered on O-atoms (B*) then eventually decomposes to diverse photoproducts such as quinones, hydroxyquinones or diepoxides depending upon the solvent conditions and substitutents. Here, we will first discuss the evolution of transmission characteristics for EPO (B) and its diradical intermediate (B*) starting from the parent pentacene (A). In the subsequent discussion, we will discuss how QI effects can be harnessed to optimize the response of EPO based junction through various possible photochemical pathways.

5.3.1 Spin resolved transport in EPO and diradical intermediate

The spin-resolved transmission spectra of parent pentacene (A), pent-EPO (B) and its diradical intermediate (B*) is shown in Fig. 5.4. For parent pentacene, molecule has a conjugated form and completely planar geometry. While for pent-EPO, the orbital hybridization of edge carbon sites of the central benzene ring changes from sp^2 to sp^3 and the molecule loses conjugation in the central benzene ring. The broken conjugation in the central ring results in butterfly bending of EPO geometry exhibiting an angle ϕ = 126.49° as already discussed in previous section and shown in Fig. 5.3. The hybridization of molecule with the gold electrodes also preserves similar geometrical features for

both pentacene as well as pent-EPO once inserted in molecular junction. Similarly, for the diradical intermediate, the cleavage of O-O bond results in planar pentacene moiety with $\phi \approx 150^{\circ}$ for both isolated molecule as well as in junction. However, the distance between two O-atoms in B* changes from 3.54 Å for isolated molecule to 2.18 Å in molecular junction.

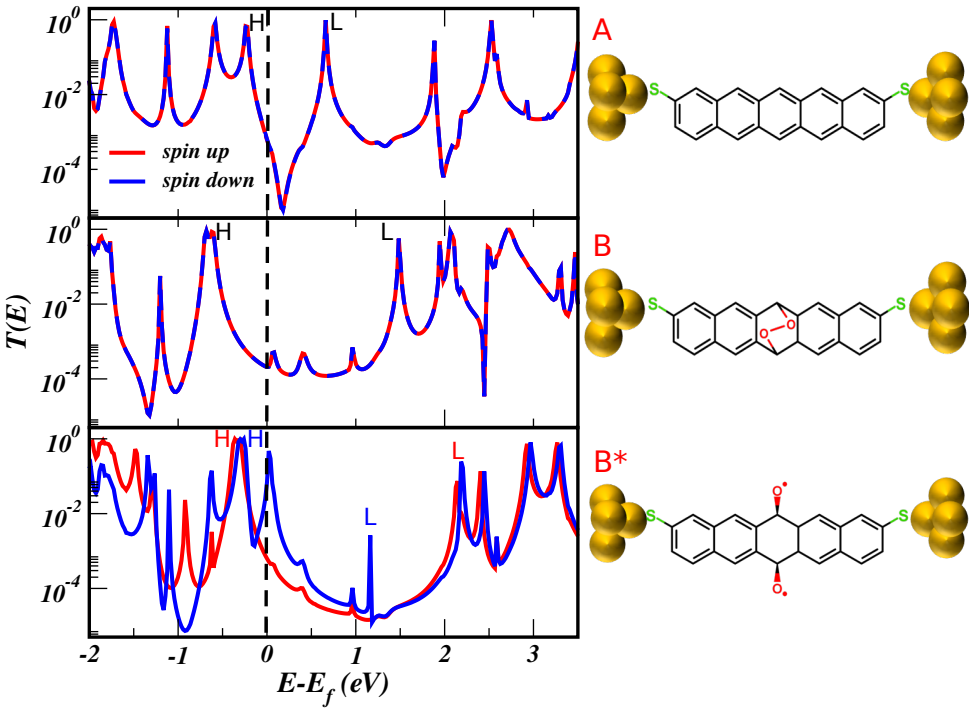

Figure 5.4: Spin-resolved transmission spectra of parent pentacene (A), pent-EPO (B) and its diradical intermediate (B*). The corresponding molecules held between two meta connected Au electrodes are illustrated alongwith. The spin-up and spin-down transmission is denoted by red and blue colors respectively. Vertical dotted line denotes the position of the Fermi energy. 'H' and 'L' marked over the peaks below and above the Fermi level points towards the HOMO and LUMO resonance respectively.

The transmission spectra (shown in Fig. 5.4) reveals that for parent pentacene, HOMO and LUMO resonance peaks are located at around -0.20 and 0.62 eV below and above the Fermi energy respectively and yields a HOMO-LUMO gap of 0.82 eV in junction with a conductance of the order of 10^{-3} at the Fermi level. This is accompanied by a sharp dip of the order of 10^{-5} located just above the Fermi energy arising due to destructive quantum interference (DQI) between the de-Broglie waves traversing along

different pathways. The DQI effects in meta connected pentacene is also discussed in details in Chapter-4. In contrast, the transmission spectra of pent-EPO (shown in middle panel of Fig. 5.4), reveals the alleviation of sharp DQI dips with two broad peaks corresponding to HOMO and LUMO resonances located at -0.60 and 1.48 eV respectively. However, due to larger HOMO-LUMO gap of 2.08 eV, conductance is deliberately reduced to the order of 10^{-4} at the Fermi level. The electronic structure calculations for isolated molecule at B3LYP/def2-TZVP level also reveals that HOMO-LUMO gap increases from 2.16 to 4.12 eV when going from fully conjugated pentacene to broken conjugated EPO (Fig. C.1 in Appendix-3).

Further for pentacene and pent-EPO, owing to spin degenerate levels, spin up transmission replicates with that of spin down displaying absence of spin polarization and zero SFE. On the other hand, the transmission spectra of diradical intermediate obtained by O-O homolytic scission (shown in bottom panel of Fig. 5.4) displays distinct α and β transmission curves especially around the Fermi level from -2.0 to 1.0 eV. The spin up transmission of B* displays two resonances at -0.30 and 2.15 eV below and above the Fermi energy respectively with a wider HOMO-LUMO gap of 2.45 eV. Akin to EPO, the spin up conductance is severely suppressed to the order of 10^{-4}. On the other hand, the spin down transmission spectra reveals three dominant peaks with two of them residing below and above the Fermi energy at -0.20 and 1.16 eV respectively and one peak anomalously centered at the Fermi energy. More interestingly, the anomalous peak located at the Fermi energy of spin down transmission spectra yields higher conductance of the order of 10^{-2} and results in perfect spin filtering behaviour with high SFE of 97.8% (calculated using Eq. 4.3).

To get a deeper understanding of the different features observed in the spin-resolved transmission spectra of B*, density of states projected (PDOS) onto the C(2p) and O(2p) atomic orbitals is shown in Fig. 5.5. Here, the quest arises that whether the anomalous spin down peak at the Fermi energy is a resonance peak associated with a molecular channel or an additional state induced as a result of orbital hybridization between molecule and gold electrode known as hybrid interface states (HIS).[191,192] To scrutinize this, we compared the total DOS of the isolated diradical B* (shown with grey color in left panel of Fig. 5.5) with the PDOS projected over the molecular atoms in junction (shown with grey color in right panel of Fig. 5.5). The total DOS of the isolated molecule reveals that the spin-down spectra exhibits two nearly degenerate peaks at ~

0.5 eV above the Fermi energy. The orbital resolved DOS further reveals that the two degenerate peaks arises from p_z-orbitals of two O-atoms. Further, the DOS projected over the p-orbitals of two individual O-atoms (Fig. C.7 in Appendix-3) affirms that the two degenerate peaks individually corresponds to the p_z-orbitals of two different O-atoms The spatial distribution of molecular orbitals of isolated molecule (shown in Fig. C.3 in Appendix-3) further indicates one to one correspondence between the two degenerate peaks and closely aligned LUMO and LUMO+1 of the molecule localized on the different O-atoms.

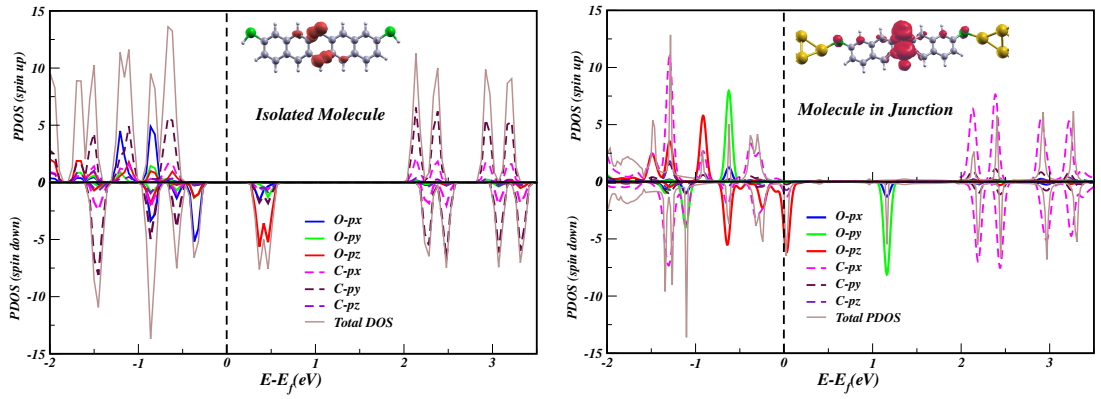

Figure 5.5: Projected density of states (PDOS) onto the C(2p) and O(2p) atomic orbitals of diradical intermediate (B*) of EPO in isolated state (left panel) and in molecular junction (right panel). Grey color indicates total DOS for isolated B*, while in junction it corresponds to PDOS onto the scattering region.

Moving to the molecular junction, the spin-resolved PDOS reveals a clear correspondence between the spin up and spin down peaks in transmission function (shown in bottom panel of Fig. 5.4) and the PDOS. However, in comparison to the DOS of the isolated molecule, the spin down PDOS spectrum in junction displays modified DOS near the Fermi level wherein no any degenerate peaks are observed at $\sim$ 0.5 eV. Instead two additional peaks originating from p-orbitals of O-atoms appears at the Fermi energy and 1.16 eV above the Fermi energy. At the Fermi energy, there is a clear contribution arising from p_z orbitals of radical centered O-atoms in the spin down PDOS, while there is no corresponding peak at the Fermi energy for spin up channel. Apart from this, the spin down PDOS spectra displays another distinct green peak originating from p_y orbitals of O-atoms at 1.16 eV above the Fermi energy. On the other hand, for spin up

configuration, the PDOS is very much featureless in the energy window of 0 to 2 eV. This clearly indicates that spin bearing oxygen atoms plays a crucial role in inducing high spin filtering in the diradical intermediate of EPO. Further, from the PDOS comparison of isolated molecule and molecule in junction, one can intuitively understand that the orbital hybridization of the molecular orbitals with gold electrodes results in lifting of degeneracy of LUMO and LUMO+1 and yields two individual peaks located at the Fermi energy and 1.16 eV above it. Apart from this, the spin density distribution of B* in isolated state and in molecular junction, computed at the same PBE level of theory, reveals ferromagnetic alignment of unpaired spins. However, for isolated B*, the unpaired spins reside in two orthogonal p-orbitals, while in junction the smaller distance between two O-atoms, that is, $d_{\text{o-o}}$ = 2.18 Å, favors mixing of p-orbitals.

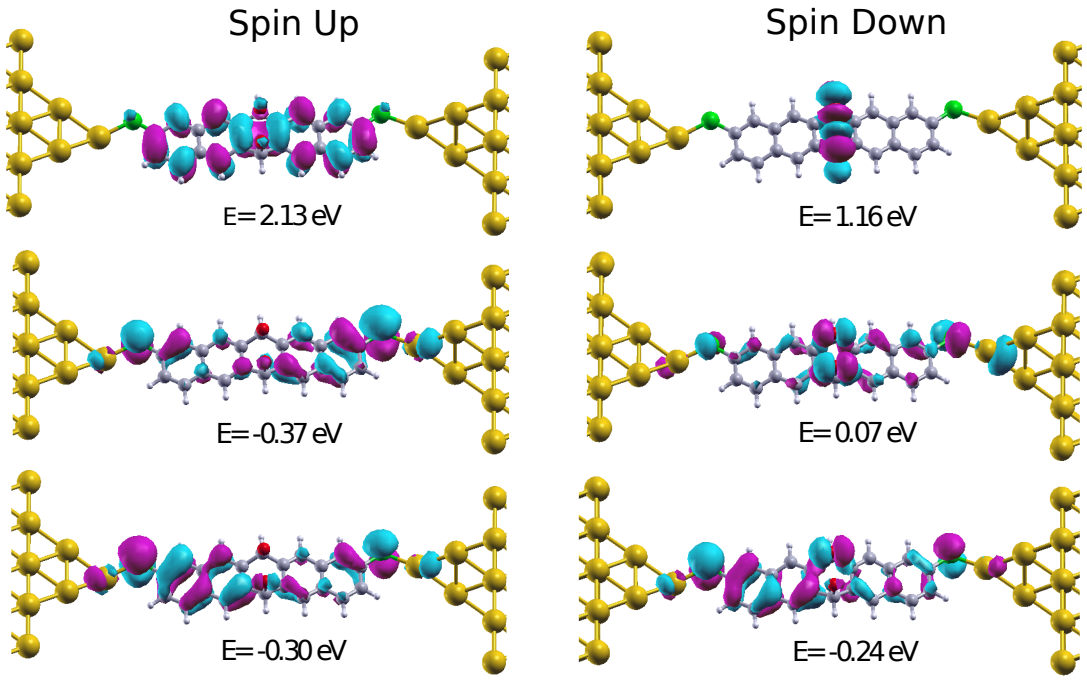

Figure 5.6: Spatial distribution of frontier MPSH states near the Fermi energy of diradical intermediate (B*) in junction. The spin up and spin down states are shown in left and right columns respectively.

To further elucidate the nature of spin dependent channels of B* in molecular junction, molecular projected self consistent Hamiltonian (MPSH) spectrum was computed. Formally, MPSH states represent modified molecular orbitals and electronic reorganiza-

tion of energy levels in the presence of surrounding electrodes. The spatial distribution of MPSH states, shown in Fig. 5.6, reveals that for spin-up configuration, there are two nearly degenerate states below the Fermi level at ~ -0.30 and -0.37 eV which are spatially separated with enhanced orbital density at the opposite sides. Further, the MPSH spectra for spin down configuration reveals an interesting phenomena. The spatial distribution of MPSH states at 0.07 eV and 1.16 eV corresponding to the two peaks reveals that the one near the Fermi energy at 0.07 eV localized on the O-atoms displays an efficient coupling with gold electrodes. Thus provides a conducting channel for spin down electrons and yields higher conductance at the Fermi level. While the other one located at 1.16 eV shows inefficient coupling with electrodes and results in transmission peak of lesser amplitude as can be seen from the transmission spectra shown in bottom panel of Fig. 5.4.

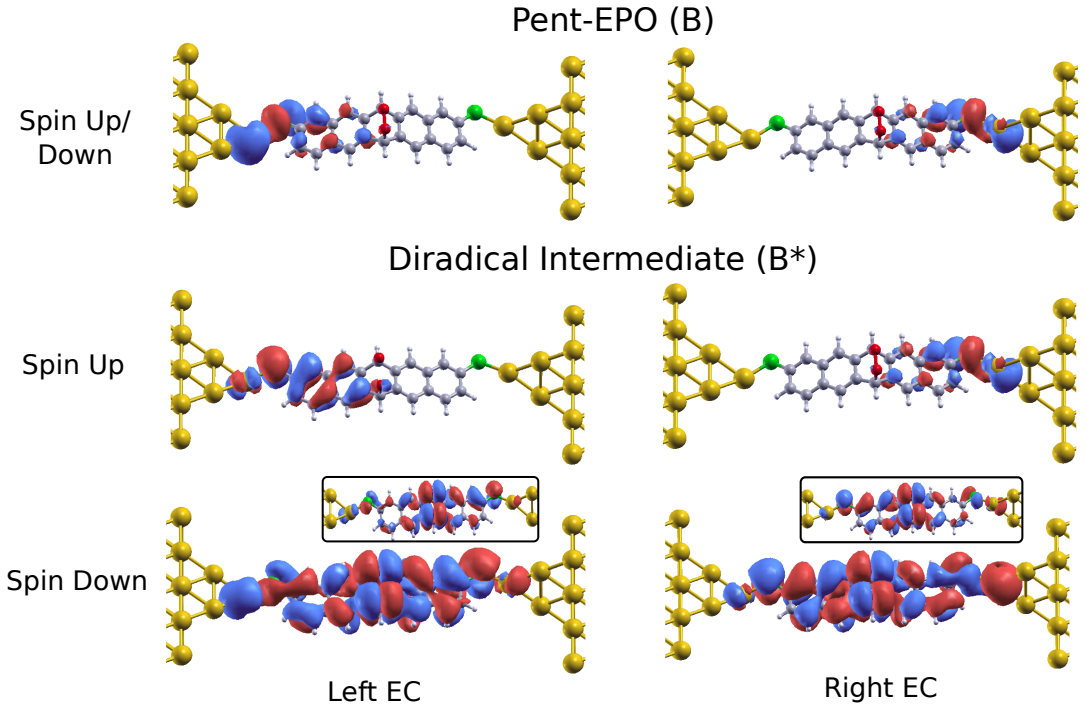

Figure 5.7: Transmission eigenchannels (EC) of pent-EPO (B) and diradical intermediate (B*) (with an isovalue of 0.02). For EPO, both Left EC and Right EC is vanished on peroxide bridge. For B*, spin up ECs replicate with B, while spin down ECs are completely delocalized. To get a clear picture of the nature of spin down ECs, a larger isovalue of 0.05 is also used as shown in the black boxes.

Finally, Transmission Eigenchannel (EC) analysis for B and B* illustrated in

Fig. 5.7 reveals that for pent-EPO, both Left EC and Right EC is vanished on the peroxide bridge. Thus indicating that the broken conjugation by the peroxide bridge introduces obstacles in the coherent charge propagation pathway by breaking the continuity of conjugation pathway between the electrodes. Hence, results in lower conductance as already inspected from the transmission spectra (shown in Fig. 5.4). For B*, spin up ECs replicates with that of of pent-EPO (B) with the ECs blocked by the peroxide bridge. In contrast, for spin down electrons, both the ECs are delocalized throughout the bridging molecule and extended on both the sides with larger amplitude than spin up ECs. Thus, indicating strong terminal coupling of spin down ECs. Further, spin down ECs plotted at larger isovalue of 0.05 (shown in inset) reveals that the spin down channel becomes conductive due to major contribution coming from radical centered O-atoms and hence results in high conductance of spin down electrons and thus high SFE.

5.3.2 Role of Quantum Interference in EPO based device

After gaining insights in to spin selective transport via the diradical intermediate of EPO, we turned out to explore quantum interference prospective in junctions containing EPO and the possible photoproducts (P1, P2 and P3) shown in Fig. 5.1. As for linearly π-conjugated molecules, it has been demonstrated that the molecules with meta connection to the electrodes often disrupts the conduction due to destructive QI (DQI). While the para connected analogs are predicted to be better conductors due to constructive QI (CQI).[193,194] Furthermore, an illusory connection between cross conjugation and QI has also been established in few of the prior reports demonstrating an evidence of DQI for para connected cross-conjugated quinone which is in contrast to linearly conjugated molecules.[195–197]

Here, across the photochemical reaction pathway of EPO, the molecule is subjected to different degrees of π-conjugation patterns. As for parent pentacene exhibits fully linearly conjugated geometry, while the formation of peroxide bridge results in broken conjugation scenario for pent-EPO (B) and its diradical intermediate (B*). Apart from this, the various possible photoproducts includes dihydroxypentacene (labelled as P1) displays fully conjugated geometry, pentaquinone (labelled as P2) is a cross conjugated molecule and diepoxypentacene (labelled as P3) has a broken conjugated skele-

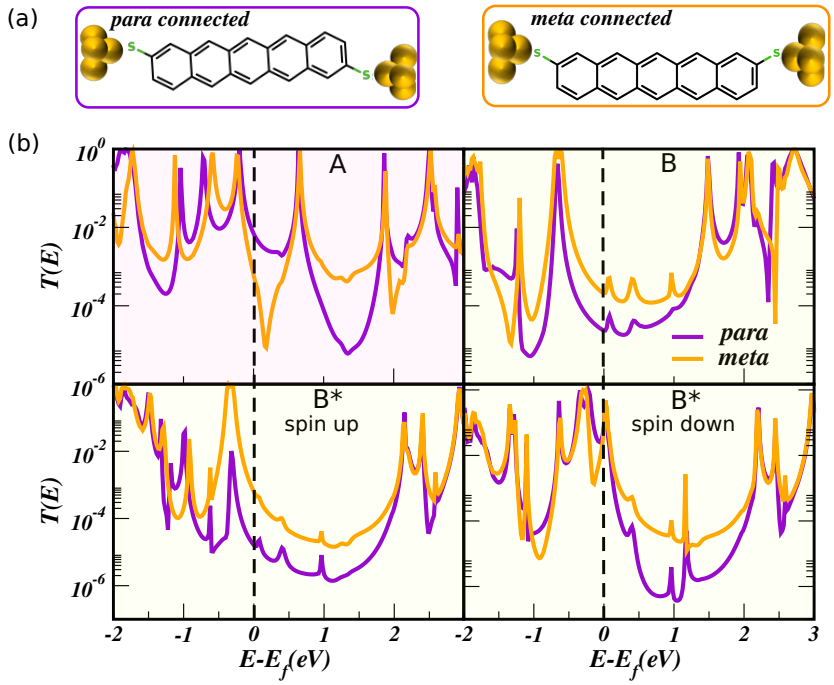

Figure 5.8: (a) Parent pentacene (A) held between two Au electrodes illustrating para and meta connections in purple and orange enclosures respectively. (b) Transmission spectra of pentacene (A), pent-EPO (B) and both spin configurations of diradical intermediate (B*), where purple and orange curves corresponds to molecules with para and meta connections respectively. The vertical dotted line denotes the position of the Fermi level.

ton. Thus, we calculated transmission spectra for pent-EPO and its photo-products with both para and meta connections to gold electrodes as shown in purple and orange enclosures of Fig. 5.8a respectively. The corresponding transmission spectra is represented by purple and orange curves for para and meta connections respectively in Fig. 5.8b. In what follows, we investigate how the different π-conjugation patterns of the molecule across the photochemical pathway of EPO can affect the molecular conductance such that QI features can be toggled on and off by the external stimuli to realize a QI based molecular switch.

As illustrated in Fig. 5.8b, for parent pentacene, QI manifests itself in the form of DQI for meta connected pentacene with a sharp dip of the order 10^{-5} near the Fermi level, while para connected pentacene yields higher conductance of the order 10^{-3} due to CQI. The appearance of CQI and DQI in the respective para and meta connections is

in complete agreement with previous theoretical and experimental studies on benzene and other polycyclic hydrocarbons.[159,198,199] In complete contrast to this, for broken conjugated EPO and its diradical intermediate (B*) in junction, the transmission spectra reveals no signatures of strong destructive interference dips in neither of the para and meta connections. To unveil whether the disappearance of strong DQI dips in EPO is associated with broken conjugated structure, we calculated transmission spectra for broken conjugated dihyrdropentacene (PH) obtained by replacing each radical centered oxygen atom of B* with a hydrogen atom at the central benzene ring of pentacene. The transmission spectra of dihyrdropentacene (Fig. C.6 in Appendix-3) also reveals no any impression of DQI dips in neither of the para and meta connections. This clearly indicates that the broken conjugated structure of EPO abandons the presence of strong DQI dips. Thus, we conclusively postulate that the photo-oxygenation of pentacene to yield EPO results in switching off the QI features, thus opening another wider area of applications in which EPO based device can serve as a stimuli responsive QI based switch. Such a unique combination of stimuli-response and quantum interference has been rarely explored in the literature.[200]

Apart from this, the calculated conductance at the Fermi energy, tabulated in Table 5.1, reveals that for pent-EPO, the conductance of para connected junction is lesser than the meta connected one with a decreased para/meta conductance ratio of 10^{-1} as compared to pentacene with para connected pentacene being more conductive as compared to meta one. Analogous to EPO, the spin up configuration of B* also reveals decreased para/meta conductance ratio of 10^{-2}. For spin-down, although the conductance values at Fermi energy are quite comparable for para and meta connection, but the transmission spectra shows lesser conductance of para connection than meta one over a wider energy range above the Fermi energy. Notably, this behavior was not observed for broken conjugated dihyrdropentacene (PH) for which the transmission spectra (shown in Fig. C.6 of Appendix-3) and calculated conductance (tabulated in Table 5.1) reveals that the transmission is slightly lower for meta connected PH as compared to the para one around the Fermi energy. This clearly indicates that the reversal of para/meta conductance in B and B* is not an absolute effect of broken conjugation, but could either be associated with the substituent effect in case of EPO or spin selective nature of its diradical intermediate.

As a well known fact, the diradical intermediate generated by homolytic O-O cleav-

Table 5.1: Calculated conductance ($\mathcal{G}$) in units of $\mathcal{G}_0$ for para and meta connected pent-EPO and the associated photo-products in junctions. The para/meta conductance ratio is also tabulated alongwith.

Molecule	$\mathcal{G}$ ($\mathcal{G}_\circ$)		para/meta
	para	meta	
Pentacene (A)	9.65×10^{-3}	1.13×10^{-3}	8.53×10^{0}
Pent-EPO (B)	2.34×10^{-5}	2.08×10^{-4}	1.12×10^{-1}
Intermediate (B*; spin up)	1.61×10^{-5}	6.30×10^{-4}	2.50×10^{-2}
Intermediate (B*; spin down)	7.94×10^{-2}	6.75×10^{-2}	1.17×10^{0}
Pent-Hydroxy (P1)	1.22×10^{-2}	4.73×10^{-3}	2.57×10^{0}
Pent-Quinone (P2)	2.45×10^{-7}	2.75×10^{-4}	8.90×10^{-4}
Pent-Diepoxy (P3)	2.91×10^{-5}	2.43×10^{-5}	1.19×10^{0}
Pent-Hydro	3.03×10^{-5}	1.41×10^{-5}	2.14×10^{0}

age of EPO has a shorter lifetime and it eventually decomposes to give diverse photo-products depending upon the solvent conditions and substituents.Fig. 5.9a illustrates the three most identified photoproducts of EPO, that is, dihyrdoxypentacene (P1) obtained by hydrogen rearrangement reaction of B*, pentaquinone (P2) obtained by elimination of H_2 from B * and diepoxypentacene (P3) which is identified as another dominant primary rearrangement product. The transmission spectra of possible photoproducts P1, P2 and P3 is shown in Fig. 5.9b. The first photoproduct, that is, fully conjugated dihyrdoxypentacene (P1) shows similar behavior as of pentacene bearing strong DQI dip for meta connected P1. The only difference is the slight shift in T(E) of P1 towards right as compared to pentacene, which is due to weak electrostatic gating effect of the oxygen atoms in P1. Another photo-product, pentaquinone (P2) bearing cross-conjugated molecular skeleton demonstrates DQI for para and CQI for meta connected P2 with para/meta conductance ratio of 10^{-4} which is in clear contrast to fully conjugated pentacene and dihyrdoxopentacene (P1). This generic feature of cross conjugated wires is well reported in several charge transport studies of cross conjugation versus linear conjugation.[161,201,202]Lastly, the third photo-product, that is, diepoxypentacene (P3) with broken conjugation reveals almost indistinguishable T(E) of para and meta connections with a decreased conductance of the order of 10^{-5} as of pent-EPO. To summarize, a significant variation in conductance can be realized starting from EPO to final photoproducts in both para and meta connections wherein QI features can be reversibly

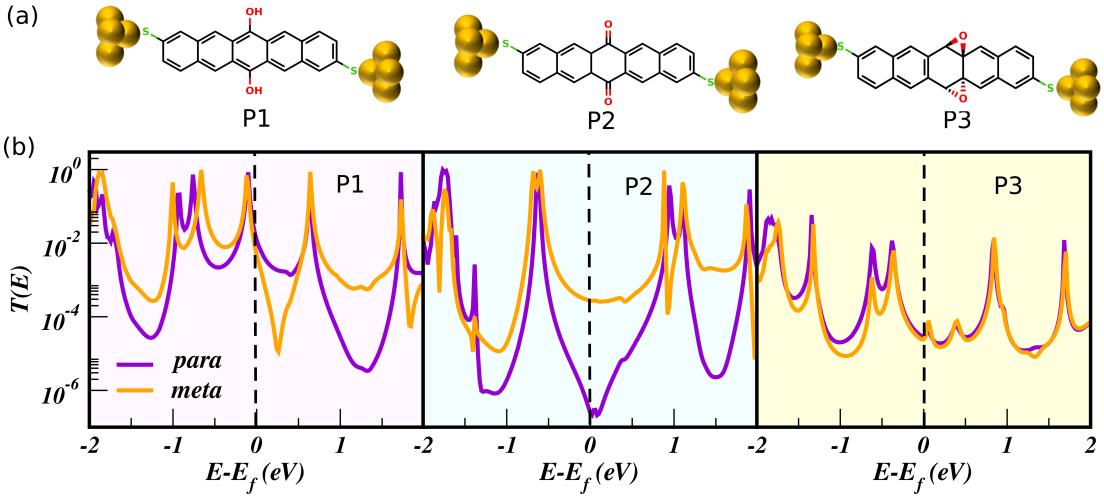

Figure 5.9: (a) Photoproducts of EPO namely dihyrdoxypentacene (P1), pentaquinone (P2) and diepoxypentacene (P3) in molecular junctions with para connections. The corresponding meta connections are shown in Fig. 5.1. (b) Calculated transmission spectra for para and meta connected P1, P2 and P3, where purple and orange curves corresponds to para and meta connections respectively. The vertical dotted line denotes the position of the Fermi level.

toggled on and off to realize a molecular switch.

5.4 Conclusions and Outlook

In summary, the work demonstrates a dual functionality integrated into a EPO based device with nearly perfect spin filtering by its diradical intermediate and switchable QI effects. A high spin filtering efficiency of 97.8% is achieved for diradical intermediate of EPO wherein molecular channels for one spin configuration are blocked by peroxide bridge. While for the other spin configuration, the radical centered O-atoms of peroxide bridge facilitates fully conducting channel. Thus, yielding a perfect candidate to realize a stimuli based spin filter activated by the action of light on EPO. Further, the altering degrees of conjugation in different products across the photochemical reaction pathway of EPO plays a dominant role in controlling the conductance. Molecules with fully conjugated structure yields higher conductance with strong CQI/DQI features in para/meta connections respectively, while cross conjugation results in the complete reversal of QI features with strong DQI in para connection. On the other hand, broken conjugated

skeleton substantially reduces the conductance and results in complete disappearance of strong DQI dips in both para and meta connections. These generic features enable the use of EPO based device as a photoactivated molecular switch in which QI features can be toggled on and off under the action of external stimuli.

Finally, we propose another prospective of using single molecule based device for the detection of reaction radical intermediates. Like diradical intermediate of EPO, free radicals are thought to be key intermediates of various biochemical processes. Thus, the identification and isolation of free radicals possess important significance for both fundamental research and practical applications. Although wide range of analytical techniques including EPR based spectroscopy have been developed to detect the radicals. However, the recognition of short-lived radical species across a reaction pathway is extremely challenging. The present work illustrates that EPO and its related photoproducts in a single molecule junction yields spin-unpolarized transmission. While for diradical intermediate of EPO, the spin discriminated transmission spectra governs the response of molecular device. This generic feature of spin polarized transmission by radical containing entity is self-explanatory and undeniable. Apart from this, one can also estimate the radicaloid character of a molecule in junction from the extent of spin polarization in the transmission spectra. Thus, we propose an idea of recognizing the radical intermediates across any reaction pathway using single molecule circuits. In this regime, scientists have already succeeded in recognition of isomers,[200] DNA[203] and carbohydrates[204] in single molecule junctions, however, the notion of detection of radical intermediates across a reaction pathway employing single molecule junction has not been discussed yet. Although sophisticated instruments and precise statistical data analysis algorithm is required in order to facilitate the radical intermediate detection in the single molecule conductance experiments, but the idea of pushing radical intermediate recognition capability to single molecule level is imperative to perceive and opens a new avenue to study the detailed mechanism of other pivotal chemical and biochemical processes.

CHAPTER 6

Anti-Ohmic Nanoconductors

6.1 Introduction

In recent years, the development and synthesis of highly conjugated polycyclic aromatic hydrocarbons (PAHs) with the intriguing open-shell characteristics have garnered substantial attention.[205] The diagnostic properties of open shell singlet diradicaloids arise from the unique combination of closed- and open-shell resonance forms and includes small energy gap between the frontier MOs.[78] Owing to the unique electronic structure and magnetic properties, the diradical hydrocarbons have been earmarked for various applications in molecular electronics, singlet fission and non-linear optics.[42,206] However, their full potential in spintronic device application has yet to be realized. Recent theoretical and experimental studies have demonstrated that the increase in the conjugation length of PAHs further leads to the increase in diradical character due to the recovery of more aromatic sextet rings in the diradical form.[207,208] This novel feature of longer PAHs could be harnessed to realize spin-dependent long-range charge transport.

Molecular nanowires mediating long range charge transport are desirable for their potential applications in future molecular scale circuitry.[209,210] Most of the conventional molecular wires suffer from an exponential decay of conductance ($\mathcal{G}$) with wire length (L) as $\mathcal{G} = Ae^{-\beta L}$, where A is a prefactor and β is attenuation (decay) factor. The posi-

tive β value signifies a decay of conductance. However, in recent years, molecular wires with unusual attenuation factors, such as β=0 (i.e., $\mathcal{G}$ independent of L) or even negative β values (i.e., $\mathcal{G}$ increasing with L) have become sparkle in the eyes of research community.[211–213] Such extraordinary wires exhibiting negative β values in phenomenological violation of the classical Ohm's law are called as anti-ohmic nanoconductors. This reversed exponential decay of conductance with length was first reported by Tada and Yoshizawa for nanographenes with zigzag edges.[214] Subsequently, the molecular wires based on porphyrin derivatives were presented with low attenuation factors[215,216] which was later endorsed by an experimental achievement by Leary et al.[217] Afterwards, several guiding principles were formulated to explain the non-trivial reversed conductance/length trends. Mandado and coworkers proposed an example of quinoid wires with exceptional anti-ohmic behavior.[218,219] Alongside, Stuyver et al. connected this behavior to diradical character.[220,221] Contrastingly, in the framework of multi-reference calculations, regular decay of conductance was observed.[222] Followed by this, unrestricted DFT calculations taking into account the spin-symmetry breaking also revealed a decrease in conductance with length for the alleged anti-ohmic wires.[223]

With these ongoing trial and error debates on the feasibility of anti-ohmic wires, we undertook a theoretical investigation of length-dependence of the conductance in molecular wires exhibiting pronounced diradical character in their ground state. In the context of diradical character, the highly conjugated polyacenes, consisting of linearly fused benzene rings, have been widely debated in literature.[224,225] While after the pioneering study by Bendikov et al., it is generally accepted that smaller acenes (up to hexacene) have a closed-shell singlet (CSS) ground state, while higher acenes are predicted to be in open-shell singlet (OSS) ground state.[69] The length dependence of conductance for acenes has remained a persistent puzzle[226–228], while the effect of spin polarized nature of higher acenes on the electron transport has been rarely considered.[83]

On the other hand, poles apart from polyacenes, there had been many speculations about 1-D linear chain of sp-hybridized carbon atoms, which potentially exist in two forms: polyynes with alternate single and triple bonds and cumulenes with consecutive double bonds.[229,230] Among the two series, cumulenes have seen the light of the day with an experimental observation of negative β values.[231,232] Notwithstanding, the synthesis of polyynes has been extensively reported, culminating with the isolation of [22]polyyne, however, due to dramatic increase in reactivity, [9]cumulene is the longest

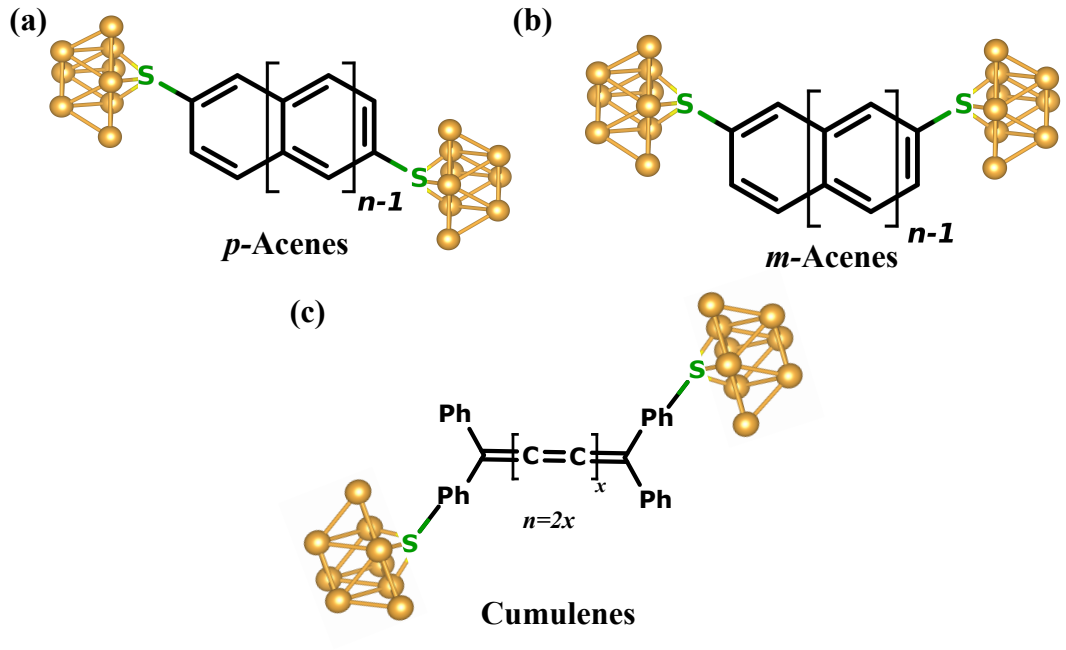

Figure 6.1: Junction schematics showing (a) para connected *p*-acenes,(b) meta connected *m*-acenes,(c) cumulenes suspended between two Au_9 clusters via thiol anchoring groups.

derivative studied to date.[233,234] This increased reactivity of [*n*]cumulenes itself points towards the open-shell character in longer cumulenes. However, the open-shell nature of cumulenes has not been reported hitherto. Here, in this work, we sought to re-examine the length dependence of molecular conductance for both acene and experimentally validated[231] cumulene series suspended between two gold electrodes, as shown in Fig. 6.1. The electrical conductance has been explicitly determined within the Landauer formalism using restricted closed-shell wavefunction for lower members in the series. While, broken symmetry (BS) wavefunction in an unrestricted formalism with spin and spatial symmetry breaking is used for higher members with OSS ground state.

6.2 Computational Methods

Electronic structure calculations: Geometry optimization of isolated dithiolated molecules are first performed by applying B3LYP/def2-TZVP[138,235] method in two distinct electronic states, i.e., closed shell singlet (CSS) and broken symmetry open shell singlet (OSS) state in ORCA[142] quantum chemical code. OSS states are treated using spin-unrestricted broken-symmetry Kohn-Sham (UKS-BS) method within the DFT framework, while spin-restricted (RKS) wavefunction is used for CSS states. Resolution of the identity (RI) approximation in conjunction with auxiliary basis set def2/J and chain of spheres (COSX) numerical integration is used to accelerate the calculations without losing its accuracy.[139] Tight convergence limits and increased integration grids (grid5) are used throughout.

Construction of Gold-Molecule-Gold junction: The molecular junctions are then constructed by placing the optimized isolated dithiol molecules between two gold electrodes after removing the terminal hydrogen atoms of thiol groups and forming the S-Au bonds. The gold electrodes are approximated by nine-atomic gold clusters, arranged in hexagonal closed-packed fcc Au-111 surface (Fig. 6.1). The Au-Au distance is set to 2.88 Å and Au-S distance is fixed to 2.40 Å.

Electron Transport calculations: The electron transport calculations are performed using Non-Equilibrium Green's Function combined with DFT (NEGF-DFT) as implemented in *Artaios*[170] using B3LYP exchange correlation functional in combination with LANL2DZ basis set. Accordingly, the model used in transmission calculations is divided into three regions: central (C) scattering region formed by the dithiolated molecule, and the left (L) and right (R) electrode consisting of Au_9 clusters. The transmission function is computed in the spirit of Landauer-Büttiker[186] formalism using equation

$$T_\sigma(E) = Tr(\Gamma_R G \Gamma_L G^\dagger)_\sigma \tag{6.1}$$

where σ represents the spin up/down electrons. $G/G^\dagger$ indicates the retarted/advanced Green's function of the central region. The coupling of central region to the electrodes is taken into account using self-energies, which are calculated by imposing a wide-band limit approximation[119] which assumes a constant density of states, independent of energy. A constant value of 0.036 eV^{-1}, taken from literature is used for the DOS of electrode.[60]

The zero bias conductance $\mathcal{G}$ in CSS limit is obtained as

$$\mathcal{G}(CSS) = \frac{2e^2}{h} T(E_F) \tag{6.2}$$

For spin-polarized systems in OSS state, transmission for spin-up (T_{up}) and spin-down (T_{down}) are different, therefore, the conductance in OSS state at the Fermi energy is computed as

$$\mathcal{G}(OSS) = \frac{e^2}{h}(T_{up}(E_F) + T_{down}(E_F)) \tag{6.3}$$

It is worth mentioning that although B3LYP functional is routinely employed for conductance calculations, however it tends to underestimate the HOMO-LUMO gap as compared to the fundamental gap (calculated as difference between ionization potential and electron affinity).[236] This is reflected in the form of overestimated conductance (by about 1-2 orders of magnitude) as compared to the experimental values. This limitation can be addressed by using a range-separated hybrid (RSH) functionals, which have been demonstrated to predict better HOMO-LUMO gaps[237] and provide realistic conductance estimates.[238,239] Thus, in an alternative approach, we also employed CAM-B3LYP, a RSH functional, beyond the commonly employed B3LYP functional. Interestingly, the calculated conductance using CAM-B3LYP, an RSH functional (Section D.6 in Appendix-4) yields similar qualitative trends as of B3LYP with improved conductance values, but at the cost of severe spin contamination in OSS state.

6.3 Results and Discussions

6.3.1 Electronic structure of isolated molecules

While the CSS ground state for lower acenes and cumulenes is well recognized in literature, but there is no clear consensus on the higher members of the series, yet. Thus, to establish the size-dependent onset of open-shell nature, ground state electronic properties are first examined for the isolated acenes and cumulenes, shown in insets of Figure 6.2. The relative energy difference between the OSS and CSS states, reveals that upto n=6 acene (Figure 6.2a) and n=12 cumulene (Figure 6.2c), OSS solutions converge to CSS state and yields $\Delta E_{OSS-CSS} \sim 0$, indicating that CSS state is ground state for the lower members of both the series. For n=7 acene, $\Delta E_{OSS-CSS}$ = -65 meV marks

the transition in ground state from CSS to OSS state. The increasing ΔE upto -650 meV for n=12, ultimately outstrip the CSS behavior of the system for higher acenes. The emergence of OSS ground state, for n ≥ 7, is in complete agreement with previous DFT calculations on higher acenes.[69,240] Interestingly, the similar kind of build-up of OSS character is also observed for cumulenes from n=14 onwards (Figure 6.2c). Although, $\Delta E_{OSS-CSS}$ for cumulenes is significantly lower than acenes, however a maxima of $\Delta E_{OSS-CSS}$ = -138 meV for n=24 cumulene clearly reveals an OSS ground state for the higher cumulenes as well.

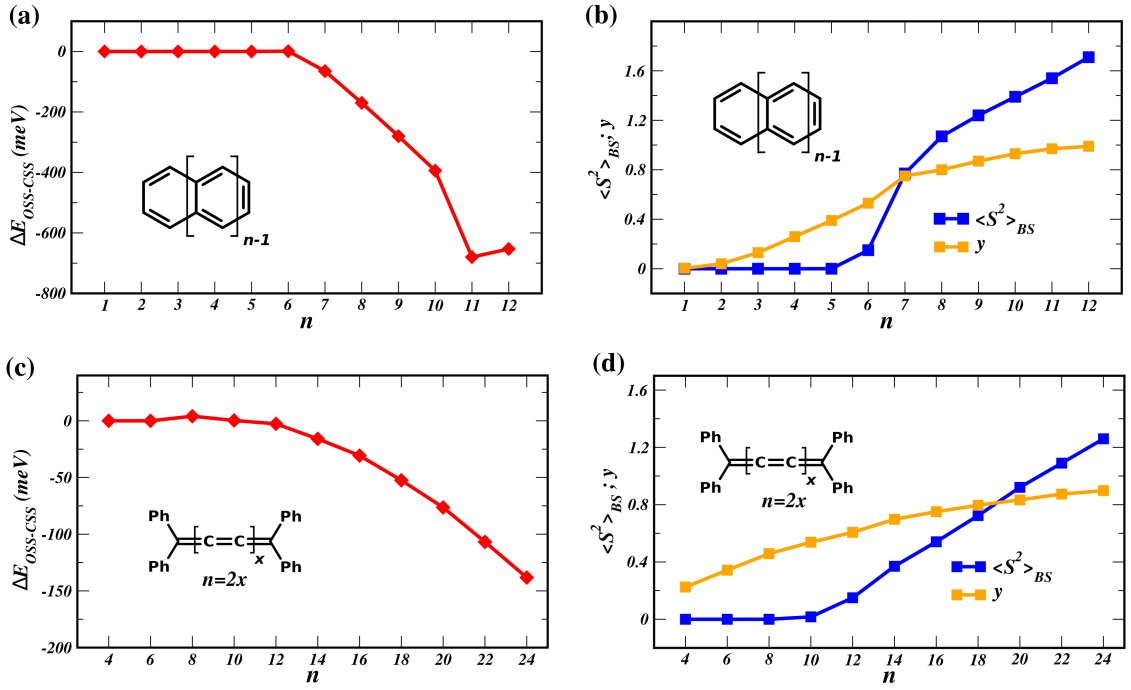

Figure 6.2: **(a, c)** Relative energy difference ($\Delta E_{OSS-CSS}$) in meV calculated at B3LYP/def2-TZVP level using unrestricted broken-symmetry DFT for OSS state and restricted DFT for CSS state for (a) n = 1 to 12 acenes, (c) n = 4 to 24 cumulenes. **(b, d)** Computed $<S^2>$ values in BS state and radicaloid character (y) for (b) acenes, (d) cumulenes, blue curve denotes variation in $<S^2>_{BS}$ values and orange curve represent y values.

To further validate the OSS character, spin-squared value $<S^2>$ in BS state and radicaloid character (y), which are used as the descriptors of diradical character of a molecule[241,242] are presented in Figure 6.2b and Figure 6.2d. The diagnostic value of $<S^2>$ in BS determinant should be 1.0. Any deviation from the expected $<S^2>_{BS}$ =1 in-

dicates spin contamination due to contributions from other low lying excited spin states. Here, $<S^2>$ =0 upto n=5 acene and n=10 cumulene indicates CSS ground state. Afterwards, the $<S^2>$ value shows a regular increase with the increasing n for both the series. For intermediate members, i.e., n=6 acene and n=12 cumulene, $<S^2>_{BS} \sim 0.17$ indicates the preferential existence of molecule in CSS ground state. Thereafter, $<S^2>_{BS}$ starts approaching towards 1.0 indicating diradical ground state for n ≥ 7 for acenes and n ≥ 14 for cumulenes. However, for the higher members, the spin contamination in OSS becomes large with $<S^2>$ = 1.69 for n=12 acene and 1.26 for n=24 cumulene pointing towards the mixing of low-lying triplets. Qualitatively, similar trends are also found in radicaloid character (y), which classify singlet molecular systems into three categories: (i) closed- shell (y = 0), (ii) intermediate diradical (0 < y < 1), (iii) pure open-shell (y = 1) systems.[243] The increasing radicaloid character with increasing length, i.e., $y > 0.6$ from n=7 acene and n=14 cumulene onwards unambiguously confirms that OSS spin polarized state supersedes the CSS state as the ground state (Section D.1 in Appendix-4).

6.3.2 Evolution of transport characteristics for Acenes

With such an understanding for the ground state electronic properties, we proceed to investigate the behavior of molecules with OSS ground state in molecular devices. Few underlying aspects have been postulated for a system to follow the non-classical increase of electrical conductance with length. Since, the transmission probability around the Fermi level is proportional to the absolute square of Green's function at the Fermi energy, thus, in this context, the most straightforward starting point is the expression of zeroth order Green's function.[174] According to orbital symmetry rules derived by Yoshizawa and coworkers[173,174], at an energy E around the Fermi level, the contributions of the transport channels connected to HOMO and LUMO are mainly responsible for Green's function written as

$$G_{lr}^{mol}(E) = \frac{C_{l,HOMO}C^{\star}_{r,HOMO}}{E - \varepsilon_{HOMO}} + \frac{C_{l,LUMO}C^{\star}_{r,LUMO}}{E - \varepsilon_{LUMO}} \tag{6.4}$$

where $C_{l/r,HOMO}$ and $C_{l/r,LUMO}$ are the MO coefficients of the HOMO and LUMO at the connecting sites l and r and $\varepsilon_{HOMO/LUMO}$ are the HOMO/LUMO orbital energies. According to Eq 6.4, the following two factors drive the conductance. First,

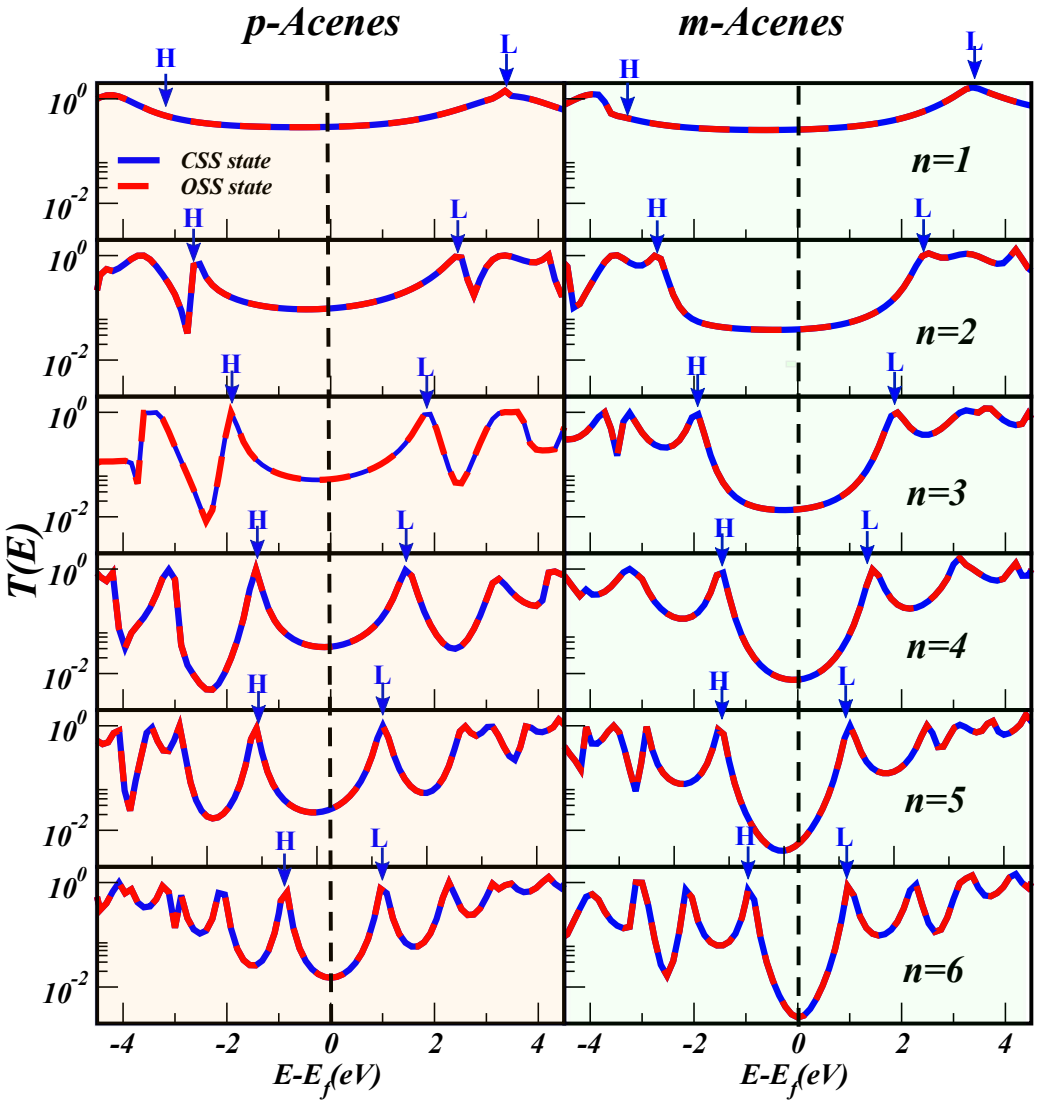

Figure 6.3: Calculated transmission spectra for n = 1 to 6 p-acenes and m-acenes. The CSS and OSS state transmission is denoted by blue and red curves, respectively. The blue arrows marked as 'H' and 'L' denote HOMO and LUMO resonance below and above the Fermi energy respectively. The vertical dotted line denotes the position of the Fermi level.

is the alignment of frontier HOMO and LUMO orbitals w.r.t the Fermi energy. The smaller HOMO-LUMO gap leads to smaller energy offset between the frontier MOs and the Fermi level of the electrode, and results in higher conductance. Thus, a wire should possess a decreasing HOMO-LUMO gap with length. The second dominant factor is the numerator of Eq.6.4, i.e., orbital coefficients at the contact sites which control the electrode–molecule coupling strength and should remain substantial with increasing length. Thus, the strong orbital localization at the contact sites and narrowing of HOMO-LUMO gap with length can commute an efficient electron transport with a plausible anti-ohmic behavior.

The transmission characteristics for n = 1 to 12 acenes in both CSS and OSS state is presented in Fig. 6.3 and Fig. 6.4. As discussed in Section B.1 of Appendix-2, that acenes with meta connection to electrodes lead to suppression of conductance as compared to their para connected analogs due to destructive quantum interference (DQI), which further intensify with increasing molecular length. Thus, taking into consideration the fundamental role played by QI effects, we have examined acenes with both para and meta connections to Au electrodes (Fig. 6.1a and Fig. 6.1b). Figure 6.3 shows the transmission spectra for n = 1 to 6 acenes in CSS state and OSS state, wherein the frontier orbital energies are marked with arrows. The evolution of transmission spectra and frontier orbital energies reveals several trends with competing effects on conductance. The first is shifting of frontier orbital energies and the corresponding transmission peaks towards the Fermi energy with increase in n. Thereby, decreasing the HOMO-LUMO gap with increasing molecular length, which acts to increase the conductance. The second is the increase in number of resonant peaks appearing in conductance spectra with the increment of the length which also favours the increase in conductance. This is in line with the increase in density of MOs with increasing n, as illustrated in orbital energy diagram plot (Fig. D.7 in Appendix-4). The other competing factor is the broadening of the frontier resonant peaks, which results from the coupling of molecular states to the extended states of the electrode.[244] Here, the reduction in the width of frontier peaks along the series implies that the coupling of acenes with electrodes gets weaken upon increasing the length which plausibly decreases the conductance. This can be directly inferred from the spatial distribution of MOs (Fig. D.3 in Appendix-4) which reveals that orbital coefficients falls off quickly at the terminal connecting sites with increasing length which eventually results in weak coupling with electrodes. With

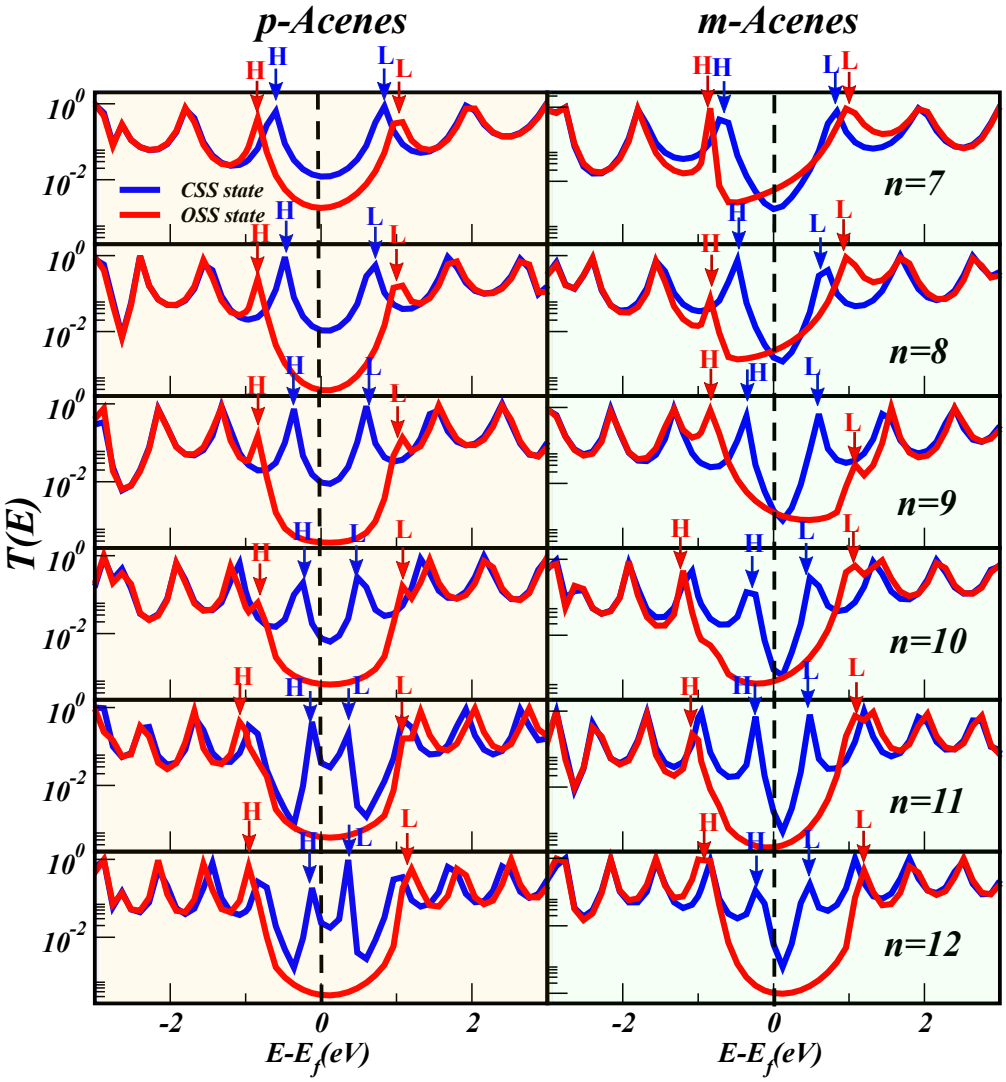

Figure 6.4: Calculated transmission spectra for n = 7 to 12 p-acenes and m-acenes. The calculated transmission in CSS and OSS state is denoted by blue and red curves, respectively. The blue/red arrows marked as 'H' and 'L' depicts frontier orbital HOMO and LUMO resonances in CSS/OSS state. The vertical dotted line denotes the position of the Fermi level.

these competing factors, the conductance, determined by the magnitude of transmission coefficient at the Fermi energy, reveals an evident decrease with the increasing molecular length. All these trends including the decrease in conductance and evolution of frontier orbital energies are robust for both *p*-acenes and *m*-acenes. However, as compared to *p*-acenes, *m*-acenes shows sharp dips near the Fermi energy owing to DQI effects associated with the phase difference between electron waves traversing across the molecule.[245,246] Noteworthy, since the electronic structure calculations in OSS state for n = 1 to 6 acenes converges to CSS ground state with $\Delta E_{OSS-CSS} = 0$ (Figure 6.2a), so does the transport calculations with identical transmission spectra and frontier orbital energies for closed shell and open shell calculations.

For higher acenes with OSS ground state, the transmission spectra for n = 7 to 12 in CSS and OSS ground state is shown in Fig. 6.4. In CSS state, the frontier transmission peaks near the Fermi energy are shifted towards the Fermi energy. Thereby, decreasing the energy gap with increasing n to ~ 0.70 eV for n= 12 acene. But in OSS state, the frontier peaks are held in fixed positions, thus saturating the energy gap at ~ 1.60 eV from n= 7 to 12 acenes. This gap saturation is consistent with HOMO-LUMO gap for isolated acenes, which saturates to a constant value of ~ 1.76 eV in OSS state, but shows a steady decrease in CSS state (Fig. D.1 in Appendix-4). Similar gap stabilization for higher acenes was also reported by Pilevarshahri et al.[83] and Wilhelm et al. using GW-based methods.[247] Apart from the gap saturation, the other competing factors, i.e., number of resonant peaks and width of frontier resonant peaks also infuse to a constant value in OSS state. These saturation factors are accompanied by a significantly decreased transmission near the Fermi level in OSS state as compared to CSS state which now appeared irrespective of para/meta configuration. For meta configuration, conductance shows an evident decrease up to n = 12, while for para configuration it saturates at n = 8.

6.3.3 Validation for Cumulenes

To bring the observed contrasting features of transmission spectra in CSS and OSS state on more solid ground, we calculated the transmission spectra for another genre of molecular wires, i.e., cumulenes, shown in Figure 6.5. To simulate the experimental data, both the ends of cumulene molecules are substituted with phenyl groups, which

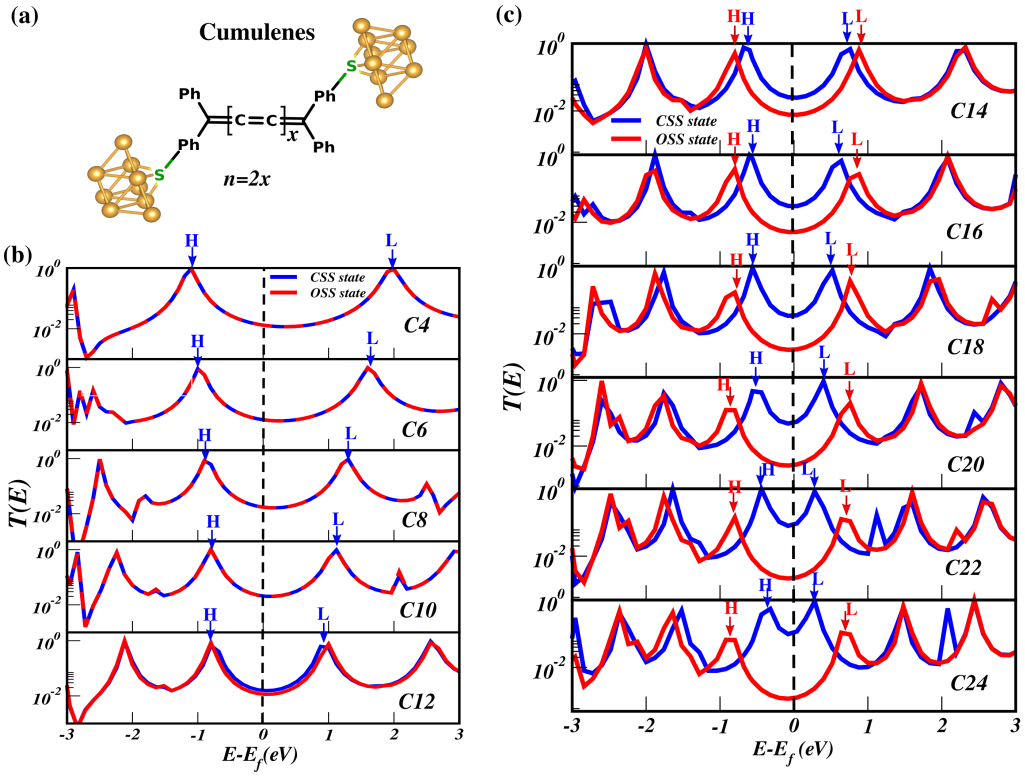

Figure 6.5: (a) Junction schematic showing phenyl-substituted cumulene ($C4$) suspended between two Au_9 clusters via thiol anchoring groups. Calculated transmission spectra as a function of energy for (b) lower cumulenes ($C4$ to $C14$), (c) for higher cumulenes ($C14$ to $C24$). The calculated transmission in CSS and OSS state is denoted by blue and red curves, respectively. The blue/red arrows marked as 'H' and 'L' depicts frontier orbital HOMO and LUMO resonances CSS/OSS state. The vertical dotted line denotes the position of the Fermi level.

enhance their stability.[233] The phenyl-substituted cumulenes are then placed between two Au_9 clusters using thiol linker atoms (Fig. 6.5a). Interestingly, corroborated with previous theoretical[248] and experimental measurements[231], cumulene wires provide us an example with desired anti-ohmic behavior. For the lower members exhibiting CSS ground state (Fig. 6.5b), the frontier transmission peaks approach towards the Fermi energy with a decreasing energy gap in CSS state, while OSS converge to CSS with a slight variation for $C12$. For higher cumulenes in OSS ground state (Fig. 6.5c), frontier resonance peaks in CSS state feature a contracting energy gap to 0.57 eV for $C24$, while transmission peaks in OSS state do evidence a gap saturation at $\sim$ 1.55 eV from $C14$ to

$C24$ cumulenes. In addition to this, OSS state yields lower transmission peak heights than those of CSS state. This results in significantly decreased transmission near the Fermi energy in OSS state as compared to CSS state. Notably, apart from the frontier transmission peaks residing near the Fermi energy, all the transmission features away from the Fermi energy are nearly identical in CSS and OSS state, implying that spin symmetry breaking effects are negligible for those states.

6.3.4 Molecular Conductance v/s Length

It is now tempting to correlate the decay coefficients, β, in CSS and OSS state. Fig. 6.6a shows the evolution of conductance as a function of n for p-acenes and m-acenes. It outlines an overall trend of decreasing conductance with increasing molecular length, which is indeed unchanged in both CSS and OSS state. However, the decay is much shallower in OSS state than that in CSS state, as can be inferred from decay constant values, i.e. $\beta = 0.216$ in CSS state, whereas it increases to 0.768 in OSS state for p-acenes. Similarly, m-acenes yield $\beta = 0.312$ in CSS state and 0.563 in OSS state. This implies that in OSS state, longer molecules lead to even higher resistance. On contrary, for cumulenes (Fig. 6.6b), inverted attenuation factors are observed. In CSS state, an increase in conductance is observed from $n = 4$ to 24 with negative β value of 0.099. The origin of anti-ohmic behavior of cumulenes is rooted in frontier MOs which are now completely delocalized over the complete molecule, in contrast to polyacenes where orbital coefficients fall off quickly at the terminal benzene rings. The substantial weight of the conducting frontier MOs on the terminal contact sites together with decreasing HOMO-LUMO gap in cumulenes engender both the factors in Eq. 6.4 to favour an increase in conductance. However in OSS state, which is ground state for higher members, yields positive β values of 0.134 with regular decay of conductance. Overall, the conductance increases upto a maximum wherein the lower members of the series with CSS ground state persist in anti-ohmic regime, in contrast, the emergence of OSS ground state for the higher members, provokes a regular decay of conductance. This indicates that anti-ohmic behavior do exists for lower cumulenes with CSS ground state, however if a restricted wavefunction is wrongly imposed to higher cumulenes with OSS ground state, it results in incorrect prediction of empirically negative β values. Thus the suggested positive correlation between diradical character and conductance[221,249] is not

as uni-equivocal.

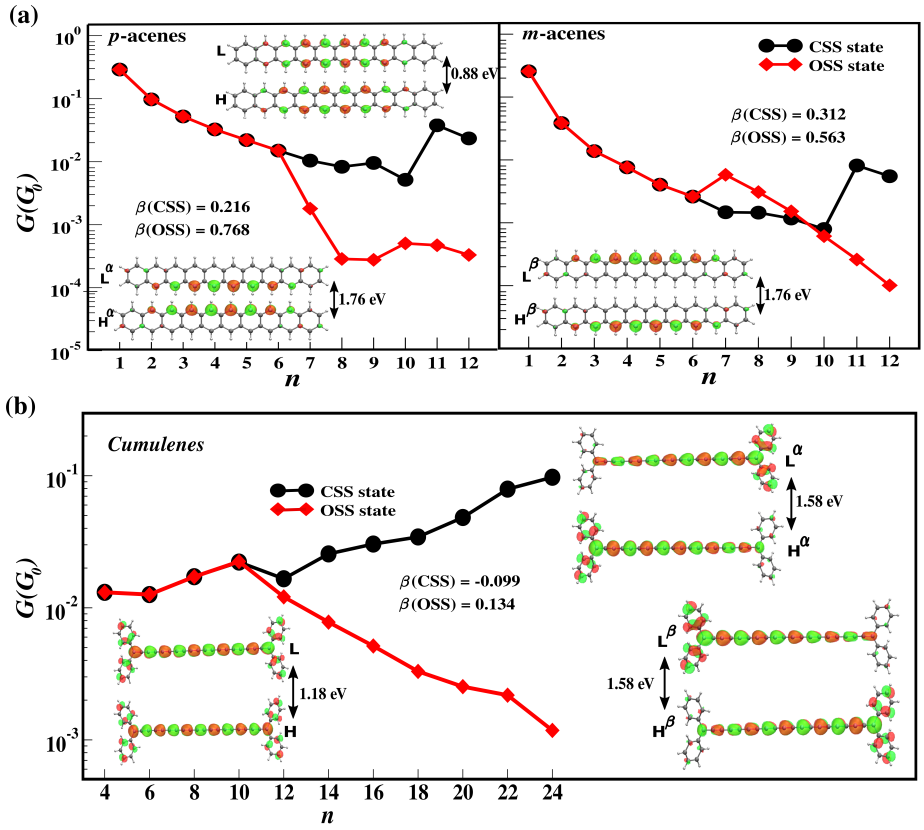

Figure 6.6: (a) Molecular conductance (in units of G_0) v/s number of benzene rings (n) in CSS state (black curve) and OSS state (red curve) for p-acenes and m-acenes. (b) Conductance versus number of C-atoms (n) for phenyl-substituted cumulenes. Spatial distribution of frontier HOMO (H) and LUMO (L) orbitals and HOMO-LUMO energ (y gaps are shown in insets for n = 10 acene and n = 20 cumulene.

To further understand the electronic structure governing the contrasting β values in CSS and OSS state, the spatial distribution of frontier HOMO and LUMO orbitals and their energy gaps is shown in insets of Figure 6.6. In OSS state, longer molecules are subjected to spin-symmetry breaking which produces different spin-split orbitals for α and β electrons.[250] For acenes, frontier orbitals are localized on both zig-zag sites of the central benzene rings in CSS state, while in OSS state, spin-split degenerate HOMOs, i.e., α-HOMO is localized on the hydrogenated C-atoms at one edge of the molecule, while β-HOMO is localized on the other edge with a disjoint character. The spin-split degenerate LUMOs also reveal the similar disjoint character. Similarly, for cumulenes

in OSS state, spin-symmetry breaking enforces the α-HOMO and β-HOMO to localize at opposite ends, thereby decreasing the delocalized character of frontier MOs in OSS state. Apart from the symmetry breaking, OSS state witnesses a higher HOMO-LUMO gap as compared to CSS state (Fig. D.1 and Fig. D.2 in Appendix-4). As discussed above, in CSS state the HOMO-LUMO gap approaches towards gap closure with the increasing length, while in OSS state, the gap is an exchange gap between the spin-split orbitals which is not strongly length dependent and saturates to a finite value. Thus, the decrease in delocalized nature of spin-split orbitals integrated with an increase of HOMO-LUMO gap in OSS state inhibits the efficient contact coupling in junction and results in an emphatic decrease in conductance.

6.4 Conclusion

In conclusion, the findings in this work add new prospective on the debate concerning the feasibility of anti-ohmic wires. The origin of anti-ohmic electron transport is rooted in to the intrinsic electronic structure of the molecule wherein the decreasing gap between frontier electronic states and its localization at the terminal connecting sites drives a nanowire into anti-ohmic regime. The current study put forth the preferential existence of the molecule in CSS state as a guiding rule to observe the desirable increase in conductance. We demonstrate that for acenes, decreasing orbital coefficients results in a regular decay of conductance in both CSS and OSS state, accompanied by a larger resistance in OSS state. On the other hand, cumulenes display a priori all of the features required to be a anti-ohmic wire. However, clouds over this horizon appear with the evolution from CSS to OSS state upon increasing length. For large enough molecules, the CSS state becomes unstable and undergoes spin-symmetry breaking which enforces α and β electrons to localize at the opposite ends of the molecule. This dramatically reduces the delocalized nature of frontier α/β channels yield a consequent decay of conductance as compared to their CSS counterparts. Overall, the findings in this work highlight that the inherent transition of intrinsic electronic structure from CSS to OSS ground state with increasing length enforces the molecule to yield a regular decay of conductance. Thus, emphasizing the existence of a molecule in closed-shell state along with the two pre-requisites of decreasing HOMO-LUMO gap and substantial orbital localization at connecting sites to observe the desired increase in conductance.

CHAPTER 7

Conclusion and Future Perspectives

The fundamental understanding of spin-dependent quantum transport phenomena is important for both the improvement of existing molecular devices and the development of new devices with spintronic applications.The goal of this thesis work is to provide insights into spin-dependent electron transport phenomena using first-principles methods and to propose new concepts to induce efficient spin polarization in molecular devices. The research work done in this direction has been presented in four individual chapters.

In *Chapter 3*, organic diradicals with strong ferromagnetic exchange interactions were modelled using super-stable Blatter's radical. The exchange interactions were investigated applying different density and wave function-based *ab initio* multi-configurational methods. It was observed that within the density based approach, CBS-DFT provides much better $2J$ values as compared to the standard BS-DFT. Among the wavefunction based multi-reference methods, the minimal CAS(2,2)+NEVPT2 proved to be a reliable choice for Blatter's based radicals. A remarkable modulation in exchange couplings were observed by employing planar analogue of parent Blatter's rad-

ical. O-annulation resulted in significant enhancement of $2J$ values for Class C diradicals, while the class B diradicals undergoes a drastic decrease in $2J$ values.

In *Chapter 4*, various stable organic radicals are incorporated in gold-molecule-gold junction to study the influence of localized spin centers on the electron transport. An anomalous behavior of quantum interference stemming from radical spins attached to the pentacene backbone was observed in molecular junction. The molecular conductance for meta-connected radicals was found to be higher than para ones, which is in complete contrast to nonmagnetic pentacene. A high spin filtering efficiency was observed for nitroxy (NO), phenoxy (PO) and methyl (CH_2) radical attached to pentacene framework. Contrary to the expectations, two of the stable radicals, i.e., nitronyl nitroxide (NN) and oxo-verdazyl (OVER) turned out to be inefficient spin filters due to the orthogonal arrangement of radical moiety w.r.t pentacene core.The planar arrangement of NN and OVER radicals obtained by incorporating ethynyl spacer produced facilitates desirable spin filtering effects.

In *Chapter 5*, photo-responsive endoperoxide (EPO) was used to generate transient spin polarization in single molecule device. A nearly perfect spin filtering was achieved for the diradical intermediate generated by the homolytic cleavage of the peroxide O–O bond. The altering degrees of conjugation of different products across the photochemical reaction pathway of EPO were found to play a dominant role in controlling the conductance by toggling on and off the QI features.

In *Chapter 6*, molecular wires with pronounced diradical character in their ground state are investigated for spin-dependent long range charge transport. It was observed that molecular wires in their open shell singlet state posses high resistance as compared to their closed counterparts. For cumulenes, an increasing conductance with molecular length was observed in closed-shell limit, while higher cumulenes in OSS ground state

produced a regular decay of conductance. Overall, this chapter emphasizes the existence of a molecule in closed-shell state to observe the desirable anti-ohmic behavior.

In summary, the results presented in this thesis provides an intuitive understanding of how the presence of radical spins effects the conducting electrons through the junction. The experimentalists working in field would benefit in achieving the radical molecular junctions with efficient spin polarization and high conductance using appropriate para/meta connections. It further opens a door for detailed investigation of all the probable configurations of radical molecular junctions possible in the experiments using *ab intio* molecular dynamics (AIMD) methods. Further, the work presented in this thesis is restricted to phase-coherent calculations at zero/low-bias voltage only. The effect of inelastic electron-phonon and electron-magnon interactions on the spin-dependent electron transport may be of significant importance and needs a detailed investigation.

APPENDIX A

Appendix-1

A.1 Spin-constraint DFT: Zone selection criteria

The careful selection of magnetic zones and confining the appropriate amount of the magnetic moment on the selected zones is necessary to obtain accurate $2J$ values using CBS-DFT. For the case of Bl-NN(C), as shown in Figure A.1, zone A is completely localized on the spin bearing N and O atoms as well as the connecting C atom of the NN radical and zone B is localized on the triazinyl ring of the Blatter's radical. The constrained magnetic moments are obtained from Löwdin spin-density of BS solutions. For NN radical, only N and O atoms are the major spin carriers. Thus, to avoid any artificial delocalization, which is a one of the major culprit in BS-DFT, one complete unit of moment is constrained on zone A. For Blatter's radical, since the natural delocalization of spin density from Blatter's triazinyl ring A to the fused benzene ring B is one of the major reason behind the super stability of this radical. To take into account this fact,~ 0.77 μ_B of magnetic moment is constrained on ring A and the rest is allowed to delocalize on ring B. For X-annulated systems, since X-annulation promotes enhanced delocalization over ring C, thus the constraint over ring A is reduced from 0.77 to 0.72 μ_B.

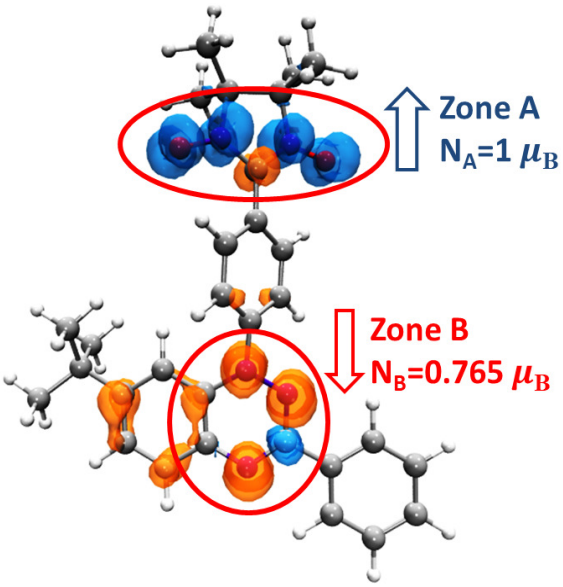

Figure A.1: CBS-DFT, selected zones for Bl-NN(C) with the constrained magnetic moment on the respective zones. The constrained magnetic moments are obtained from Löwdin spin-density of BS calculations. The α and β spins are shown in blue and orange colours respectively with isovalue of 0.002 μ_B/Å^3.

A.2 Selection of CASSCF active space

The success of multi-configurational methods depends on the choice of active space and the set of actual starting orbitals. A set of guiding rules to select prime candidates for active orbitals were also formulated in an early report by Roos et al.[251] In this work, unrestricted natural orbitals (UNOs) are used for defining the active space and providing starting guess orbitals for CASSCF.[107] Apart from the minimal CAS(2,2) space, taking into account the distribution of two unpaired electrons in two SOMOs, a common recipe is followed for the systematic expansion of active space up to CAS(10,10). The frontier orbitals near HOMO and LUMO are included in the active space by taking into consideration following intuitive points. The orbitals are then more or less explicitly ordered with some perceived importance keeping the most needed ones.

1. Ring D of Blatter's radical which plays a negligible role in controlling the spin-spin interactions between the two radical moieties is left inactive.

2. The electronic states obtained from CASSCF calculations are confirmed by keeping an eye on the occupation number of the converged CASSCF orbitals. The active space constituted by the orbitals bearing fractional occupancy between 1.98 and 0.01 is considered to be appropriate for the further treatment of dynamical correlation by

NEVPT2.

3. For Bl-NN(C), ring C acts as a coupler between two radical sites and is thus taken into account starting from minimal CAS(2,2) space. However, for Bl-NN(B), the large dihedral angle between ring A and C of Blatter's radical, i.e., ϕ_{AC} = 51.40° indicates that ring C is not effectively coupled and do not play a significant role in controlling the exchange interactions and is thus left inactive.

4. For X-annulated counterparts, due to smaller dihedral angle, ϕ_{AC}, ring C is also included along with the X-atomic center in the extended CAS spaces for both Class B and Class C diradicals.

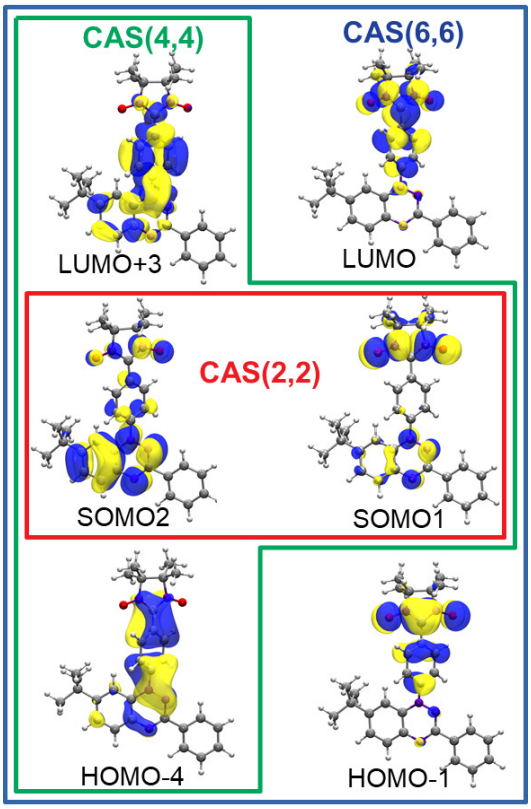

Figure A.2: Selected active space orbitals for CASSCF calculations of **Bl-NN(C)**.

Fig. A.2 shows the selected active space orbitals for Bl-NN(C). For the minimal CAS space i.e. CAS(2,2) two magnetic orbitals containing two unpaired electrons in the radical centers are involved. These magnetic orbitals (shown in red enclosure of Fig. A.2) are essentially the singly occupied natural orbitals (SONOs). SONOs are mainly localized on the two radical centers. However, one of the SONO is indeed delocalized on the central phenyl coupler as well. Thus, along with the radical centers

the two SONOs have also taken into account the contributions of the couplers in the exchange interactions.

As the π orbitals stemming from the coupler connecting the two radical centers plays an important role in exchange coupling. Thus, extending the active space to CAS(4,4), along with the two magnetic orbitals we have taken into account the orbitals which involves the π orbitals of the central phenyl coupler. HOMO-4 and LUMO+3 are the two additional orbitals involved. LUMO+3 is also delocalized on the extended part i.e. fused benzene ring of the Blatter's radical. CAS(4,4) space is further enlarged to CAS(6,6) by adding π orbitals of the NN radical moiety and central phenyl coupler. In CAS(6,6) active space, along with LUMO+3 and HOMO-4 (also taken in CAS(4,4) active space) LUMO and HOMO-1 are considered. The additional orbitals are localized on NN moiety and the phenyl coupler.

The CAS(8,8) active space consisted 8 electrons in 8 active orbitals by extending the previously selected CAS(6,6) space by adding other two π orbitals of the phenyl coupler. LUMO+7 and HOMO-8 (see Fig. A.3) are the two additional orbitals involved in CAS(8,8) along with all the orbitals considered in CAS(6,6) space.

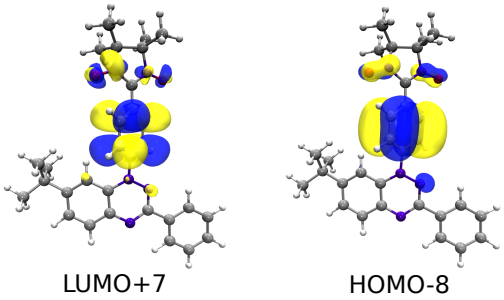

Figure A.3: Additional natural orbitals selected for CAS(8,8) space along with all the orbitals considered in CAS(6,6) space with isovalue of 0.02 a.u.

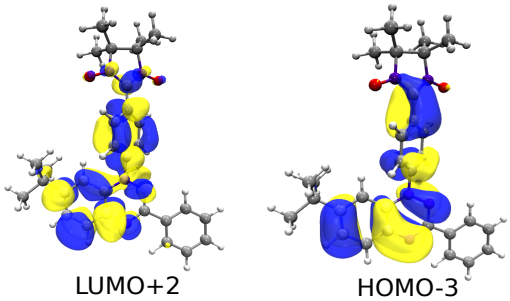

Figure A.4: Additional natural orbitals selected for CAS(10,10) space along with all the orbitals considered in CAS(8,8) space with isovalue of 0.02 a.u.

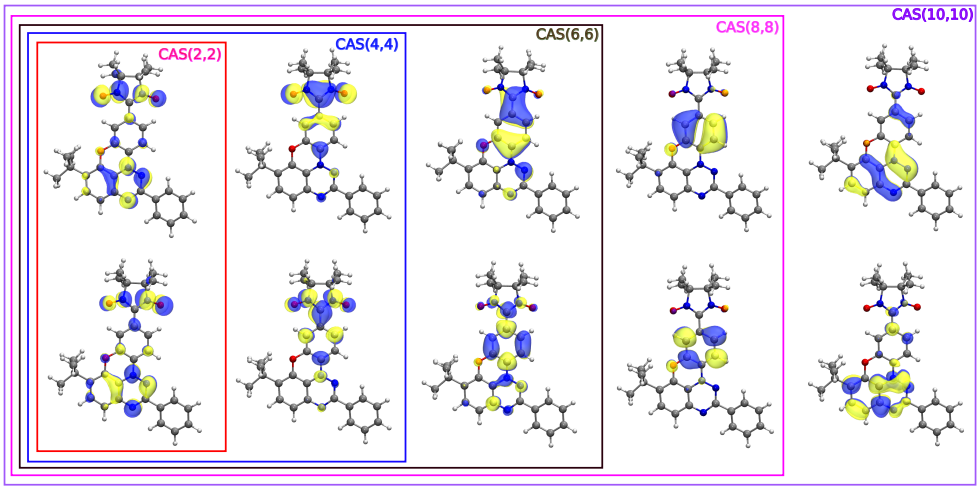

Figure A.5: Selected active space orbitals for CASSCF calculations of **O-Bl-NN(C)**.

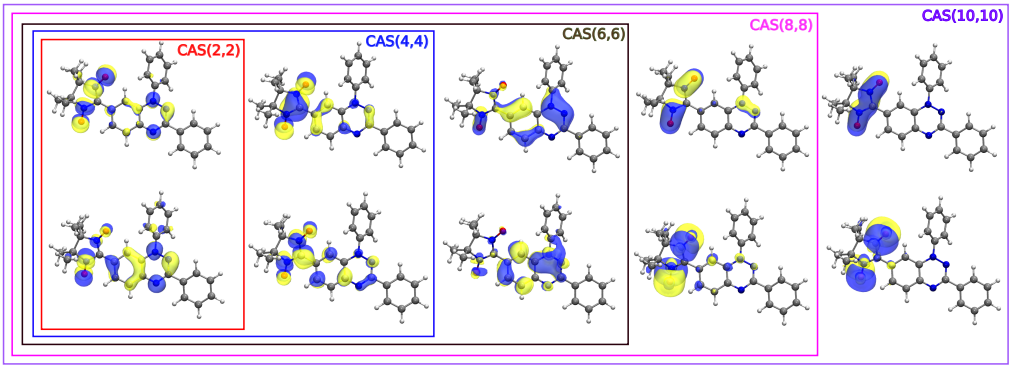

Figure A.6: Selected active space orbitals for CASSCF calculations of **Bl-NN(B)**.

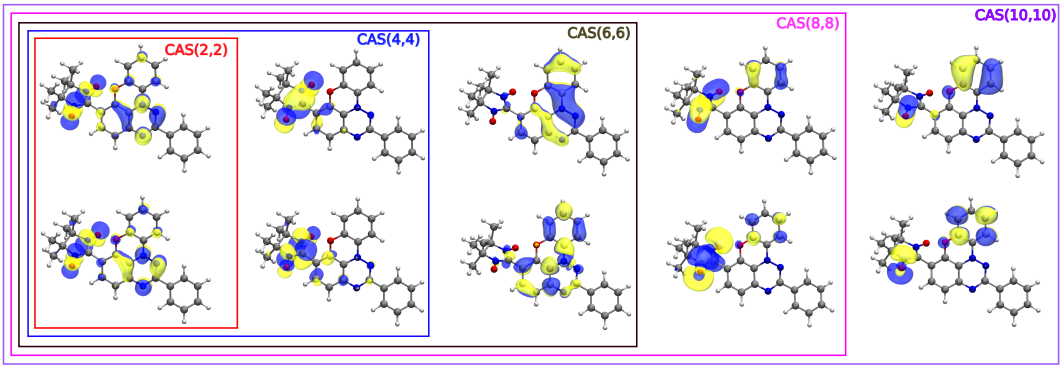

Figure A.7: Selected active space orbitals for CASSCF calculations of **O-Bl-NN(B)**.

A.3 Tuning the spin-delocalization of Blatter's mono-radical: Merostabilisation

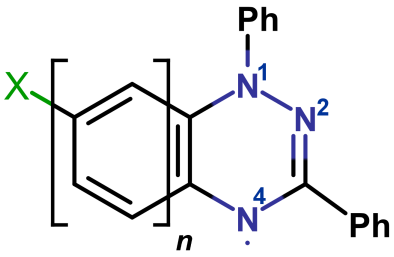

Figure A.8: 1,2,4-Benzotriazinyl (Blatter's) radical with X= $-CMe_3$,$-H$ $-CF_3$. The benzene ring fused with the triazinyl ring A is referred as the extended part of the radical where n corresponds to number of fused benzene rings. The phenyl ring connected to N_1 is referred as coupler phenyl ring.

The stability of Blatter's radical is rationalized in terms of merostabilisation i.e. the radicals are stabilized by resonance and steric hindrance. The introduction of three endocyclic nitrogen atoms in to a carbon backbone gives rise to a distribution where spin-density is highly localized on the three N-atoms of the triazinyl ring. The delocalization of spin-density is further facilitated by the extended part of the radical i.e. fused benzene ring, which being coplanar with triazinyl moiety provides an easy pathway for spin delocalization in the heterocyclic radical. Thus, the stability of radical is owed to the extensive delocalization of spin-density on both the benzene ring as well as endocyclic N-atoms. The stability of the radical is further enhanced by modifying the molecular framework by extended conjugation i.e. on increasing the number of coplanar fused benzene rings (Fig. A.8). The Löwdin spin-density on three nitrogen atoms along with the total spin-density on the triazinyl ring with the increasing number of rings is tabulated in Table A.1.

Table A.1: Löwdin spin-density on N-atoms and triazinyl ring of Blatter's mono-radical with increasing number of fused benzene rings using B3LYP/def2-TZVP method.

No. of rings (n)	μ_{N_1}	μ_{N_2}	μ_{N_4}	$\sum\mu_{N_i}$	Total(triazinyl)[a]
1	0.220	0.240	0.235	0.695	0.791
2	0.201	0.250	0.221	0.672	0.719
3	0.198	0.256	0.210	0.664	0.690
4	0.188	0.254	0.205	0.647	0.660

[a] Total triazinyl ring spin-densities are obtained as $\sum(\mu_{N_i} + \mu_{C_i}(triazinyl))$

The decrease in spin-density on the triazinyl ring with the increase of n clearly indicates the delocalization of spin-densities from the radical centers to the extended part of the radical. Thus, the enhanced spin delocalization and hence merostabilisation is accelerated through extended conjugation of molecular structure.

A.4 Interplay between stability of the organic radicals and the magnetic exchange interactions

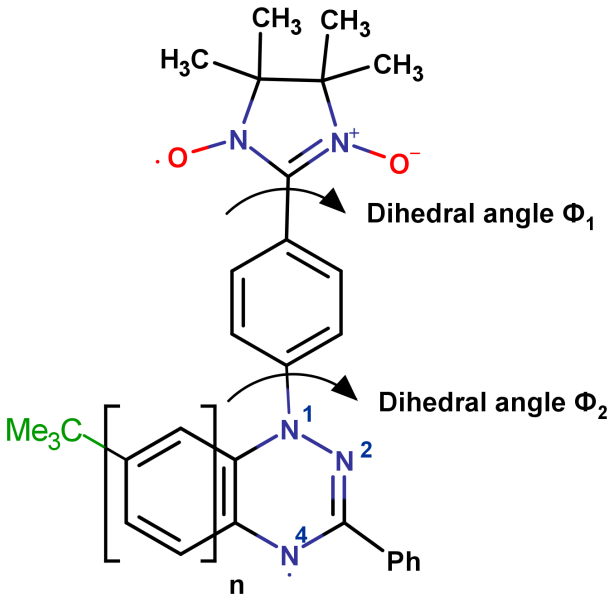

Figure A.9: Blatter's coupled with NN, Bl-NN(C), n corresponds to number of fused benzene rings, ϕ_1 and ϕ_2 are the dihedral angles which the central phenyl ring makes with NN and Blatter's radical respectively.

It has been realized that the stability of the Blatter's radical could be enhanced by attaching the additional coplanar fused benzene rings, which facilitates the delocalization of spin-densities from the radical sites. Do this enhanced stability of Blatter's coupled diradicals affect the magnetic exchange interactions? To find an answer, we have investigated the magnetic exchange interactions of Bl-NN(C) diradicals by increasing the number of fused benzene rings of the Blatter's radical from n=1 to n=4. (see Fig. A.9). The results are tabulated in Table A.2. As we increase the number of the rings, we observed the significant decrease in the $2J$ values. This negative correlation between

Table A.2: Comparison of calculated magnetic exchange coupling constants for Bl-NN using BS-DFT, CBS-DFT ,CASSCF(2,2), CASSCF(2,2)-NEVPT2 with corresponding Dihedral Angles ϕ_1 and ϕ_2

No. of Rings	$2J(cm^{-1})$				ϕ_1 and ϕ_2
	BS-DFT	CBS-DFT	CASSCF(2,2)	CASSCF(2,2)+ NEVPT2	
1	397.80	219.47	96.56	177.77	21.3/46.2
2	285.58	263.36	70.23	149.24	14.6/59.2
3	134.38	122.90	32.92	74.62	21.8/67.2
4	146.82	136.07	37.31	79.01	21.4/65.4

number of rings and $2J$ is reflected in the four different methods including CBS-DFT and CASSCF-NEVPT2 methods.

Along with the exchange coupling, the dihedral angle which the central phenyl ring makes with the Blatter's radical and NN radical is also found to change significantly, as the number of the benzene rings increases from n=1 to 4. The dihedral angles ϕ_1 and ϕ_2 (shown in Fig.A.9 are listed in Table A.2. The strength of the magnetic exchange couplings indeed strongly depends on the dihedral angles.[252] Elimination of the contributions of the dihedral angle is necessary to evaluate the sole effect of the merostabilising the radical on the magnetic interactions.

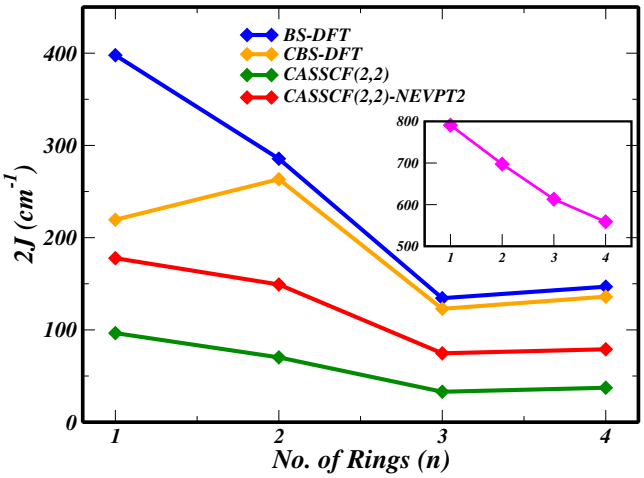

Figure A.10: Graph showing the variation of exchange coupling constant $2J$ (cm^{-1}) with increasing number of fused benzene rings *(n)*. The inset of the graph shows the variation of $2J$ with n for constrained geometry using BS-DFT, B3LYP/def2-TZVP level.

To do so, we have constrained both the dihedral angles to zero, making the configu-

ration planar. The inset of Fig. A.10 shows the computed exchange interactions for the constrained geometries using BS-DFT at B3LYP/def2-TZVP level. Due to the more effective overlap of the magnetic molecular orbitals, the planar configuration results in enhanced $2J$ values and with a continuous decrease in coupling constants with the increasing number of the rings. Thus, spin delocalization plays a major role in controlling the exchange coupling constant. With increasing number of rings and hence spin delocalization, the stability of diradical is increasing but at the cost of reduced magnetic exchange interactions.

A.5 Bl-NN(B) crystal geometry: Calculated $2J$ values

Table A.3: Computed magnetic coupling constants ($2J$) and spin-states energies for Bl-NN(B) using crystal geometry employing different density and wave function based methods.

Method	Energy(Eh)		$2J(cm^{-1})$
	HS	LS	
BS-DFT	-1429.256195	-1429.253752[a]	1072.26
CBS-DFT	-1429.562045	-1429.560754[a]	566.74
CASSCF(2,2)	-1421.104857	-1421.102768	458.53
CASSCF(4,4)	-1421.149799	-1421.14806	381.71
CASSCF(6,6)	-1421.164395	-1421.162424	432.63
CASSCF(8,8)	-1421.184075	-1421.18206	442.29
CASSCF(10,10)	-1421.203603	-1421.201501	461.38
CASSCF(12,12)	-1421.218511	-1421.216370	469.94
CASSCF(2,2)-NEVPT2	-1427.237921	-1427.234349	784.05
CASSCF(4,4)-NEVPT2	-1427.222557	-1427.219000	780.76
CASSCF(6,6)-NEVPT2	-1427.207374	-1427.203932	755.51
CASSCF(8,8)-NEVPT2	-1427.205017	-1427.201768	713.15
CASSCF(10,10)-NEVPT2	-1427.204535	-1427.201529	659.81
CASSCF(12,12)-NEVPT2	-1427.201243	-1427.198220	663.54
exp. (Rajca et al.)	-	-	608.50

[a] Instead of LS state, the energy of the broken-symmetry (BS) state is provided.

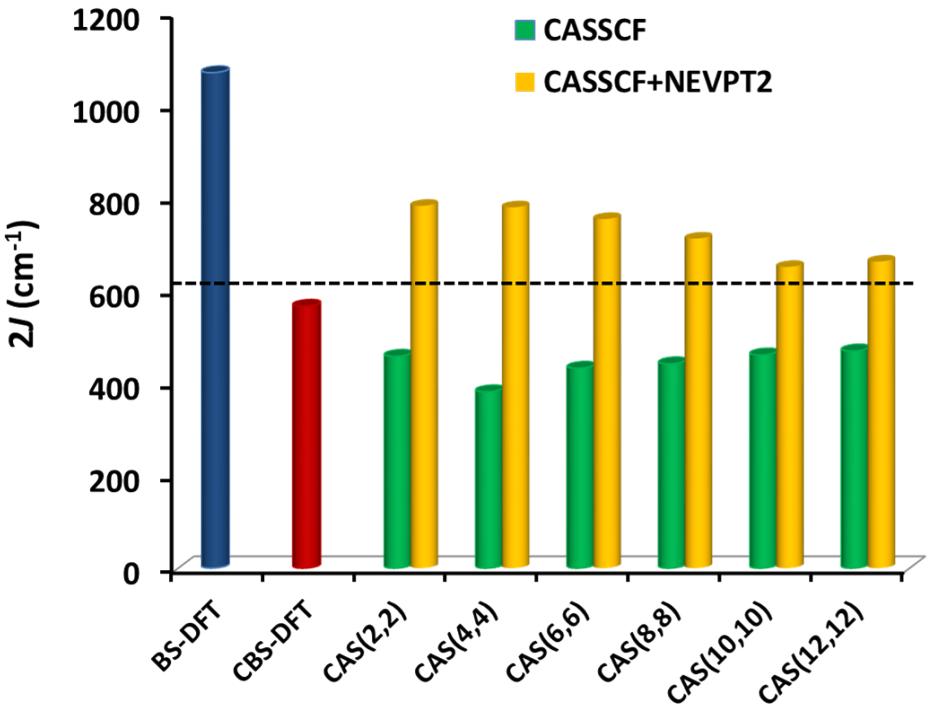

Figure A.11: Variation of 2J values using different density and wave-function based methods for **Bl-NN(B)** using crystal geometry.

A.6 DFT: Role of exact exchange admixture

In order to analyse the effect of exact exchange admixture on exchange coupling constants within the DFT regime, we reparametrized the hybrid B3LYP functional and calculated exchange coupling constants by varying the percentage of exact exchange admixture in B3LYP from 0 to 25% using both BS-DFT and CBS-DFT methods. Fig. A.12 shows the variation in 2J values for Bl-NN(C) and Bl-NN(B) by varying the amount of Hartree-Fock (HF) exchange. We observed that 2J values decreases upon decreasing the amount of HF exchange. Surprisingly, the one with 0% of the exchange (equivalent to local BLYP functional) produces 2J values closer to the experimental values with BS-DFT. Among the BS-DFT and CBS-DFT methods, BS-DFT yields strong dependence of 2J values on the fraction of exact exchange as compared to CBS-DFT, as represented by slope (m) shown in Fig. A.12 which decreases by a factor of 2 with CBS-DFT.

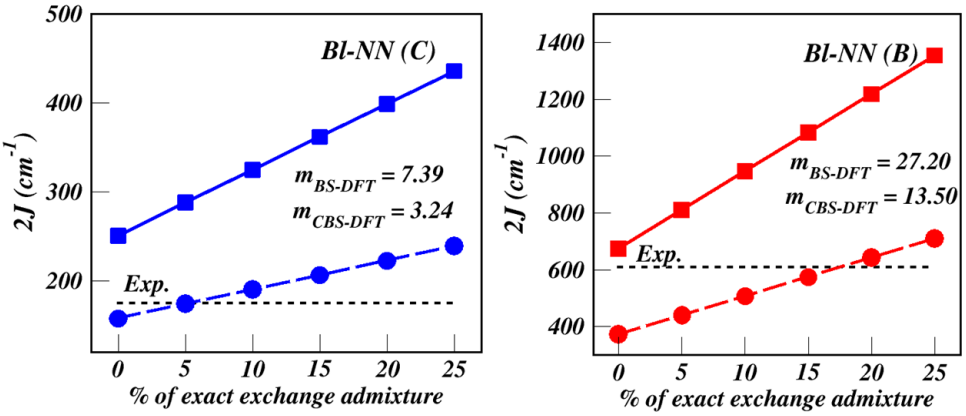

Figure A.12: Variation of 2J with the % of exact exchange admixture in hybrid B3LYP functional for Bl-NN (C) and Bl-NN (B) using BS-DFT and CBS-DFT methods. m denotes the calculated slope for the respective curves.

APPENDIX B

Appendix-2

B.1 Quantum Interference in parent non-magnetic Acenes

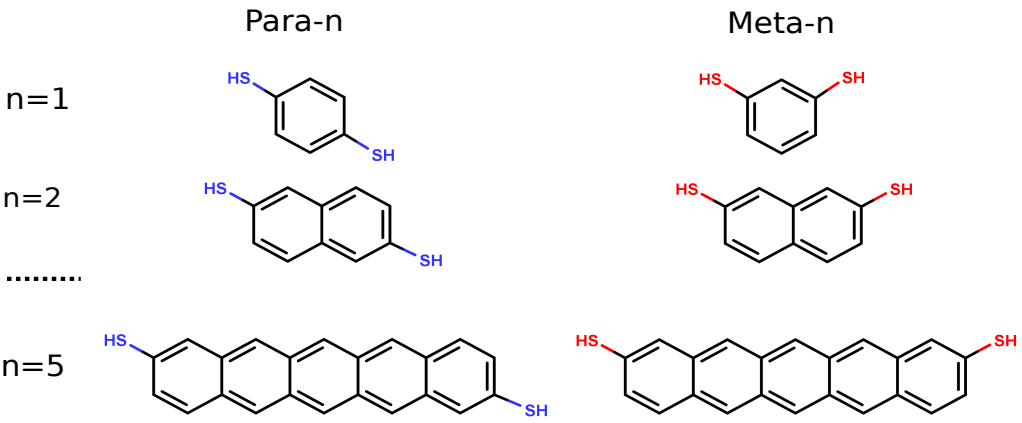

Figure B.1: Molecular structure of acenes systems (n=1-5) with para and meta terminal connections.

The low transmission caused by QI effects in para and meta connected benzene are well understood. Due to equal path lengths, interference manifests itself in a constructive way leading to high transmission probability and high conductance in *p*-benzene. However, in *m*-benzene, the phase difference between the pathways is equal to π, which gives

rise to destructive QI and hence less conductance in *m*-benzene.[253,254] In higher acenes, multiple charge transport pathways are created by utilizing π conjugated rings. To understand the modification in the DQI pattern brought about by increasing the molecular length, the electronic structure of isolated acenes (n =1 to 5) is first investigated. The transmission spectra is then calculated for a series of acenes (n =1 to 5), considering both para and meta linkage of the terminal benzene rings, where thiol end groups serve as linkers to gold electrodes, shown in Fig. B.1.

B.1.1 Energetics of frontier molecular orbitals of isolated acenes

Fig. B.2 and Table B.1 illustrates HOMO, LUMO energies and HOMO-LUMO gap (ΔE_{HL}) for n=1 to 5 acenes in gas phase (shown in Fig. B.1) calculated at PBE/def2-TZVP level of theory. ΔE_{HL} is decreasing continuously with increasing length, i.e. on moving from n =1 to 5. Further, the comparison of ΔE_{HL} gap for para and meta connected acenes reveals that Meta-n always exhibits high ΔE_{HL} than Para-n. The difference between ΔE_{HL} is maximum for Para-1 and Meta-1 and it vanishes for Para-5 and Meta-5, being 1.16 eV for both Para-5 and Meta-5.

Table B.1: Gas-phase energies (eV) of HOMO, LUMO and HOMO-LUMO gap (ΔE_{HL}) for n=1 to 5 acenes with para and meta connections of thiol groups calculated at PBE/def2-TZVP level.

n	Anchoring Position	E(HOMO)	E(LUMO)	ΔE_{HL}(eV)
1	Para	-5.10	-1.57	3.53
	Meta	-5.35	-1.42	3.93
2	Para	-4.99	-2.18	2.81
	Meta	-5.21	-2.17	3.04
3	Para	-4.85	-2.69	2.16
	Meta	-4.87	-2.66	2.21
4	Para	-4.58	-3.01	1.57
	Meta	-4.58	-3.00	1.58
5	Para	-4.41	-3.25	1.16
	Meta	-4.43	-3.27	1.16

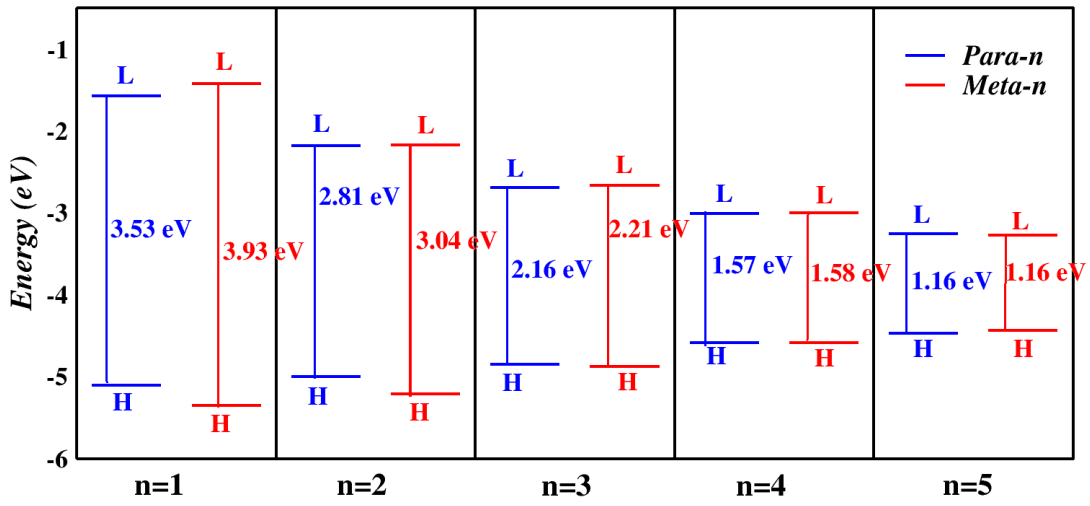

Figure B.2: The energy level diagram presenting HOMO(H), LUMO(L) and HOMO-LUMO gap (ΔE_{HL}) in eV for acenes (n=1 to 5) with para and meta connections of thiol groups in gas phase calculated at PBE/def2-TZVP level. The blue color denotes energy levels of acenes with para connections (Para-n) and red color corresponds to meta connections (Meta-n).

B.1.2 Transmission spectra: Periodic models

Fig. B.3 shows the evolution of transmission spectra using periodic models. For all the para and meta connected acenes (n =1 to 5), the alignment of HOMO with respect to the Fermi level of electrode is virtually the same (within 0.2 eV) for both para and meta connected acenes in junctions (shown in Fig. B.3 by arrows marked below Fermi level). However, the electronic structure of isolated acene molecules reveal that HOMO of the molecule is shifted by 0.69 and 0.92 eV for para and meta connection respectively on moving from benzene to pentacene (Fig. B.2). Thus, pointing towards the occurrence of HOMO level pinning in acene based molecular junctions. The evidence of such a pinning has also been provided in recent studies.[255] Further, the evolution of resonance peaks arising from LUMO (shown in Fig. B.3 by arrows marked above Fermi level) reveals that LUMO tends to get closer to the Fermi level on moving from benzene to pentacene, thus promoting the reduction of HOMO-LUMO gap on increasing length of acene molecules.

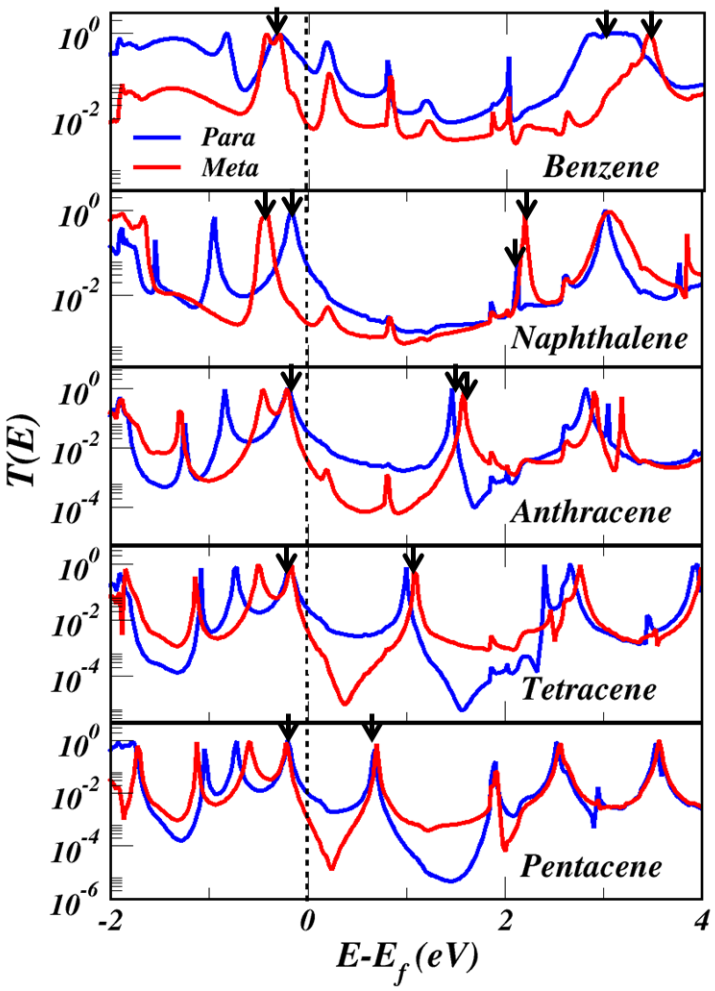

Figure B.3: Transmission spectra for para and meta connected acenes, n =1-5, where blue and red curves correspond to acenes with para and meta connections respectively. The vertical dotted line denotes the position of Fermi level. The arrows marked over the peaks below and above Fermi energy corresponds to HOMO and LUMO resonance respectively.

Further, the transmission spectra of para and meta connected acenes reveals that the position of resonance peaks which correspond to the conduction channel through molecular orbitals is identical for both para and meta connections. Along with the resonance peaks, the position of the dips residing between the resonance peaks arising due to the absence of the molecular states is also identical irrespective of the para and meta connection. Fig. B.3 also reveals that for all the n =1 to 5 acenes, the dip residing between HOMO and LUMO resonances near Fermi energy is always sharper for meta connected acenes than para ones. This clearly indicates that the electron transmission

through meta connected acenes is governed by DQI near Fermi energy leading to low conductance. On the other hand, electron transmission occurs constructively through para connections. Moreover, the sharpness of this dip for meta connected acenes further manifests itself with increasing molecular length in such a way that the difference between the dips of para and meta connected pentacene shoots to the maxima of two orders of magnitude. This indicates that QI effects intensify with increasing molecular length in such a way that most evident signatures of QI are observed in pentacene.

B.2 Pentacene based radicals

B.2.1 Spin density distribution

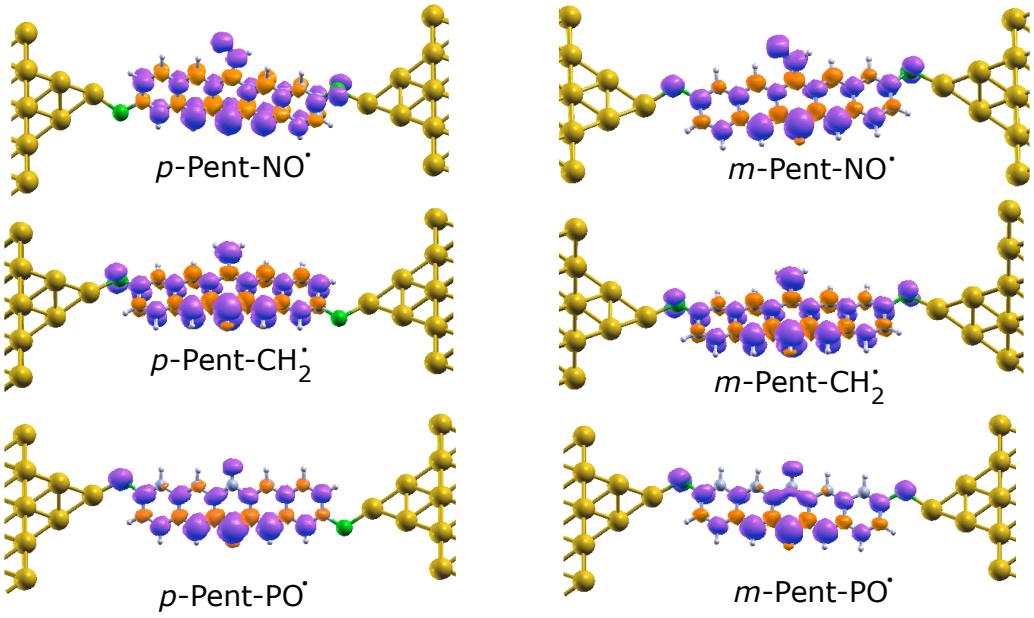

Figure B.4: Spin-density plots for the junctions containing pentacene based radicals. Spin-up and spin-down are shown in purple and orange color respectively with isovalue 0.001 $\mu_B/Å^3$.

B.2.2 Spin resolved transmission: cluster approach

Fig. B.5 illustrates spin resolved transmission spectra for pentacene based radicals placed between two Au_9 clusters, calculated at B3LYP/LANL2DZ level of theory. The reversal of para/meta conductance relation on attaching a radical is quite evident from the dips residing between HOMO and LUMO. For spin-up channel, these dips are encountered above Fermi level and for spin-down, they are located below Fermi level.

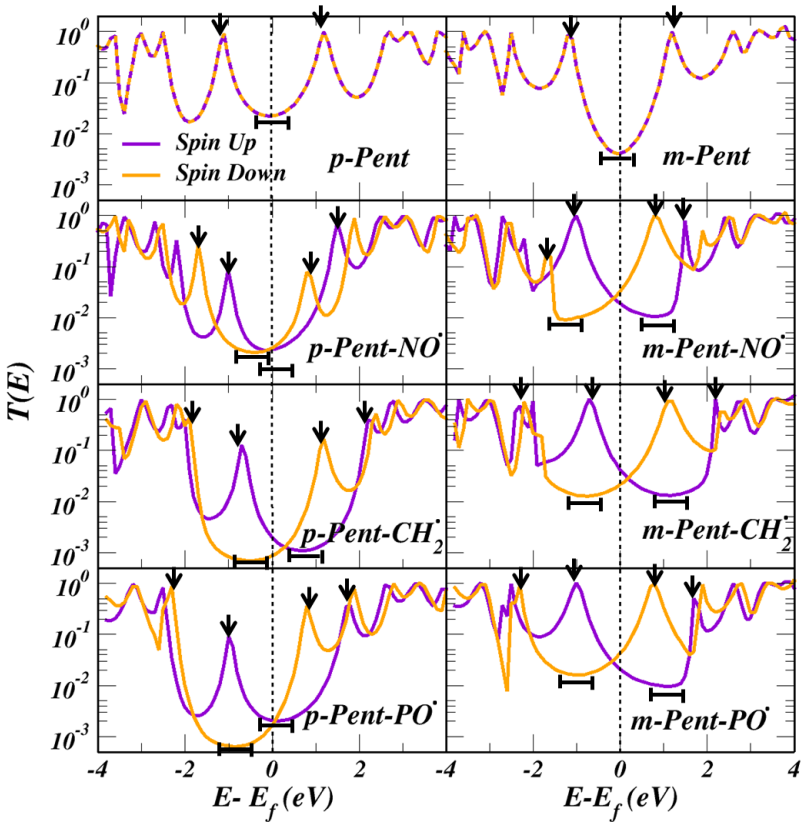

Figure B.5: Spin-resolved transmission spectra for para and meta connected pentacene (top panel) and pentacene based radicals (NO$^{\bullet}$, $CH_2^{\bullet}$, PO$^{\bullet}$) placed between two Au_9 clusters, calculated using B3LYP/LANL2DZ method. Spin-up and spin-down transmission is denoted by purple and orange respectively. The energies are shifted by system's Fermi energy using E_F= -4.2 eV.

B.3 Local Transmission Analysis

To get further insight into the spin-resolved transport properties of radical molecular junctions, the local transmission maps for the transmission spectra associated with cluster approach using *ARTAIOS* code are evaluated. From local transmission plots one can obtain a qualitative understanding of how the electron flows through the molecule from contact to contact. In these plots, the local transmission components are represented by arrows along molecular geometry in such a way that diameter of arrow is proportional to the value of local transmission between pair of atoms. Blue arrows indicate local transport contributions in the same direction as of overall current, i.e., when the transmission from the first atom to second atom is positive and the second atom lies further along the transport direction (left to right) thereby contributing to the current, whereas the red arrows give the components corresponding to the negative transmission, thereby reducing the net current. An arrow is only drawn when the magnitude of local transmission is at least 10% of the maximum local transmission at that energy. Previously, Solomon et al. demonstrated how QI effects can be characterized from the description of local transmissions. The dips in transmission spectra of m-Benzene associated with QI were characterized by ring current reversal, while none of these features were observed for p-Benzene.[256] These striking features of cyclic currents are also connected to signatures of QI in a recent report by Stuyver et al.[257]

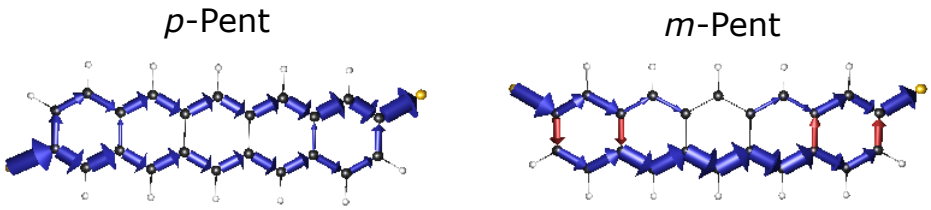

Figure B.6: Local transport contributions in *p*-Pent and *m*-Pent associated with QI dips at Fermi level. The diameter of the arrow is proportional to the magnitude of local transmission contribution, which are depicted only if they are 10% of the maximum local transmission between two atoms. Arrows in the transport direction are colored blue and the ones opposite to it are red.

Fig. B.6 shows local transport contributions for *p*-Pent and *m*-Pent at Fermi energy where QI features are prominent. Both *p*-Pent and *m*-Pent exhibit currents in the terminal benzene rings wherein three consecutive arrows are circulating clockwise (CW) and the remaining three are circulating in anti-clockwise (ACW) direction. For *p*-Pent, CW and ACW pathways are interfering constructively (with both blue colored arrows meeting each other). While for *m*-Pent, the conjoint of blue and red colored arrows reveal destructive interference between CW and ACW pathways, thus reducing the net transmission.

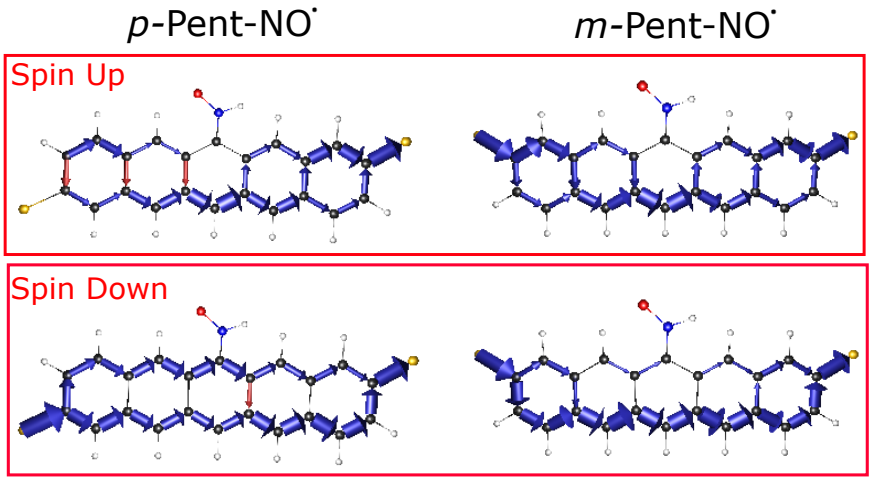

Figure B.7: Local transport contributions in *p*-Pent-NO• and *m*-Pent-NO• at energies close to QI dips near Fermi level.

For *p*-Pent-NO• and *m*-Pent-NO•, the local transmissions are plotted at the energies close to QI dips around Fermi level and are illustrated in Fig. B.7. For *p*-Pent-NO•, the conjoint of red and blue arrows in the terminal and central benzene rings of spin-up and spin-down electrons respectively reveals the signatures of DQI. On the other hand, *m*-Pent-NO• yields constructively interfering pathways. This scenario is in complete contrast to the one observed for parent pentacene and vividly supports the anomalous behavior of QI effects by attachment of radical. Besides the QI features, the local transport plots also suggest that conducting electrons go through the pentacene backbone while not directly interacting with radical. Thus, although there is no direct participation of radical in electron transport, however, significant spin polarization is induced by radical owing to the complete delocalization of spin density on the pentacene backbone.

APPENDIX C

Appendix-3

C.1 Frontier orbitals of isolated molecules

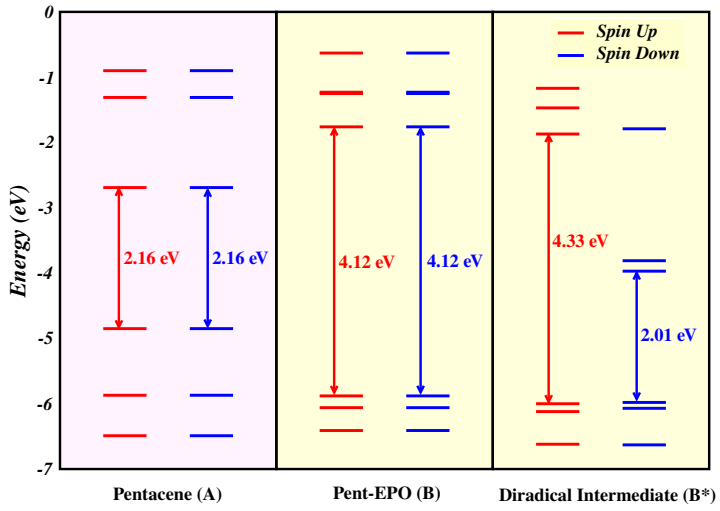

Figure C.1: Frontier MO energies computed at B3LYP/def2-TZVP level for pentacene (A), pent-EPO (B) and its diradical intermediate (B*). The different background pink and yellow colors denotes different degrees of conjugation, that is, fully conjugated for pentacene and broken conjugated for B and B*.

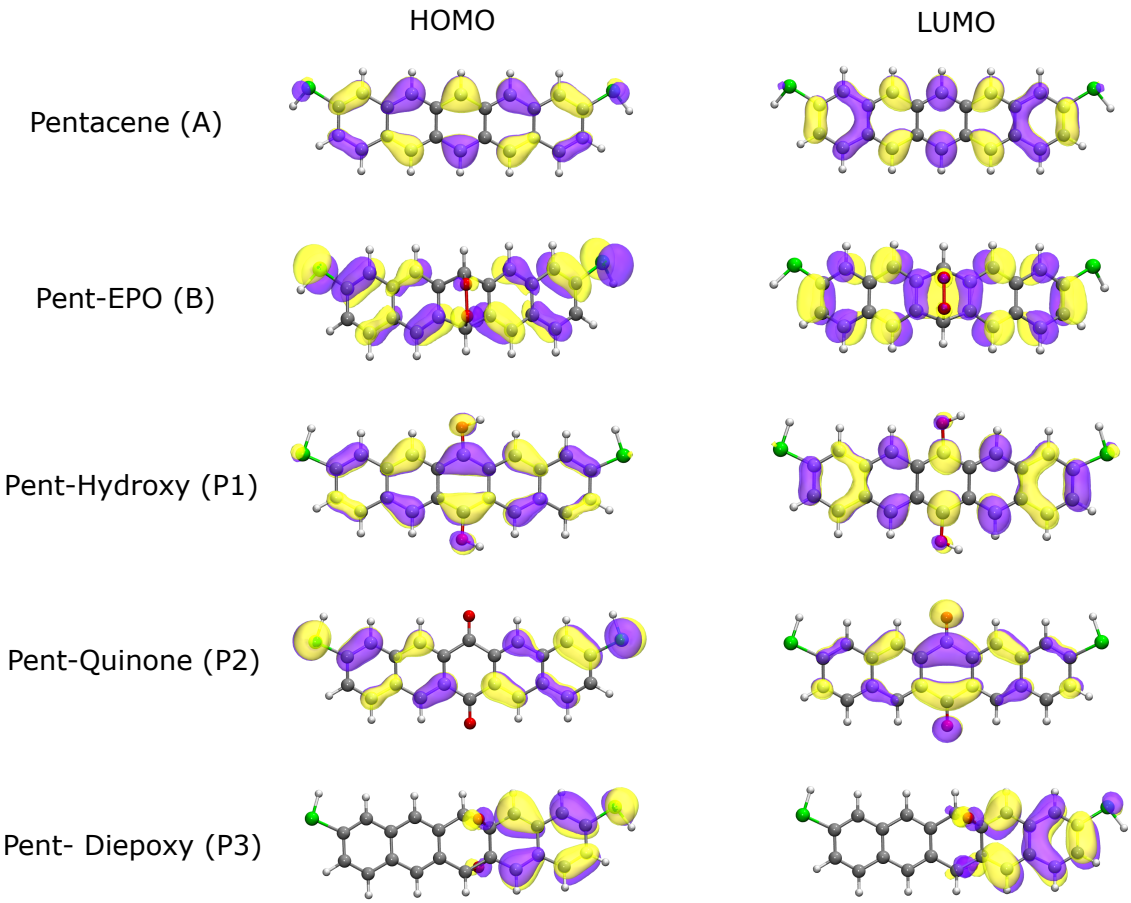

Figure C.2: Spatial distribution of frontier HOMO and LUMO of pentacene (A), pent-EPO (B) and related photoproducts P1, P2 and P3 computed using B3LYP/def2-TZVP method at an isovalue of 0.03.

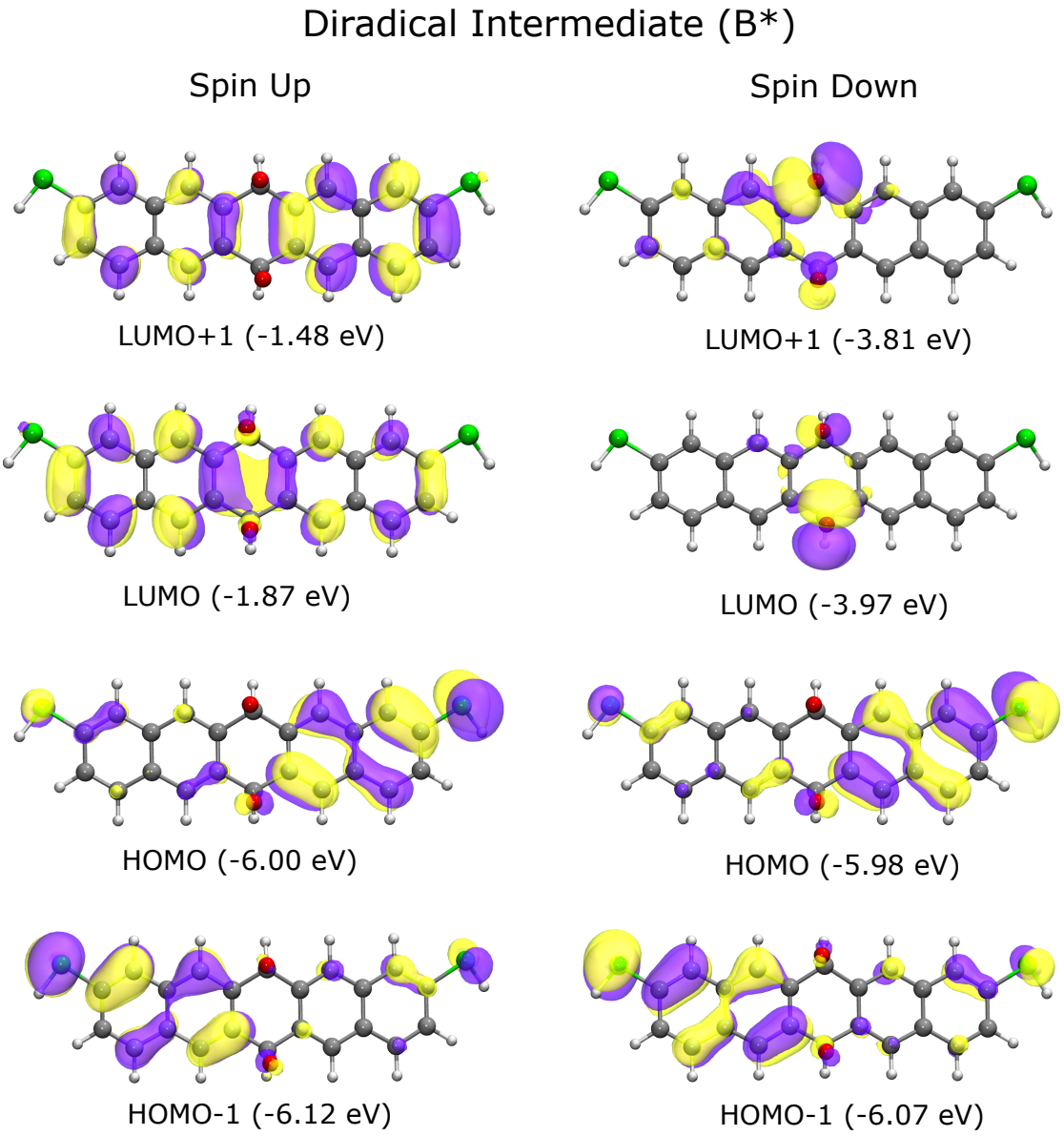

Figure C.3: Spatial distribution of spin up and spin down frontier molecular orbitals of diradical intermediate of pent-EPO (B*) computed using B3LYP/def2-TZVP method at an isovalue of 0.03.

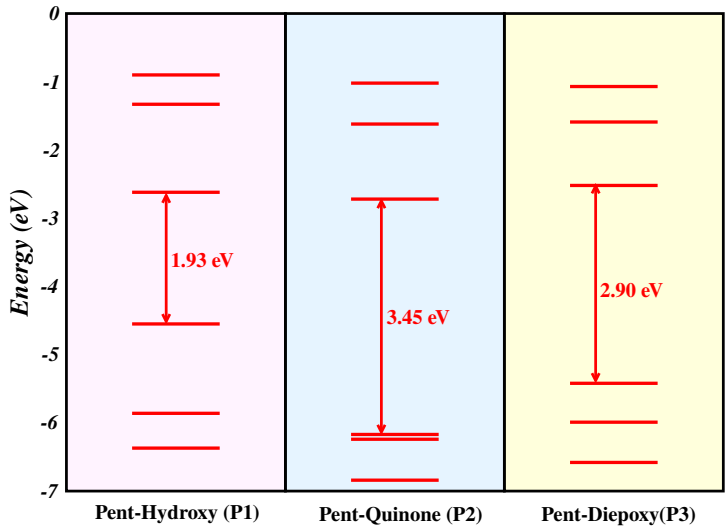

Figure C.4: Frontier MO energies computed at B3LYP/def2-TZVP level for photoproducts of pent-EPO including dihydroxypentacene (P1), pentaquinone (P2) and diepoxypentacene (P3). The background pink, blue and yellow colors represent the different degrees of conjugation, that is, fully conjugated, cross conjugated and broken conjugated respectively.

C.2 Para connected diradical intermediate

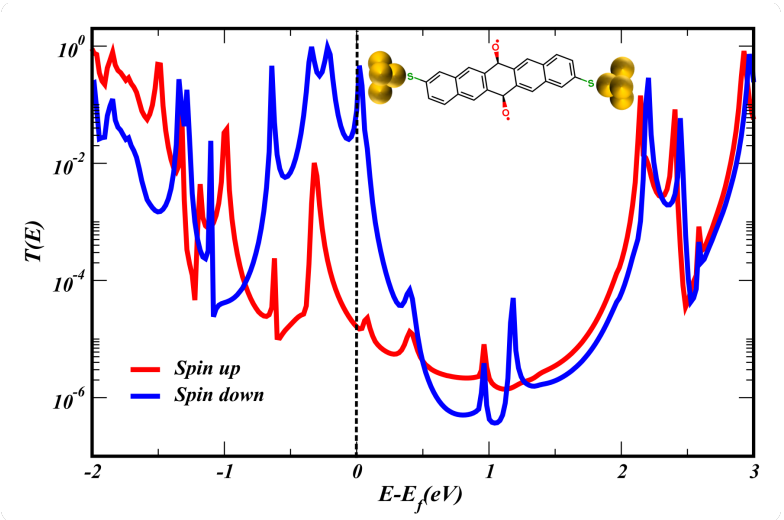

Figure C.5: Spin resolved transmission spectra of diradical intermediate with para connection to gold electrodes. A high SFE of 99.0% is obtained for B* in para connection.

C.3 Broken conjugated Dihydropentacene

To understand the changes in QI patterns brought about by broken conjugation of pent-EPO, we calculated the transmission spectra of broken conjugated dihydropentacene (PH) obtained by replacing each radical oxygen atom of B* with H-atom at the central benzene ring for both para and meta connections, as shown in Fig. C.6a. The transmission spectra reveals almost indistinguishable transmission spectra with no signatures of strong DQI dips in either of para and meta connections. At Fermi energy, meta-PH is found to be slightly less conductive than para-PH.

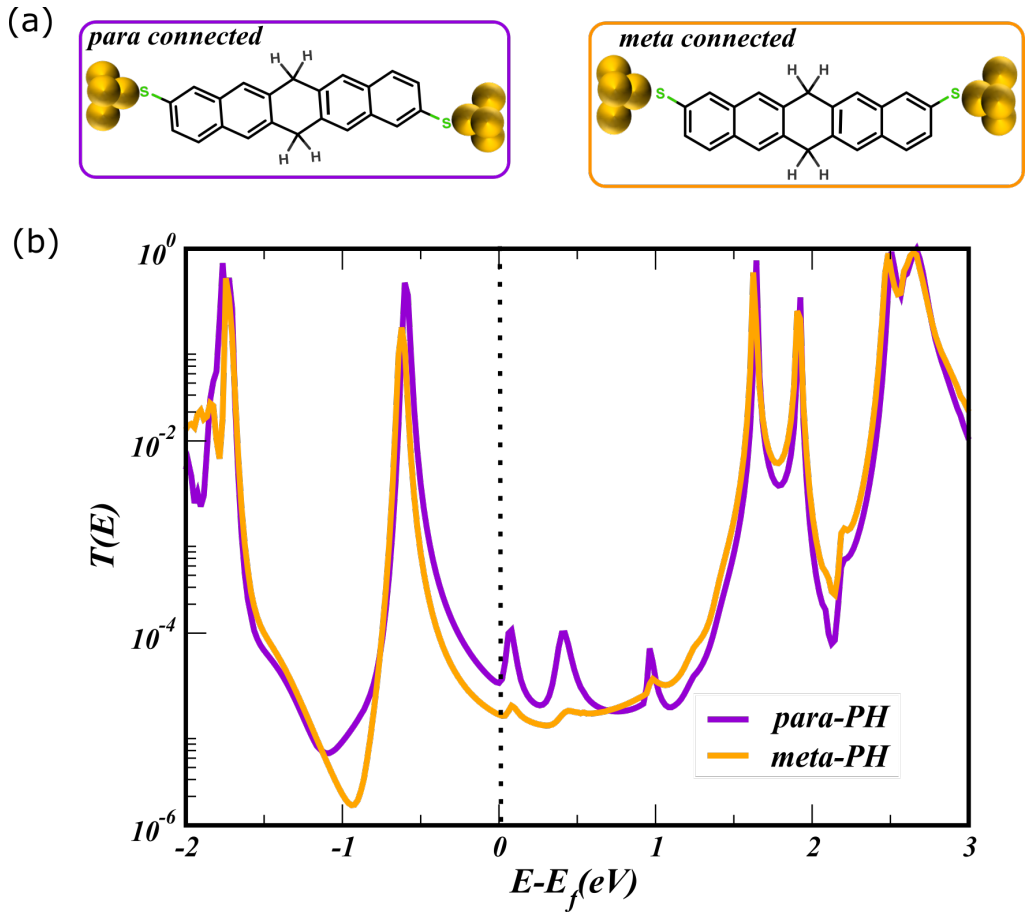

Figure C.6: (a) Dihydropentacene (PH) held between two Au electrodes illustrating para and meta connections in purple and orange enclosures respectively. (b) Computed transmission spectra of para-PH and meta-PH shown by purple and orange curves respectively. The vertical dotted line denotes the position of Fermi level.

C.4 PDOS of Diradical Intermediate

The PDOS on to the 2p orbitals of individual O-atoms reveals that for B* in isolated state, the two degenerate peaks at ~ 0.5 eV corresponds to the different O-atoms. While in molecular junction, the two dominant peaks at Fermi energy and at 1.16 eV, arising due to the lifting of degeneracy, shows the contribution of both O-atoms in both the peaks.

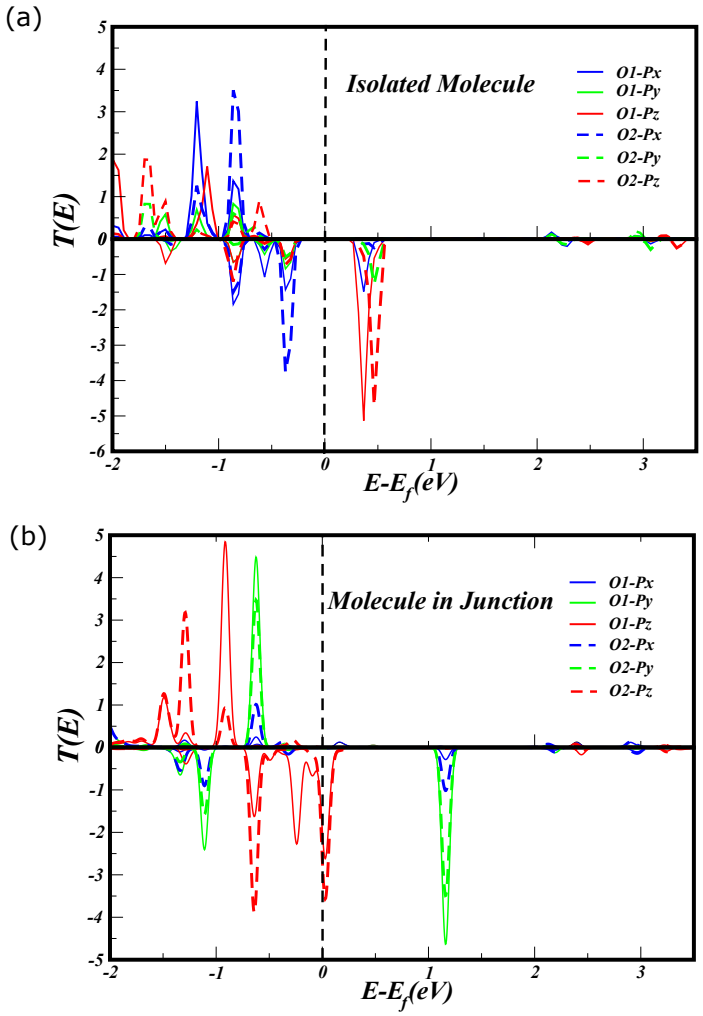

Figure C.7: Projected density of states (PDOS) onto individual O(2p) atomic orbitals of diradical intermediate (B*) of EPO in isolated state (left panel) and in molecular junction (right panel). Solid lines indicates the PDOS on the 2p orbitals of first oxygen atom, while the dotted lines corresponds to second O-atom.

APPENDIX **D**

Appendix-4

D.1 Computed $<S^2>$ values and radicaloid character

Table D.1: Computed $<S^2>$ values in broken symmetry states ($<S^2>_{BS}$) at UB3LYP/def2-TZVP level for isolated acenes and acenes in junction (n = 1 to 12) with both para and meta connections.

Acenes (n)	$<S^2>_{BS}$		
	Isolated Molecule	Junction(para)	Junction(meta)
1	0.00	0.00	0.00
2	0.00	0.00	0.00
3	0.00	0.00	0.00
4	0.00	0.00	0.00
5	0.00	0.00	0.00
6	0.15	0.00	0.00
7	0.77	0.67	0.67
8	1.07	0.96	0.99
9	1.24	1.19	1.18
10	1.39	1.35	1.36
11	1.54	1.50	1.50
12	1.71	1.68	1.69

Table D.2: Computed $<S^2>$ values in broken symmetry states ($<S^2>_{BS}$) at UB3LYP/def2-TZVP level for phenyl-substituted cumulenes ($C4$ to $C24$) in gas phase and in molecular junction.

Cumulenes (n)	$<S^2>_{BS}$	
	Isolated Molecule	Junction
C4	0.00	0.00
C6	0.00	0.00
C8	0.00	0.00
C10	0.01	0.00
C12	0.15	0.25
C14	0.37	0.57
C16	0.54	0.77
C18	0.72	0.92
C20	0.91	1.04
C22	1.09	1.13
C24	1.26	1.20

For the lower members of the series, $<S^2>_{BS} = 0$ indicates that BS solution do no exist and hence diradical character is zero. As the length is increased, $<S^2>_{BS}$ monotonically increases in all the cases in such a way that $<S^2>_{BS}$ tends to 1 indicating a perfect diradical states for those cases. Further, only a slight change in observed in $<S^2>$ values upon placing the molecules in junctions, indicating that the molecule retains its same ground state in junction as in isolated gas phase.

Radicaloid character: (y) To estimate the extent of increasing radical character with length in both acenes and cumulenes, the radicaloid character (y-value) is quantified from the occupancy of UHF based orbitals as proposed by Yamaguchi et al., using Eq. D.1

$$y = 1 - \frac{2T}{1 + T^2} \tag{D.1}$$

where,

$$T = \frac{n_{HOMO} - n_{LUMO}}{2} \tag{D.2}$$

where n_{HOMO} and n_{LUMO} are the occupancies of the frontier natural orbitals. To evaluate y, BS calculations with unrestricted Hartree-Fock (UHF) using a def2-TZVP basis set are performed using ground state geometry, i.e., RKS optimized geometry is used for lower members of the series with CSS ground state, while UKS-BS optimized geometry is used for higher members with OSS ground state. The occupancy of highest occupied n_{HOMO} and lowest unoccupied n_{LUMO} and the calculated radicaloid character y are tabulated in Table D.3 and Table D.4 for acenes and cumulenes respectively. The

trends observed in the occupancy of frontier orbitals and *y*-value indicates increasing diradical character with length.

Table D.3: Calculated radicaloid character (*y*) for polyacenes (*n* = 1 to 12) and occupancy of highest occupied (n_{HOMO}) and lowest unoccupied (n_{LUNO}) UHF orbitals calculated using def2-TZVP Method.

Acenes (*n*)	n_{HONO}	n_{LUNO}	*y*
1	1.90	0.09	0.005
2	1.74	0.25	0.04
3	1.58	0.41	0.13
4	1.44	0.55	0.26
5	1.33	0.66	0.39
6	1.24	0.75	0.53
7	1.15	0.84	0.75
8	1.10	0.89	0.80
9	1.06	0.93	0.87
10	1.03	0.96	0.93
11	1.01	0.98	0.97
12	1.00	0.99	0.99

Table D.4: Calculated radicaloid character (*y*) for phenyl-substituted cumulenes (*C*4 to *C*24) along with the occupancy of highest occupied (n_{HOMO}) and lowest unoccupied (n_{LUNO}) UHF orbitals calculated using def2-TZVP Method.

Cumulenes			
n	n_{HONO}	n_{LUNO}	*y*
C4	1.47	0.52	0.22
C6	1.37	0.62	0.34
C8	1.29	0.70	0.45
C10	1.24	0.75	0.53
C12	1.20	0.79	0.60
C14	1.15	0.84	0.69
C16	1.12	0.87	0.75
C18	1.10	0.89	0.79
C20	1.08	0.91	0.83
C22	1.06	0.93	0.87
C24	1.05	0.94	0.89

D.2 Central subsystem frontier orbitals

The frontier orbital energies of cluster-molecule-cluster model for all the systems are obtained from central subsytem molecular orbitals. Following the methodology by Hermann et al.[60], central subsystem MOs are evaluated by solving the secular equation for the central subsystem block of the Hamiltonian matrix (here, only molecule constitutes the central region). Since, peaks in transmission spectra are located at the energies of the central subsystem MOs, therefore, only subsystem MOs are analyzed rather than full junction MOs which are similar in shape but slightly shifted in energy due to renormalization of molecular electronic levels in molecular junction.[258] The designation of HOMO and LUMO is made by comparing the central subsystem MOs with the isolated molecule HOMO and LUMO orbitals. Since, we have set the Fermi level of the electrodes to -4.00 eV throughout this work, thus the frontier orbital energies are also shifted against the estimated Fermi energy of -4.00 eV.

Table D.5: Energies of central subsystem frontier HOMO and LUMO orbitals and the corresponding energy gap ΔE_{HL} for meta connected acenes placed between two Au_9 clusters in CSS and OSS state. The energies of the orbitals are shifted against estimated Fermi energy of -4 eV.

***m*-acenes**	**CSS state**			**OSS state**		
n	E(HOMO)	E(LUMO)	ΔE_{HL}	E(HOMO)	E(LUMO)	ΔE_{HL}
1	-3.37	3.23	**6.60**	-3.37	3.23	**6.60**
2	-2.43	2.35	**4.78**	-2.43	2.35	**4.78**
3	-1.80	1.81	**3.61**	-1.80	1.81	**3.61**
4	-1.38	1.43	**2.81**	-1.38	1.43	**2.81**
5	-1.09	1.17	**2.26**	-1.09	1.17	**2.26**
6	-0.85	0.98	**1.83**	-0.86	0.98	**1.84**
7	-0.63	0.79	**1.42**	-0.83	0.97	**1.80**
8	-0.48	0.67	**1.15**	-0.79	0.98	**1.77**
9	-0.37	0.58	**0.95**	-0.77	1.00	**1.77**
10	-0.28	0.52	**0.80**	-0.77	1.00	**1.77**
11	-0.21	0.48	**0.69**	-0.76	1.03	**1.79**
12	-0.16	0.35	**0.51**	-0.78	1.06	**1.84**

Table D.6: Energies of central subsystem frontier HOMO and LUMO orbitals and the corresponding energy gap ΔE_{HL} for para connected acenes placed between two Au_9 clusters in CSS and OSS state. The energies of the orbitals are shifted against estimated Fermi energy of -4 eV.

p-acenes	CSS state			OSS state		
n	E(HOMO)	E(LUMO)	ΔE_{HL}	E(HOMO)	E(LUMO)	ΔE_{HL}
1	-3.07	3.32	**6.39**	-3.07	3.32	**6.39**
2	-2.40	2.36	**4.76**	-2.40	2.36	**4.76**
3	-1.79	1.82	**3.61**	-1.79	1.82	**3.61**
4	-1.36	1.45	**2.81**	-1.36	1.45	**2.81**
5	-1.07	1.19	**2.26**	-1.09	1.19	**2.26**
6	-0.84	1.00	**1.84**	-0.84	1.00	**1.84**
7	-0.61	0.81	**1.42**	-0.80	1.01	**1.81**
8	-0.47	0.73	**1.20**	-0.79	1.01	**1.80**
9	-0.36	0.59	**0.95**	-0.79	1.02	**1.81**
10	-0.26	0.53	**0.80**	-0.77	1.04	**1.81**
11	-0.13	0.34	**0.47**	-0.75	1.04	**1.79**
12	-0.14	0.37	**0.51**	-0.76	1.05	**1.81**

Table D.7: Energies of central subsystem frontier HOMO and LUMO orbitals and the corresponding energy gap ΔE_{HL} for phenyl-substituted cumulenes placed between two Au_9 clusters in CSS and OSS state. The energies of the orbitals are shifted against estimated Fermi energy of -4 eV.

Cumulenes	CSS state			OSS state		
n	E(HOMO)	E(LUMO)	ΔE_{HL}	E(HOMO)	E(LUMO)	ΔE_{HL}
C4	-1.03	1.93	**2.96**	-1.03	1.93	**2.96**
C6	-0.89	1.61	**2.50**	-0.89	1.61	**2.50**
C8	-0.80	1.27	**2.07**	-0.80	1.27	**2.07**
C10	-0.73	1.11	**1.84**	-0.73	1.11	**1.84**
C12	-0.70	0.95	**1.65**	-0.73	1.11	**1.73**
C14	-0.56	0.74	**1.30**	-0.72	0.90	**1.62**
C16	-0.55	0.61	**1.16**	-0.78	0.84	**1.62**
C18	-0.51	0.51	**1.02**	-0.79	0.80	**1.59**
C20	-0.47	0.41	**0.87**	-0.81	0.73	**1.54**
C22	-0.40	0.33	**0.73**	-0.76	0.69	**1.45**
C24	-0.35	0.29	**0.63**	-0.81	0.70	**1.51**

D.3 Frontier orbitals for isolated molecules

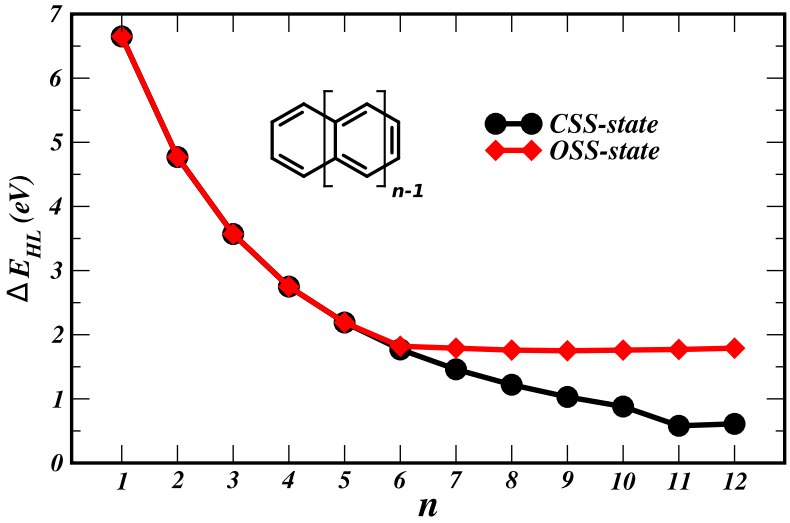

Figure D.1: Computed HOMO-LUMO gap (in eV) in CSS state (black curve) and OSS state (red curve) for isolated acenes. In CSS state, HLG shows a steady decay while in OSS state, it saturates ta a constant value of ~ 1.70 eV.

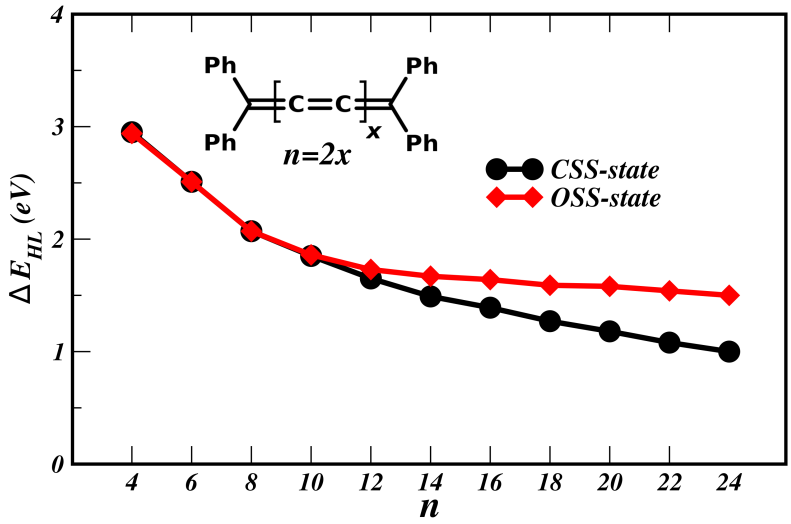

Figure D.2: Computed HOMO-LUMO gap (in eV) in CSS state (black curve) and OSS state (red curve) for phenyl-substituted cumulenes. In CSS state, HLG shows a steady decay while in OSS state, it saturates ta a constant value of ~ 1.50 eV.

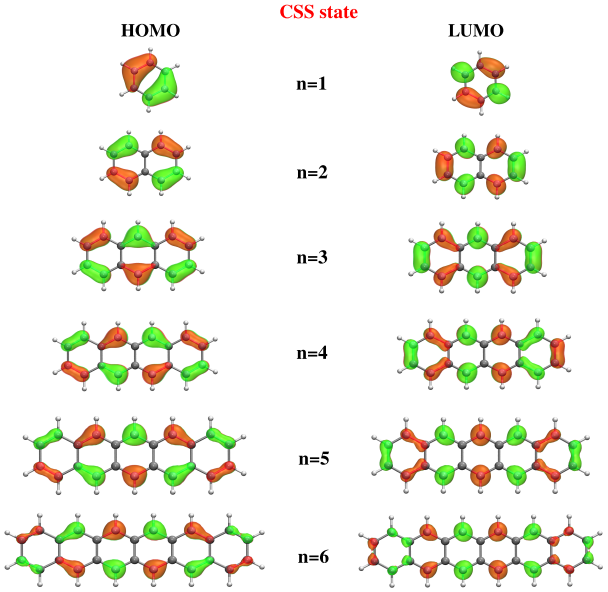

Figure D.3: Spatial distribution of frontier HOMO and LUMO for isolated acene series from $n = 1$ to 6 in CSS ground state.

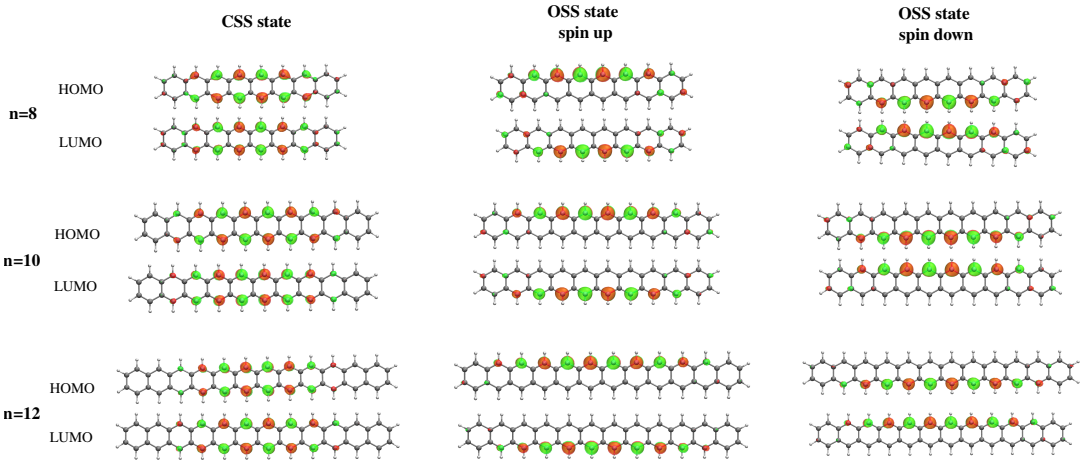

Figure D.4: Spatial distribution of frontier HOMO and LUMO for higher acenes in CSS state and both the spin configurations of OSS ground state. In CSS state, MOs are localized at central benzene rings, while in OSS state spin-split orbitals are localized at the opposite ziz-zag edges.

D.4 Spin density distribution

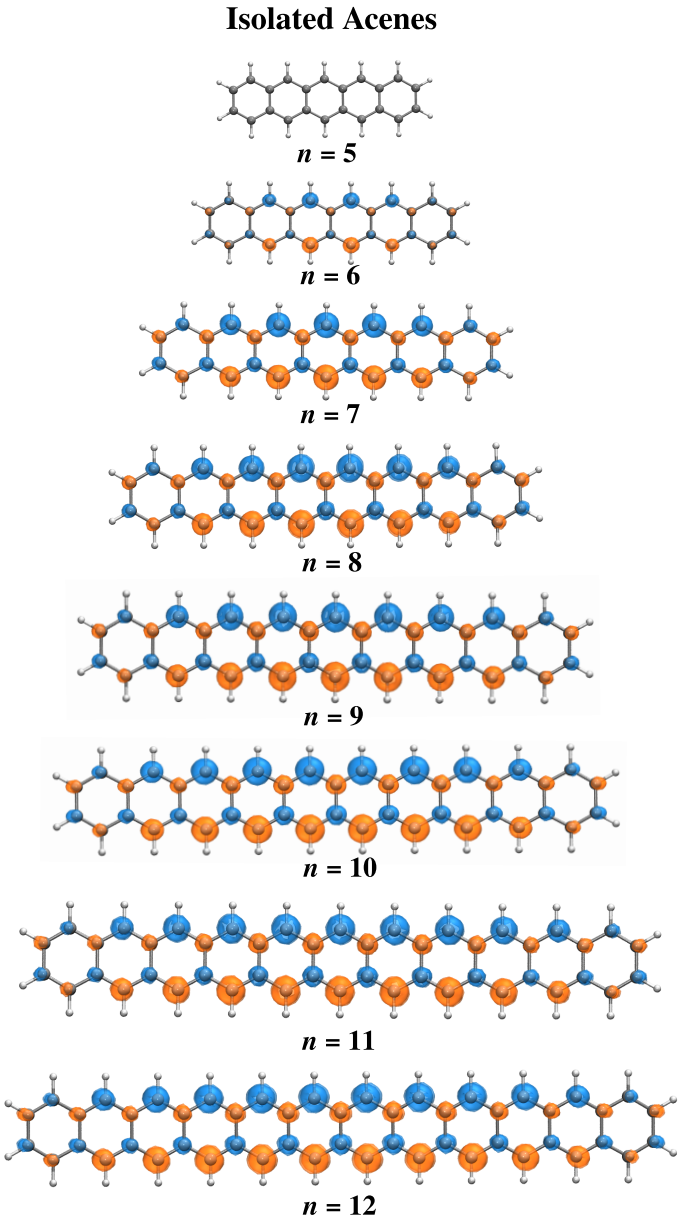

Figure D.5: Spin density distribution in BS state for isolated acenes n = 5 to 12 computed at UB3LYP/def2-TZVP level. Blue and orange color represents α and β spin with an isovalue of 0.005 $\mu_B/Å^3$. The edges of molecule are spin polarized with equal and opposite magnetic moments at the atoms of upper and lower edges.

D.4 Spin density distribution

The spin density distribution for acenes n = 5 to 12 in broken symmetry state is shown in Fig. D.5. It reveals that acenes features an anti-ferromagnetic coupling of unpaired electrons localized at two opposite edges. For n = 5, no spin density appears at the benzene rings, indicating that BS solution do not exists and n = 5 is stable in CSS state. Spin density for n = 6 illustrates that magnitude of spin moment at the edges is small as compared to n ≥ 7, indicating that n = 6 case is at borderline in transition from CSS to OSS state.

For phenyl-substituted cumulenes, spin density is uniformly delocalized at the complete molecule (Fig. D.6). C10 bears no spin density indicating CSS ground state, while C12 with small spin density is at borderline.

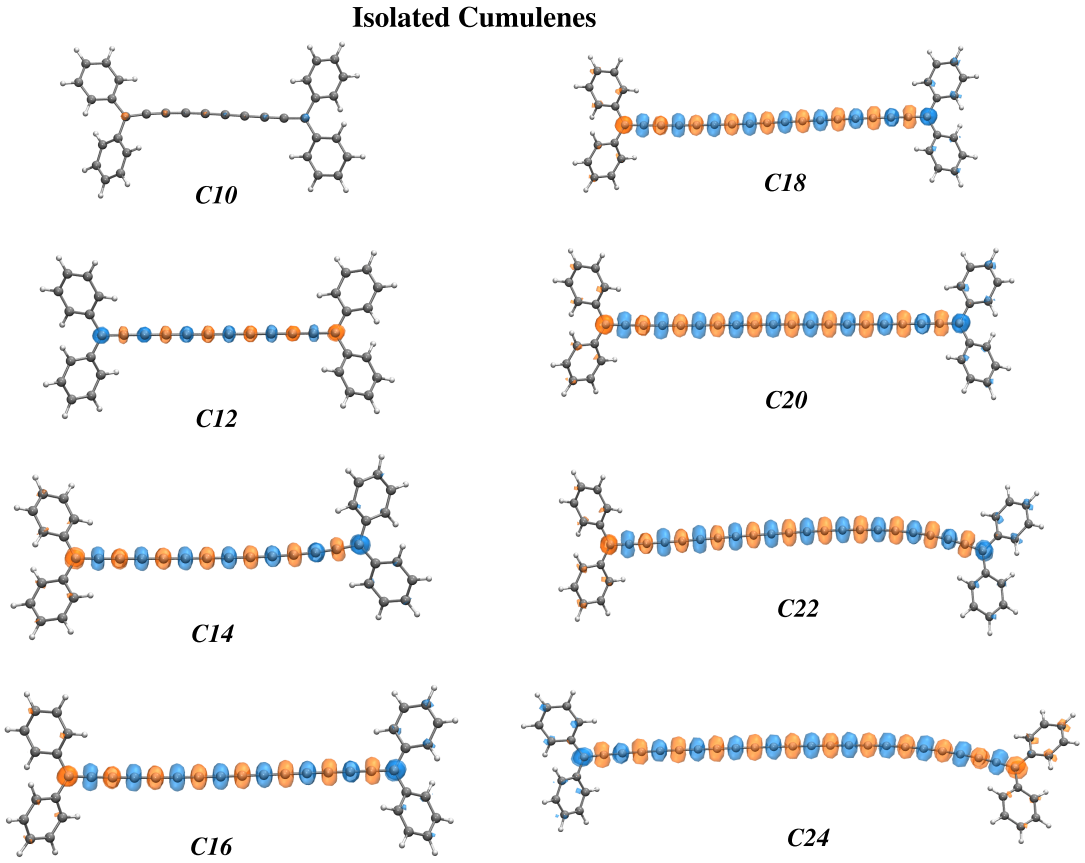

Figure D.6: Spin density distribution in BS state for isolated phenyl-substituted cumulenes n = 10 to 24 computed at UB3LYP/def2-TZVP level. Blue and orange color represents α and β spin with an isovalue of 0.005 $\mu_B/Å^3$.

D.5 Energetics of molecular states

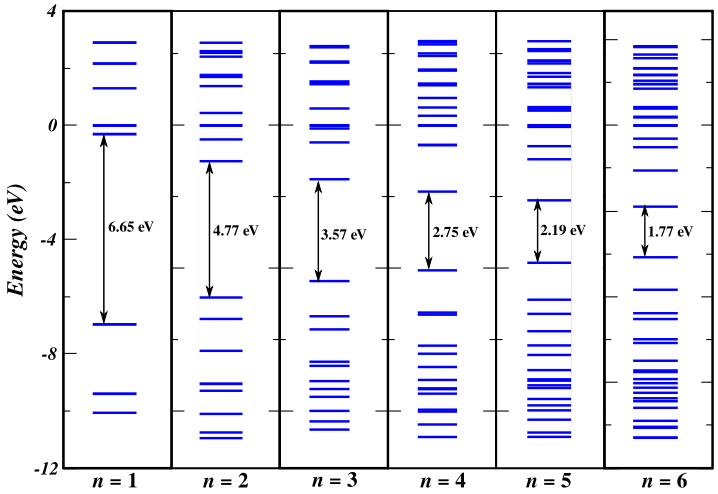

Figure D.7: Molecular orbital bands calculated at B3LYP/def2-TZVP level for n = 1 to 6 isolated acenes in CSS state within an energy window spanning -11 to 3 eV. Density of molecular levels is increasing with increasing n.

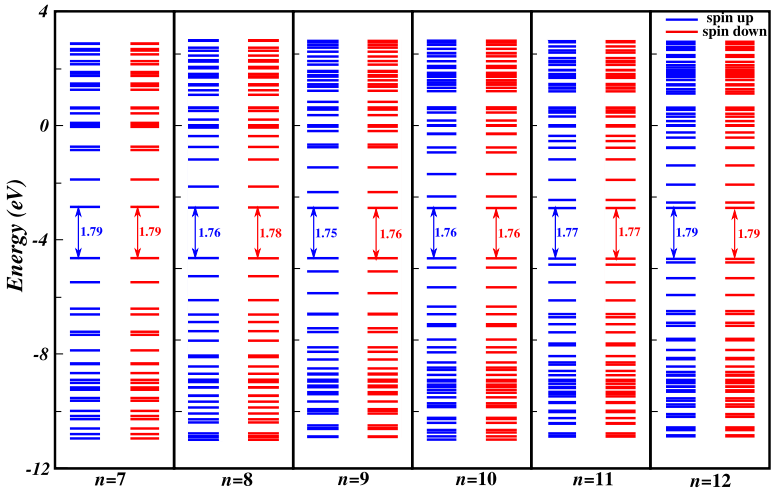

Figure D.8: Spin-resolved molecular orbital bands calculated at UB3LYP/def2-TZVP level for n = 7 to 12 isolated acenes in OSS ground state within an energy window spanning -11 to 3 eV. Spin-up and spin-down energy levels (shown with blue and red color) are degenerate.

D.6 CAM-B3LYP computed conductance

Since, LDA based functionals including hybrid functionals tends to suffer from a deficiency of underestimated HOMO-LUMO gap, that contributes to overestimated conductance by these funnctionals. This limitation has been addressed by employing CAM-B3LYP as one of the RSH functional which provides improved agreement to experimental values as compared to B3LYP. As illustrated in Fig. D.9, CAM-B3LYP functional provides HOMO-LUMO gap, which is in better agreement to experimental data and our calculated CSSD(T) gaps as compared to B3LYP.

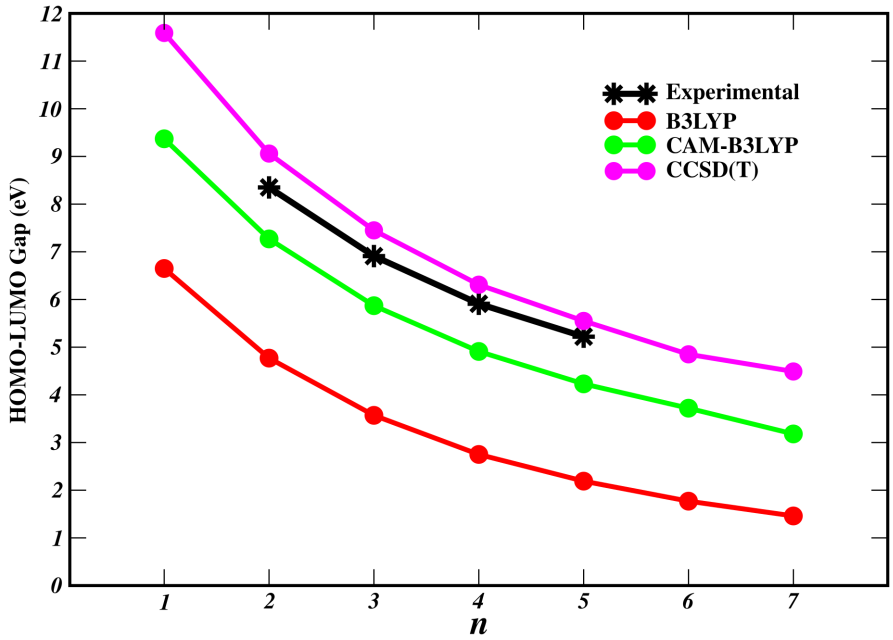

Figure D.9: Comparison of computed HOMO-LUMO gaps for n =1 to 7 acenes using hybrid functional B3LYP and range-separated hybrid functional CAM-B3LYP. CCSD(T) gaps are calculated using def2-TZVP basis set.

Proceeding towards conductance calculations, we begin by benchmarking against experimental STM-BJ measurements for lower cumulenes. Table D.8 illustrates the computed conductance using B3LYP and CAM-B3LYP methods and experimentally reported values by Zang et al.[231]. It reveals that CAM-B3LYP based values are within 1 order of magnitude of the experimental values, whereas B3LYP values overestimate the conductance by upto 2 orders of magnitude. Overall, CAM-B3LYP values overestimate the conductance by a factor of $\sim$ 4, as compared to factor of $\sim$ 20 for B3LYP. Thus, an improved quantitative description of conductance can be obtained with CAM-B3LYP.

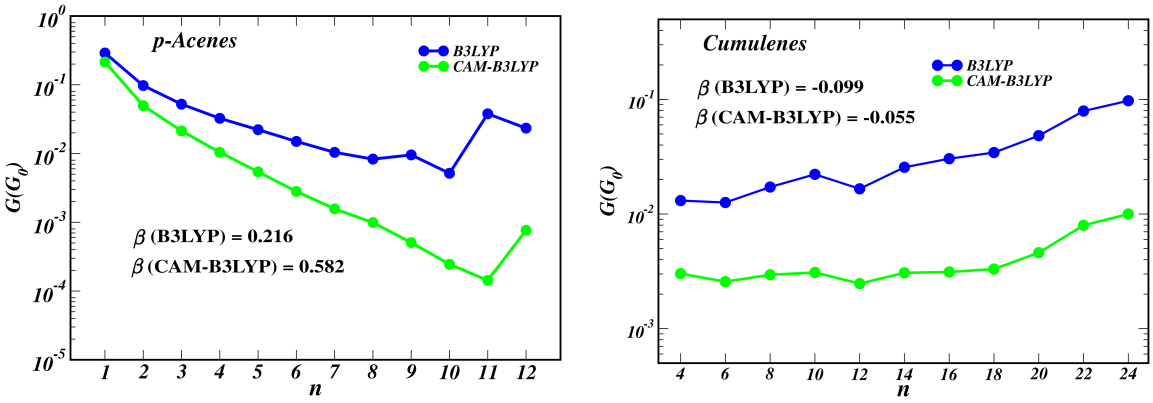

Figure D.10: Computed molecular conductance using B3LYP and CAM-B3LYP for *p*-acenes (left panel) and phenyl-substituted cumulenes (right panel). CAM-B3LYP results in larger β values as compared to B3LYP.

Table D.8: Comparison of computed conductance ($\mathcal{G}$ in units of $\mathcal{G}_0$) for phenyl-substituted cumulenes using B3LYP and CAM-B3LYP methods with experimentally reported values.

Cumulenes	$\mathcal{G}(\mathcal{G}_0)$		
	B3LYP	**CAM-B3LYP**	**Experiment**[a]
C4	1.31×10^{-2}	3.02×10^{-3}	6.40×10^{-4}
C6	1.26×10^{-2}	2.57×10^{-3}	7.40×10^{-4}
C8	1.72×10^{-2}	2.95×10^{-3}	8.31×10^{-4}

[a] Experimental values are taken from Zang et al.

We next consider the trend of molecular conductance v/s length using B3LYP and CAM-B3LYP in CSS state. As illustrated in Fig. D.10, an underestimated orbital gap associated with B3LYP yields an expected overestimated conductance about 2 orders of magnitude higher than CAM-B3LYP. This is reflected in the form of higher β values with CAM-B3LYP.

Fig. D.11 and Fig. D.12 illustrates the evolution of conductance in CSS and OSS state for *p*-acenes and phenyl-substituted cumulenes using CAM-B3LYP. It reveals that overall qualitative trends for both acenes and cumulenes are preserved with both B3LYP and CAM-B3LYP methods. Cumulenes yields inverted β values in CSS and OSS state, while acenes results in a decaying conductance in both CSS and OSS state, accompanied by a larger resistance in OSS state.

Although CAM-B3LYP succeeds in providing better HOMO-LUMO gaps and consequent better conductance values as compared to B3LYP, however, the performance of

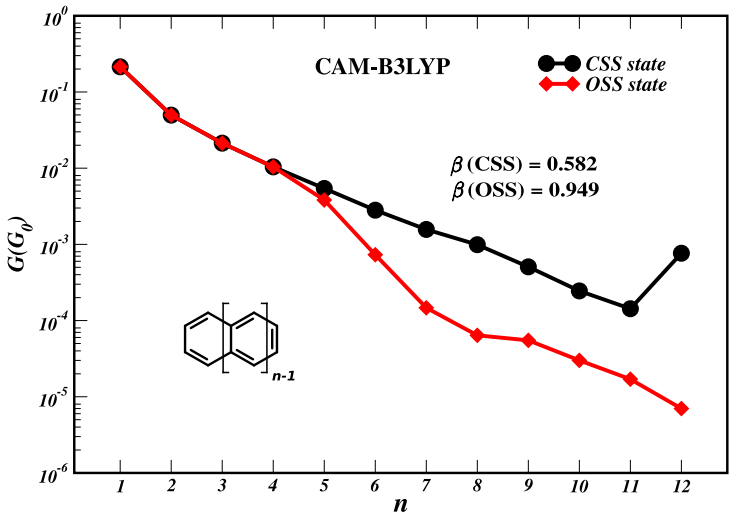

Figure D.11: Molecular conductance (in units of $\mathcal{G}_0$) v/s number of phenyl rings n in CSS state (black curve) and OSS state (red curve) for p-acenes using CAM-B3LYP method.

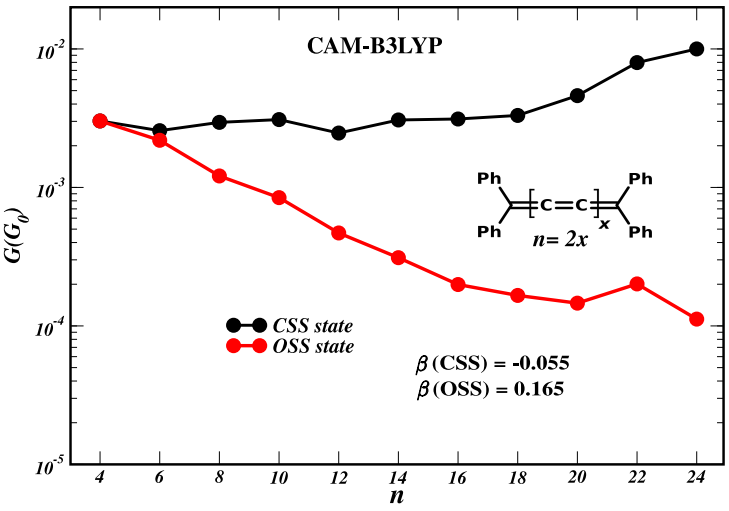

Figure D.12: Molecular conductance (in units of $\mathcal{G}_0$) v/s number of C-atoms n in CSS state (black curve) and OSS state (red curve) for phenyl-substituted cumulenes CAM-B3LYP method.

CAM-B3LYP for open shell singlets is still inferior as compared to traditional B3LYP. The computed $< S^2 >$ values in BS state (Table D.9) shows that CAM-B3LYP yields large $< S^2 >$ values as compared to B3LYP, which even exceeds 2.00 for higher acenes. This indicates that CAM-B3LYP suffers from severe spin contamination. The high spin contamination eventually results into the emergence of open shell singlet as a ground state from n=5 onwards, which is in contrast to the reported CSS ground state in literature.

Table D.9: Comparison of $< S^2 >$ values in broken-symmetry state for isolated acenes using B3LYP and CAM-B3LYP.

Acenes (n)	$< S^2 >_{BS}$	
	B3LYP	**CAM-B3LYP**
1	0.00	0.00
2	0.00	0.00
3	0.00	0.00
4	0.00	0.00
5	0.00	0.25
6	0.15	0.70
7	0.77	1.17
8	1.07	1.45
9	1.24	1.68
10	1.39	1.92
11	1.54	2.18
12	1.71	2.44

References

[1] Moore, G. E., et al. Cramming more components onto integrated circuits. 1965.

[2] Ratner, M. A. Introducing molecular electronics. *Mater. Today* **2002**, *5*, 20–27.

[3] Aviram, A.; Ratner, M. A. Molecular rectifiers. *Chem. Phys. Lett.* **1974**, *29*, 277–283.

[4] Staykov, A.; Nozaki, D.; Yoshizawa, K. Theoretical study of donor- π-bridge-acceptor unimolecular electric rectifier. *J. Phys. Chem. C* **2007**, *111*, 11699–11705.

[5] Guo, C.; Wang, K.; Zerah-Harush, E.; Hamill, J.; Wang, B.; Dubi, Y.; Xu, B. Molecular rectifier composed of DNA with high rectification ratio enabled by intercalation. *Nat. Chem.* **2016**, *8*, 484–490.

[6] Donhauser, Z.; Mantooth, B.; Kelly, K.; Bumm, L.; Monnell, J.; Stapleton, J. J.; Price Jr, D.; Rawlett, A.; Allara, D.; Tour, J., et al. Conductance switching in single molecules through conformational changes. *Science* **2001**, *292*, 2303–2307.

[7] Zhang, J. L.; Zhong, J. Q.; Lin, J. D.; Hu, W. P.; Wu, K.; Xu, G. Q.; Wee, A. T.; Chen, W. Towards single molecule switches. *Chem. Soc. Rev.* **2015**, *44*, 2998–3022.

[8] Kushmerick, J. Molecular transistors scrutinized. *Nature* **2009**, *462*, 994–995.

[9] Samanta, M.; Tian, W.; Datta, S.; Henderson, J.; Kubiak, C. Electronic conduction through organic molecules. *Phys. Rev. B* **1996**, *53*, R7626.

[10] Wang, C.; Hu, Y.; Lieber, C. M.; Sun, S. Ultrathin Au nanowires and their transport properties. *J. Am. Chem. Soc.* **2008**, *130*, 8902–8903.

[11] Baibich, M. N.; Broto, J. M.; Fert, A.; Van Dau, F. N.; Petroff, F.; Etienne, P.; Creuzet, G.; Friederich, A.; Chazelas, J. Giant magnetoresistance of (001) Fe/(001) Cr magnetic superlattices. *Phys. Rev. Lett.* **1988**, *61*, 2472.

[12] Binasch, G.; Grünberg, P.; Saurenbach, F.; Zinn, W. Enhanced magnetoresistance in layered magnetic structures with antiferromagnetic interlayer exchange. *Phys. Rev. B* **1989**, *39*, 4828.

[13] Bhatti, S.; Sbiaa, R.; Hirohata, A.; Ohno, H.; Fukami, S.; Piramanayagam, S. Spintronics based random access memory: a review. *Mater. Today* **2017**, *20*, 530–548.

[14] Rajput, P. J.; Bhandari, S. U.; Wadhwa, G. A Review on—Spintronics an Emerging Technology. *Silicon* **2022**, 1–16.

[15] Sanvito, S. Molecular spintronics. *Chem. Soc. Rev.* **2011**, *40*, 3336–3355.

[16] Hueso, L. E.; Pruneda, J. M.; Ferrari, V.; Burnell, G.; Valdes-Herrera, J. P.; Simons, B. D.; Littlewood, P. B.; Artacho, E.; Fert, A.; Mathur, N. D. Transformation of spin information into large electrical signals using carbon nanotubes. *Nature* **2007**, *445*, 410–413.

[17] Ababei, R.; Pichon, C.; Roubeau, O.; Li, Y.-G.; Bréfuel, N.; Buisson, L.; Guionneau, P.; Mathoniere, C.; Clérac, R. Rational design of a photomagnetic chain: Bridging single-molecule magnets with a spin-crossover complex. *J. Am. Chem. Soc.* **2013**, *135*, 14840–14853.

[18] Frisenda, R.; Harzmann, G. D.; Celis Gil, J. A.; Thijssen, J. M.; Mayor, M.; Van Der Zant, H. S. Stretching-induced conductance increase in a spin-crossover molecule. *Nano Lett.* **2016**, *16*, 4733–4737.

[19] Johnson, M.; Silsbee, R. H. Interfacial charge-spin coupling: Injection and detection of spin magnetization in metals. *Phys. Rev. Lett.* **1985**, *55*, 1790.

[20] Emberly, E. G.; Kirczenow, G. Molecular spintronics: spin-dependent electron transport in molecular wires. *Chem. Phys.* **2002**, *281*, 311–324.

[21] Heersche, H.; De Groot, Z.; Folk, J.; Van Der Zant, H.; Romeike, C.; Wegewijs, M.; Zobbi, L.; Barreca, D.; Tondello, E.; Cornia, A. Electron transport through single Mn_{12} molecular magnets. *Phys. Rev. Lett.* **2006**, *96*, 206801.

[22] Reed, M. A.; Zhou, C.; Muller, C.; Burgin, T.; Tour, J. Conductance of a molecular junction. *Science* **1997**, *278*, 252–254.

[23] Xu, B.; Tao, N. J. Measurement of single-molecule resistance by repeated formation of molecular junctions. *Science* **2003**, *301*, 1221–1223.

[24] Frisenda, R.; Gaudenzi, R.; Franco, C.; Mas-Torrent, M.; Rovira, C.; Veciana, J.; Alcon, I.; Bromley, S. T.; Burzurí, E.; Van der Zant, H. S. Kondo effect in a neutral and stable all organic radical single molecule break junction. *Nano Lett.* **2015**, *15*, 3109–3114.

[25] Pal, A. N.; Li, D.; Sarkar, S.; Chakrabarti, S.; Vilan, A.; Kronik, L.; Smogunov, A.; Tal, O. Nonmagnetic single-molecule spin-filter based on quantum interference. *Nat. Commun.* **2019**, *10*, 1–8.

[26] Liu, J.; Isshiki, H.; Katoh, K.; Morita, T.; Breedlove, K., Brian; Yamashita, M.; Komeda, T. First observation of a Kondo resonance for a stable neutral pure organic radical, 1, 3, 5-triphenyl-6-oxoverdazyl, adsorbed on the Au (111) surface. *J. Am. Chem. Soc.* **2013**, *135*, 651–658.

[27] Requist, R.; Modesti, S.; Baruselli, P. P.; Smogunov, A.; Fabrizio, M.; Tosatti, E. Kondo conductance across the smallest spin 1/2 radical molecule. *Proc. Natl. Acad. Sci.* **2014**, *111*, 69–74.

[28] Christou, G.; Gatteschi, D.; Hendrickson, D. N.; Sessoli, R. Single-molecule magnets. *MRS Bull.* **2000**, *25*, 66–71.

[29] Bogani, L.; Wernsdorfer, W. *Nanoscience and technology: a collection of reviews from nature journals*; World Scientific, 2010; pp 194–201.

[30] Hayakawa, R.; Karimi, M. A.; Wolf, J.; Huhn, T.; Zollner, M. S.; Herrmann, C.; Scheer, E. Large magnetoresistance in single-radical molecular junctions. *Nano Lett.* **2016**, *16*, 4960–4967.

[31] Patera, L. L.; Sokolov, S.; Low, J. Z.; Campos, L. M.; Venkataraman, L.; Repp, J. Resolving the Unpaired-Electron Orbital Distribution in a Stable Organic Radical by Kondo Resonance Mapping. *Angew. Chem. Int. Ed.* **2019**, *58*, 11063–11067.

[32] Naaman, R.; Waldeck, D. H. Spintronics and chirality: Spin selectivity in electron transport through chiral molecules. *Annu. Rev. Phys. Chem* **2015**, *66*, 263–281.

[33] Aragonès, A. C.; Medina, E.; Ferrer-Huerta, M.; Gimeno, N.; Teixidó, M.; Palma, J. L.; Tao, N.; Ugalde, J. M.; Giralt, E.; Díez-Pérez, I., et al. Measuring the spin-polarization power of a single chiral molecule. *Small* **2017**, *13*, 1602519.

[34] Chen, Z.; Li, Y.; Huang, F. Persistent and stable organic radicals: Design, synthesis, and applications. *Chem* **2021**, *7*, 288–332.

[35] Ratera, I.; Veciana, J. Playing with organic radicals as building blocks for functional molecular materials. *Chem. Soc. Rev.* **2012**, *41*, 303–349.

[36] Gomberg, M. An instance of trivalent carbon: Triphenylmethyl. *J. Am. Chem. Soc.* **1900**, *22*, 757–771.

[37] Ullman, E. F.; Osiecki, J. H.; Boocock, D.; Darcy, R. Stable free radicals. X. Nitronyl nitroxide monoradicals and biradicals as possible small molecule spin labels. *J. Am. Chem. Soc.* **1972**, *94*, 7049–7059.

[38] Brough, P.; Pécaut, J.; Rassat, A.; Rey, P. Pyrimidinyl nitronyl nitroxides. *Chem.–Eur. J.* **2006**, *12*, 5134–5141.

[39] Koivisto, B. D.; Hicks, R. G. The magnetochemistry of verdazyl radical-based materials. *Coord. Chem. Rev.* **2005**, *249*, 2612–2630.

[40] Hicks, R. G. What's new in stable radical chemistry? *Org. Biomol. Chem.* **2007**, *5*, 1321–1338.

[41] Ji, Y.; Long, L.; Zheng, Y. Recent advances of stable Blatter radicals: synthesis, properties and applications. *Mater. Chem. Front.* **2020**, *4*, 3433–3443.

[42] Abe, M. Diradicals. *Chem. Rev.* **2013**, *113*, 7011–7088.

[43] Ali, M. E.; Datta, S. N. Broken-symmetry density functional theory investigation on bis-nitronyl nitroxide diradicals: influence of length and aromaticity of couplers. *J. Phys. Chem. A* **2006**, *110*, 2776–2784.

[44] Ali, M. E.; Datta, S. N. Polyacene spacers in intramolecular magnetic coupling. *J. Phys. Chem. A* **2006**, *110*, 13232–13237.

[45] Faust, T. B.; Tuna, F.; Timco, G. A.; Affronte, M.; Bellini, V.; Wernsdorfer, W.; Winpenny, R. E. Controlling magnetic communication through aromatic bridges by variation in torsion angle. *Dalton Trans.* **2012**, *41*, 13626–13631.

[46] Ko, K. C.; Cho, D.; Lee, J. Y. Systematic approach to design organic magnetic molecules: strongly coupled diradicals with ethylene coupler. *J. Phys. Chem. A* **2012**, *116*, 6837–6844.

[47] Song, M.; Song, X.; Bu, Y. Tuning the Spin Coupling Interactions in the Nitroxide-Based Bisphenol-Like Diradicals. *ChemPhysChem* **2017**, *18*, 2487–2498.

[48] Shil, S.; Misra, A. Photoinduced antiferromagnetic to ferromagnetic crossover in organic systems. *J. Phys. Chem. A* **2010**, *114*, 2022–2027.

[49] Latif, I. A.; Hansda, S.; Datta, S. N. High magnetic exchange coupling constants: a density functional theory based study of substituted Schlenk diradicals. *J. Phys. Chem. A* **2012**, *116*, 8599–8607.

[50] Shil, S.; Roy, M.; Misra, A. Role of the coupler to design organic magnetic molecules: LUMO plays an important role in magnetic exchange. *RSC Adv.* **2015**, *5*, 105574–105582.

[51] Burnea, F. K. B.; Nam, Y.; Lee, J. Y. H-Bonding on spin centres enhances spin–spin coupling for organic diradicals. *J. Mater. Chem. C* **2020**, *8*, 3402–3408.

[52] Mas-Torrent, M.; Crivillers, N.; Mugnaini, V.; Ratera, I.; Rovira, C.; Veciana, J. Organic radicals on surfaces: towards molecular spintronics. *J. Mater. Chem.* **2009**, *19*, 1691–1695.

[53] Poggini, L.; Cucinotta, G.; Sorace, L.; Caneschi, A.; Gatteschi, D.; Sessoli, R.; Mannini, M. Nitronyl nitroxide radicals at the interface: A hybrid architecture for spintronics. *Rendiconti Lincei. Scienze Fisiche e Naturali* **2018**, *29*, 623–630.

[54] Bejarano, F.; Olavarria-Contreras, I. J.; Droghetti, A.; Rungger, I.; Rudnev, A.; Gutiérrez, D.; Mas-Torrent, M.; Veciana, J.; Van Der Zant, H. S.; Rovira, C., et al. Robust organic radical molecular junctions using acetylene terminated groups for C–Au bond formation. *J. Am. Chem. Soc.* **2018**, *140*, 1691–1696.

[55] Souto, M.; Yuan, L.; Morales, D. C.; Jiang, L.; Ratera, I.; Nijhuis, C. A.; Veciana, J. Tuning the rectification ratio by changing the electronic nature (open-shell and closed-shell) in donor–acceptor self-assembled monolayers. *J. Am. Chem. Soc.* **2017**, *139*, 4262–4265.

[56] Yasui, R.; Shimizu, D.; Matsuda, K. Large Enhancement of the Single-Molecular Conductance of a Molecular Wire through a Radical Substituent. *Chem.–Eur. J.* **2022**, e202104242.

[57] Liu, J.; Zhao, X.; Al-Galiby, Q.; Huang, X.; Zheng, J.; Li, R.; Huang, C.; Yang, Y.; Shi, J.; Manrique, D. Z., et al. Radical-Enhanced Charge Transport in Single-Molecule Phenothiazine Electrical Junctions. *Angew. Chem. Int. Ed.* **2017**, *129*, 13241–13245.

[58] Naghibi, S.; Sangtarash, S.; Kumar, V. J.; Wu, J.-Z.; Judd, M. M.; Qiao, X.; Gorenskaia, E.; Higgins, S. J.; Cox, N.; Nichols, R. J., et al. Redox-addressable single-molecule junctions incorporating a persistent organic radical. *Angew. Chem. Int. Ed.* **2022**, e202116985.

[59] Herrmann, C.; Solomon, G. C.; Ratner, M. A. Organic radicals as spin filters. *J. Am. Chem. Soc.* **2010**, *132*, 3682–3684.

[60] Herrmann, C.; Solomon, G. C.; Ratner, M. A. Designing organic spin filters in the coherent tunneling regime. *J. Chem. Phys.* **2011**, *134*, 224306.

[61] Smeu, M.; DiLabio, G. A. Calculations of electron transport through simple π- and σ-type radicals. *J. Phys. Chem. C* **2010**, *114*, 17874–17879.

[62] Smeu, M.; Monti, O. L.; McGrath, D. Phenalenyls as tunable excellent molecular conductors and switchable spin filters. *Phys. Chem. Chem. Phys.* **2021**, *23*, 24106–24110.

[63] Shil, S.; Bhattacharya, D.; Misra, A.; Klein, D. J. A high-spin organic diradical as a spin filter. *Phys. Chem. Chem. Phys.* **2015**, *17*, 23378–23383.

[64] Hu, X.; Wang, W.; Wang, D.; Zheng, Y. The electronic applications of stable diradicaloids: present and future. *J. Mater. Chem. C* **2018**, *6*, 11232–11242.

[65] Nakano, M. Electronic structure of open-shell singlet molecules: Diradical character viewpoint. *Top. Curr. Chem.* **2017**, *375*, 1–67.

[66] Solà, M. Forty years of Clar's aromatic π-sextet rule. *Front. Chem.* **2013**, 22.

[67] Sun, Z.; Lee, S.; Park, K. H.; Zhu, X.; Zhang, W.; Zheng, B.; Hu, P.; Zeng, Z.; Das, S.; Li, Y., et al. Dibenzoheptazethrene isomers with different biradical characters: an exercise of Clar's aromatic sextet rule in singlet biradicaloids. *J. Am. Chem. Soc.* **2013**, *135*, 18229–18236.

[68] Konishi, A.; Hirao, Y.; Kurata, H.; Kubo, T.; Nakano, M.; Kamada, K. Anthenes: Model systems for understanding the edge state of graphene nanoribbons. *Pure Appl. Chem.* **2014**, *86*, 497–505.

[69] Bendikov, M.; Duong, H. M.; Starkey, K.; Houk, K.; Carter, E. A.; Wudl, F. Oligoacenes: theoretical prediction of open-shell singlet diradical ground states. *J. Am. Chem. Soc.* **2004**, *126*, 7416–7417.

[70] Intorp, S. N.; Hodecker, M.; Müller, M.; Tverskoy, O.; Rosenkranz, M.; Dmitrieva, E.; Popov, A. A.; Rominger, F.; Freudenberg, J.; Dreuw, A., et al. Quinoidal azaacenes: 99% diradical character. *Angew. Chem. Int. Ed.* **2020**, *132*, 12496–12501.

[71] Zeng, Z.; Wu, J. Stable π-Extended p-Quinodimethanes: Synthesis and Tunable Ground States. *Chem. Rec.* **2015**, *15*, 322–328.

[72] Shimizu, A.; Kishi, R.; Nakano, M.; Shiomi, D.; Sato, K.; Takui, T.; Hisaki, I.; Miyata, M.; Tobe, Y. Indeno [2, 1-b] fluorene: A 20-π-Electron Hydrocarbon with Very Low-Energy Light Absorption. *Angew. Chem. Int. Ed.* **2013**, *125*, 6192–6195.

[73] Barker, J. E.; Dressler, J. J.; Cárdenas Valdivia, A.; Kishi, R.; Strand, E. T.; Zakharov, L. N.; MacMillan, S. N.; Gómez-García, C. J.; Nakano, M.; Casado, J., et al. Molecule isomerism modulates the diradical properties of stable singlet diradicaloids. *J. Am. Chem. Soc.* **2019**, *142*, 1548–1555.

[74] Doehnert, D.; Koutecky, J. Occupation numbers of natural orbitals as a criterion for biradical character. Different kinds of biradicals. *J. Am. Chem. Soc.* **1980**, *102*, 1789–1796.

[75] Head-Gordon, M. Characterizing unpaired electrons from the one-particle density matrix. *Chem. Phys. Lett.* **2003**, *372*, 508–511.

[76] Bachler, V.; Olbrich, G.; Neese, F.; Wieghardt, K. Theoretical evidence for the singlet diradical character of square planar nickel complexes containing two o-semiquinonato type ligands. *Inorg. Chem.* **2002**, *41*, 4179–4193.

[77] Stuyver, T.; Chen, B.; Zeng, T.; Geerlings, P.; De Proft, F.; Hoffmann, R. Do diradicals behave like radicals? *Chem. Rev.* **2019**, *119*, 11291–11351.

[78] Sun, Z.; Ye, Q.; Chi, C.; Wu, J. Low band gap polycyclic hydrocarbons: from closed-shell near infrared dyes and semiconductors to open-shell radicals. *Chem. Soc. Rev.* **2012**, *41*, 7857–7889.

[79] Ni, Y.; Gopalakrishna, T. Y.; Phan, H.; Herng, T. S.; Wu, S.; Han, Y.; Ding, J.; Wu, J. A Peri-tetracene Diradicaloid: Synthesis and Properties. *Angew. Chem. Int. Ed.* **2018**, *130*, 9845–9849.

[80] Konishi, A.; Kubo, T. Benzenoid quinodimethanes. *Physical Organic Chemistry of Quinodimethanes* **2017**, 69–105.

[81] Yang, K.; Zhang, X.; Harbuzaru, A.; Wang, L.; Wang, Y.; Koh, C.; Guo, H.; Shi, Y.; Chen, J.; Sun, H., et al. Stable organic diradicals based on fused quinoidal oligothiophene imides with high electrical conductivity. *J. Am. Chem. Soc.* **2020**, *142*, 4329–4340.

[82] Stuyver, T.; Zeng, T.; Tsuji, Y.; Geerlings, P.; De Proft, F. Diradical character as a guiding principle for the insightful design of molecular nanowires with an increasing conductance with length. *Nano Lett.* **2018**, *18*, 7298–7304.

[83] Pilevarshahri, R.; Rungger, I.; Archer, T.; Sanvito, S.; Shahtahmassebi, N. Spin transport in higher n-acene molecules. *Phys. Rev. B* **2011**, *84*, 174437.

[84] Kim, Y.; Kim, Y.-J.; Kim, Y.-A.; Jung, E.; Mok, Y.; Kim, K.; Hwang, H.; Park, J.-J.; Kim, M.-G.; Mathur, S., et al. Open-Shell and Closed-Shell Quinoid–Aromatic Conjugated Polymers: Unusual Spin Magnetic and High Charge Transport Properties. *ACS Appl. Mater. Interfaces* **2021**, *13*, 2887–2898.

[85] Hohenberg, P.; Kohn, W. Inhomogeneous electron gas. *Phys. Rev.* **1964**, *136*, B864.

[86] Kohn, W.; Sham, L. J. Self-consistent equations including exchange and correlation effects. *Phys. Rev.* **1965**, *140*, A1133.

[87] Von Barth, U.; Hedin, L. A local exchange-correlation potential for the spin polarized case. i. *J. Phys. C: Solid State Phys.* **1972**, *5*, 1629.

[88] Langreth, D. C.; Mehl, M. Beyond the local-density approximation in calculations of ground-state electronic properties. *Phys. Rev. B* **1983**, *28*, 1809.

[89] Perdew, J. P. Accurate density functional for the energy: Real-space cutoff of the gradient expansion for the exchange hole. *Phys. Rev. Lett.* **1985**, *55*, 1665.

[90] Tolba, S. A.; Gameel, K. M.; Ali, B. A.; Almossalami, H. A.; Allam, N. K. The DFT+ U: Approaches, accuracy, and applications. *Density Functional Calculations-Recent Progresses of Theory and Application* **2018**, *1*, 5772.

[91] Dudarev, S. L.; Botton, G. A.; Savrasov, S. Y.; Humphreys, C.; Sutton, A. P. Electron-energy-loss spectra and the structural stability of nickel oxide: An LSDA+ U study. *Phys. Rev. B* **1998**, *57*, 1505.

[92] Heyd, J.; Scuseria, G. E.; Ernzerhof, M. Hybrid functionals based on a screened Coulomb potential. *J. Chem. Phys.* **2003**, *118*, 8207–8215.

[93] Noodleman, L. Valence bond description of antiferromagnetic coupling in transition metal dimers. *J. Chem. Phys.* **1981**, *74*, 5737–5743.

[94] Noodleman, L.; Davidson, E. R. Ligand spin polarization and antiferromagnetic coupling in transition metal dimers. *Chem. Phys.* **1986**, *109*, 131–143.

[95] Ruiz, E.; Cano, J.; Alvarez, S.; Alemany, P. Broken symmetry approach to calculation of exchange coupling constants for homobinuclear and heterobinuclear transition metal complexes. *J. Comput. Chem.* **1999**, *20*, 1391–1400.

[96] Caballol, R.; Castell, O.; Illas, F.; de PR Moreira, I.; Malrieu, J. Remarks on the proper use of the broken symmetry approach to magnetic coupling. *J. Phys. Chem. A* **1997**, *101*, 7860–7866.

[97] Martin, R. L.; Illas, F. Antiferromagnetic exchange interactions from hybrid density functional theory. *Phys. Rev. Lett.* **1997**, *79*, 1539.

[98] Nishino, M.; Yamanaka, S.; Yoshioka, Y.; Yamaguchi, K. Theoretical approaches to direct exchange couplings between divalent chromium ions in naked dimers, tetramers, and clusters. *J. Phys. Chem. A* **1997**, *101*, 705–712.

[99] Kaduk, B.; Kowalczyk, T.; Van Voorhis, T. Constrained density functional theory. *Chem. Rev.* **2012**, *112*, 321–370.

[100] Dederichs, P.; Blügel, S.; Zeller, R.; Akai, H. Ground states of constrained systems: Application to cerium impurities. *Phys. Rev. Lett.* **1984**, *53*, 2512.

[101] Rudra, I.; Wu, Q.; Van Voorhis, T. Accurate magnetic exchange couplings in transition-metal complexes from constrained density-functional theory. *J. Chem. Phys.* **2006**, *124*, 024103.

[102] Ali, M. E.; Staemmler, V.; Marx, D. Magnetostructural dynamics of rieske versus ferredoxin iron–sulfur cofactors. *Phys. Chem. Chem. Phys.* **2015**, *17*, 6289–6296.

[103] Olsen, J. The CASSCF method: A perspective and commentary. *Int. J. Quantum Chem.* **2011**, *111*, 3267–3272.

[104] Roos, B. O.; Taylor, P. R.; Sigbahn, P. E. A complete active space SCF method (CASSCF) using a density matrix formulated super-CI approach. *Chem. Phys.* **1980**, *48*, 157–173.

[105] Andersson, K.; Malmqvist, P.-Å.; Roos, B. O. Second-order perturbation theory with a complete active space self-consistent field reference function. *J. Chem. Phys.* **1992**, *96*, 1218–1226.

[106] Angeli, C.; Cimiraglia, R.; Evangelisti, S.; Leininger, T.; Malrieu, J.-P. Introduction of n-electron valence states for multireference perturbation theory. *J. Chem. Phys.* **2001**, *114*, 10252–10264.

[107] Keller, S.; Boguslawski, K.; Janowski, T.; Reiher, M.; Pulay, P. Selection of active spaces for multiconfigurational wavefunctions. *J. Chem. Phys.* **2015**, *142*, 244104.

[108] Suaud, N.; Ruamps, R.; Guihéry, N.; Malrieu, J.-P. A strategy to determine appropriate active orbitals and accurate magnetic couplings in organic magnetic systems. *J. Chem. Theory Comput.* **2012**, *8*, 4127–4137.

[109] Maassen, J.; Harb, M.; Michaud-Rioux, V.; Zhu, Y.; Guo, H. Quantum transport modeling from first principles. *Proceedings of the IEEE* **2012**, *101*, 518–530.

[110] Taylor, J.; Guo, H.; Wang, J. Ab initio modeling of quantum transport properties of molecular electronic devices. *Phys. Rev. B* **2001**, *63*, 245407.

[111] Rego, L.; Rocha, A.; Rodrigues, V.; Ugarte, D. Role of structural evolution in the quantum conductance behavior of gold nanowires during stretching. *Phys. Rev. B* **2003**, *67*, 045412.

[112] Emberly, E. G.; Kirczenow, G. Theoretical study of electrical conduction through a molecule connected to metallic nanocontacts. *Phys. Rev. B* **1998**, *58*, 10911.

[113] Büttiker, M.; Imry, Y.; Landauer, R.; Pinhas, S. Generalized many-channel conductance formula with application to small rings. *Phys. Rev. B* **1985**, *31*, 6207.

[114] Soler, J. M.; Artacho, E.; Gale, J. D.; García, A.; Junquera, J.; Ordejón, P.; Sánchez-Portal, D. The SIESTA method for ab initio order-N materials simulation. *J. Phys.: Condens. Matter* **2002**, *14*, 2745.

[115] Troullier, N.; Martins, J. L. Efficient pseudopotentials for plane-wave calculations. *Phys. Rev. B* **1991**, *43*, 1993.

[116] Stokbro, K.; Taylor, J.; Brandbyge, M.; Ordejon, P. TranSIESTA: a spice for molecular electronics. *Ann. N.Y. Acad. Sci.* **2003**, *1006*, 212–226.

[117] Brandbyge, M.; Mozos, J.-L.; Ordejón, P.; Taylor, J.; Stokbro, K. Density-functional method for nonequilibrium electron transport. *Phys. Rev. B* **2002**, *65*, 165401.

[118] Verzijl, C.; Seldenthuis, J.; Thijssen, J. Applicability of the wide-band limit in DFT-based molecular transport calculations. *J. Chem. Phys.* **2013**, *138*, 094102.

[119] Herrmann, C.; Solomon, G. C.; Subotnik, J. E.; Mujica, V.; Ratner, M. A. Ghost transmission: How large basis sets can make electron transport calculations worse. *J. Chem. Phys.* **2010**, *132*, 024103.

[120] Lee, H.-J.; Cui, H.-B.; Fujiwara, H.; Kobayashi, H.; Fujiwara, E.; Kobayashi, A. Development of new magnetic organic conductors based on donor molecules with stable organic radical part. Journal de Physique IV (Proceedings). 2004; pp 533–535.

[121] Lahti, P. M. *Adv Phys Org Chem*; Elsevier, 2011; Vol. 45; pp 93–169.

[122] Wolf, S.; Awschalom, D.; Buhrman, R.; Daughton, J.; Von Molnar, S.; Roukes, M.; Chtchelkanova, A. Y.; Treger, D. Spintronics: a spin-based electronics vision for the future. *Science* **2001**, *294*, 1488–1495.

[123] Powell, B.; McKenzie, R. H. Dependence of the superconducting transition temperature of organic molecular crystals on intrinsically nonmagnetic disorder: A signature of either unconventional superconductivity or the atypical formation of magnetic moments. *Phys. Rev. B* **2004**, *69*, 024519.

[124] Ratera, I.; Veciana, J. Playing with organic radicals as building blocks for functional molecular materials. *Chem. Soc. Rev.* **2012**, *41*, 303–349.

[125] Casu, M. B. Nanoscale studies of organic radicals: Surface, interface, and spinterface. *Acc. Chem. Res.* **2018**, *51*, 753–760.

[126] Gilroy, J. B.; McKinnon, S. D.; Kennepohl, P.; Zsombor, M. S.; Ferguson, M. J.; Thompson, L. K.; Hicks, R. G. Probing electronic communication in stable benzene-bridged verdazyl diradicals. *J. Org. Chem.* **2007**, *72*, 8062–8069.

[127] Rajca, A.; Shiraishi, K.; Rajca, S. Stable diarylnitroxide diradical with triplet ground state. *Chem. Commun.* **2009**, 4372–4374.

[128] Rudebusch, G. E.; Zafra, J. L.; Jorner, K.; Fukuda, K.; Marshall, J. L.; Arrechea-Marcos, I.; Espejo, G. L.; Ortiz, R. P.; Gómez-García, C. J.; Zakharov, L. N., et al. Diindeno-fusion of an anthracene as a design strategy for stable organic biradicals. *Nat. Chem.* **2016**, *8*, 753.

[129] Gallagher, N. M.; Bauer, J. J.; Pink, M.; Rajca, S.; Rajca, A. High-spin organic diradical with robust stability. *J. Am. Chem. Soc.* **2016**, *138*, 9377–9380.

[130] Gallagher, N.; Zhang, H.; Junghoefer, T.; Giangrisostomi, E.; Ovsyannikov, R.; Pink, M.; Rajca, S.; Casu, M. B.; Rajca, A. Thermally and magnetically robust triplet ground state diradical. *J. Am. Chem. Soc.* **2019**, *141*, 4764–4774.

[131] Blatter, H. M.; Lukaszewski, H. A new stable free radical. *Tetrahedron Lett.* **1968**, *9*, 2701–2705.

[132] Constantinides, C. P.; Koutentis, P. A.; Krassos, H.; Rawson, J. M.; Tasiopoulos, A. J. Characterization and magnetic properties of a "Super Stable" radical 1, 3-Diphenyl-7-trifluoromethyl-1, 4-dihydro-1, 2, 4-benzotriazin-4-yl. *J. Org. Chem.* **2011**, *76*, 2798–2806.

[133] Morgan, I. S.; Mansikkamäki, A.; Zissimou, G. A.; Koutentis, P. A.; Rouzières, M.; Clérac, R.; Tuononen, H. M. Coordination complexes of a neutral 1, 2, 4-benzotriazinyl radical ligand: Synthesis, molecular and electronic structures, and magnetic properties. *Chem. Eur. J.* **2015**, *21*, 15843–15853.

[134] Berezin, A. A.; Constantinides, C. P.; Mirallai, S. I.; Manoli, M.; Cao, L. L.; Rawson, J. M.; Koutentis, P. A. Synthesis and properties of imidazolo-fused benzotriazinyl radicals. *Org. Biomol. Chem.* **2013**, *11*, 6780–6795.

[135] Kawakami, T.; Saito, T.; Sharma, S.; Yamanaka, S.; Yamada, S.; Nakajima, T.; Okumura, M.; Yamaguchi, K. Full-valence density matrix renormalisation group calculations on meta-benzyne based on unrestricted natural orbitals. Revisit of seamless continuation from broken-symmetry to symmetry-adapted models for diradicals. *Mol. Phys.* **2017**, *115*, 2267–2284.

[136] Calzado, C. J.; Angeli, C.; de Graaf, C.; Caballol, R. Analysis of the magnetic coupling in nitroxide organic biradicals. *Theor. Chem. Acc.* **2011**, *128*, 505–519.

[137] Becke, A. D. Density-functional thermochemistry. III. The role of exact exchange. *J. Chem. Phys.* **1993**, *98*, 5648–5652.

[138] Weigend, F.; Ahlrichs, R. Balanced basis sets of split valence, triple zeta valence and quadruple zeta valence quality for H to Rn: Design and assessment of accuracy. *Phys. Chem. Chem. Phys.* **2005**, *7*, 3297–3305.

[139] Neese, F.; Wennmohs, F.; Hansen, A.; Becker, U. Efficient, approximate and parallel Hartree–Fock and hybrid DFT calculations. A 'chain-of-spheres' algorithm for the Hartree–Fock exchange. *Chem. Phys.* **2009**, *356*, 98–109.

[140] Mori-Sánchez, P.; Cohen, A. J.; Yang, W. Many-electron self-interaction error in approximate density functionals. *J. Chem. Phys.* **2006**, *125*, 201102.

[141] Bao, J. L.; Gagliardi, L.; Truhlar, D. G. Self-interaction error in density functional theory: An appraisal. *J. Phys. Chem. Lett.* **2018**, *9*, 2353–2358.

[142] Neese, F. The ORCA program system. *Wiley Interdiscip. Rev. Comput. Mol. Sci.* **2012**, *2*, 73–78.

[143] Valiev, M.; Bylaska, E. J.; Govind, N.; Kowalski, K.; Straatsma, T. P.; Van Dam, H. J.; Wang, D.; Nieplocha, J.; Apra, E.; Windus, T. L., et al. NWChem: a comprehensive and scalable open-source solution for large scale molecular simulations. *Comput. Phys. Commun.* **2010**, *181*, 1477–1489.

[144] Angeli, C.; Calzado, C. J. The role of the magnetic orbitals in the calculation of the magnetic coupling constants from multireference perturbation theory methods. *J. Chem. Phys.* **2012**, *137*, 034104.

[145] Pulay, P.; Hamilton, T. P. UHF natural orbitals for defining and starting MC-SCF calculations. *J. Chem. Phys.* **1988**, *88*, 4926–4933.

[146] Kaszyński, P.; Constantinides, C. P.; Young Jr, V. G. The Planar Blatter Radical: Structural Chemistry of 1, 4-Dihydrobenzo [e][1, 2, 4] triazin-4-yls. *Angew. Chem.* **2016**, *128*, 11315–11318.

[147] Bartos, P.; Anand, B.; Pietrzak, A.; Kaszynski, P. Functional Planar Blatter Radical through Pschorr-Type Cyclization. *Org. Lett.* **2019**, *22*, 180–184.

[148] David, G.; Guihery, N.; Ferre, N. What are the physical contents of Hubbard and Heisenberg Hamiltonian interactions extracted from broken symmetry DFT calculations in magnetic compounds? *J. Chem. Theory Comput.* **2017**, *13*, 6253–6265.

[149] Calzado, C. J.; Cabrero, J.; Malrieu, J. P.; Caballol, R. Analysis of the magnetic coupling in binuclear complexes. I. Physics of the coupling. *J. Chem. Phys.* **2002**, *116*, 2728–2747.

[150] Schmidt, J.; Shenvi, N.; Tully, J. C. Controlling spin contamination using constrained density functional theory. *J. Chem. Phys.* **2008**, *129*, 114110.

[151] Okumura, M.; Yamaguchi, K.; Awaga, K. Ferromagnetic intermolecular interaction of the cation radical ofm-N-methylpyridinium nitronyl nitroxide. A CASSCF study. *Chem. Phys. Lett.* **1994**, *228*, 575–582.

[152] Ali, M. E.; Datta, S. N. Broken-symmetry density functional theory investigation on bis-nitronyl nitroxide diradicals: influence of length and aromaticity of couplers. *J. Phys. Chem. A* **2006**, *110*, 2776–2784.

[153] Hirose, K.; Kobayashi, N. *Quantum transport calculations for nanosystems*; Jenny Stanford Publishing, 2014.

[154] Rocha, A. R.; Garcia-Suarez, V. M.; Bailey, S. W.; Lambert, C. J.; Ferrer, J.; Sanvito, S. Towards molecular spintronics. *Nat. Mater.* **2005**, *4*, 335–339.

[155] Pramanik, S.; Stefanita, C.-G.; Patibandla, S.; Bandyopadhyay, S.; Garre, K.; Harth, N.; Cahay, M. Observation of extremely long spin relaxation times in an organic nanowire spin valve. *Nat. Nanotechnol.* **2007**, *2*, 216.

[156] Lach, S.; Altenhof, A.; Tarafder, K.; Schmitt, F.; Ali, M. E.; Vogel, M.; Sauther, J.; Oppeneer, P. M.; Ziegler, C. Metal–organic hybrid interface states of a ferromagnet/organic semiconductor hybrid junction as basis for engineering spin injection in organic spintronics. *Adv. Funct. Mater* **2012**, *22*, 989–997.

[157] Su, T. A.; Neupane, M.; Steigerwald, M. L.; Venkataraman, L.; Nuckolls, C. Chemical principles of single-molecule electronics. *Nat. Rev. Mater.* **2016**, *1*, 16002.

[158] Li, X.; Tan, Z.; Huang, X.; Bai, J.; Liu, J.; Hong, W. Experimental investigation of quantum interference in the charge transport through molecular architectures. *J. Mater. Chem. C* **2019**, *7*, 12790–12808.

[159] Hansen, T.; Solomon, G. C.; Andrews, D. Q.; Ratner, M. A. Interfering pathways in benzene: An analytical treatment. *J. Chem. Phys* **2009**, *131*, 194704.

[160] Arroyo, C. R.; Tarkuc, S.; Frisenda, R.; Seldenthuis, J. S.; Woerde, C. H.; Eelkema, R.; Grozema, F. C.; Van Der Zant, H. S. Signatures of quantum interference effects on charge transport through a single benzene ring. *Angew. Chem* **2013**, *52*, 3152–3155.

[161] Markussen, T.; Stadler, R.; Thygesen, K. S. The relation between structure and quantum interference in single molecule junctions. *Nano Lett.* **2010**, *10*, 4260–4265.

[162] Berritta, M.; Manrique, D. Z.; Lambert, C. J. Interplay between quantum interference and conformational fluctuations in single-molecule break junctions. *Nanoscale* **2015**, *7*, 1096–1101.

[163] Valli, A.; Amaricci, A.; Brosco, V.; Capone, M. Quantum interference assisted spin filtering in graphene nanoflakes. *Nano Lett.* **2018**, *18*, 2158–2164.

[164] Valli, A.; Amaricci, A.; Brosco, V.; Capone, M. Interplay between destructive quantum interference and symmetry-breaking phenomena in graphene quantum junctions. *Phys. Rev. B* **2019**, *100*, 075118.

[165] Bergfield, J. P.; Solomon, G. C.; Stafford, C. A.; Ratner, M. A. Novel quantum interference effects in transport through molecular radicals. *Nano Lett.* **2011**, *11*, 2759–2764.

[166] Saraiva-Souza, A.; Smeu, M.; Zhang, L.; Souza Filho, A. G.; Guo, H.; Ratner, M. A. Molecular spintronics: Destructive quantum interference controlled by a gate. *J. Am. Chem. Soc.* **2014**, *136*, 15065–15071.

[167] Paulsson, M.; Brandbyge, M. Transmission eigenchannels from nonequilibrium Green's functions. *Phys. Rev. B* **2007**, *76*, 115117.

[168] Toher, C.; Filippetti, A.; Sanvito, S.; Burke, K. Self-interaction errors in density-functional calculations of electronic transport. *Phys. Rev. Lett.* **2005**, *95*, 146402.

[169] Kim, W. Y.; Choi, Y. C.; Min, S. K.; Cho, Y.; Kim, K. S. Application of quantum chemistry to nanotechnology: electron and spin transport in molecular devices. *Chem. Soc. Rev* **2009**, *38*, 2319–2333.

[170] Deffner, M.; Gross, L.; Steenbock, T.; Voigt, B.; Solomon, G.; Herrmann, C. Artaios—a code for postprocessing quantum chemical electronic structure calculations. 2010.

[171] Larade, B.; Taylor, J.; Zheng, Q.; Mehrez, H.; Pomorski, P.; Guo, H. Renormalized molecular levels in a $Sc_3N@C_{80}$ molecular electronic device. *Phys. Rev. B* **2001**, *64*, 195402.

[172] Stokbro, K.; Taylor, J.; Brandbyge, M.; Mozos, J.-L.; Ordejon, P. Theoretical study of the nonlinear conductance of Di-thiol benzene coupled to Au (1 1 1) surfaces via thiol and thiolate bonds. *Comput. Mater. Sci* **2003**, *27*, 151–160.

[173] Yoshizawa, K. An orbital rule for electron transport in molecules. *Acc. Chem. Res* **2012**, *45*, 1612–1621.

[174] Yoshizawa, K.; Tada, T.; Staykov, A. Orbital views of the electron transport in molecular devices. *J. Am. Chem. Soc* **2008**, *130*, 9406–9413.

[175] Ke, G.; Duan, C.; Huang, F.; Guo, X. Electrical and spin switches in single-molecule junctions. *InfoMat* **2020**, *2*, 92–112.

[176] Huang, X.; Li, T. Recent progress in the development of molecular-scale electronics based on photoswitchable molecules. *J. Mater. Chem. C* **2020**, *8*, 821–848.

[177] Roldan, D.; Kaliginedi, V.; Cobo, S.; Kolivoska, V.; Bucher, C.; Hong, W.; Royal, G.; Wandlowski, T. Charge transport in photoswitchable dimethyldihydropyrene-type single-molecule junctions. *J. Am. Chem. Soc.* **2013**, *135*, 5974–5977.

[178] Jia, C.; Migliore, A.; Xin, N.; Huang, S.; Wang, J.; Yang, Q.; Wang, S.; Chen, H.; Wang, D.; Feng, B., et al. Covalently bonded single-molecule junctions with stable and reversible photoswitched conductivity. *Science* **2016**, *352*, 1443–1445.

[179] Han, X.; Mi, W.; Wang, D. Tunneling magnetoresistance and light modulation in $Fe_4N(La_{2/3}Sr_{1/3}MnO_3)/C_{60}/Fe_4N$ single molecule magnetic tunnel junctions. *J. Mater. Chem. C* **2020**, *8*, 3137–3146.

[180] Reddy, A. R.; Bendikov, M. Diels–Alder reaction of acenes with singlet and triplet oxygen–theoretical study of two-state reactivity. *Chem. Commun.* **2006**, 1179–1181.

[181] Bauch, M.; Klaper, M.; Linker, T. Intermediates in the cleavage of endoperoxides. *J. Phys. Org. Chem.* **2017**, *30*, e3607.

[182] Slezáková, S.; Ruda-Kucerova, J. Anticancer activity of artemisinin and its derivatives. *Anticancer Res.* **2017**, *37*, 5995–6003.

[183] Geroldinger, G.; Tonner, M.; Fudickar, W.; De Sarkar, S.; Dighal, A.; Monzote, L.; Staniek, K.; Linker, T.; Chatterjee, M.; Gille, L. Activation of anthracene Endoperoxides in Leishmania and impairment of mitochondrial functions. *Molecules* **2018**, *23*, 1680.

[184] Sharma, S.; Ali, E. Non-reductive Homolytic Scission of Endoperoxide Bond for Activation of Artemisinin: A Parallel Mechanism to Heterolytic Cleavage. *J. Phys. Org. Chem.* **2022**, DOI: https://doi.org/10.1002/poc.4392.

[185] Datta, S. Nanoscale device modeling: the Green's function method. *Superlattices Microstruct* **2000**, *28*, 253–278.

[186] Pastawski, H. M. Classical and quantum transport from generalized Landauer-Büttiker equations. *Phys. Rev. B* **1991**, *44*, 6329.

[187] Eisenthal, K.; Turro, N.; Dupuy, C.; Hrovat, D.; Langan, J.; Jenny, T.; Sitzmann, E. State-selective photochemistry of singlet oxygen precursors: kinetics and wavelength dependence of the photodissociation of anthracene endoperoxides. *J. Phys. Chem.* **1986**, *90*, 5168–5173.

[188] Schmidt, R.; Schaffner, K.; Trost, W.; Brauer, H. Wavelength-dependent and dual photochemistry of the endoperoxides of anthracene and 9, 10-dimethylanthracene. *J. Phys. Chem.* **1984**, *88*, 956–958.

[189] Martínez-Fernández, L.; González-Vázquez, J.; González, L.; Corral, I. Time-resolved insight into the photosensitized generation of singlet oxygen in endoperoxides. *J. Chem. Theory Comput.* **2015**, *11*, 406–414.

[190] Mollenhauer, D.; Corral, I.; González, L. Four Plus Four State Degeneracies in the O- O Photolysis of Aromatic Endoperoxides. *J. Phys. Chem. Lett.* **2010**, *1*, 1036–1040.

[191] Gruber, M.; Ibrahim, F.; Boukari, S.; Joly, L.; Da Costa, V.; Studniarek, M.; Peter, M.; Isshiki, H.; Jabbar, H.; Davesne, V., et al. Spin-dependent hybridization between molecule and metal at room temperature through interlayer exchange coupling. *Nano Lett.* **2015**, *15*, 7921–7926.

[192] Qiu, S.; Miao, Y.-Y.; Zhang, G.-P.; Ren, J.-F.; Wang, C.-K.; Hu, G.-C. Manipulating current spin polarization in magnetic single-molecule junctions via destructive quantum interference. *J. Phys. Chem. C* **2020**, *124*, 12144–12152.

[193] Solomon, G. C.; Andrews, D. Q.; Hansen, T.; Goldsmith, R. H.; Wasielewski, M. R.; Van Duyne, R. P.; Ratner, M. A. Understanding quantum interference in coherent molecular conduction. *J. Chem. Phys.* **2008**, *129*, 054701.

[194] Huang, B.; Liu, X.; Yuan, Y.; Hong, Z.-W.; Zheng, J.-F.; Pei, L.-Q.; Shao, Y.; Li, J.-F.; Zhou, X.-S.; Chen, J.-Z., et al. Controlling and observing sharp-valleyed quantum interference effect in single molecular junctions. *J. Am. Chem. Soc.* **2018**, *140*, 17685–17690.

[195] Alqahtani, J.; Sadeghi, H.; Sangtarash, S.; Lambert, C. J. Breakdown of curly arrow rules in anthraquinone. *Angew. Chem. Int. Ed.* **2018**, *57*, 15065–15069.

[196] Pedersen, K. G.; Borges, A.; Hedegard, P.; Solomon, G. C.; Strange, M. Illusory connection between cross-conjugation and quantum interference. *J. Phys. Chem. C* **2015**, *119*, 26919–26924.

[197] Valkenier, H.; Guédon, C. M.; Markussen, T.; Thygesen, K. S.; van der Molen, S. J.; Hummelen, J. C. Cross-conjugation and quantum interference: a general correlation? *Phys. Chem. Chem. Phys.* **2014**, *16*, 653–662.

[198] Kiguchi, M.; Nakamura, H.; Takahashi, Y.; Takahashi, T.; Ohto, T. Effect of anchoring group position on formation and conductance of a single disubstituted benzene molecule bridging Au electrodes: change of conductive molecular orbital and electron pathway. *J. Phys. Chem. C* **2010**, *114*, 22254–22261.

[199] Gantenbein, M.; Wang, L.; Al-Jobory, A. A.; Ismael, A. K.; Lambert, C. J.; Hong, W.; Bryce, M. R. Quantum interference and heteroaromaticity of para- and meta-linked bridged biphenyl units in single molecular conductance measurements. *Sci. Rep.* **2017**, *7*, 1–9.

[200] Zhang, Y.-P.; Chen, L.-C.; Zhang, Z.-Q.; Cao, J.-J.; Tang, C.; Liu, J.; Duan, L.-L.; Huo, Y.; Shao, X.; Hong, W., et al. Distinguishing diketopyrrolopyrrole isomers in single-molecule junctions via reversible stimuli-responsive quantum interference. *J. Am. Chem. Soc.* **2018**, *140*, 6531–6535.

[201] Darwish, N.; Díez-Pérez, I.; Da Silva, P.; Tao, N.; Gooding, J. J.; Paddon-Row, M. N. Observation of electrochemically controlled quantum interference in a single anthraquinone-based norbornylogous bridge molecule. *Angew. Chem. Int. Ed.* **2012**, *51*, 3203–3206.

[202] Li, X.; Tan, Z.; Huang, X.; Bai, J.; Liu, J.; Hong, W. Experimental investigation of quantum interference in charge transport through molecular architectures. *J. Mater. Chem. C* **2019**, *7*, 12790–12808.

[203] Heerema, S. J.; Dekker, C. Graphene nanodevices for DNA sequencing. *Nat. Nanotechnol.* **2016**, *11*, 127–136.

[204] Im, J.; Biswas, S.; Liu, H.; Zhao, Y.; Sen, S.; Biswas, S.; Ashcroft, B.; Borges, C.; Wang, X.; Lindsay, S., et al. Electronic single-molecule identification of carbohydrate isomers by recognition tunnelling. *Nat. Commun.* **2016**, *7*, 1–7.

[205] Gopalakrishna, T. Y.; Zeng, W.; Lu, X.; Wu, J. From open-shell singlet diradicaloids to polyradicaloids. *Chem. Commun.* **2018**, *54*, 2186–2199.

[206] Nakano, M.; Kishi, R.; Nitta, T.; Kubo, T.; Nakasuji, K.; Kamada, K.; Ohta, K.; Champagne, B.; Botek, E.; Yamaguchi, K. Second hyperpolarizability (γ) of singlet diradical system: dependence of γ on the diradical character. *J. Phys. Chem. A* **2005**, *109*, 885–891.

[207] Dong, S.; Herng, T. S.; Gopalakrishna, T. Y.; Phan, H.; Lim, Z. L.; Hu, P.; Webster, R. D.; Ding, J.; Chi, C. Extended bis (benzothia) quinodimethanes and their dications: from singlet diradicaloids to isoelectronic structures of long acenes. *Angew. Chem. Int. Ed.* **2016**, *55*, 9316–9320.

[208] Zeng, W.; Qi, Q.; Wu, J. Toward long rylene ribbons and quinoidal rylene diradicaloids. *Eur. J. Org. Chem.* **2018**, *2018*, 7–17.

[209] Tao, N. J. *Nanoscience And Technology: A Collection of Reviews from Nature Journals*; World Scientific, 2010.

[210] Weiss, E. A.; Ahrens, M. J.; Sinks, L. E.; Gusev, A. V.; Ratner, M. A.; Wasielewski, M. R. Making a molecular wire: charge and spin transport through para-phenylene oligomers. *J. Am. Chem. Soc.* **2004**, *126*, 5577–5584.

[211] Lee, H. J.; Cho, S. J.; Kang, H.; He, X.; Yoon, H. J. Achieving Ultralow, Zero, and Inverted Tunneling Attenuation Coefficients in Molecular Wires with Extended Conjugation. *Small* **2021**, *17*, 2005711.

[212] Gunasekaran, S.; Hernangómez-Pérez, D.; Davydenko, I.; Marder, S.; Evers, F.; Venkataraman, L. Near length-independent conductance in polymethine molecular wires. *Nano Lett.* **2018**, *18*, 6387–6391.

[213] Kuang, G.; Chen, S.-Z.; Wang, W.; Lin, T.; Chen, K.; Shang, X.; Liu, P. N.; Lin, N. Resonant charge transport in conjugated molecular wires beyond 10 nm range. *J. Am. Chem. Soc.* **2016**, *138*, 11140–11143.

[214] Tada, T.; Yoshizawa, K. Reverse exponential decay of electrical transmission in nanosized graphite sheets. *J. Phys. Chem. B* **2004**, *108*, 7565–7572.

[215] Li, Z.; Park, T.-H.; Rawson, J.; Therien, M. J.; Borguet, E. Quasi-ohmic single molecule charge transport through highly conjugated meso-to-meso ethyne-bridged porphyrin wires. *Nano Lett.* **2012**, *12*, 2722–2727.

[216] Sedghi, G.; García-Suárez, V. M.; Esdaile, L. J.; Anderson, H. L.; Lambert, C. J.; Martín, S.; Bethell, D.; Higgins, S. J.; Elliott, M.; Bennett, N.; et al., Long-range electron tunnelling in oligo-porphyrin molecular wires. *Nat. Nanotechnol.* **2011**, *6*, 517–523.

[217] Leary, E.; Limburg, B.; Alanazy, A.; Sangtarash, S.; Grace, I.; Swada, K.; Esdaile, L. J.; Noori, M.; González, M. T.; Rubio-Bollinger, G.; et al., Bias-driven conductance increase with length in porphyrin tapes. *J. Am. Chem. Soc.* **2018**, *140*, 12877–12883.

[218] Ramos-Berdullas, N.; Mandado, M. Electronic Properties of p-Xylylene and p-Phenylene Chains Subjected to Finite Bias Voltages: A New Highly Conducting Oligophenyl Structure. *Chem. Eur. J.* **2013**, *19*, 3646–3654.

[219] Gil-Guerrero, S.; Ramos-Berdullas, N.; Mandado, M. Can aromaticity enhance the electron transport in molecular wires? *Org. Electron.* **2018**, *61*, 177–184.

[220] Stuyver, T.; Fias, S.; De Proft, F.; Geerlings, P.; Tsuji, Y.; Hoffmann, R. Enhancing the conductivity of molecular electronic devices. *J. Chem. Phys.* **2017**, *146*, 092310.

[221] Stuyver, T.; Zeng, T.; Tsuji, Y.; Geerlings, P.; De Proft, F. Diradical character as a guiding principle for the insightful design of molecular nanowires with an increasing conductance with length. *Nano Lett.* **2018**, *18*, 7298–7304.

[222] Gil-Guerrero, S.; Peña-Gallego, Á.; Ramos-Berdullas, N.; Martin Pendas, A.; Mandado, M. Assessing the reversed exponential decay of the electrical conductance in molecular wires: the undeniable effect of static electron correlation. *Nano Lett.* **2019**, *19*, 7394–7399.

[223] Ramos-Berdullas, N.; Gil-Guerrero, S.; Peña-Gallego, Á.; Mandado, M. The effect of spin polarization on the electron transport of molecular wires with diradical character. *Phys. Chem. Chem. Phys.* **2021**, *23*, 4777–4783.

[224] Houk, K.; Lee, P. S.; Nendel, M. Polyacene and cyclacene geometries and electronic structures: bond equalization, vanishing band gaps, and triplet ground states contrast with polyacetylene. *J. Org. Chem.* **2001**, *66*, 5517–5521.

[225] Dos Santos, M. Electronic properties of acenes: Oligomer to polymer structure. *Phys. Rev. B* **2006**, *74*, 045426.

[226] Visontai, D.; Grace, I.; Lambert, C. Electron transport through ribbonlike molecular wires calculated using density-functional theory and Green's function formalism. *Phys. Rev. B* **2010**, *81*, 035409.

[227] Kaliginedi, V.; Moreno-García, P.; Valkenier, H.; Hong, W.; García-Suárez, V. M.; Buiter, P.; Otten, J. L.; Hummelen, J. C.; Lambert, C. J.; Wandlowski, T. Correlations between molecular structure and single-junction conductance: a case study with oligo (phenylene-ethynylene)-type wires. *J. Am. Chem. Soc.* **2012**, *134*, 5262–5275.

[228] Valdiviezo, J.; Rocha, P.; Polakovsky, A.; Palma, J. L. Nonexponential Length Dependence of Molecular Conductance in Acene-Based Molecular Wires. *ACS sensors* **2021**, *6*, 477–484.

[229] Wang, C.; Batsanov, A. S.; Bryce, M. R.; Martin, S.; Nichols, R. J.; Higgins, S. J.; Garcia-Suarez, V. M.; Lambert, C. J. Oligoyne single molecule wires. *J. Am. Chem. Soc.* **2009**, *131*, 15647–15654.

[230] Jasper-Tönnies, T.; Garcia-Lekue, A.; Frederiksen, T.; Ulrich, S.; Herges, R.; Berndt, R. Conductance of a freestanding conjugated molecular wire. *Phys. Rev. Lett.* **2017**, *119*, 066801.

[231] Zang, Y.; Fu, T.; Zou, Q.; Ng, F.; Li, H.; Steigerwald, M. L.; Nuckolls, C.; Venkataraman, L. Cumulene wires display increasing conductance with increasing length. *Nano Lett.* **2020**, *20*, 8415–8419.

[232] Xu, W.; Leary, E.; Hou, S.; Sangtarash, S.; González, M. T.; Rubio-Bollinger, G.; Wu, Q.; Sadeghi, H.; Tejerina, L.; Christensen, K. E.; et al., Unusual Length Dependence of the Conductance in Cumulene Molecular Wires. *Angew. Chem. Int. Ed.* **2019**, *131*, 8466–8470.

[233] Wendinger, D.; Tykwinski, R. R. Odd [n] cumulenes (n= 3, 5, 7, 9): synthesis, characterization, and reactivity. *Acc. Chem. Res.* **2017**, *50*, 1468–1479.

[234] Januszewski, J. A.; Wendinger, D.; Methfessel, C. D.; Hampel, F.; Tykwinski, R. R. Synthesis and Structure of Tetraarylcumulenes: Characterization of Bond-Length Alternation versus Molecule Length. *Angew. Chem. Int. Ed.* **2013**, *52*, 1817–1821.

[235] Beck, A. D. Density-functional thermochemistry. III. The role of exact exchange. *J. Chem. Phys* **1993**, *98*, 5648–6.

[236] Stein, T.; Eisenberg, H.; Kronik, L.; Baer, R. Fundamental gaps in finite systems from eigenvalues of a generalized Kohn-Sham method. *Phys. Rev. Lett.* **2010**, *105*, 266802.

[237] Refaely-Abramson, S.; Baer, R.; Kronik, L. Fundamental and excitation gaps in molecules of relevance for organic photovoltaics from an optimally tuned range-separated hybrid functional. *Phys. Rev. B* **2011**, *84*, 075144.

[238] Yamada, A.; Feng, Q.; Hoskins, A.; Fenk, K. D.; Dunietz, B. D. Achieving predictive description of molecular conductance by using a range-separated hybrid functional. *Nano Lett.* **2016**, *16*, 6092–6098.

[239] Bhandari, S.; Yamada, A.; Hoskins, A.; Payne, J.; Aksu, H.; Dunietz, B. D. Achieving Predictive Description of Negative Differential Resistance in Molecular Junctions Using a Range-Separated Hybrid Functional. *Adv. Theory Simul.* **2021**, *4*, 2000016.

[240] Trinquier, G.; David, G.; Malrieu, J.-P. Qualitative views on the polyradical character of long acenes. *J. Phys. Chem. A* **2018**, *122*, 6926–6933.

[241] Khurana, R.; Bajaj, A.; Ali, M. E. Tuning the magnetic properties of a diamagnetic di-Blatter's zwitterion to antiferro-and ferromagnetically coupled diradicals. *Phys. Chem. Chem. Phys.* **2022**, *24*, 2543–2553.

[242] Kaur, P.; Ali, M. E. First principle investigations of long-range magnetic exchange interactions via polyacene couplers. *Int. J. Quantum Chem.* **2021**, *121*, e26756.

[243] Yamaguchi, K. The electronic structures of biradicals in the unrestricted Hartree-Fock approximation. *Chem. Phys. Lett.* **1975**, *33*, 330–335.

[244] Moth-Poulsen, K.; Bjørnholm, T. Molecular electronics with single molecules in solid-state devices. *Nat. Nanotechnol.* **2009**, *4*, 551–556.

[245] Aggarwal, A.; Kaliginedi, V.; Maiti, P. K. Quantum Circuit Rules for Molecular Electronic Systems: Where Are We Headed Based on the Current Understanding of Quantum Interference, Thermoelectric, and Molecular Spintronics Phenomena? *Nano Lett.* **2021**, *21*, 8532–8544.

[246] Soni, S.; Ye, G.; Zheng, J.; Zhang, Y.; Asyuda, A.; Zharnikov, M.; Hong, W.; Chiechi, R. C. Understanding the Role of Parallel Pathways via In-Situ Switching of Quantum Interference in Molecular Tunneling Junctions. *Angew. Chem. Int. Ed.* **2020**, *59*, 14308–14312.

[247] Wilhelm, J.; Del Ben, M.; Hutter, J. GW in the Gaussian and plane waves scheme with application to linear acenes. *J. Chem. Theory Comput* **2016**, *12*, 3623–3635.

[248] Garner, M. H.; Li, H.; Chen, Y.; Su, T. A.; Shangguan, Z.; Paley, D. W.; Liu, T.; Ng, F.; Li, H.; Xiao, S.; Nuckolls, C.; Venkataraman, L.; Solomon, G. C. Comprehensive suppression of single-molecule conductance using destructive σ-interference. *Nature* **2018**, *558*, 415–419.

[249] Tsuji, Y.; Okazawa, K.; Chen, B.; Yoshizawa, K. Mechanical Control of Molecular Conductance and Diradical Character in Bond Stretching and π-Stack Compression. *J. Phys. Chem. C* . **2020**, *124*, 22941–22958.

[250] Malrieu, J.-P.; Trinquier, G. Can a topological approach predict spin-symmetry breaking in conjugated hydrocarbons? *J. Phys. Chem. A* **2016**, *120*, 9564–9578.

[251] Veryazov, V.; Malmqvist, P. Å.; Roos, B. O. How to select active space for multiconfigurational quantum chemistry? *Int. J. Quantum Chem.* **2011**, *111*, 3329–3338.

[252] Ali, M. E.; Roy, A. S.; Datta, S. N. Molecular tailoring and prediction of strongly ferromagnetically coupled trimethylenemethane-based nitroxide diradicals. *J. Phys. Chem. A* **2007**, *111*, 5523–5527.

[253] Xiao, X.; Xu, B.; Tao, N. J. Measurement of single molecule conductance: Benzenedithiol and benzenedimethanethiol. *Nano Lett.* **2004**, *4*, 267–271.

[254] Kamiński, W.; Topolnicki, R.; Hapala, P.; Jelínek, P.; Kucharczyk, R. Tuning the conductance of benzene-based single-molecule junctions. *Org. Electron* **2016**, *34*, 254–261.

[255] Rodriguez-Gonzalez, S.; Xie, Z.; Galangau, O.; Selvanathan, P.; Norel, L.; Van Dyck, C.; Costuas, K.; Frisbie, C.; Rigaut, S.; Cornil, J. Homo level pinning in molecular junctions: Joint theoretical and experimental evidence. *J. Phys. Chem. Lett.* **2018**, *9*, 2394–2403.

[256] Solomon, G. C.; Herrmann, C.; Hansen, T.; Mujica, V.; Ratner, M. A. Exploring local currents in molecular junctions. *Nat. Chem.* **2010**, *2*, 223.

[257] Stuyver, T.; Blotwijk, N.; Fias, S.; Geerlings, P.; De Proft, F. Exploring Electrical Currents through Nanographenes: Visualization and Tuning of the through-Bond Transmission Paths. *ChemPhysChem* **2017**, *18*, 3012–3022.

[258] Neaton, J. B.; Hybertsen, M. S.; Louie, S. G. Renormalization of molecular electronic levels at metal-molecule interfaces. *Phys. Rev. Lett.* **2006**, *97*, 216405.

List of Publications

Publications included in thesis

- **Bajaj, A.**; Ali, Md. E. Anti-ohmic Nanoconductors: Myth, Reality and Promise. *ChemRxiv* **2022**, DOI:10.26434/chemrxiv-2021-bf1nx-v2.

- **Bajaj, A.**; Khurana, R.; Ali, Md. E. Quantum Interference and Spin Filtering Effects in Photo-responsive Single Molecular Device *J. Mater. Chem. C* **2021**, *9*, 1242-11251.

- **Bajaj, A.**; Khurana, R.; Ali, Md. E. Auxiliary Atomic Relay Center Facilitates Enhanced Magnetic Couplings in Blatter's Radical *J. Phys. Chem. A* **2021**, *125*, 4133-4142.

- **Bajaj, A.**; Kaur, P.; Sud, A.; Berrita, M.; Ali, Md. E. Anomalous Effect of Quantum Interference in Organic Spin Filters, *J. Phys. Chem. C* **2020**, *124*, 24361-24371.

- **Bajaj, A.**; Ali, Md. E. Tuning of spin-polarized current in high spin organic molecules *Physica B* **2020**, *124*, 412396.

- **Bajaj, A.**; Ali, Md. E. First-Principle Design of Blatter's Diradicals with Strong Ferromagnetic Exchange Interactions. *J. Phys. Chem. C* **2019**, *123*, 15186-15194.

Publications not a part of thesis

- Khurana, R.; **Bajaj, A.**; Ali, Md. E. Tuning the Magnetic Properties of Diamagnetic Di-Blatter's Zwitterion to Antiferro-and Ferromagnetically Coupled Diradicals *Phys. Chem. Chem. Phys.* **2022**, *24*, 2543-2553.

- Khurana, R.; **Bajaj, A.**; Ali, Md. E. How Plausible Is Getting Ferromagnetic Interactions by Coupling Blatter's Radical via Its Fused Benzene Ring? *J. Phys.Chem. A*, **2020** *124*, 6707-6713.

- Ali, S., **Bajaj, A.**; Ali, Md. E. Quantum Interference Controlled Spin-Polarized Electron Transmission in Graphene Nanoribbons *ChemRxiv* **2022**, doi:10.26434/chemrxiv-2022-1wm97.

- Gowri, V.; Jalwal, S.; Dar, A. H.; Gopal, A.; Muthukrishnan, A.; **Bajaj, A.**; Ali, Md. E.; Jayamurugan, G. A subtle change in substituent enabled multi-ways fluorine anion signals including paper-strip colorimetric detection using urea-functionalized push–pull chromophore receptor. *J. Photochem. Photobiol. A* **2021**, *410*, 113163.

- Dar, A. H.; Gowri, V.; Gopal; A.; Muthukrishnan, A., **Bajaj, A.**; Sartaliya, S.; Selim, A.; Ali, Md. E., Jayamurugan, G. Designing of push–pull chromophores with tunable electronic and luminescent properties using urea as the electron donor. *J. Org. Chem.* **2019**, *84*, 8941-8947.

- Shah, S.; **Bajaj, A.**; Shibu, A.; Ali, Md. E.; Neelakandan, P. Iodo-Functionalized Salicylideneimine-Boron Complexes: Synthesis and Photosensitized Degradation of Organic Water Pollutants. *Chem. Eur. J.* **2018**, *24*, 18788-18794.

Author's Biography

Ashima (Reg. No. **PH17226**) joined the **Institute of Nano Science and Technology, Mohali** (INST-Mohali) in January 2018 for her doctoral dissertation by research and registered at the **Indian Institute of Science Education and Research Mohali** (IISER-Mohali) for the award of the ***Degree of Doctor of Philosophy***. She earned her Bachelor of Science (Hons. Physics) degree and Master of Science (Hons. Physics) degree from Panjab University, Chandigarh. Her scientific expertise and area of research include: *Ab Initio* investigation of magnetic and transport properties of organic molecular magnets for potential applications in molecular spintronic devices.